

CREEP OF HI-NICALON^{TM} S CERAMIC FIBER TOWS AT 800°C IN AIR AND IN SILICIC ACID-SATURATED STEAM

DISSERTATION

Scott J. Robertson, Major, USAF

AFIT-ENY-DS-15-S-067

DEPARTMENT OF THE AIR FORCE
AIR UNIVERSITY

AIR FORCE INSTITUTE OF TECHNOLOGY

Wright-Patterson Air Force Base, Ohio

DISTRIBUTION STATEMENT A. APPROVED FOR PUBLIC RELEASE,

DISTRIBUTION UNLIMITED

The views expressed in this document are those of the author(s) and do not reflect the official policy or position of the United States Air Force, Department of Defense, or the United States Government. This material is declared a work of the U.S. Government and is not subject to copyright protection in the United States.

AFIT-ENY-DS-15-S-067

CREEP OF HI-NICALON^{TM} S CERAMIC FIBER TOWS AT 800°C IN AIR AND IN SILICIC ACID-SATURATED STEAM

DISSERTATION

Presented to the Faculty

Graduate School of Engineering and Management

Air Force Institute of Technology

Air University

Air Education and Training Command

in Partial Fulfillment of the Requirements for the

Degree of Doctor of Philosophy

Scott J. Robertson, BSME, MSME

Major, USAF

December 26, 2015

DISTRIBUTION STATEMENT A. APPROVED FOR PUBLIC RELEASE,

DISTRIBUTION UNLIMITED

AFIT-ENY-DS-15-S-067

CREEP OF HI-NICALON^{TM} S CERAMIC FIBER TOWS AT 800°C IN AIR AND IN SILICIC ACID-SATURATED STEAM

Scott J. Robertson, BSME, MSME
Major, USAF

Committee Membership:

Marina B. Ruggles-Wrenn, Ph.D.
Chair

Eric D. Swenson, Ph.D.
Member

Robert L. Hengehold, Ph.D.
Member

Randall S. Hay, Ph.D.
Member

Adedeji B. Badiru, Ph.D.
Dean, Graduate School of Engineering
and Management

Abstract

Ceramic matrix composites (CMCs) derive their exceptional high-temperature properties from the mechanical properties of their fiber and matrix constituents. SiC-based CMCs have better high-temperature properties and significantly outperform oxide CMCs in creep resistance. This is particularly significant in applications where excessive creep can be catastrophic, such as is the case with turbine fan blades. If CMCs are to be safely used in advanced aerospace applications, such as turbine engines, their durability at elevated temperatures and in harsh environments must be assured. To this end, a thorough understanding of degradation and failure mechanisms in SiC fibers under these conditions is imperative. This research effort investigated the mechanical behavior of Hi-Nicalon^{TM} Type S fiber tows, a new type of SiC fiber with great potential for aerospace applications, in air and in silicic acid-saturated steam environments at 800°C. A facility was designed, built and validated that successfully resolved problems highlighted by previous attempts to study SiC fibers in steam. Monotonic tension and creep tests were conducted to characterize the fibers and results were compared to previous work. Environmentally assisted (subcritical) crack growth (EACG) has been shown to cause the tensile strength of ceramic fiber tows to increase with applied stress rate. The tensile strength of the fibers in this work showed little dependence on applied stress rate, indicating a resistance to EACG. Silicic acid-saturated steam had a degrading effect on the mechanical performance of the fibers, but much less than unsaturated steam environments. The Monkman-Grant relationship was demonstrated for Hi-Nicalon^{TM} S fibers and may be used to predict creep lifetime of fibers, fiber tows, and CMCs. Microstructural analysis showed a dependence of oxide thickness on applied stress.

To my mother and father,

who laid a firm foundation for my education and my faith...

To my wife,

who continued my education and enhanced my faith...

To my children,

who added to my education and both required and enhanced my faith...

And to God,

the source of all knowledge and the author and finisher of my faith.

Acknowledgements

This milestone in my life would have been unreachable without the generous and patient help of several people. The technicians in AFIT's Department of Aeronautical and Astronautical Engineering Mechanics of Advanced Aerospace Materials Laboratory were invaluable. BP, CZ, MT, WL, JH, and JS...thank you. Your time, knowledge, patience, and helpfulness have meant and will always mean a lot to me.

I would like to thank the some individuals in the Air Force Research Lab's Materials and Manufacturing Directorate for their academic and technical support. Randy Hay - for his willingness to impart his vast knowledge of ceramics and oxidation kinetics, and to serve on my committee. JP and KS - for the use of and help with the scanning electron microscope.

One of my professors had a profound impact on me. SM, thank you for teaching me to believe and be confident in my own abilities, even in the face of great opposition.

I developed several great friendships during the course of this work. My friends were a great source of comfort and inspiration. KS, MK, SK, and AD, thanks for chatting, supporting, listening, suggesting, and laughing with me through it all.

I'd also like to thank KS for his friendship and brotherhood throughout this process. Not only was he a friend and a brother in Christ, his collaboration on the development of the test facility was a great help. He listened to me, offered great feedback and ideas, and was always quick to get his hands dirty to help. Your encouragement and hands-on support, along with your friendship, meant a lot to me, especially on days when things weren't working.

I would like to thank my committee for their service, excellent questions, and feedback and my advisor for her careful and kind tutelage. She always expressed confidence in me while guiding my learning and growth. She always made herself very available and took whatever time I needed to help me. Thank you!

My family has been a huge support to me throughout this endeavor. It's been fun and challenging for "Dad" to be in school, too, and the kids have been great about it. M, K, E, E, H, and L, thank you for your love and support! I love you! Next to God himself, my wife gets most of the credit for my accomplishment. She has been a joyful, patient, supportive and vocal devoted "fan" of mine for many years and she has only increased her love and support during this challenging and rewarding experience. I cannot adequately express my love for and gratitude towards her.

Foremost above all, my thanks and gratitude are to my Heavenly Father and my Savior, Jesus Christ. Who I am and what I have accomplished is a result of the gifts and talents my Heavenly Father has given me and of the enabling grace of Jesus Christ that has made it possible for me to overcome weakness, fear, and doubt to fully apply those gifts and talents. All praise be to them for the great works they do in my life...indeed, in all our lives.

Scott J. Robertson

Table of Contents

Page

Abstract iv

Acknowledgements vi

List of Figures x

List of Tables xv

List of Abbreviations xvi

List of Symbols xix

I. Introduction 1

1.1 Organization of Dissertation 1
1.2 Ceramic Composite Materials 1
1.3 Motivation 12
1.4 Problem Statement 15
1.5 Material Description 17
1.6 Methodology 18

II. Background 20

2.1 Ceramic Matrix Composites 20
2.2 Non-Oxide (SiC) Fibers 26
2.3 Creep in Ceramics 38
2.4 Environmental Effects on the Durability of SiC Fibers and SiC/SiC CMCs 46
2.5 Implications for Current Research 57

III. Experimental Methods 59

3.1 Creep Testing of Fiber Tows 60
3.1.1 Furnace Temperature Profile 65
3.1.2 Strain Measurement 67
3.2 Creep Testing in Air a Elevated Temperature 71
3.3 Tensile Testing of Fiber Tows 72
3.4 Test Specimen Preparation 73
3.5 Silicic Acid-Saturated Steam Generation 75
3.5.1 Reaching Desired Temperatures 78
3.5.2 Saturating the Steam 86
3.6 Post-Test Microstructural Analysis 88

Page

IV. Mechanical Behavior of Hi-Nicalon^{TM} S Fiber Tows 90

4.1 Tensile Behavior 90
4.1.1 Subcritical Crack Growth Parameters 94
4.2 Creep Behavior 96
4.3 Predicting Creep Lifetime 104
4.4 Creep Rupture and the Monkman-Grant Relationship 107

V. Oxidation Kinetics of Hi-Nicalon^{TM} S Fiber Tows 115

5.1 Verification of Silicic Acid Saturation of Steam 115
5.1.1 Optical Microscopy 115
5.1.2 Scanning Electron Microscopy 117
5.2 Common Features of Oxidized Fibers 124
5.3 Oxidation in Air and Silicic Acid-Saturated Steam 139
5.3.1 Evidence of Preferential Oxide Growth and Crystallization 150

VI. Conclusions and Recommendations 161

6.1 Summary 161
6.2 Conclusions 162
6.3 Contributions 164
6.4 Recommendations for Future Work 166
6.4.1 Oxidation at Lower Temperatures 167
6.4.2 Creep and Oxidation at Higher Temperatures 167
6.4.3 Removal of Sizing 168
6.4.4 Oxidation Kinetics Model 169
6.4.5 "Rogue" Fiber Phenomenon 169
6.4.6 SiC Fiber-Reinforced CMCs 170

Appendix A. Effective Gauge Lengths 171

A.1 Air 171
A.2 Steam 174

Appendix B. SEM Images 178

B.1 Air 178
B.2 Saturated Steam 178
Bibliography 179

Vita 195

List of Figures

Figure		Page
1	Composites Use in Military Aircraft	5
2	Composites Use in Commercial Transport Aircraft	5
3	Notional Comparison of Stress-strain Behaviors	6
4	Strength-to-Weight Ratios of Engineering Materials for Aerospace Applications	7
5	Failure of CFCCs with Strong and Weak Interface Bonding	10
6	Design Methods for Damage Tolerant CMCs	11
7	Fiber Pullout	21
8	Current Design Philosophies for Damage Tolerant CMCs	22
9	Fugitive Coating Interface	23
10	Environmental Degradation due to Oxidation in SiC CMCs	25
11	Yajima Process for Making SiC Fibers	27
12	Microstructures of Nicalon^{TM} Fibers	30
13	Hi-Nicalon^{TM} S Production Process	31
14	Temperature-Dependent Fiber Strength	33
15	Creep of SiC Fibers	34
16	Phases of Creep	39
17	Creep of Two 3rd-Generation Fibers	44
18	Creep of Hi-Nicalon^{TM} S Fiber Tows (Steffens)	45
19	Creep of Hi-Nicalon^{TM} S Fiber Tows (Shillig)	46
20	Two-Zone Furnace	62
21	Susceptor & Feed Tube Assembly	63

Figure Page

22 Creep Test Facility . . . 64

23 Temperature Profiles in Air . . . 66

24 Temperature Profiles in Saturated Steam . . . 67

25 MTS Tensile Test Facility . . . 73

26 Fiber Tow Specimen Preparation . . . 74

27 Steam Generator . . . 76

28 Effect of Steam Impinging on Fiber Tows . . . 77

29 Steam Bleed-off Assembly . . . 84

30 Steam Bleed-off Tube . . . 85

31 Saturated Steam Creep Test Facility . . . 86

32 Steam Saturation Chamber . . . 87

33 AFIT Optical Microscope . . . 88

34 AFIT SEM . . . 89

35 Failure Stress as a Function of Stress Rate in Air . . . 92

36 Failure Stress as a Function of Stress Rate in Silicic Acid-Saturated Steam . . . 92

37 Creep Strain Rates of Hi-Nicalon^{TM} S Fiber Tows . . . 99

38 Creep Lifetimes of Hi-Nicalon^{TM} S Fiber Tows . . . 101

39 Creep of Hi-Nicalon^{TM} S Fiber Tows in Air . . . 102

40 Early Creep of Hi-Nicalon^{TM} S Fiber Tows in Air . . . 102

41 Creep of Hi-Nicalon^{TM} S Fiber Tows in Silicic Acid-Saturated Steam . . . 103

42 Early Creep of Hi-Nicalon^{TM} S Fiber Tows in Silicic Acid-Saturated Steam . . . 103

43 Comparison of Predicted and Experimental Lifetime Data . . . 106

Figure Page

44 Monkman-Grant Plot for Hi-Nicalon^{TM} S SiC Fiber Tow Specimens 110

45 Monkman-Grant Plot for Hi-Nicalon^{TM} S SiC Fiber Tow Specimens 111

46 Monkman-Grant Plot for SiC Fiber Tows and SiC/SiC CMCs 113

47 Constructive and Destructive Interference in Light 116

48 Variations Along the Fiber Tow in Unsaturated Steam 118

49 Fiber Appearance in Lower Section 118

50 Fiber Appearance in Center Section 119

51 Fiber Appearance in Upper Section 119

52 Compositional Spectrograph of Light Fiber Surface 120

53 Compositional Spectrograph of Dark Fiber Surface 121

54 Compositional Spectrograph of Fiber Cross-Section 122

55 Common Fiber Tow Surface Features 123

56 Smooth Surface of Fibers 125

57 Brittle Fracture in Air 126

58 Brittle Fracture in Silicic Acid-Saturated Steam 127

59 Fracture due to Fiber Interactions 128

60 Fiber Interactions 129

61 Rough Dark Area 130

62 Fracture Surface Near Rough Dark Area 131

63 Silica Deposits - Tendrils 132

64 Silica Deposits - Crystals 133

65 Fracture in Air due to Contaminants 134

Figure Page

66 Contaminant Effects in Air 135

67 Contaminant Effects in Silicic Acid-Saturated Steam 136

68 "Rogue" Fibers in Air 137

69 "Rogue" Fibers in Silicic Acid-Saturated Steam 138

70 Schematic of Basic Oxidation 140

71 Schematic of TEM Image 147

72 Optical Image of Rogue Fibers 151

76 Optical Image of Rogue Fibers from Parallel Study, 700°C 154

77 Optical Image of Rogue Fibers from Parallel Study, 800°C 154

78 Compositional Spectrograph of "Rogue" Fiber 157

79 Silica Phase Diagram 158

80 Silicic Acid Equilibrium Partial Pressures 159

A.1 Effective Gauge Length in 400°C Air 171

A.2 Effective Gauge Length in 500°C Air 171

A.3 Effective Gauge Length in 600°C Air 172

A.4 Effective Gauge Length in 700°C Air 172

A.5 Effective Gauge Length in 800°C Air 173

A.6 Effective Gauge Length in 900°C Air 173

A.7 Effective Gauge Length in 1000°C Air 174

A.8 Effective Gauge Length in 400°C Saturated Steam 174

A.9 Effective Gauge Length in 500°C Saturated Steam 175

A.10 Effective Gauge Length in 600°C Saturated Steam 175

A.11 Effective Gauge Length in 700°C Saturated Steam 176

Figure Page

A.12 Effective Gauge Length in 800°C Saturated Steam 176

A.13 Effective Gauge Length in 900°C Saturated Steam 177

A.14 Effective Gauge Length in 1000°C Saturated Steam 177

List of Tables

Table		Page
1	Applications of CFCCs	8
2	Characteristics of CMCs	9
3	Test Material Properties	18
4	Chemical Composition and Temperature Limits of SiC Fibers	32
5	Mechanical Properties of SiC Fibers	32
6	Creep Mechanisms in Ceramics	42
7	Creep Parameters for Non-Oxide Fibers	43
8	Effective Gauge Lengths	71
9	Constant Stress Rate Tensile Strength at 800°C	91
10	Subcritical Crack Growth Parameters at 800°C	96
11	Creep Results at 800°C	98
12	Predicted Creep Lifetimes at 800°C	106
13	Preliminary TEM Results at 800°C	148

List of Abbreviations

Abbreviation		Page
GFRP	Glass Fiber Reinforced Plastic	3
USAF	United States Air Force	4
CMCs	Ceramic Matrix Composites	6
CFCCs	Continuous Fiber Ceramic Composites	8
C	Carbon	9
SiC	Silicon Carbide	9
Si_3N_4	Silicon Nitride	9
AFIT	Air Force Institute of Technology	13
$Si[OH]_4$	Silicic Acid	14
SEM	Scanning Electron Microscope/Microscopy	24
BN	Boron Nitride	24
TiB_2	Titanium Diboride	25
CVD	Chemical Vapor Deposition	26
MMC	Metal Matrix Composite	27
PCS	Polycarbosilane	27
SiO_2	Silica	28
Ti	Titanium	28
GPa	Gigapascals (10^9 pascals)	28
msi	Megapounds per square inch (10^6 psi)	28
CVI	Chemical Vapor Infiltration	28
PIP	Polymer Infilitration and Pyrolysis	28
wt%	Weight %	28

Abbreviation		Page
nm	Nanometer (10^{-9} meters)	29
ksi	Kilopounds per square inch (10^3 psi)	29
kJ	Kilojoules	29
Btu	British Thermal Unit	29
μm	Micron or Micrometer (10^{-6} meters)	32
mm	Millimeter	32
in.	Inch	32
RT	Room Temperature	32
MPa	Megapascals (10^6 pascals)	38
h	Hours	38
GBS	Grain Boundary Sliding	40
LD	Lattice Diffusion	42
GBD	Grain Boundary Diffusion	42
IR	Interface Reaction	42
Ar	Argon	42
SCC	Stress Corrosion Cracking	47
EACG	Environmentally Assisted Crack Growth	47
CO	Carbon Monoxide	49
H_2O	Water	49
vol%	Volume %	49
atm	Atmosphere	49
O_2	Oxygen	50
HP-Ar	High-Purity Argon	50
ppm	Parts Per Million	50

Abbreviation		Page
UHP-Ar	Ultra-High-Purity Argon	50
ppb	Parts Per Billion	50
KJMA	Kolmogorov-Johnson-Mehl-Avrami	52
MI	Melt-Infiltration	54
3D	Three-Dimensional	54
TEM	Transmission Electron Microscopy	60
ENY	Department of Aeronautics and Astronautics	60
g	Grams	61
psi	Pounds per square inch	61
LVDT	Linear Variable Differential Transformer	61
AFRL	Air Force Research Laboratory	88
CTE	Coefficient of Thermal Expansion	97
LEFM	Linear Elastic Fracture Mechanics	104
EDS	Energy Dispersive Spectroscopy	115
PVA	Polyvinyl Alcohol	136
TEM	Transmission Electron Microscopy	139
EBC	Environmental Barrier Coating	162

List of Symbols

Symbol		Page
$\dot{\varepsilon}$	Strain Rate	41
B	Power Law Creep Constant	41
D	Diffusion Coefficient	41
μ	Shear Modulus	41
b	Magnitude of the Burgers Vector	41
k	Boltzmann Constant	41
T	Absolute Temperature	41
d	Grain Size (Diameter)	41
σ	Applied Tensile Stress	41
p	Power Law Creep Grain Size Exponent	41
n	Power Law Creep Stress Exponent	41
D_o	Diffusion Coefficient Frequency Factor	41
Q	Activation Energy	41
R	Universal Gas Constant	41
A	Temperature-dependent Coefficient in Norton-Bailey Power Law	45
v	Crack Velocity	94
a	Crack Size	94
t	Time	94
K_I	Mode I Stress Intensity Factor	94
K_{IC}	Critical Stress Intensity Factor or Fracture Toughness	94
M	Slow Crack Growth Parameter	94
m	Slow Crack Growth Parameter	94

Symbol		Page
Y	Crack Growth Geometry Factor	95
σ_f	Degraded Fracture Strength under Slow Crack Growth	95
σ_i	Degraded Fracture Strength under Slow Crack Growth	95
B	Material and Environment Parameter	95
C	Slow Crack Growth Parameter	95
Δt	Change in Temperature	97
$\Delta \epsilon$	Change in Strain	97
t_f	Time to Failure	104
K_{Ii}	Initial Stress Intensity Factor	104
q	Monkman-Grant Parameter	108
G	Monkman-Grant Parameter	108
F_1	Mass Transport Flux at Gas-Oxide Interface	140
F_2	Diffusion Flux through Oxide Layer	140
F_3	Oxidation Reaction Rate	140
h	Gas-Phase Transport Coefficient	140
C_0	Concentration of Oxidant on the Oxide Surface	140
C^*	Equilibrium Concentration of Oxidant in the Oxide Layer	140
D_{eff}	Effective Diffusion Coefficient	141
C_i	Oxidant Concentration near the Oxide-Material Boundary	141
x_0	Oxide Thickness	141
k	Rate Coefficient for a Specific Oxidant-Oxidizing Material Pair	141
F	Steady-State Flux	141

Symbol		Page
N_1	Number of Oxidant Molecules/Unit Volume of Oxide	141
x_i	Initial Oxide Layer Thickness	141
τ	Time Shift Associated with Initial Oxide Layer	142
B	Parabolic Rate Constant	142
k_f	Rate Coefficient for a Specific Oxidant-Oxidizing Material Pair	143
k_r	Rate Coefficient for Out-Diffusing of Oxidation Reaction Byproduct	143

CREEP OF HI-NICALON^{TM} S CERAMIC FIBER TOWS
AT 800°C IN AIR AND IN SILICIC ACID-SATURATED STEAM

I. Introduction

1.1 Organization of Dissertation

In the first chapter of this prospectus, an overview of the history of ceramic composite materials is presented, with an emphasis on their use in engineering applications. The motivation for the current research and the problem statement are then given. An introduction to the material and to the experimental methodology are also provided.

Chapter two provides a general background of engineered ceramic matrix composites and the research conducted in this field to date. A detailed description of the experimental methods and facilities is given in chapter three for this research. Concluding remarks are offered in chapter four.

1.2 Ceramic Composite Materials

Since the dawn of time, mankind has used its gifts of reason and intellect to continuously find more effective and efficient ways of accomplishing its desires. Whether driven by survival instincts, grand visions of a better world, or something in between, mankind has succeeded time after time in finding a better way, improving on what has been done in the past. This has led to the countless process, design, and material improvements that add up to the world as it is today. Looking back, it is clearly evident that the development of new materials and new material processing techniques

has been a large part of what has happened since the invention of hand tools and the wheel. Indeed, history is marked by these material developments: the Stone Age, the Bronze Age, and the Iron Age.

This legacy continues today, with more emphasis than ever on materials development. As the performance limits of monolithic materials have been reached in many engineering applications over the past century, materials scientists and engineers have had to develop ways of combining different materials to achieve desired properties. As one author put it, "The world is currently at a time where technology is driven by harnessing the individual performance characteristics of two or more constituent materials in a synergistic mass, [sic] hence what may be called 'The Composite Age'" [1].

Due to the somewhat ambiguous nature of the term "composites," it is helpful to clarify what is meant by the term. Clauser gives a good definition, "...a mixture of macroscopic phases that are composed of materials in a divided state that generally differ in form or in chemical composition or in both" [2]. The emphasis, here, is on the macroscopic phases of the material, and not the microstructure.

Designs that use composite materials to accomplish this synergistic combination of individual properties have appeared throughout history. One of the earliest recorded instances is that of Egyptian brick making. As far back as approximately 1500 BC, Egyptians added straw to clay for bricks [3]. This method achieved the desired strength of the bricks without the need to fire them in a kiln, enabling the Egyptians to build structures that have lasted for millennia [4]. Another recorded use of composite materials is by the Mongols of Genghis Khan to make bows in the 12th century AD. In this case, layers of cattle tendon and horn were placed on opposite sides of bamboo and affixed using a wrapping made of silk and pine rosin [2, 5, 6]. Recently, some

surviving bows of this period were restrung and tested, coming it at an impressive 80% (approximately) of the strength of composite bows of today [6].

Despite these and other examples, the vast majority of materials development in history has focused on naturally occurring and monolithic materials, rather than composites, up until the latter half of the 19th century and particularly in the 20th century. Early examples of composites in the late 1800's are reinforced concrete, laminated wood (plywood), linoleum, and plasterboard [2]. However, it was the rise of the aircraft industry that caused composite material development to take off and World War II that caused an explosion in the industrial development and production of composites. In the late 1930's, Douglas Aircraft used fiberglass with phenolic resin to make reinforced plastic dies for forging prototype aircraft parts [536]. This proved to be much faster and easier than the traditional metal dies and use of reinforced plastic in other aircraft tooling soon followed. The 1930's and 1940's also saw the advent of honeycomb structures and Glass Fiber Reinforced Plastic (GFRP), which became commercially viable in 1939 [2, 7].

During World War II, aircraft were being designed and manufactured very rapidly, almost "on the fly." Ducting tended to be one of the last considerations in the design process. The ducts had to fit in to whatever space was left, often resulting in very complex geometries difficult to fabricate out of traditional materials (metals). Composites were used, instead, due to the ease of manufacture and light-weight [8]. Other aircraft uses for composites were in engine nacelles (light-weight), radomes (radar transparent), and in one instance, even a wing box beam (stiff, light-weight). Some non-aircraft uses were cotton-phenolic ship bearings, asbestos-phenolic switchgears, cotton/asbestos-phenolic brake linings, and cotton-acetate bayonet scabbards [8].

In 1942, as US involvement in World War II ramped up, there began to be a concern about the availability of metal supplies for the war effort. In response to this con-

cern, the US Government instructed engineers at Wright Field, now Wright-Patterson Air Force Base, to survey composites manufacturers and develop best practices, recognizing that composites could fill supply gaps left by insufficient metal supplies [8]. This cemented the prominence of composites in modern design for engineering applications.

After the war, cars and boats began to be made with composite bodies, but it was the space race and booming aircraft industry that continued to drive composite material development. The 1950's and 1960's saw rocket motor casings made of composites using filament winding [8], metal and then ceramic rocket nose caps [9], and the development of carbon, boron, and aramid (Kevlar^{TM}) fibers [8, 10]. According to Scala, the driving factors through this time period were threefold: a demand for lighter weight, stiffer material, a strong US economy, and solid-state theory predictions that materials with extremely high tensile strength and elastic modulus (crystals) were possible [9].

Since 1965, when the United States Air Force (USAF) embarked on a major effort to turn high-performance fiber composites into a reality [2], the Air Force and its partners have been at the forefront of composite material development for high-performance engineering applications. Composites have been used extensively in both military and commercial transport aircraft. Figures 1 and 2 show the progression of composite use in aircraft in the past 50 years.

Though composites got their start in the defense and aerospace industries, the majority of the market in the 21st century is not in defense and aerospace. As reported by Strong in 2002:

> "...the largest market is still in transportation (31%), but construction (19.7%), marine (12.4%), electrical/electronic equipment (9.9%), consumer (5.8%), and appliance/business equipment are also large markets. The aircraft/aerospace market represents only 0.8%[,] which is surprising in light [of] its importance in the origins of composites." [8]

This shift in market share illustrates commercialization of composite materials and the comparatively low output of defense and aerospace applications.

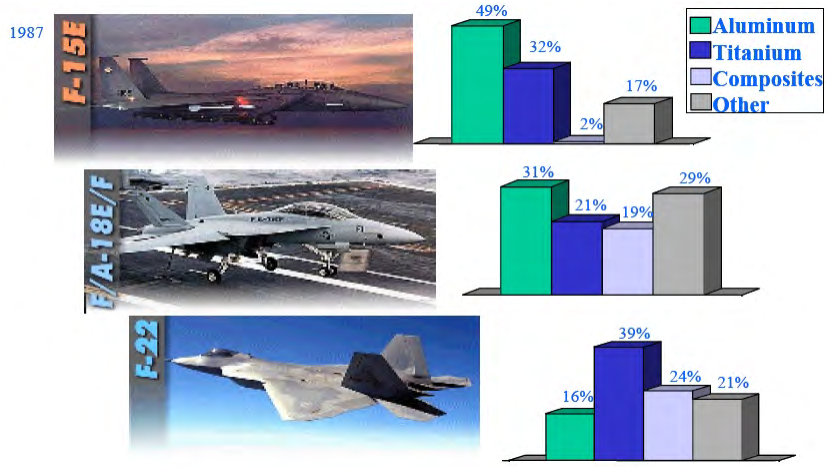


Figure 1. Composites Use in Military Aircraft. Note the dramatic increase in just 30 years. Reproduced from [11].

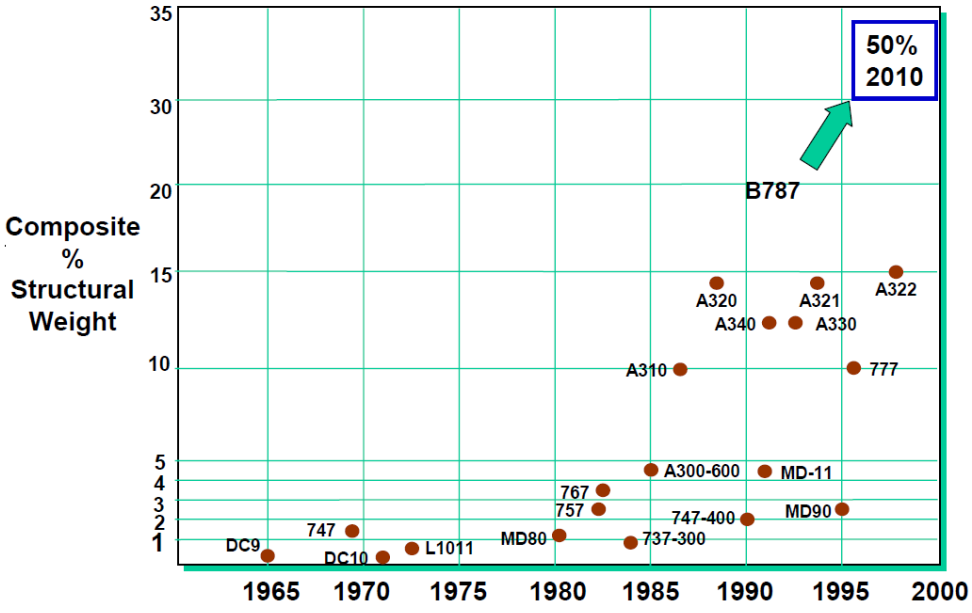


Figure 2. Composites Use in Commercial Transport Aircraft. Again, note the dramatic increase in the past 50 years. The Boeing 787 did indeed reach 50% composites by weight. Reproduced from [11].

As mentioned earlier, one of the motivations for the development of composites was the demand for lighter, stiffer materials, particularly ones that could maintain

their properties at high temperatures and in corrosive environments. This demand drove research and development toward ceramics with some success. Engineered ceramics have been used in structural components in harsh environments like gas turbine engines, exhaust nozzles, space, nuclear power plants, and biomedical [4, 12]. However, although exhibiting excellent corrosion resistance, high-temperature strength, low density, and high stiffness, monolithic ceramics are particularly susceptible to sudden brittle fracture.

Another driver was theoretical predictions of materials with extremely high tensile strength and elastic modulus, i.e. orders of magnitude higher than current materials. Materials with properties approaching these theoretical predicted values have been demonstrated with single crystal and glass ceramics, but only on a such a small scale as to make them impractical. At larger scales, it becomes quite challenging to eliminate flaws. In the presence of small flaws, not only will monolithic ceramics experience catastrophic failure as depicted in Figure 3, but they will fail at stresses much lower than theoretical predicted values.

Producing ceramics of any useful size without these flaws has proven an elusive goal. As a result, the research for the last few decades, especially for advanced engineering applications, has focused on finding ways to decrease the susceptibility to flaws, leading to the development of Ceramic Matrix Composites (CMCs).

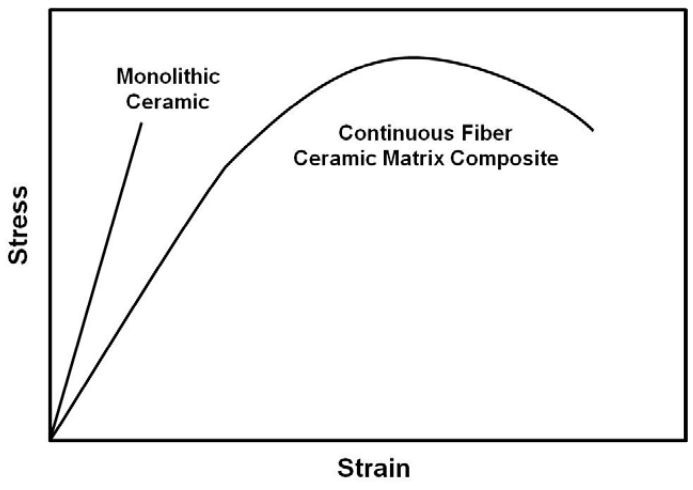


Figure 3. Notional comparison of stress-strain behaviors of a monolithic ceramic and a CMC, reproduced from [4]

CMCs have successfully bridged the gap, maintaining sufficient flaw tolerance (toughness or damage tolerance) to avoid sudden catastrophic failures and fail gracefully (Figure 3), while still providing the desired strength, weight, and high-temperature properties [13], as shown in Figure 4.

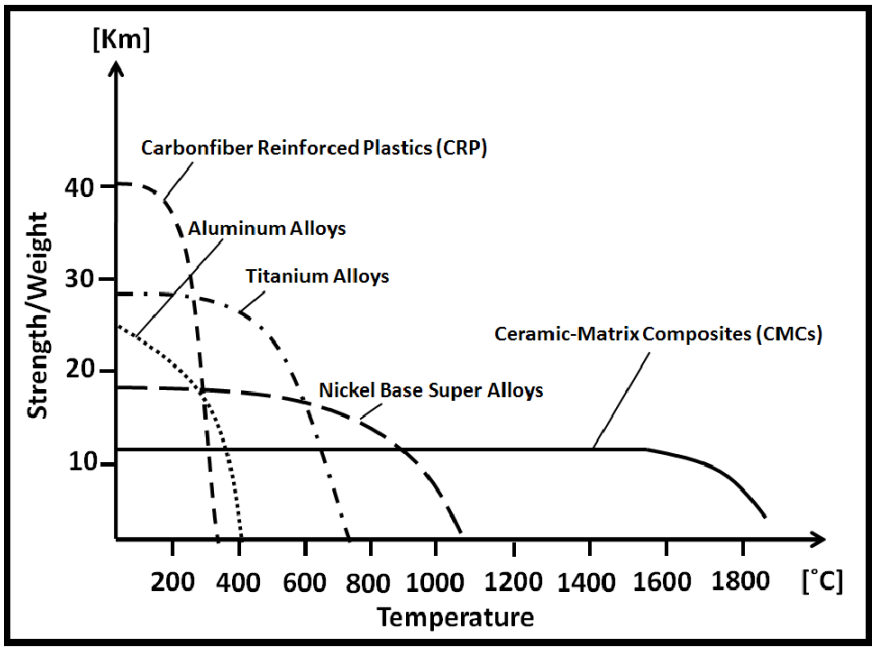


Figure 4. Strength-to-weight ratios of engineering materials for aerospace applications. Note the significant improvement of CMCs over traditional materials at high temperatures. Reproduced from [13], pg. 410, Copyright ©2004, with permission from Elsevier and from the original author [14].

CMCs are prime candidates for applications such as hypersonic aircraft, rockets, jet and gas turbine engines, spacecraft shielding, fusion reactors, furnaces for heat treatment, and aircraft brakes [12, 15–17]. Indeed, as of 2001, CMCs were being evaluated for use in various parts of hypersonic aircraft including leading edges, nose sections, inlet cowlings, and nozzles [15]. Use in engines can result in increased fuel efficiency and the elimination of cooling systems [12, 18]. Other applications are listed in Table 1.

Table 1. Applications of Continuous Fiber Ceramic Composites, reproduced from [15]

Applications / Sectors	Continuous Fiber CMCs		
MILITARY	• F414 and F110 Nozzle Flaps and Seals • F117 Aft Deck Heat Shields • Engine Vanes • Flame Holders	• Orbital Transfer Engine Thrusters • Low Cost Large Rocket Thruster (Million Pound) Heavy Lift Launch • Tactical Missile Combustors, Rotors • Divert and Attitude Control Thrusters	• Turboramjet Variable Area Nozzles • Surveillance OTV Thrusters • Hypersonic Leading Edges, Inlet Cowlings and Nozzles • Linear Aerospike Engine, Thrust Cells and Ramp
Commercial/Dual Use	• Heat Exchangers • Radiant Burner Tubes • Land-Based Gas Turbines • Candle Filters	• MDH Air Preheater Tubes • Immersion Heaters • Seal-less Magnetic Pumps • Motorcycle Brakes	• Diesel Components • Valve Guides • Pistons • Turbocharger Rotors

There are two types of CMCs: Discontinuous Reinforced and Continuous Fiber. Discontinuous CMCs are reinforced with particulate, platelet, whisker, fiber and in situ second phases [15] and tend to be somewhat limited in their benefits over monolithic materials [17]. Continuous Fiber Ceramic Composites (CFCCs), though more expensive, are in general significantly better than their monolithic counterparts [17]. Table 2 breaks CFCCs into carbon fiber reinforced carbon composites and other continuous fiber ceramic composites and lists the differing characteristics of the various types of CMCs. Though discontinuous CMCs can reach strengths approaching 1000 MPa (145 ksi), two to three times that of CFCCs, their fracture toughness is approximately one third that of CFCCs [15]. As a result, designs of advanced CMCs for harsh environments overwhelmingly favor CFCCs, and this will be the focus moving forward.

Fibers are generally classified into oxide and non-oxide categories. Whereas oxide fibers are much more resistant to oxidizing and corrosive environments than non-

Table 2. Characteristics of Ceramic Matrix Composites, reproduced from [15]

Carbon-Carbon	Continuous CMCs	Discontinuous CMCs
Exceptional High Temp Mech Properties	Excellent High Temp Mech. Properties	Excellent High Temp Mech Properties
High Specific Strength and Stiffness High Fracture Toughness	High Specific Strength and Stiffness High Fracture Toughness	High Specific Strength and Stiffness Higher Useful Strengths.
Dimensional Stability Low Thermal Expansion	Dimensional Stability Low Thermal Expansion	Fracture Toughness Good but Inferior to Continuous CMCs
High Thermal Shock Resistance Graceful Failure Modes	Good Thermal Shock Resistance Graceful Failure Mode	Thermal Shock Resistance Inferior to Continuous CMCs
Tailorable Properties Machinability Poor Oxidation Resistance	Oxidation Resistance Machining More Difficult Processing More Complicated and Expensive	Amenable to Cheaper Conventional Processes Machining Expensive

oxide fibers, non-oxide fibers tend to have better strength and creep characteristics and better thermal conductivity, especially at high temperatures [19, 20]. Examples of oxide fibers are silica (SiO_2) and alumina (Al_2O_3). Examples of non-oxide fibers include carbon (C), silicon carbide (Silicon Carbide (SiC)) and silicon nitride (Silicon Nitride (Si_3N_4)).

CFCCs achieve improved flaw/damage tolerance over monolithic ceramics by enabling cracks to propagate without sudden catastrophic failure. They accomplish this by deflecting cracks propagating through the matrix around the reinforcing fibers and by mechanically isolating fibers from one another, allowing them to fail individually over time and not all together, as happens in a brittle failure, as shown in Figure 5a. When cracks are deflected around the fibers, debonding of the fiber-matrix interface, crack bridging, and fiber pullout occur, resulting in additional energy absorption and higher overall energy required to cause failure (i.e. greater toughness) [12].

Crack deflection and fiber isolation have been accomplished in multiple ways, the more common of which are through fiber coating or the use of a porous matrix [4, 16]. Fiber coating was a serendipitous discovery by Prewo and Brennan while using Nicalon^{TM} fibers to reinforce a borosilicate matrix [21, 22]. By applying a thin coating to the reinforcing fiber, a relatively weak interface bond is created between

the coated fiber and the matrix. While the matrix is able to transfer load to the fibers, this bond is sufficiently weak to allow the matrix to debond from the fiber in the presence of an advancing crack tip, thereby deflecting the crack along or around the fiber, rather than allowing the crack to proceed through the fiber [4, 12, 16]. Since the fiber remains intact, so does its load-carrying capability. This behavior is depicted in Figure 5b and Figure 6a. A secondary benefit to this method is that the coating can also protect the fiber from corrosive and oxidizing environments, thus prolonging the life of the fiber and, hence, the CMC.

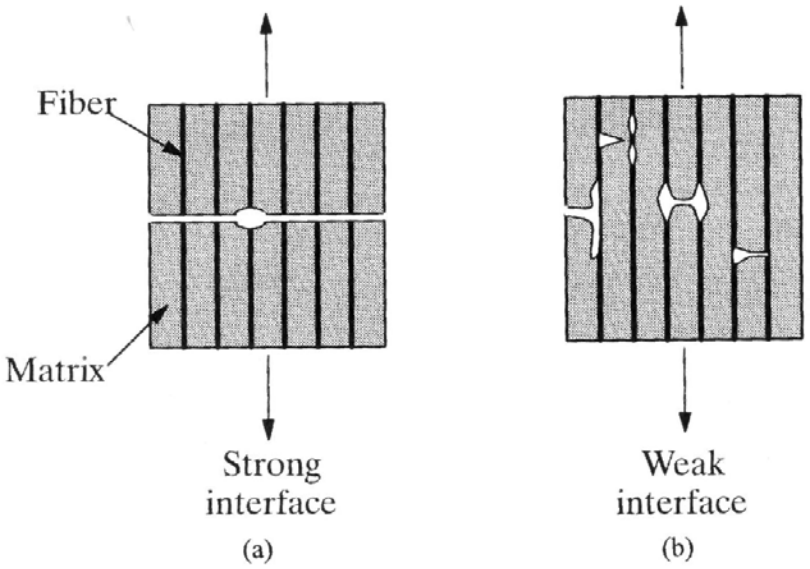


Figure 5. Failure of CFCCs showing crack propagation for strong and weak interface bonding. Reproduced with kind permission from Springer Science & Business Media B.V. [12] pg. 148, Chapter 5: Interface, Figure 5.6. Copyright ©2003 by Kluwer Academic Publishers. All rights reserved. No part of this work may be reproduced, stored in a retrieval system, or transmitted in any form or by any means, electronic, mechanical, photocopying, microfilming, recording or otherwise, without the written permission from the Publisher, with the exception of any material supplied specifically for the purpose of being entered and executed on a computer system, for exclusive use by the purchaser of the work.

The second approach to damage tolerant design of CMCs eliminated the need for a weak fiber-matrix interface and, thus, a fiber coating. This approach is helpful because of the challenges involved in the uniform application of coatings to fibers, and particularly so for oxide fibers because coatings that meet the requirements for oxide

fibers have not been widely developed [16]. This method employs a porous matrix, as seen in Figure 6b, rather than the dense matrix of the CMCs designed using the fiber coating approach. Here, a balance is struck such that the matrix is sufficiently strong to transfer load to the fibers and to support off-axis loads, but weak enough that it takes less energy for a propagating crack to deflect around a fiber, staying within the matrix, than it would to continue through the fiber [4, 16]. However, it is not straightforward to achieve this balance.

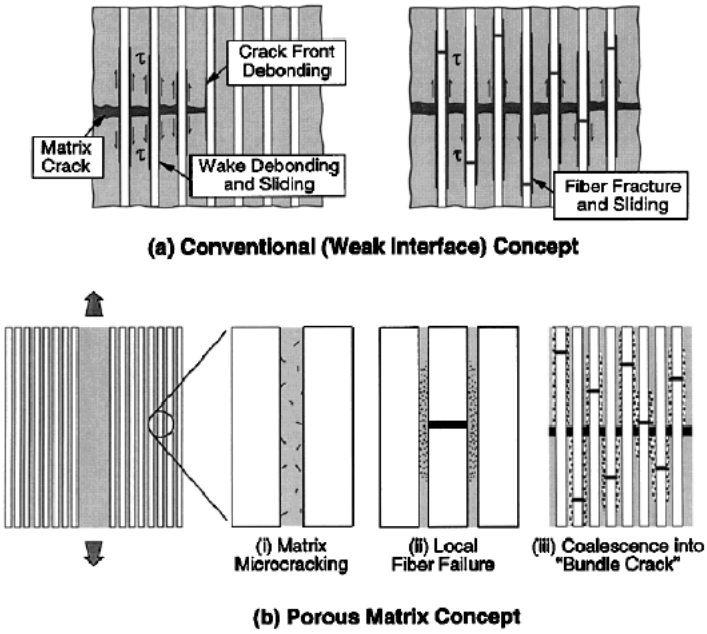


Figure 6. Design Methods for Damage Tolerant CMCs: a) fiber coating with weak fiber/matrix interface and b) porous matrix [16], reproduced with permission from Wiley.

Much progress has been made in developing damage tolerant CMCs using both of these approaches. The fiber coating approach is typically employed to produce non-oxide fiber/non-oxide matrix CMCs, whereas the porous matrix approach is used to produce oxide-oxide CMCs. Generally speaking, the fiber coating approach, which has been explored widely for SiC fibers, yields CMCs with superior high-temperature properties, particularly with respect to creep, but the porous matrix method is more

affordable [16]. This same comparison is true for non-oxide and oxide CMCs. Non-oxide fiber/non-oxide matrix CMCs consistently outperform oxide-oxide CMCs in strength and creep at high temperatures, but they are more expensive and highly susceptible to oxidizing and corrosive environments.

1.3 Motivation

Ceramic matrix composites derive their exceptional high-temperature properties from the mechanical properties of their fiber and matrix constituents and from the manner in which those constituents are joined to make the CMC. Oxide materials are naturally resistant to oxidation, which enables them to retain their high-temperature properties better than non-oxide materials that are more susceptible to oxidation. However, coatings have been developed that shield non-oxide fibers from the oxidizing environment and slow their oxidation.

Non-oxide materials have better overall high-temperature properties and significantly outperform oxide materials in creep resistance. This is particularly significant in applications where excessive creep can be catastrophic, such as is the case with turbine fan blades. The rotation of the turbine creates a tensile load within each fan blade. Over time, the total accumulated creep deformation will be sufficient for the fan blade to contact the wall of the turbine, causing significant wear and eventual fracture of the fan blade. At the high angular velocity of turbines, this results in significant damage. If the tensile creep rate is high, the fan blades must be replaced more frequently to avoid this type of catastrophic failure.

If CMCs are to be safely used in advanced aerospace applications, such as turbine engines, their durability at elevated temperatures and in harsh environments must be assured. To this end, a thorough understanding of degradation and failure mechanisms in non-oxide fibers under these conditions is imperative. Previously, two

preliminary studies were conducted by Steffens and Shillig at the Air Force Institute of Technology (AFIT), on the creep behavior of the non-oxide fiber Hi-Nicalon^{TM} S at 800 and 1100°C [1] and at 800, 900, 1000, and 1100°C [23] in air and steam. These efforts provided valuable insight into the facility and procedural challenges associated with testing this non-oxide fiber, but they were unable to resolve those challenges and provide significant insight into the mechanical performance and oxidation mechanisms.

Steffens applied the test methodology developed by Armani for testing of oxide fiber tows [4] to test SiC-based fiber tows in air and in steam. He identified problems with the steam delivery system that caused all of the test specimens to fail at the steam point of entry. Steffens recommended testing over a broader range of test temperatures and conducting a thorough analysis of the microstructure of tested fiber tows. Shillig attempted to perform both of these tasks. However, Shillig's test results were inconsistent with those obtained previously under similar load and environmental conditions. In addition, sodium and aluminum contaminants were detected on many of the fiber tows tested in steam [23]. As a result, it was not possible to definitively identify creep mechanisms or to assess creep performance of the fiber tows. Nevertheless, Shillig was able to solve the problem with the steam delivery system by modifying the feeding tube such that flow of the steam was deflected away from the fiber tow, rather than impinging on it. This modification led to a more realistic distribution of fiber failure locations. Post-test microstructural investigation of Steffens' fiber tow specimens revealed that the effects of steam on fiber microstructure varied along the length of the fiber tow. Specifically, portions of the fiber tow located at the top of the hot zone were affected differently than those at the bottom of the hot zone. The steam enters at the bottom and travels up through the test chamber along the fiber tow. The hot zone consists of a 60 - 70 cm portion of the test chamber where the

fiber tow temperature is uniform at the test temperature, within about one percent (5-10°C). Fiber degradation, as evidenced by pitting and cross-section reduction, were readily apparent at the lower end, whereas no significant loss of cross-section was apparent in the upper end. The observed differences suggest that the steam is chemically altered as it travels along the fiber tow, leeching Si from the fiber tow and becoming saturated with silicic acid ($Si[OH]_4$) as it reaches the top of the hot zone. It is thought that this same saturation also takes place in the operational environment. As steam moves along the surface of a SiC-based CMC and down through cracks in the surface, it becomes saturated with silicic acid. This would suggest that the reinforcing fibers are exposed to silicic-acid saturated steam, rather than unsaturated steam. Shillig recommended heating the steam to test temperature and saturating it with $Si[OH]_4$ before it enters the test chamber, but did not test his recommendation.

This research effort aimed to solve the test facility and methodology problems that Steffens and Shillig identified in order to enable meaningful, repeatable testing of SiC fiber tows at elevated temperature in air and in steam. It was proposed to design, develop, build, and validate a test facility and methodology and use it to evaluate the mechanical performance, creep behavior, and creep mechanisms of the non-oxide fiber Hi-Nicalon^{TM} S at 800°C in air and in heated, silicic acid-saturated steam. Mechanical testing of SiC fiber tows in steam at elevated temperatures is not a trivial matter. Control of the temperature and containment of the corrosive high-temperature steam are problematic. The two main challenges to overcome were to develop an approach to preheat the steam to test temperature and to saturate the steam prior to introducing the steam into the test chamber. These challenges were overcome and the test facility and methodology were validated.

Hi-Nicalon^{TM} S fibers are known to have excellent creep resistance [19], better than most other non-oxide fibers and significantly better than oxide fibers. These

fibers have a near-stoichiometric SiC composition (~1 at% oxygen and ~2 at% carbon) [24], so they are a strong candidate for use in advanced CMCs. There is a good understanding of SiC oxidation kinetics, but not in a stressed state. Understanding oxidation in the stressed state is of interest because the advanced engineering applications for which CMCs are being considered are structural in nature and the materials will experience significant stresses while exposed to oxidizing environments. Additionally, stress concentrations due to small flaws or damage are unavoidable in CMCs. These concentrations of (tensile) stress increase the oxidation rate [25–27]. As such, there is considerable need to understand the stressed oxidation kinetics of the Hi-Nicalon^{TM} S fibers in order to improve the oxidation resistance of CMCs reinforced with these fibers and to develop models that accurately predict the effects of stressed oxidation on the mechanical performance of these CMCs. To this end, the post-test microstructure was examined in order to determine damage and failure mechanisms.

1.4 Problem Statement

The work by Steffens [1] showed that the methodology used by Armani for investigating the high-temperature performance of oxide fibers would not work for non-oxide fibers. Shillig [23] provided additional insight into the challenges with the test methodology and identified further challenges. Each of these efforts constituted an important step forward in understanding the needs for testing SiC fiber tows. The next step was to overcome the challenges Steffens and Shillig identified in a repeatable way, so as to enable meaningful investigation of the mechanical behavior of Hi-Nicalon^{TM} S fiber tows at elevated temperature in steam. Developing a test facility and methodology that overcomes these challenges had to be done in order to elucidate dominant creep mechanisms and gain insight into the interaction between creep and the oxi-

dation process. The experimental results obtainable from such a facility can provide the basis for and guide the development of the predictive models and manufacturing process, leading to more capable CMCs for a wide variety of applications.

The main objective of this research effort had two parts. The first part was to design, develop, build, and validate a test facility and methodology for mechanical testing of Hi-Nicalon^{TM} S SiC fiber tows at elevated temperature in air, preheated steam, and preheated silicic acid-saturated steam. Since the experimental facility designed by Armani for testing of oxide fiber tows was shown by Steffens [1] and Shillig [23] to be inadequate for testing of higher strength non-oxide fiber tows in steam, this facility had to be completely redesigned. The test method developed in this work enables testing of fiber tows at temperatures up to and including 1000°C in air, steam, and silicic acid-saturated steam environments, while permitting accurate load control and, most importantly, accurate strain measurement. The steam delivery system used by Steffens and Shillig introduced steam at approximately 100°C into the test chamber, where the steam was further heated to the test temperature. In this study, the steam delivery system was redesigned in order to introduce steam into the test chamber already at or near the test temperature. The design was successful and results are discussed.

The second aspect of the main objective of this effort was to study the effect of steam on the mechanical performance of Hi-Nicalon^{TM} S fiber tows 800°C in static creep tests and tensile tests to failure and conduct post-test microstructural investigation of the fiber tow specimens in order to determine the degradation and failure mechanisms. Due to the fact that silicic acid-saturated steam eliminates the degradation of the fiber tow near the bottom of the hot zone and creates a protective layer of oxide, sealing off the surface, mechanical performance was improved and active oxidation was greatly reduced. Optical microscopy and SEM techniques provided

only minor insight into damage and failure mechanisms. Microstructural analysis can also be used to guide the development of a predictive model that accounts for the oxidation kinetics of the fiber tows. The model developed by Deal and Grove [28] has been successfully applied to SiC fiber tows. Further microstructural analysis of the results of this effort may enable this model to be refined to better predict SiC fiber tow oxide growth. Additionally, the Monkman-Grant relationship has been shown to apply to previous generations of SiC fiber tows and can be used to predict creep lifetime based on steady-state creep rate. For fiber tows that have been susceptible to environmentally assisted subcritical crack growth, a predictive model of creep lifetime can be developed. In this work, the Monkman-Grant relationship was shown to apply to Hi-Nicalon^{TM} S fibers tows and a predictive model based on environmentally assisted subcritical crack growth was developed.

The objectives of this research can be summarized in the following problem statement:

Design, develop, build, validate, and implement a test facility and methodology for creep and tensile tests of fiber tows at elevated temperatures in steam, introducing steam at near test temperatures and using either unsaturated or silicic acid-saturated steam. Employ this facility and methodology to gain insight into the effects of silicic acid-saturated steam on the tensile and creep rupture performance of Hi-Nicalon^{TM} S fibers tows at 800°C. Determine the applicability of the Monkman-Grant relationship and a predictive model of environmentally assisted subcritical crack growth to Hi-Nicalon^{TM} S fiber tows.

1.5 Material Description

This research effort focused solely on Hi-Nicalon^{TM} S, a non-oxide fiber made by Nippon Carbon Co. (Tokyo, Japan), in the form of a fiber tow or bundle. Hi-

Nicalon^{TM} S is a silicon carbide fiber with very low oxygen content, consisting of approximately 69% Si, 31% C, and 0.2% O by weight [19, 20]. Each tow consists of approximately 500 fibers with an average fiber diameter of 12 μm. The material properties for the fiber tows to be used in this research effort are listed in Table 3. Based on these properties, the total fiber bundle cross-sectional area is 6.6366 $\times$ 10^{-8} m^2.

Table 3. Hi-Nicalon^{TM} S Test Fiber Material Properties, reproduced from [23]

Property	**Value**	**Units**
Density	3.01	g/cc
Tensile Strength	3.13	GPa
Tensile Modulus	366	GPa
Sizing Amount	0.8	wt%
Oxygen Content	0.82	wt%

1.6 Methodology

The key objectives outlined in the problem statement were accomplished by performing the following tasks:

1. Design, develop, build, and validate an experimental facility for testing SiC fiber tows at elevated temperature in an air and in a steam environment to:
   (a) Deliver silicic acid-saturated steam.
   (b) Control the steam temperature and flow rate.
2. Investigate the effect of air and steam environments on creep performance and tensile strength of Hi-Nicalon^{TM} S fibers tows at elevated temperature.
   (a) Perform creep tests and tension tests to failure. Evaluate the data obtained in mechanical tests and gain insight into the dominant creep mechanism(s).

(b) Perform post-test microstructural investigation. Evaluate oxidation damage and elucidate damage and failure mechanisms.

3. Investigate the efficacy of the Monkman-Grant relationship and a environmentally assisted subcritical crack growth model for Hi-Nicalon^{TM} S fiber tows.

II. Background

Metallic engineering alloys and superalloys have exhibited excellent performance in many engineering applications over the years. However, while still useful, these materials have reached their performance limits. Today's aerospace applications require materials that are stable at higher operating temperatures than ever before and still exhibit excellent oxidation resistance, fracture toughness, damage tolerance, strength, and stiffness. Additionally, these materials must have high fatigue life and be lightweight (low density). Ceramics have proven to have most of these attributes, including high melting temperatures, good oxidation resistance, excellent stiffness and strength, and low density. These attributes have resulted in increases in efficiency and performance as well as significant savings in weight.

While these improvements have been marked, ceramics are brittle and suffer from their inherent susceptibility to flaws and cracks. These attributes make sudden catastrophic failure common with ceramics and difficult to predict, a combinations that is undesirable in engineering applications. The development of Ceramic Matrix Composites (CMCs) has enabled designers to harness the desired attributes of ceramics while minimizing the undesirable, resulting in materials that are strong, stiff, light, oxidation resistant, stable at high temperatures, and yet also damage tolerant and tough.

2.1 Ceramic Matrix Composites

The advantage of CMCs over monolithic ceramics lies in their increased toughness, decreased susceptibility to cracks and defects, and their ability to fail gracefully rather than in a sudden catastrophic manner. These benefits are realized through damage tolerant design methodologies. There are three approaches to achieve damage tolerant

CMCs. These microstructural design philosophies enable uncorrelated fiber failure within the CMC, which dissipates more energy as the fibers fail, debond, and are pulled out of the matrix separately from one another [12, 16, 29]. Figure 7 shows an example of fiber pullout in SiC/BN/SiC CMC after a tensile fatigue test. Figure 8a presents a schematic of this process, which results in higher strength and graceful failure.

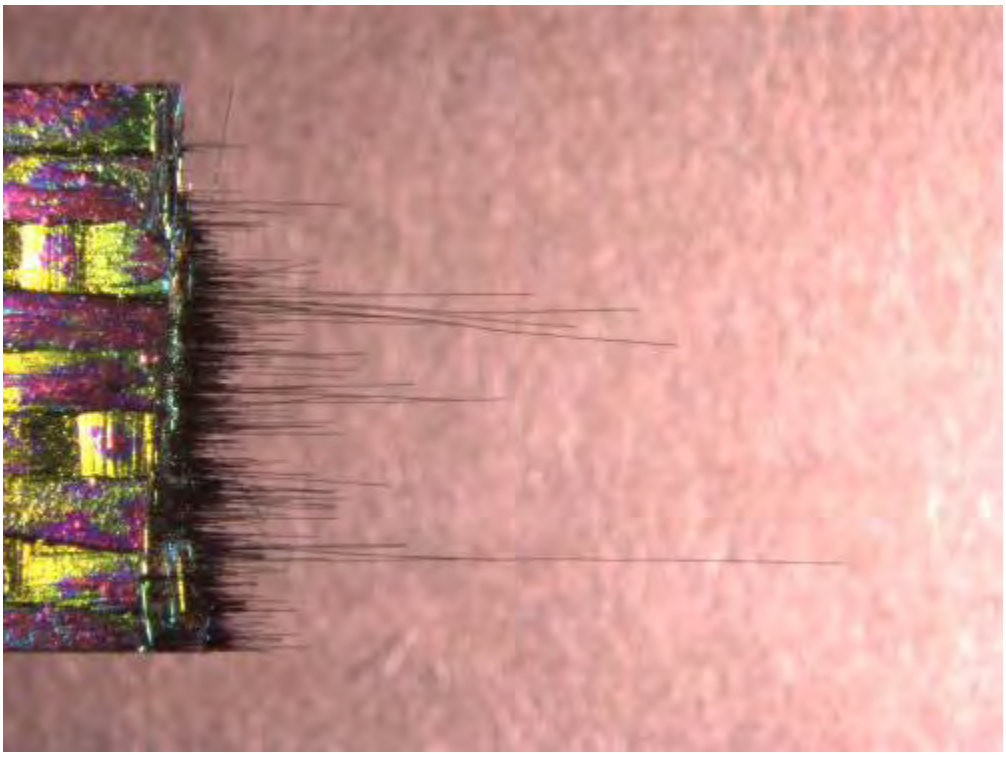


Figure 7. Fiber pullout in SiC/BN/SiC CMC after a tensile fatigue test at 1200°C in air. Note the substantial amount of fiber pullout. Reproduced from [30].

Figure 8b depicts a weak fiber/matrix interface bond, which deflects an advancing crack along or around the fiber and enables fiber pullout. This method is well documented [31–33]. Figure 8c depicts a strong fiber-matrix interface bond with a porous matrix. The porous matrix also enables cracks to deflect around the fiber and has been successfully demonstrated [34–38]. See Zok and Levi [16] and Zok [29] for an extensive review of the mechanisms and mechanical properties of porous-matrix

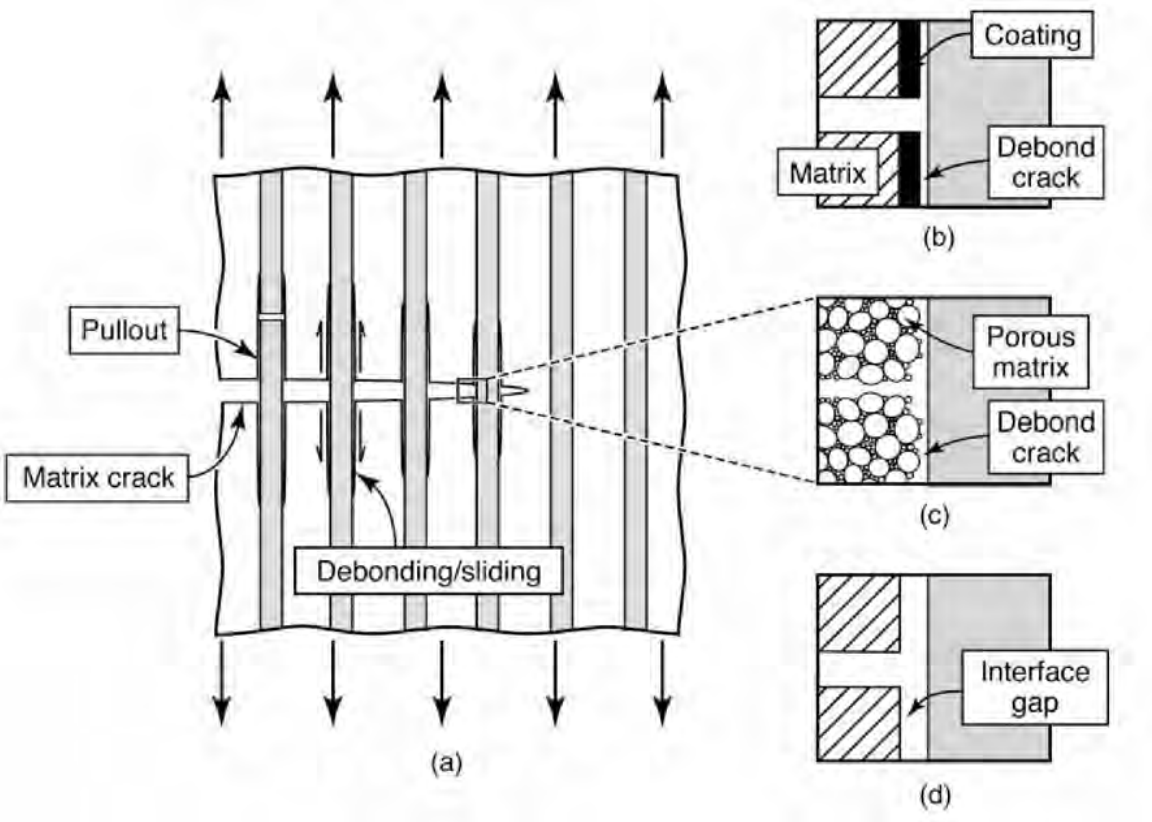


Figure 8. Current Design Philosophies for Damage Tolerant CMCs: a) damage tolerant design concept showing uncorrelated fiber failure, debonding, and pullout b) fiber coating with weak fiber/matrix interface, c) porous matrix, and d) fugitive coating [29], reproduced with permission from Wiley.

CMCs. Figure 8d depicts a more recent design philosophy using fugitive coatings. Here, a fiber coating is applied, then volatized by oxidation during the fabrication of the CMC, leaving a very small gap between the fiber and the matrix [35, 39]. Like the weak interface bond of the first approach, this gap also protects the fiber from an advancing crack in the matrix. Load transfer from the matrix to the fiber is enabled by the rough nature of the matrix and fiber surfaces at the interface, as can be seen in Figure 9.

Each of these design philosophies achieves a damage tolerant design by deflecting matrix cracks around fibers, and each has its own advantages and disadvantages. Whichever approach is used, it remains that the CMC must be able to carry op-

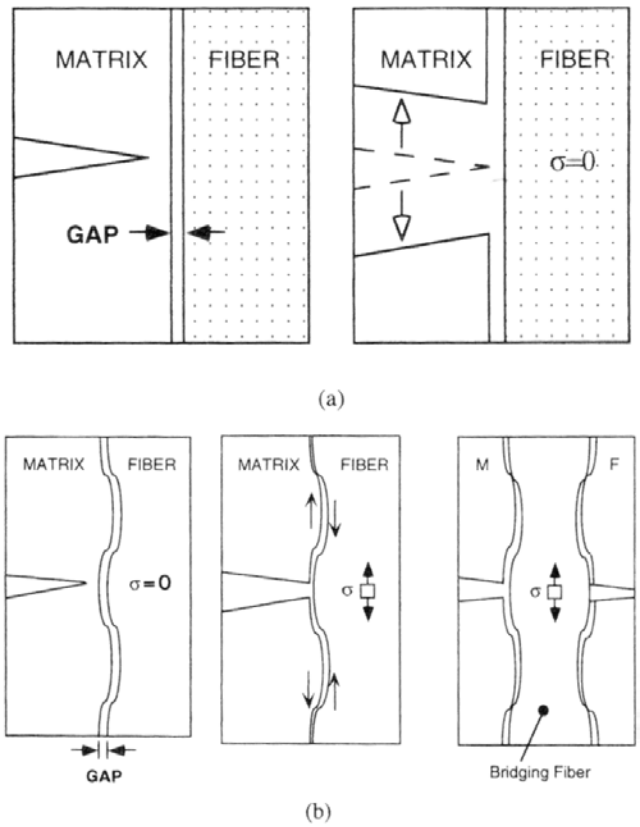


Figure 9. Load Transfer at Fiber/Matrix Interfaces with a Fugitive Coating: a) An idealized (smooth) interface would protect the fiber from the matrix crack, but no load transfer would occur, whereas b) in reality, the interface is rough and load transfer occurs while still protecting the fiber [39], reproduced with permission from Wiley.

erational loads at operational temperatures and service environments. While oxide fiber/oxide matrix CMCs have been demonstrated using the porous matrix approach, the fiber coating method is generally preferred for CMCs made with non-oxide constituents. Fiber coatings can be engineered to provide the desired mechanical properties (i.e. load transfer and crack deflection) and also to shield the fiber from the oxidizing environment. It has been well documented in literature that non-oxide fiber-reinforced CMCs experience significant degradation in their desired properties at operating temperatures due to oxidation [29, 32, 35, 38–40]. This dual use of the fiber coating makes the superior strength and creep resistance of non-oxide fiber-reinforced CMCs available for advanced engineering applications.

Although there has been much progress and the manufacturing is mature, non-oxide CMCs still suffer from problems with environmental degradation at the fiber/-matrix interface, affecting both the fiber coating and the fiber itself. Oxidation embrittlement is a particular problem [18, 29, 41, 42] in which oxygen reacts with the fibers and matrix of a CMC, causing them to form strong bonds and defeating the crack-deflecting properties intended. Oxidation embrittlement tends to occur at intermediate temperatures (600-900°C) and is a serious concern for engineering applications that experience operating temperatures in or gradients that span these temperatures [42]. In non-oxide fiber/matrix CMCs, oxygen gains access to the fiber coating and then the fiber primarily through cracks that form in the matrix under loading [41, 43]. In non-oxide fiber/oxide matrix CMCs, the diffusivity of oxygen through the matrix as well as the oxygen in the matrix itself causes degradation in addition to access through cracks. This is why non-oxide fibers are usually only used with non-oxide matrix materials. An example of this degradation due to oxidation can be seen in the scanning electron microscope (SEM) images in Figure 10.

Oxide CMCs have been developed to address the environmental degradation problem. However, though thermomechanically stable at high temperatures in the operating environment, oxide CMCs suffer from poor creep resistance. Non-oxide CMCs have excellent creep resistance, so there has been a return to non-oxide CMCs and an increased effort to overcome the degrading environmental effects. Indeed, environmental durability is the critical factor for today's CMCs [44, 45].

Non-oxide CMCs are made of a variety of fiber/coating/matrix combinations and are often referred to by the chemical compositions of their constituents. For example, a CMC that uses a C fiber coated with boron nitride (BN) in a SiC matrix is denoted as a C/BN/SiC CMC. However, most of the literature only includes the fiber/matrix combination in the shortened notation, such as C/SiC. The most common non-oxide

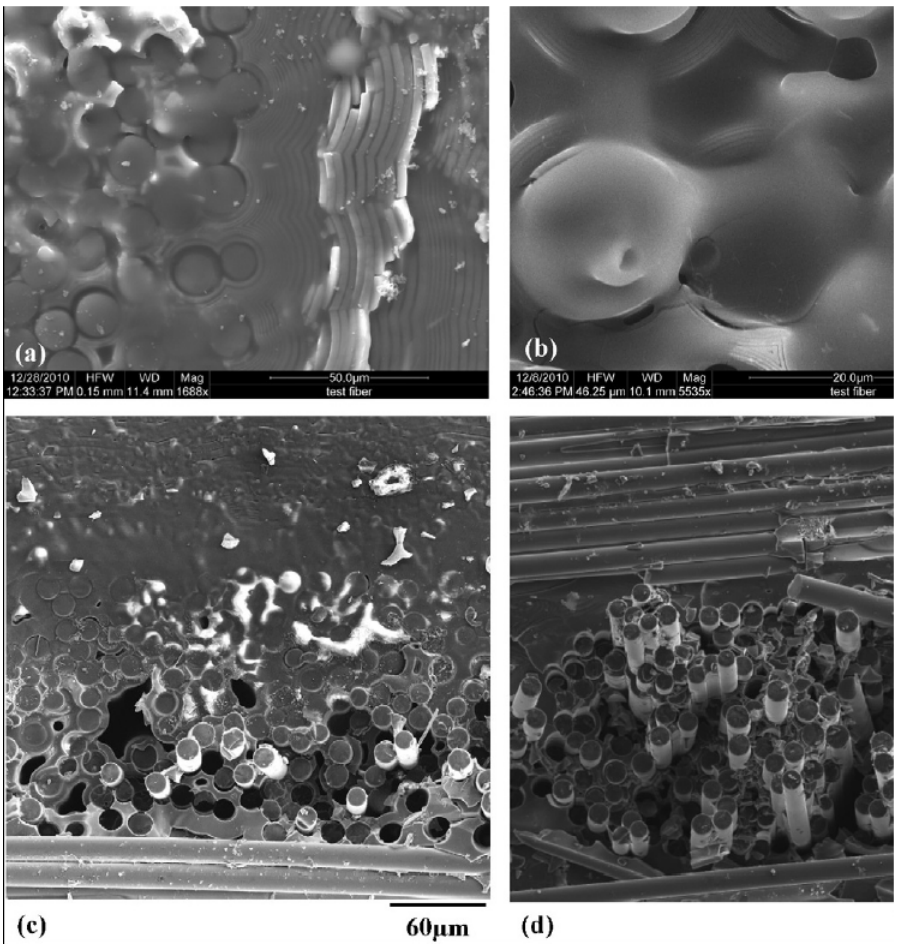


Figure 10. Environmental Degradation due to Oxidation in a SiC/BN/SiC CMC. SEM images showing: (a) oxidation of fibers and matrix, (b) glassy phase in the oxidized region, (c) oxidized region in the top half of the image transitioning to the non-oxidized region in the bottom half of the image, and (d) fiber pull-out typical of the non-oxidized region. Reproduced from [30].

fibers are C, SiC, Si_3N_4 and titanium diboride (TiB_2) [12]. Coatings have historically been C or BN, but there is ongoing research into the development of other coatings due to the susceptibility of C and BN to oxidation [35, 38]. Common matrix materials include glass, carbides, aluminides, and nitrides [12].

Carbon/Carbon, C/SiC and SiC/SiC CMCs have been extensively studied and reported on in the literature [19, 20, 46–84]. These non-oxide CMCs have excellent high-temperature mechanical properties and retain these properties well, for the most part. SiC/SiC CMCs have been evaluated and tested in hot-section components of

turbine engines [29, 72] and are also being considered for other high temperature aerospace applications such as leading edges on hypersonic vehicles due to their superior creep performance and the high strength of SiC fibers. These high-temperature oxidizing environments demand materials that are thermodynamically stable and oxidation resistant.

Despite historical struggles with oxidation resistance, non-oxide CMCs are desired because of their excellent creep resistance. As such, many efforts have been and continue to be made to overcome the oxidation problem. This has lead to the development of self-healing matrix materials [85–91], fiber coatings that shield the fiber from the oxidizing environment [47, 92], and improvements in SiC fibers to reduce oxygen content and achieve near-stoichiometric fibers [19, 20, 93].

2.2 Non-Oxide (SiC) Fibers

Non-oxide fibers are fibers whose crystallographic structure does not include oxygen. The only non-oxide fibers that have shown general applicability to advanced CMCs are carbon fibers and silicon-based fibers [94]. SiC and Si_3N_4 are the most common silicon-based fibers. Whereas Si_3N_4 is tougher and stronger at room temperature, it is much less resistant to creep [95] and a much lower thermal conductivity than SiC. As such, SiC fiber is better suited for high-temperature CMC applications. SiC fiber, particularly Hi-Nicalon^{TM} S, is the subject of the present work.

SiC fibers were first produced in the 1960's by chemical vapor deposition (CVD) onto a carbon or a tungsten core. CVD typically produces fibers with large diameters (100-150 μm). Examples include SCS-type fibers, with diameters ranging from 78-140 μm [12]. This large diameter results in fibers that are not particularly flexible,

making them only suitable for use as reinforcing fibers of metal matrix composites (MMC) [12, 20]. In the latter half of the 1970's, Yajima et al. [96–100] developed a method for producing much smaller diameter (10-15 μm) SiC fibers via controlled pyrolysis of the polymeric precursor polycarbosilane (PCS). The process is depicted in Figure 11. This development enabled the use of SiC fibers in high-temperature structural CMCs starting in the 1980s. In 1982, Nippon Carbon Co. produced the first SiC fibers for commercial use under the trade name Nicalon^{TM}. This was a significant achievement because these new materials had the potential to operate at much higher temperatures than the best nickel super-alloys. Though improvements have been made, SiC fibers today are still produced via melt spinning, crosslinking, and pyrolysis of a polymer precursor. Other fibers have been developed by Ube Industries and Dow Corning under the trade names Tyranno^{TM} and Sylramic^{TM}, respectively [19, 20].

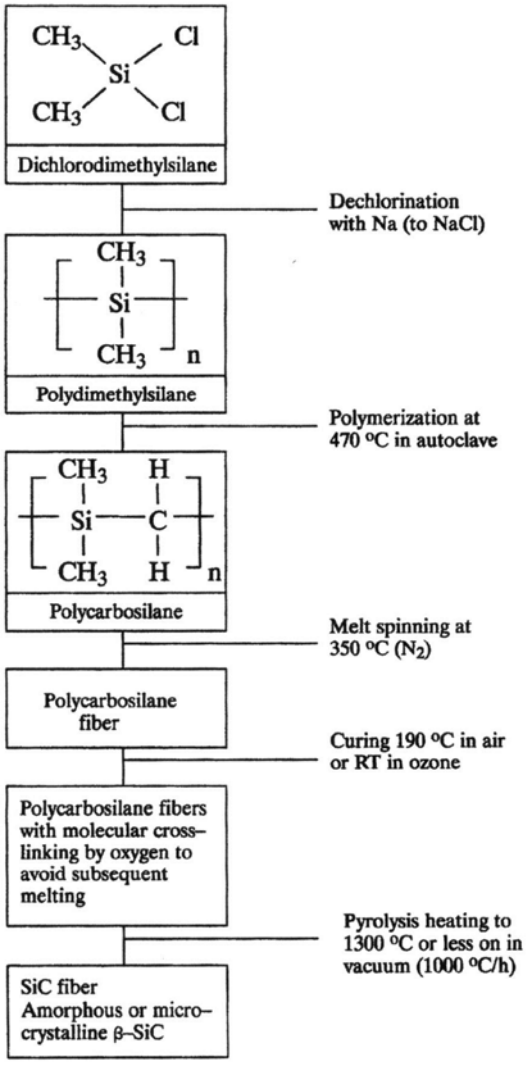


Figure 11. Notional comparison of stress-strain behaviors of a monolithic ceramic and a CMC. Reproduced with kind permission from Springer Science & Business Media B.V. [12] pg. 81, Chapter 3: Ceramic Reinforcements, Figure 3.20. Copyright ©2003 by Kluwer Academic Publishers. All rights reserved. No part of this work may be reproduced, stored in a retrieval system, or transmitted in any form or by any means, electronic, mechanical, photocopying, microfilming, recording or otherwise, without the written permission from the Publisher, with the exception of any material supplied specifically for the purpose of being entered and executed on a computer system, for exclusive use by the purchaser of the work.

The first fibers consisted of free carbon and nanocrystals (1-2 nm) of β-SiC within an amorphous matrix of SiC_xO_y ($x+y=4$) [1, 19, 23] as is depicted in Figure 12. The chemical composition of Nicalon^{TM} was approximately 65% SiC, 23% silica (SiO_2) and 12% C [23], while the elemental composition by weight was 56.6% SiC, 31.7% C, and 11.7% O with a C/Si ratio of 1.31 (i.e. 1.31 C atoms for every Si atom) [19]. The Tyranno^{TM} fibers had a similar composition with 34% Si, 31.6% C, 12.4% O, and 2% titanium (Ti) and C/Si ratio of 1.36.

The early excitement at the potential of these new fibers was soon tempered as it became clear that the properties of the first generation of fibers were not close to those of bulk SiC, as had been expected. For example, the Young's modulus of these fibers was approximately half that of bulk SiC (~400 GPa, 58 msi) [19, 20]. Strength and creep resistance where not as expected either. Extensive study [43, 101–112] of these first generation fibers found that these fibers begin to lose their creep resistance and short-term strength at 1000°C, with severe losses above 1200°C [19], due to their non-stoichiometric compositions, particularly the amorphous intergranular Si-O-C phase. These temperature barriers restrict production processes for CMCs using these fibers to those that can be accomplished at lower temperatures, such as chemical vapor infiltration (CVI) and polymer infilitration and pyrolysis (PIP) [1, 23]. It follows that these CMCs would also be limited to applications with operational temperatures below the 1200°C threshold.

If the goal of approaching the properties of bulk SiC was to be realized, fibers with near stoichiometric compositions would have to be developed. The second generation of SiC fibers made significant headway toward that end by changing the method of cross-linking from an oxygen-induced method to one using electron irradiation [19]. This method reduced the amount of oxygen in the fibers made from a PCS precursor to 0.5 wt%, giving rise to Nippon Carbon's Hi-Nicalon^{TM}. Other second generation

fibers did not experience such a dramatic drop in oxygen content. This reduced the Si-O-C phase significantly, producing a more stoichiometric fiber and enabling higher processing temperatures. In the Hi-Nicalon^{TM} fibers, the SiC nanocrystals averaged 5-10 nm in size (see Figure 12) and were embedded in a matrix of amorphous Si and C atoms resulting in a C/Si ratio of 1.39. The reduction of the Si-O-C phase resolved the problem of fiber decomposition at temperatures above 1200°C that was prevalent in the first generation. Stiffness improved by 35% and the creep resistance and strength were retained up to 1200°C [19, 23]. Bunsell and Piant reported that:

> "Hi-Nicalon fibre was found not to creep below 1000°C and to possess the highest creep threshold and the lowest strain rate of the first and second generation fibres...The creep rates of all the first and second generation fibres were very similar at 1400°C, at around $5 \times 10^{-7} s^{-1}$ under a stress of 0.3 GPa (43.5 ksi). The activation energy for the creep of Hi-Nicalon fibres was around 360 kJ/mol (341 Btu/mol) and could be explained by grain boundary sliding accommodated by interface-controlled diffusion mechanisms. The carbon layers, between the grains, could facilitate this sliding. Ultimate failure in creep of the fibres was found not to be due to a lack of accommodation, as is the case for bulk ceramics, but related to surface defects, such as cavities or porous zones growing from local chemical heterogeneities." [19]

Heat treatment at temperatures above 1300°C further increased the stiffness up to 295 GPa (42.8 msi)[19] by volatilizing SiO, CO, CH_4, etc. and inducing SiC grain growth. Heat treatment at 1400-1600°C resulted in an increase in creep resistance at temperatures up to ~1400°C [113]. These results agreed with those of Bodet et al., who also found that Hi-Nicalon had superior rupture strength at room temperature and greater creep resistance than Si-O-C fibers [114]. Hi-Nicalon^{TM} clearly showed the greatest gains among the second generation of SiC fibers.

While much improved, the second generation fibers still did not achieve the properties of bulk SiC and were, as yet, not meeting the demands of the high-temperature aerospace applications in which it was hoped they would replace nickel-based super-

alloys. The next challenge was to reduce the excess carbon content, driving the C/Si ratio towards unity, and achieve as near stoichiometry as possible. Nippon Carbon employed the process for Hi-Nicalon^{TM} fiber using a radiation cured precursor as an intermediate step. The Hi-Nicalon^{TM} fiber was heated in a hydrogen-rich environment to approximately 1500°C, reducing the excess carbon and the C/Si ratio to 1.05. This fiber is called Hi-Nicalon^{TM} S or Type S [19]. Figure 12 illustrates schematically the three generations of SiC fibers made by Nippon Carbon.

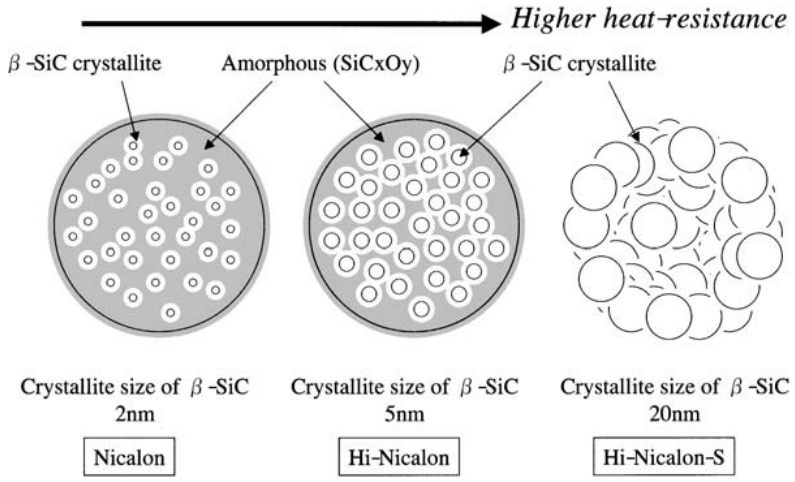


Figure 12. Microstructures of three generations of Nicalon^{TM} fibers. Reproduced with kind permission from Springer Science & Business Media B.V. [20] pg. 118, Figure 9. Copyright ©2005 by Springer-Verlag Berlin Heidelberg.

Hi-Nicalon^{TM} S achieves properties near those of bulk SiC. It has a stiffness of approximately 400 GPa (58 msi) and retains its strength and stiffness up to 1400°C [19]. The average nanocrystal grain size is 50 nm, leading to the excellent strength retention. The reduction in excess carbon and the treatment at high temperatures results in a fiber that has excellent chemical and thermal stability and is more oxidation and creep resistant than the previous generations [19, 113]. The production process of Hi-Nicalon^{TM} S fibers is depicted in Figure 13.

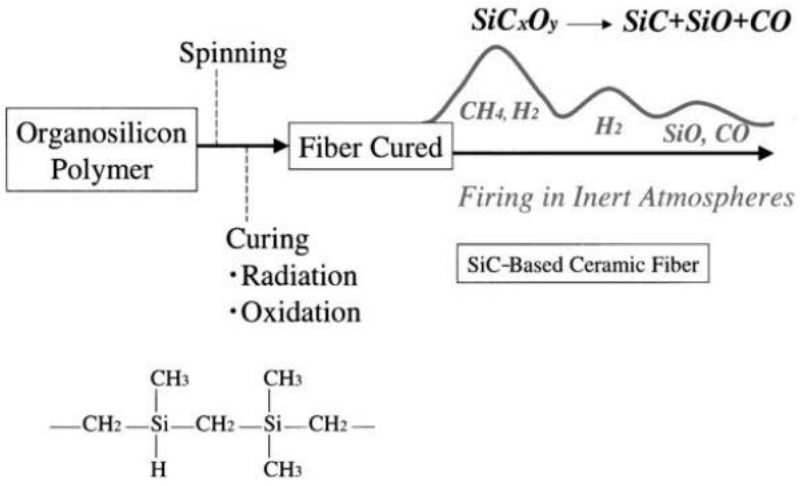


Figure 13. Production process for Hi-Nicalon^{TM} S SiC fibers by electron irradiation curing and pyrolysis. Reproduced with kind permission from Springer Science & Business Media B.V. [20] pg. 117, Figure 8. Copyright ©2005 by Springer-Verlag Berlin Heidelberg.

Ube Industries and Dow Corning also produced near-stoichiometric fibers based on adding sintering aids such as aluminum and boron, respectively, to a PCS precursor. These fibers are the Tyranno^{TM} SA family and the Sylramic^{TM} families, respectively. They have SiC nanocrystals on the order of 20-200 nm, and their C/Si ratios range from 1.00-1.08 [113]. The chemical compositions and mechanical properties of all three generations of SiC fibers are given in Tables 4 and 5.

As the temperature increases, fiber strength decreases in general. This is due to a number of factors including oxidation, outgasing of carbon oxides, and eventual decomposition of the fiber [19]. However, all of the third generation SiC fibers retain their room temperature strength up to 1400°C, with the Tyranno^{TM} SA series able to retain it out to nearly 2000°C. This is a significant step forward in the development of CMCs for advanced engineering applications. Figure 14 shows the strength as a function of temperature for third generation SiC fibers.

Table 4. Chemical Composition and Temperature Limits of Three Generations of SiC Fibers (Note: the chemical composition of Sylramic^{TM} iBN is essentially the same as the regular Sylramic^{TM} except that it has a BN layer at the surface rather than just boron). Data reproduced in part with kind permission from Springer Science & Business Media B.V. [19] pg. 826, Table III. Copyright ©2006 by Springer Science & Business Media, Inc. Copyright of Journal of Materials Science is the property of Springer Science & Business Media B.V. and its content may not be copied or emailed to multiple sites or posted to a listserv without the copyright holder's express written permission. However, users may print, download, or email articles for individual use.

Gen.	Trademark	Approx. Max. Prod. Temp. (°C)	Elemental Composition (wt%)	Density (g/cm^3)	Avg. Diam. (μm)
First	Nicalon 200	1200	56Si + 32C + 12O	2.55	14
	Tyranno LOX-M	1200	54Si + 32C +12O + 2Ti	2.48	11
Second	Hi-Nicalon	1300	62.5Si + 37C + 0.5O	2.74	12
	Tyranno LOX-E	1300	55Si + 37.5 +5.5O + 2Ti	2.39	11
	Tyranno ZM	1300	57Si + 34.5C + 7.5O + 1Zr	2.48	11
	Tyranno ZE	1300	58.5Si + 38.5C + 2O + 1Zr	2.55	11
Third	Tyranno SA1	1700	68Si + 32C + 0.6Al	3.02	11
	Tyranno SA3	1700	68Si + 32C + 0.6Al	3.1	7.5
	Sylramic	1700	67Si + 29C + 0.8O + 2.3B + 0.4N + 2.1Ti	3.05	10
	Sylramic iBN	1700	*see note*	3.05	10
	Hi-Nicalon Type-S	1500	69Si + 31C + 0.2O	3.05	12

Table 5. Mechanical Properties of Three Generations of SiC Fibers with a 25 mm (~1 in.) gauge length (RT = room temperature). Data reproduced in part with kind permission from Springer Science & Business Media B.V. [19] pg. 826, Table IV. Copyright ©2006 by Springer Science & Business Media, Inc. Copyright statement from previous table applies.

Generation	Trademark	RT Strength (GPa)	RT Young's Modulus (GPa)
First	Nicalon 200	3	200
	Tyranno LOX-M	3.3	185
Second	Hi-Nicalon	2.8	270
	Tyranno LOX-E	2.9	200
	Tyranno ZM	3.4	200
	Tyranno ZE	3.5	233
Third	Tyranno SA1	2.8	375
	Tyranno SA3	2.9	375
	Sylramic	3.2	400
	Sylramic iBN	3.5	400
	Hi-Nicalon Type-S	2.5	400

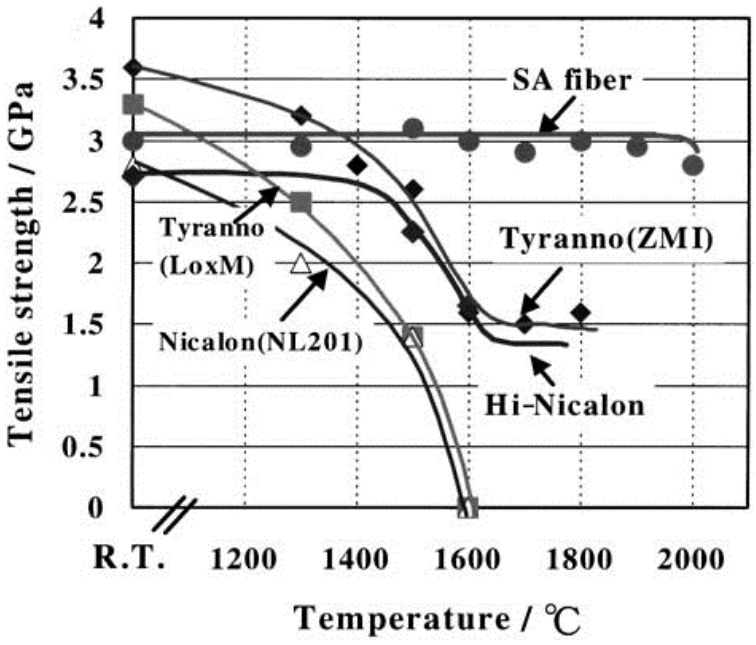


Figure 14. Temperature-dependent strength of third generation SiC fibers. Reproduced with kind permission from Springer Science & Business Media B.V. [20] pg. 121, Figure 14. Copyright ©2005 by Springer-Verlag Berlin Heidelberg.

Aside from strength, high creep resistance and low creep rate are also key fiber properties for developing CMCs for advanced engineering applications. Creep rates of the third generation SiC fibers are shown in Figure 15. The Tyranno^{TM} and Sylramic^{TM} fibers creep at a rate of $8 \times 10^{-7} s^{-1}$ and $4 \times 10^{-6} s^{-1}$, respectively, at a stress of 0.3 GPa (43.5 ksi) and at 1400°C. Hi-Nicalon^{TM} S produced creep rates that were one to two orders of magnitude better, i.e. ~$4 \times 10^{-8} s^{-1}$ [19, 20]. Since the Hi-Nicalon^{TM} S fibers have small grains, there is even the potential for further reduction in creep by inducing grain growth by heat treatment. It is also evident that Hi-Nicalon^{TM} S has better creep resistance. Figure 15 shows the onset of creep to require significantly higher stresses for the Hi-Nicalon^{TM} S fibers than for other third generation fibers. A recent improvement on the Sylramic^{TM} fiber, Sylramic^{TM} iBN, has been developed by the NASA Glenn Research Center. This fiber has the same basic composition as the regular Sylramic^{TM} fiber except that the boron sintering

aids are removed and it has a protective BN layer formed in-situ on the surface. Sylramic^{TM} iBN exhibits superior oxidation and creep resistance [19, 93, 94].

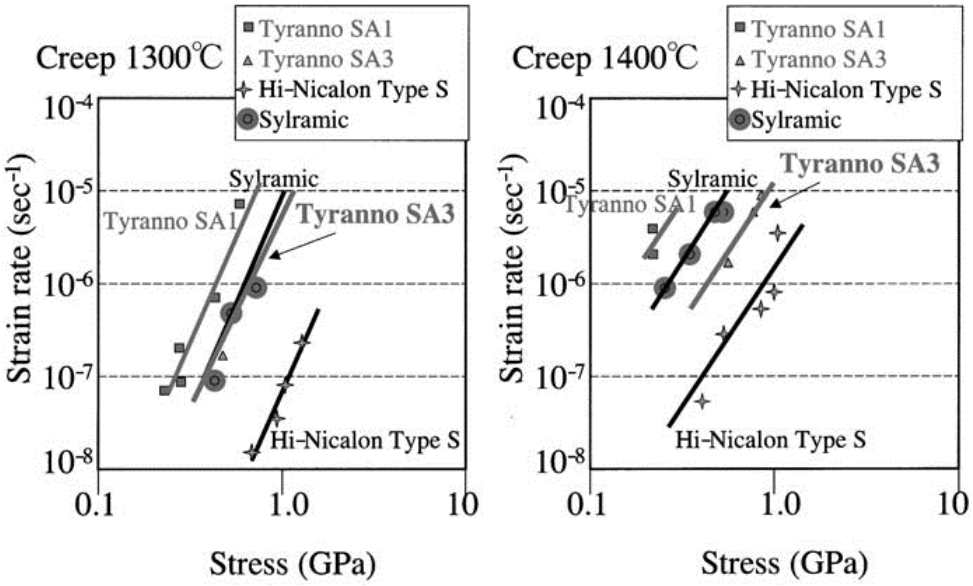


Figure 15. Creep of third generation SiC fibers. Reproduced with kind permission from Springer Science & Business Media B.V. [20] pg. 122, Figure 15. Copyright ©2005 by Springer-Verlag Berlin Heidelberg.

As mentioned above, SiC fibers have been and continue to be evaluated for use in CMCs for advanced engineering applications such as jet engines, leading edges of hypersonic aircraft, spacecraft, and nuclear power plants. It is widely recognized that fiber properties like strength, oxidation resistance, creep resistance, and damage tolerance dominate the performance of CMCs. As such, fiber performance in high-temperature, oxidizing environments is critical to the development of CMCs for these applications. Reinforcing fibers are typically included in CMCs as bundles or "tows" of several hundred filaments rather than as single filaments. Early studies by Yun and DiCarlo suggested that fiber tow strength can be predicted by testing of individual filaments [115]. However, later studies found that bundles fail at lower than predicted strength due to mechanical interaction/bonding between fibers, causing bundle rupture when the weakest fiber ruptures. This behavior is enhanced by

removal of the sizing/intrinsic carbon layer or by bonding due to oxidation caused by treatment at high temperatures [116]. Hammond and Elzey demonstrated that fiber tow predictions from single filament data were not always accurate, noting that heat treatment can result in sintering between fibers, causing the tow to behave less like a bundle of separate fibers [117]. Dassios et al. argued that testing of fiber tows provided more accurate results for fiber strength than testing of individual filaments [118]. Multifilament tows are more damage tolerant than single filaments. Dassios et al. point out that in the process of extracting single filaments for testing from fiber tows, only the stronger filaments are successfully extracted intact, thus single filament testing tends to overpredict the strength of fiber tows. Testing of fiber tows provides more representative results, taking into account the variations in the individual fibers within the tow. Calard and Lamon found that load sharing between the fibers in a tow lowers the tow strength from that predicted by single fibers. They successfully modeled fiber tow failure by taking into account imperfect local load sharing among the fibers in a fiber tow [119]. Whereas it would be ideal to individually test each fiber within a tow in order to obtain a true statistical picture of the fiber tow strength, this is problematic for the reasons stated above and due to the time involved. Although there exist trade-offs in testing tows as opposed to individual fibers, it is often less problematic to test fiber tows, while still being useful.

Multifilament fiber tows are the fundamental unit in textile composites and can be incorporated uniaxially or as weaves. As a matrix material fails, load is transferred to the fiber tows, which control the ultimate failure of the CMC. Therefore, understanding the mechanical, thermal, and oxidation behavior of multifilament fiber tows is critical to producing CMCs for advanced engineering applications. This has been the focus of several research efforts over the past two decades [1, 23, 62, 115–117, 120–124]. Forio et al. investigated the lifetime of Nicalon^{TM} fiber tows in air at

intermediate temperature (600-700°C) [120]. They found that delayed failure under low stress (near the proportional limit) was a result of slow crack growth activated by oxidation. Gauthier and Lamon studied the delayed failure of Hi-Nicalon^{TM} and Hi-Nicalon^{TM} S fiber tows and single fibers under constant load at temperatures between 500 and 800°C in air [121]. A model of delayed failure was developed that satisfactorily predicted the fiber tow rupture strength for temperatures below 800°C in the absence of creep. The model successfully captured the dependence of the rupture strength on the applied load and temperature and also predicted the lifetime of multifilament tows in the temperature range of the study. The model was based on subcritical crack growth in single filaments. Hi-Nicalon^{TM} S fiber was found to be the most resistant to slow crack growth under constant stress. In the same experimental effort, Gauthier et al. analyzed the oxidation of the SiC fibers [125]. It was found that delayed failure was caused by slow crack growth of surface defects, which growth was induced by the oxidation of free carbon at the grain boundaries and of SiC nanograins or silicon oxycarbide at the crack tip. Gauthier et al. conlcuded that "In order to improve the fatigue resistance of these fibers in air at intermediate temperatures between 400°C and 800°C, the manufacturers will have to reduce drastically the amounts of oxygen and free carbon near the fiber surface and also eliminate the surface defects, in order to limit the oxidation" [125].

Recent work in this area includes studies by Ladevèze and Genet [126], R'Mili and Lamon [127], Sauder and his colleagues [128–130], Steffens [1], and Shillig [23]. Ladevèze and Genet introduced a new approach to modeling subcritical crack growth in ceramic fibers based on the true oxygen flux reacting at the crack tip, rather than on temperature. The model accounts for the two phases of crack growth that have been consistently observed in several studies: the *reaction-controlled* stage and the *diffusion-controlled* stage. First, the crack tip is exposed and is damaged directly

by oxygen and water, with crack growth being limited only by the speed of the chemical reaction, hence *reaction-controlled*. Once the whole surface has oxidized, oxygen and water must diffuse through the newly formed oxide layer, resulting in a *diffusion-controlled* stage. The model was validated for Hi-Nicalon^{TM} in dry air up to 1000°C. R'Mili and Lamon have demonstrated a method for investigating subcritical crack growth using load relaxation tests [127]. This approach offers the advantage of each fiber in the tow experiencing the same constant stress during the test. This method provides a statistically significant database of rupture time data wherein there is the same amount of data points as there are fibers in the bundle. The rank of each failing fiber can be determined from relaxation of the load on the bundle, making it possible to determine the reference strength of each failing fiber. This method enabled a closed form expression for fiber lifetimes and was validated by the experimental results. Although R'Mili and Lamon's work was done with E-glass fibers, this method is equally applicable to other fibers, including SiC.

Sauder et al. studied the correlation between the mechanical behavior and the fiber/matrix interface characteristics of SiC/SiC minicomposite test specimens. A minicomposite is made up of one fiber tow encased in a small amount of matrix. Tyranno^{TM} SA3 and Hi-Nicalon^{TM} S fiber tows were examined. A strong correlation was shown between the tensile behavior and the interface characteristics and fiber surface roughness. Tyranno^{TM} SA3 minicomposites exhibited premature failure associated with strong interface bonds, while Hi-Nicalon^{TM} S exhibited failure controlled by the fiber tow strength and limited matrix crack density associated with weak interface bonds [128]. These results have been corroborated in more recent studies by Sauder and his colleagues. For example, Buet et al. studied the influence of chemical and physical properties of the fibers [129] and of surface fiber properties and pyrocarbon interphase texture [130] on the mechanical behavior of SiC/SiC com-

posites reinforced with Tyranno^{TM} SA3 and Hi-Nicalon^{TM} S fiber tows. It was found that Tyranno^{TM} SA3 fibers had a rough granular surface, resulting in an increase in residual and interfacial shear stress. The texture of the pyrocarbon interphase also affected the interfacial shear stress, leading to the conclusion that the interphase processing technique is important in the effort to improve damage tolerance.

Steffens [1] and Shillig [1] both investigated creep of Hi-Nicalon^{TM} S ceramic fiber tows at elevated temperature (800-1100°C) in air and in steam. Using a test facility developed by Armani [4] for oxide fiber tow testing, Steffens developed a methodology for testing SiC fiber tows and reported creep stresses for Hi-Nicalon^{TM} S fiber tows ranging from 76 to 1560 MPa (11 to 226 ksi). Creep run-out was defined as 100 h at the creep stress. Steffens further reported that steam reduced the creep lifetimes of the Hi-Nicalon^{TM} S fiber tows at both 800 and 1100°C by approximately an order of magnitude. Shillig continued Steffens' work by investigating the creep performance of Hi-Nicalon^{TM} S fiber tows at temperatures of 800, 900, 1000, and 1100°C. Creep stresses ranged from 154 to 1250 MPa (22 to 181 ksi). The deleterious effect of steam decreased with increasing temperature. Although Shillig attributed this to the transition from passive oxidation at 800-1000°C to active oxidation at 1100°C, subsequent microstructural analysis suggests that both passive and active oxidation occurred to some degree throughout the temperature regime.

2.3 Creep in Ceramics

Creep resistance is of great importance in advanced CMCs, because they experience significant stresses at high temperatures for long duration over many use cycles. To understand the importance of creep resistance, one has only to think of the catastrophic results should a CMC turbine fan blade in a jet engine experience excessive creep deformation due to insufficent creep resistance. Hence, it is important to review

creep and the mechanisms that cause it. Creep is the phenomenon where a material experiences a continued increase in strain over time under a constant, subcritical stress [131], i.e. a stress below the ultimate stress of the material. Figure 16 is a schematic of a typical tensile creep curve. Note an initial strain at time zero. This is the strain resulting from the application of the load and is sometimes referred to in literature as the elastic strain.

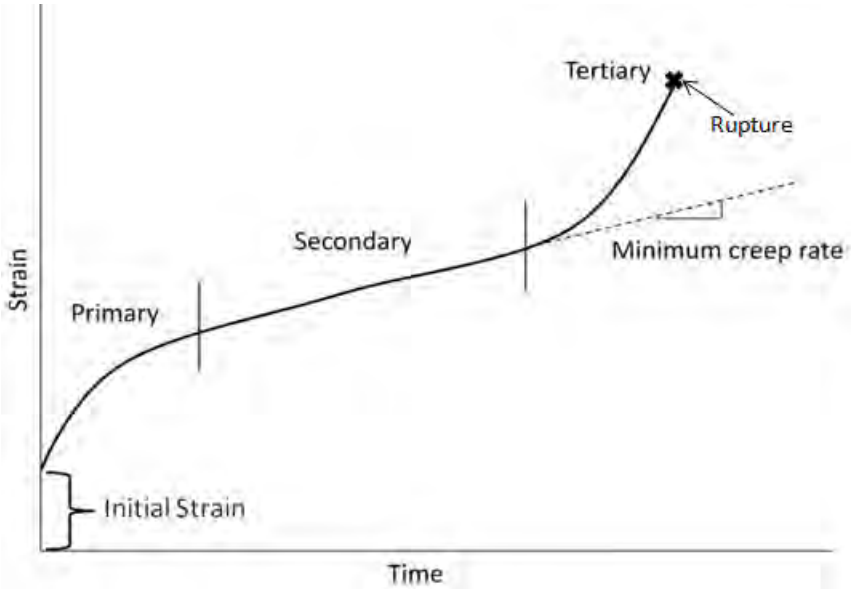


Figure 16. Phases of a typical creep curve. Reproduced from [4], with initial strain and rupture notations added.

Over time, three stages of creep emerge. The primary stage may be either short or long in duration and is characterized by a continual decrease in the strain rate. The mechanisms active in primary creep are stress redistribution and/or changes in microstructure, such as grain size and dislocation density [4]. For long load periods, the strain accumulated during the primary stage will be relatively small compared to that of the later stages [131]. At some point, the creep rate reaches a minimum, as depicted in Figure 16, and creep continues at this minimum rate for a period of time. This is secondary or steady-state creep and may also be short or long in duration. Secondary creep is due to deformation of the microstructure [4]. Creep transitions

into the tertiary stage when the creep rate begins to increase again. Tertiary creep is often short in duration by comparison to primary and secondary creep and the increase in strain rate is often exponential. Tertiary creep is associated with the onset of failure, in the form or voids and cracks, and, ultimately, failure itself. Failure is often referred to in literatures as rupture. In ceramics, tertiary creep is usually very short in duration and is sometimes not exhibited at all [4].

Steady-state creep is the primary focus in ceramics. Because most CMC constituents are polycrystalline, the current discussion is limited to creep in polycrystalline ceramic materials. At high temperatures, creep in ceramics is generally dominated by one of two mechanisms: ***diffusional creep*** or ***grain boundary sliding***. Both are always present, as the effects are coupled, but one or the other tends to dominate. ***Diffusional creep*** is creep due to mass transport and can be further divided into two subsets: *Nabarro-Herring* creep and *Coble* creep. The former refers to diffusion that takes place through the grains (i.e. lattice diffusion) while the latter is diffusion that occurs along the grain boundaries. In both cases, the grains elongate in the direction of the applied load. *Coble* creep occurs preferentially at low temperatures because the activation energy of diffusion along the grain boundary is lower than that through the grain [132], resulting in higher mass transport along the grain boundaries. In ***Grain boundary sliding*** (GBS), whole grains move with respect to one another to relieve local stresses, causing elongation in the direction of the applied load. This is usually due to the softening at high temperatures of a grain-boundary glassy phase that is used to densify ceramics [4] and to the presence of small grains that more easily move past one another. When reporting the mechanism of creep in a ceramic, often only the dominant one, i.e. the one that results in the greater amount of strain, is given and it is understood that the other is present but results in less strain. However, it should be noted that the lesser of the two is also the one

that controls or limits the creep strain rate [133]. These two creep mechanisms can, therefore, be thought of more in the context of, in Poirier's words, "...the two end-members of a continuum: GBS-controlled diffusion creep, in which most of the strain is due to transport of matter, and diffusion-creep-controlled GBS, in which most of the strain is due to GBS" [133].

It has been shown and is widely accepted that most creep mechanisms can be modeled using the following equation, given in the form provided by Wachtman et al. [132]:

$$\dot{\varepsilon} = B\frac{D\mu b}{kT}\left(\frac{b}{d}\right)^{p}\left(\frac{\sigma}{\mu}\right)^{n} \tag{1}$$

where $\dot{\varepsilon}$ is the strain rate, B is a constant, D is the diffusion coefficient, μ is the shear modulus, b is magnitude of the Burgers vector, k is the Boltzmann constant, T is the absolute temperature d is grain size (diameter), σ is the applied tensile stress, and p and n are power law creep exponents for grain size and stress, respectively [4, 132]. The diffusion coefficient is given by the well known expression:

$$D = D_o \exp\left(\frac{-Q}{RT}\right) \tag{2}$$

where D_o is a frequency factor [4], Q is the activation energy of diffusion, and R is the universal gas constant.

Using experimental creep data, the values of p and n in Equation 1 can be determined. These values correspond to different creep mechanisms, thus the primary creep mechanism in a given test specimen can be identified. Armani summarized the predominant mechanisms of creep in fine-grained polycrystalline ceramics and their associated power law creep exponents [4]. Creep mechanisms and the associated values of p and n are presented here in Table 6. Of note is the difference in the grain size exponent, p, for the two types of diffusional creep: $p = 2$ for Nabarro-Herring

creep and $p = 3$ for Coble creep. This inverse cubic dependence of Coble creep on the grain size causes it to be the dominant mechanism at small grain sizes [132].

Table 6. Creep mechanisms in fine-grained polycrystalline ceramics (LD: lattice diffusion, GBD: grain boundary diffusion, GBS: grain boundary sliding, IR: interface reaction). Values reproduced from [1, 4].

Mechanism	p **grain size exponent**	n **stress exponent**
Nabarro-Herring: LD	2	1
Coble: GBD	3	1
Dislocation: Climb controlled	0	5
GBS + (IR/GBD): IR controlled	2	2
GBS + (IR/LD): IR controlled	1	2
GBS + cavities nucleation/growth	3	4
GBS: diffusion in liquid grain boundary controlled	3	1

In the classical treatment of diffusional creep, it is assumed that the grain boundary acts as a perfect source or sink for matter/vacancies [134]. Treatment of diffusional flow of a polycrystalline material as a continuum problem has proved quite successful, agreeing well with and explaining much of the experimental data. However, under conditions where this assumption is not valid and the sources and sinks are more discrete, the diffusion is controlled by a reaction at the interface, hence: interface reaction-controlled creep. Here the grain boundary or the lattice diffusion happens so quickly that the creation and annihilation of point defects at the grain boundary controls the process [4, 134, 135].

Due to their relatively recent development, creep of third generation SiC fibers such as Hi-Nicalon^{TM} S has not been as extensively studied as that of previous generations, however several researchers have made it their focus over the past 15 years. Sha et al. studied the effects of heat treatment on the creep resistance of Hi-Nicalon^{TM}, Hi-Nicalon^{TM} S, and Tyranno^{TM} SA fibers [136, 137]. The fibers were heat treated in an argon (Ar) environment for 1 h at temperatures in the range of 1300-1900°C. It was found that creep resistance was improved by heat treatment, especially when the

heat treatment was carried out at temperatures above the processing temperatures of the fibers. Creep activation energy increased with an increase in the heat treatment temperature. The improvement in creep resistance was found to be related to the grain size and to the composition at/near the grain boundaries.

Sauder and Lamon investigated the tensile creep behavior of individual Tyranno^{TM} SA3 and Hi-Nicalon^{TM} S fibers at various tempertures in a vacuum [138]. Evidence of all three stages of creep was found, with primary creep due, primarily, to viscoelastic deformation of carbon at the grain boundaries. Steady-state creep, with a stress exponent, n, of 2.5 was found to be due to grain boundary sliding with no grain elongation or glassy phase. This corresponds to the Rachinger creep mechanism. Stress exponents and the activation energy for these fibers are reported in Table 7 and tensile creep rates at 850 MPa (123 ksi) are given in Figure 17. The activation energy of Hi-Nicalon^{TM} S (~770 kJ/mol, 730 Btu/mol) is consistent with carbon diffusion within the grains. Tertiary creep was also observed and was found to be a result of silicon volatilization starting at the surface and proceeding toward the core.

Table 7. Power law creep parameters for third generation non-oxide fibers [138], data reproduced with permission from Wiley.

Fibers	**Temperature Range (°C)**	**Activation Energy Q (kJ/mol)**	**Stress Exponent** n
SA3 (1)	1150-1500	370 (360-370)	2.5 (2.35-2.6)
SA3 (2)	1150-1500	370 (360-370)	2.5 (2.3-2.6)
Hi-Nicalon^{TM} S	1300-1500	770 (750-770)	2.6 (2.4-2.9)

At this point it is important to address a difference in terminology that exists in different scientific circles and what is included when using the term "creep." In geological sciences and in the field of ceramics, the term "creep" has a very narrow meaning: inelastic deformation of the constituents of a material under constant load. In other circles, such as organic (polymer) matrix composites, the term "creep" is used to describe a broader set of behaviors that result in permanent deformation of a

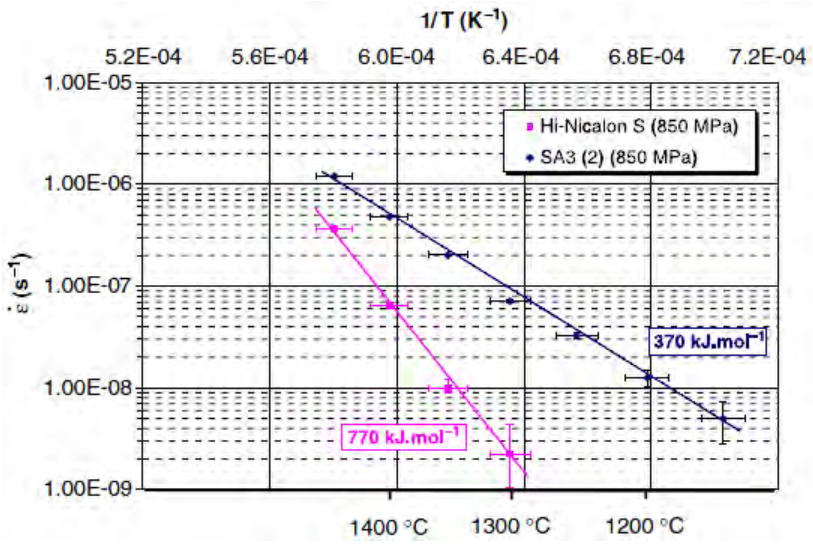


Figure 17. Creep of Tyranno^{TM} SA3 and Hi-Nicalon^{TM} S fibers at 850 MPa (123 ksi)[138], reproduced with permission from Wiley.

material exposed to a constant load. For example, a CMC subjected to a constant load over time may develop cracks and deform. When the load is removed, some of these cracks may not close, perhaps due to friction, resulting in a permanent deformation. Under the broader use of the term, this would be considered creep, but not so under the more narrow definition. Those using the more narrow definition would use a term such as "static fatigue" or "creep rupture" to describe this. For the purposes of this work, and to maintain consistency with the previous work of Steffens [1], Shillig [23], and Sprinkle [139] the term "creep" is used in the broader sense in this work. It is recognized that creep in the narrower sense is not expected to occur to any significant degree in SiC at 800°C.

Steffens studied creep of Hi-Nicalon^{TM} S fiber tows at 800 and 1100°C in air and in steam. The stress exponent, n, was determined by fitting the data to a temperature-independent Norton-Bailey form of the power law creep equation:

$$\dot{\varepsilon} = A\sigma^n \tag{3}$$

where A is a temperature-dependent coefficient that accounts for the activation energy, grain size and other variables in the full form of the power law, Equation 1. Values of $n = 4.8$ and $n = 3.8$ were reported in air and steam, respectively, leading to a conclusion of climb-controlled dislocation creep in air and GBS with cavity growth in steam [1]. Microstructural analysis to confirm this conclusion was not performed. Figure 18 shows the creep rate data.

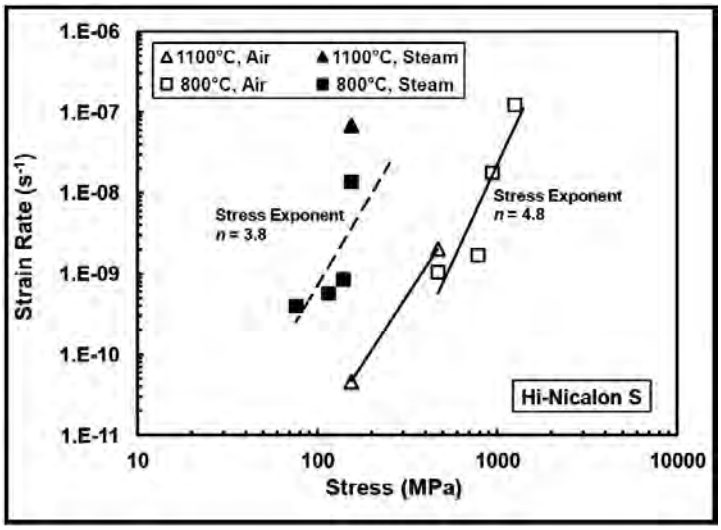


Figure 18. Creep of Hi-Nicalon^{TM} S fibers at 800 and 1100°C in air and in steam, reproduced from [1]

Shillig studied creep of Hi-Nicalon^{TM} S fiber tows at temperatures ranging from 800 to 1100°C in air and in steam. The stress exponent, n, was also determined by fitting the data to Equation 3. However, due to the considerable scatter in the data, as can be seen in Figure 19, the author chose not to report those values.

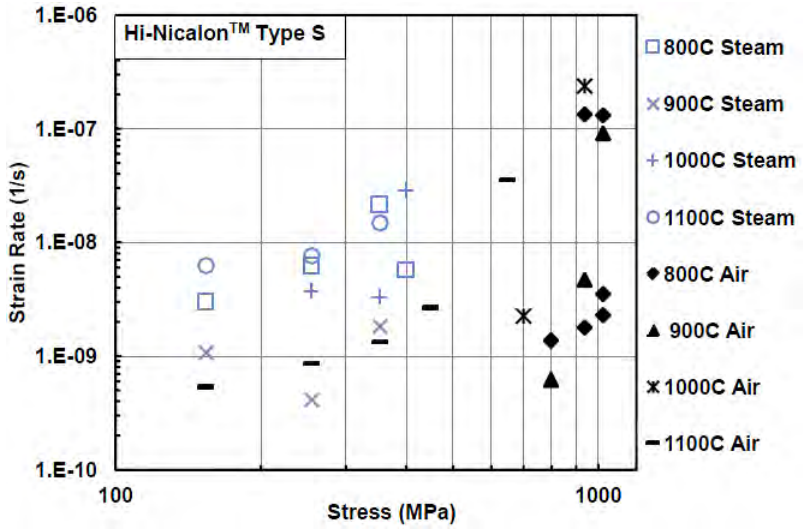


Figure 19. Creep of Hi-Nicalon^{TM} S fibers at 800-1100°C in air and in steam. Note the considerable scatter in the data, making a reliable estimate of the stress exponents impractical. Reproduced from [23].

2.4 Environmental Effects on the Durability of SiC Fibers and SiC/SiC CMCs

Silicon carbide fibers and fiber reinforced CMCs have been shown to be susceptible to environmental degradation [116, 140]. Oxide fibers and CMCs reinforced with them are not as susceptible to environmental degradation, making them an important alternative. However, SiC fibers and SiC-based CMCs consistently exhibit better high-temperature properties than oxide fibers and oxide/oxide CMCs, particularly in the areas of strength, creep resistance, creep rate, and accumulated creep strain [141]. This is especially true of the more recent third generation fibers, whose near-stoichiometric composition has increased their chemical and environmental stability. Since SiC fiber-reinforced CMCs are being developed for hot-section components of gas-based turbine engines that require long life cycles in a combustion gas environment [71, 94], it is critical to understand environmental effects on SiC fibers. That understanding rests on a foundational understanding of topics such

as fracture toughness, subcritical crack growth, and environmentally assisted crack growth (or stress corrosion cracking). A review of these concepts is in order.

The ability of a material that contains flaws, voids, or cracks to resist fracture is called its fracture toughness. It is a measure of the energy required to cause a crack to grow to the point of fracture. Fracture toughness can be measured and is considered a material property. Typically, a material fails once the stress at the tip of an existing crack is high enough (critical point) to result in a stress intensity factor that exceeds the material's fracture toughness, causing a crack to grow rapidly to failure. However, ceramics sometimes exhibit a different behavior. Under certain conditions, ceramics can experience slow crack growth even though the stress intensity factor is well below the critical point. This phenomenon is called *subcritical crack growth* or *delayed failure*.

At room temperature, the primary mechanism behind subcritical crack growth is *stress corrosion cracking* (SCC) [132], now more commonly referred to as *environmentally assisted crack growth* (EACG). EACG is a stress-assisted chemical reaction with the environment, particularly water, that breaks down a small portion of the material. In silicon-containing CMCs, water vapor reacts with the silicon to form silica (SiO_2). Because of the tensile load, the crack remains open and the corrosive environment can gain access to the interior of the matrix and even the fibers. Depending on the material and the environment, a protective film may develop that inhibits further corrosion, as is the case with SiC, where a thin film of silica forms and adheres to the parent matrix or fiber, slowing the environmental degradation. This is called passivation or passive oxidation. While the adsorption will still take place and the crack will grow, it takes longer because the environmental species must diffuse through the silica layer. Subcritical crack growth is also affected by the rate of the reaction between the environmental species and the matrix/fiber material. At

high temperatures, diffusion of the environmental species to the crack tip is the controlling mechanism [132]. The higher the temperature, the faster the diffusion can take place. Subcritical crack growth is very sensitive to temperature, applied load, and the concentration of the corrosive environmental species [4].

Several studies have investigated the thermal stability of SiC fibers in oxidizing environments and the effects of oxidation on SiC fibers and its relation to subcritical crack growth (delayed failure) [24, 43, 49, 105, 111, 121, 123–126, 142–158]. Lara-Curzio modeled the effects of oxidation on the stress-rupture behavior of fiber bundles and presented results for Nicalon^{TM} fibers. It was found that the life of the fiber bundles decreased with increasing temperature and stress and that the temperature dependence of failure times was the same as that of the oxidation process. This oxidation-induced loss of fiber strength resulted in delayed failure of the fiber bundle [123]. As mentioned earlier, Forio et al. found that delayed failure under low stress was a result of slow crack growth activated by oxidation [120]. Gauthier and Lamon developed a model of delayed failure that satisfactorily predicted strength dependence on applied load and temperature at temperatures below 800°C in the absence of creep as well as the lifetime of multifilament tows in the temperature range of the study. The model was based on subcritical crack growth in single filaments [121]. Gauthier et al. suggested that delayed failure was caused by slow crack growth of surface defects, which growth was induced by the consumption of free carbon at the grain boundaries and and local stresses at the crack tip caused by the transformation of SiC to SiO_2 [125].

Takeda et al. compared the microstructure and oxidative degradation behavior of Hi-Nicalon ^{TM} S fiber to that of its predecessors, Nicalon ^{TM} and Hi-Nicalon ^{TM} [158]. The fibers were oxidized in dry and wet air for 1-100 h at temperatures of 1000-1500°C. Oxide layer thickness was determined by SEM measurement (thicknesses >0.5 μm)

or by calculation of the oxygen content of the fiber based on the chemical reaction $Si_xC_yO_z + [x + (y - z)/2]O_2 \longrightarrow xSiO_2 + yCO$. Single filament tensile strength was measured. It was demonstrated that strength decreased with an increase in oxide layer thickness. Microstructural observations showed that fracture began at or near the oxide/fiber interface and revealed large numbers of pores in the earlier fibers due to volatilization of C and the release of carbon monoxide (CO) gas, whereas there were no pores in the Hi-Nicalon ^{TM} S fibers, resulting in the best oxidation resistance of the fibers tested.

Opila studied the dependence of the oxidation rate of SiC on water vapor pressure [157]. CVD SiC was subjected to temperatures of 1000-1400°C in H_2O/O_2 and H_2O/Ar environments with 10-90 vol% water vapor and a total pressure of 1 atm. It was seen that the oxidation kinetics increased with an increase in water vapor pressure and that the parabolic oxidation rates were a full order of magnitude higher than those evident in dry oxygen. Bubbles were also noted to form in the silica scale at water vapor pressures greater than 25% and increased with an increase in water vapor pressure. Opila later investigated the oxidation and volatilization of silica formers in water vapor [152]. A paralinear kinetic model was adapted to describe the steady-state oxidation/volatilization of silica. Steady-state is achieved when the oxidation rate at which silica is formed equals the volatilization rate of silicic acid, $Si[OH]_4$. The model was successful, with limitations, at predicting the steady-state rate, and model predictions compared well to the experimental data. A series of recession rate maps were also developed to provide a framework for understanding the limitations of the model [152].

It has been shown that the partial pressure of the oxygen has a large effect on the oxidation of SiC fibers [144, 148–150, 154]. Shimoo et al. found that SiC fibers experience active oxidation at low oxygen partial pressure and passive oxidation at

medium and higher partial pressures [144, 150]. In active oxidation, material within the fiber is volatilized, resulting in gaseous products and significant damage to the SiC fibers. Shimoo et al. reported that after passive oxidation, Nicalon^{TM}, Hi-Nicalon^{TM}, and Hi-Nicalon^{TM} S fibers showed the formation of a silica scale and a retention of 40-80% of their initial strength. Hi-Nicalon^{TM} S fibers exhibited the greatest retention of strength. After active oxidation, Hi-Nicalon^{TM} S retained 35% of its initial strength while the others experienced a complete loss of their strength [144]. Jacobson and Myers studied the transition between active and passive oxidation (and vice versa) of SiC in an oxygen (O_2)/Ar environment and in pure O_2. It was found that both transitions happen at approximately the same pressure of oxygen based on processes at the interface between the SiC and SiO_2 surface layer. No appreciable difference was evident between the partial pressure of oxygen in the O_2/Ar environment versus the total pressure in the pure O_2, but the morphology was different due to the volatilization of SiO_2 in the partial pressure case. Several models were also evaluated. None were found to completely explain all observed phenomena, but the models were able to explain some of the phenomena [154].

Between 2005 and 2009, Sha and associates conducted a series of studies on the thermal and mechanical properties of Hi-Nicalon^{TM}, Hi-Nicalon^{TM} S and Tyranno^{TM} SA fibers, looking at the effects of varying oxygen partial pressures at elevated temperatures [159–163]. Sha et al. annealed these fibers as fiber tows in air (O_2: 20%), high-purity Ar (HP-Ar, O_2: 2 ppm) and ultra high-purity Ar (UHP-Ar, O_2: 0.1 ppb) at 1000-1500°C and then extracted individual fibers for evaluation of their properties [160, 162, 163]. Tensile strength was found to be highly dependent on O_2 partial pressure, with room temperature strength decreasing with a decrease in O_2 partial pressure while creep resistance was higher in the low O_2 partial pressure environment. The degree of oxidation increased with an increase in temperature and/or stress and

with a decrease in O_2 partial pressure. The transition from passive to active oxidation was accelerated by a reduction in the O_2 partial pressure. Sha et al. also found evidence of EACG with accelerated nucleation and growth of flaws/cracks [159, 161].

Hay and his colleagues have done several studies on SiC fibers, particulary focusing on Hi-Nicalon^{TM} S [24, 142, 153, 155, 164]. Hay et al. measured the strength of Hi-Nicalon^{TM} S fibers after oxidation in dry air at temperatures between 800 and 1200°C [164]. They found that fiber strength increased by ~10% with the growth of silica scale up to approximately 100 nm, but decreased for thicker scales. The increase in strength with thin scales was attributed to the compressive residual stress within the scale due to its formation and may also be due to healing of surface flaws. The increase in strength is related to the residual compressive thermal and growth stresses in the silica scale. The decrease in strength for the larger scale case is likely due to the scale having crystallized into α-crystobalite, which is accompanied by a volume decrease during a phase transition and generates tensile residual stress in the scale. Cracks and partial debonding were noted in the crystallized scale [164].

Hay et al. later expanded the temperature range of their investigation into the strength of Hi-Nicalon^{TM} S fibers after oxidation in dry air to 700-1400°C. The oxidation and scale crystallization kinetics of these fibers was also studied [24, 153]. It was found that the amorphous silica scale, with some carbon content, forms initially, followed by crystallization into crystobalite and tridymite. Tridymite was predominant, but both were exhibited. Amorphous scales were smooth and uncracked, while crystallized scale often exhibited through thickness and debond cracks, resulting in an end to passivation and enhanced oxidation in these areas. Crystallized silica scale was thinner than amorphous scale. Amorphous scale oxidation kinetics followed the

Deal-Grove relationship as modified by Song et al [165]:

$$\frac{dx}{dt} = \frac{B}{(A + 2x)} \tag{4}$$

with $A = A_0 exp\left(\frac{-Q_a}{RT}\right)$ and $B = B_0 exp\left(\frac{-Q_b}{RT}\right)$, where B is the parabolic rate constant, B/A is the linear rate constant, A_0 and B_0 are pre-exponential constants, Q_a and Q_b are the activation energies, and R and T are as described previously. A is the silica thickness at which the change from linear to parabolic kinetics occurs. The activation energy for parabolic oxidation for amorphous silica scale was 248 kJ/mol (235 Btu/mol). The crystallization kinetics Kolmogorov-Johnson-Mehl-Avrami (KJMA) model parameters were found to be extremely sensitive to SiC impurities and the environment. Crystallization had an activation energy of 514 kJ/mol (487 Btu/mol) and began within 100 h at 1000°C and 1 h at 1300°C, and was complete within 80 h at 1100°C, 30 h at 1200°C and 1 h at 1300°C. Crystallization was always found to nucleate from the surface [24] with much more rapid growth parallel to the surface than through the thickness [153]. A strong correlation was seen between the crystallization of the scale and the onset of loss of strength. This was due to tensile thermal stress in the crystallized scale [153].

In 2012, Hay proposed a method to calculate growth stress in SiO_2 scales formed during Hi-Nicalon^{TM} S SiC fiber oxidation [142]. Using data from previous efforts [24, 142, 153, 164], compressive stresses of approximately 25 GPa (3.63 msi) were calculated. These stresses were caused by a volume expansion of 2.2 times during the formation of the silica, but were rapidly relaxed to negligible levels at temperatures above 1200°C by flow of the silica. At 700-900°C, compressive axial and hoop stress is still in the GPa range, but radial stresses are much smaller. Axial growth stresses were found to have the largest effect on fiber strength. Radial expansion created tensile hoop stress in the outer portions of the scale. Tensile hoop and axial stresses

were seen to reach values of 2.8 and 0.8 GPa (406 and 116 ksi), respectively for long times at 700°C. The accuracy of this calculation method depends on the accuracy of amorphous silica viscosity data, which, in turn, are affected by impurities in the SiC fiber. Lack of availability of viscosity data for crystobalite and tridymite precluded calculation of growth stresses in crystallized silica, but they are assumed to be much higher than those in the amorphous silica. For very thick crystallized scales, through thickness and debond cracks were observed, with accompanied fiber strength degradation [142].

Hay et al. continued with Hi-Nicalon^{TM} S fibers by repeating the work above in wet air instead of dry air [155]. Experiments measuring strength, oxidation kinetics and scale crystallization kinetics were conducted in wet air at temperatures between 700 and 1300°C. Crystallization again began within 100 h at 1000°C and 1 h at 1300°C but was slightly slower than in dry air. The activation energy for parabolic oxidation for amorphous silica scale (249 kJ/mol, 236 Btu/mol) was almost identical to that in dry air, but the pre-exponential constants, A_0 and B_0 were about two times higher. As in dry air, fibers experienced approximately a 10% increase in strength with silica scales of up to 100 nm thick. Strength decreased for thicker scales, with no significant degradation observed for amorphous scales. Again, fibers with significantly degraded strength exhibited crystallization in the scale with cracks from thermal stress, polymorphic phase transformations, and tensile hoop growth stress [155].

As mentioned earlier, Steffens [1] and Shillig [23] both investigated creep of Hi-Nicalon^{TM} S ceramic fiber tows at elevated temperatures (800-1100°C) in air and in steam. Steffens reported that steam reduced the creep (or static fatigue) performance of the Hi-Nicalon^{TM} S fiber tows at both 800 and 1100°C significantly. Specifically, at 800°C, the creep rates of the Hi-Nicalon^{TM} S fiber tows increased by at least one

order of magnitude and the creep lifetimes decreased by more than three orders of magnitude due to steam. Creep run-out, defined as 100 h at creep stress, was achieved at 780 MPa (113 ksi) in air, but at only 139 MPa (20 ksi) in steam. Additional tests at 1100°C showed that the higher temperature degraded the creep performance in air, but improved it in steam. In air, the creep lifetimes decreased by about one order of magnitude, whereas they increased by at least one order of magnitude in steam. This was attributed to the formation of a silica scale that protected the surface from the active oxidizing species, slowing the growth of surface defects and delaying fiber failure. There was no significant difference in creep rates produced at the two test temperatures. Shillig's work [23] at temperatures of 800, 900, 1000, and 1100°C corroborated Steffens' findings [1] to some extent, but was complicated by contaminants and by evidence of active and passive oxidation throughout the temperature regime. These efforts were preliminary and highlighted the challenges associated with testing SiC fiber tows in steam. By elucidating these challenges, Steffens' and Shillig's work identified a strong need for a different test facility and methodology.

Several studies have also been performed on SiC-based CMCs. Kim et al. studied the fatigue behavior of Hi-Nicalon^{TM} S/BN/SiC CMCs using a burner rig that simulates a combustion environment [42]. The melt-infiltrated (MI) CMCs were fabricated by General Electric using two different methods: slurry cast woven CMC and prepreg CMC. In both cases, oxidation was observed on the fracture surface in the wake of the advancing crack tip. However, the oxidative damage was noticeably less in prepreg due to the greater physical/chemical isolation of each fiber. This oxidation led to embrittlement, which is a significant life-reducing factor. Wu et al. investigated the oxidation behavior of 3D Hi-Nicalon^{TM}/SiC composites in wet and simulated air environments above 1200°C [166]. Silica formed mainly on the surface of the CMC

and oxidation in both environments was rate-controlled by the diffusion of oxygen through the silica, though it was greatly enhanced in the presence of water vapor. In both cases, the surface morphology and amount of oxidation was strongly related to temperature, increasing with an increase in temperature, but oxide layers were thicker in wet air. It was also found that, above 1200°C, the strength dropped off rapidly with an increase in temperature due to degradation of the fibers.

In the past five years, further studies of environmental effects on the mechanical performance of SiC/SiC CMCs have been conducted by Ruggles-Wrenn and her associates at AFIT [85, 89–91, 167, 168]. Ruggles-Wrenn and Sharma investigated the behavior of SiC/(SiC+Si_3N_4) CMCs subjected to tension-tension fatigue at 1300°C in laboratory air and in steam [168]. CMCs consisted of woven Sylramic^{TM} or Sylramic^{TM} iBN fibers in a crystalline silicon carbide/silicon nitride matrix. Tension-tension fatigue tests were conducted at stresses in the range of 100 to 180 MPa (14.5 to 26 ksi). It was found that steam significantly degraded the fatigue performance of the CMCs. The number of cycles to failure in steam was much lower than that in air, showing up to an order of magnitude drop. The creep strain was higher in steam than in air. Optical and SEM analysis revealed significant disintegration of the matrix in the specimens subjected to steam. Ruggles-Wrenn et al. studied the effects of air and steam environments on the fatigue behavior of a CVI Hi-Nicalon^{TM}/SiC CMC [167] and a CVI Hi-Nicalon^{TM}/(SiC+B_4C) CMC [89] at 1200°C. Specimens were tested in tension-tension fatigue with stresses ranging from 60 to 140 MPa (8.7 to 20.3 ksi). The damage mechanisms were found to be oxidation embrittlement and fiber degradation due to creep-controlled flaw growth. Damage due to oxidation embrittlement was significantly accelerated in the presence of steam. This detrimental effect of steam resulted in a fatigue life degradation of one to two orders of magnitude. Also, in all of these studies, tension-to-failure tests were conducted on specimens that

achieved fatigue run-out, defined as 10^5 or 2×10^5 cycles, depending on the frequency of the fatigue test. Each of these tests showed fatigue in steam to have a greater degrading effect on the retained modulus than fatigue in air.

The work on SiC/SiC CMCs continued as Ruggles-Wrenn and Jones studied the fatigue behavior at 1200°C of a CMC made with Hi-Nicalon^{TM} fibers coated with pyrolytic carbon with a boron carbide overlay in a SiC-based matrix [91]. The tension-compression fatigue tests were conducted with maximum stresses of 80 to 200 MPa (11.6 to 29 ksi) in air and in steam and had a minimum to maximum stress ratio of -1. Damage and failure resulted from oxidation embrittlement. As in previous studies, the damage development and failure were significantly accelerated in the presence of steam. Ruggles-Wrenn and Kurtz investigated the effect of holes on the fatigue behavior of a Hi-Nicalon^{TM}/(SiC-B_4C) CMC at 1200°C in air and in steam [90]. Specimens with a center hole were tested in tension-tension fatigue at stresses in the range of 100 to 140 MPa (14.5 to 20.3 ksi) and results were compared with those of specimens without holes. While notch sensitivity was not appreciably different in air or steam environments, it was shown that steam had a much more degrading effect on fatigue life and retained modulus than air. Ruggles-Wrenn and Pope examined the creep behavior of Hi-Nicalon^{TM}/(SiC-B_4C) CMC in interlaminar shear [85]. Tests were conducted at 1200°C in air and in steam with interlaminar shear stresses of 16 to 22 MPa (2.3 to 3.2 ksi). While creep strain rates and creep lifetimes were only moderately affected by the presence of steam, accumulated creep strain in steam was significantly higher, reaching as much as three times that in air. The presence of steam also decreased the retained interlaminar shear strength by 25%.

Clearly, the environment has a significant impact on the strength and durability of SiC fibers over time, especially at elevated temperatures. For SiC fibers, it is evident that oxygen-containing environments, and particularly water vapor [1, 23, 85, 89–

91, 142, 152, 155, 157, 167–169], cause degradation of the fiber performance. Since fiber performance determines the ultimate performance of the CMC [24, 153, 155], it is critical to understand fiber behavior in general and particularly in the working environment of the CMC.

2.5 Implications for Current Research

Results of the aforementioned studies on SiC fibers and CMCs reveal the degrading effect of air and, particularly, steam on the creep performance of fiber-reinforced CMCs. The fiber dominates the mechanical behavior of a composite with 0/90 fiber orientation under tensile loading [4, 159], so fiber degradation is a significant part of composite degradation [166]. It is recognized that the Hi-Nicalon^{TM} S fiber has the highest creep resistance of any commercially available non-oxide fiber. The superior creep performance of the Hi-Nicalon^{TM} S fiber is due to a reduced amount of free carbon, as compared to its predecessors, that limits grain growth that would otherwise be extensive at high temperatures and to the presence of larger grains than its predecessors. Another factor is the absence of sintering aids that can cause higher creep rates and poor strength retention in fibers. In spite of these advantages, degradation of the creep performance of Hi-Nicalon^{TM} S fibers in the presence of steam is likely the primary cause of the degraded creep performance of the Hi-Nicalon^{TM} S-reinforced CMCs in a steam environment. Active and passive oxidation significantly affect creep performance and are dictated by the thickness and crystallization rate of the silica scale. The formation of the silica scale, in turn, depends on the temperature, environment, and applied stress. A thorough understanding of the creep performance of Hi-Nicalon^{TM} S fiber tows in the presence of steam is key to understanding the mechanisms behind the degradation of the creep resistance of SiC-based CMCs in steam. Therefore, it is important to investigate the creep behavior of Hi-Nicalon^{TM} S fiber

tows, to determine the creep rates, and to identify the underlying microstructural creep mechanisms operating at elevated temperature in steam. Though Steffens and Shillig have made progress on this front, this task has yet to be completed, mainly because of the need identified by their work for different test facility and methodology. This different facility was successfully developed as a part of the current work.

III. Experimental Methods

> "The experimentist in solid mechanics has two main challenges. The first and by far the most important is to establish the form and content of constitutive equations in the wide variety of solids extant in nature. This is a function which he and he alone can perform. The second...is to determine experimentally whether or not restricted specified forces and/or displacements applied to finite bodies of defined geometry actually do produce the stress, strain, displacement, particle velocity, rotational distributions, and magnetic, electrical, and thermal fields, which the assumptions of a given set of constitutive equations would suggest." [170]

The above quote from "Mechanics of Solids, Vol. 1: The Experimental Foundation of Solid Mechanics" by James F. Bell captures the essence of what it means to be an experimentist, namely, to provide the substance of models of physical phenomena and to verify that the model's predictions actually do occur in the physical world. This experimental research effort is squarely in line with Bell's comments. The experimental methods used and developed in this research effort specifically addressed the following objectives:

- Determine the effects of silicic acid-saturated steam on the strength and creep performance of Hi-Nicalon^{TM} S non-oxide SiC fibers at 800°C
- Evaluate the efficacy of the Monkman-Grant relationship and a environmentally assisted subcritical crack growth model for Hi-Nicalon^{TM} S fiber tows
- Evaluate oxidation damage and elucidate damage and failure mechanisms of Hi-Nicalon^{TM} S fiber tows

In order to achieve these objectives, an appropriate test facility and methodology had to first be designed, developed, built, and validated. This was done and preliminary results addressing each of the above objectives were successfully obtained. The test facility was built to generate steam at or near test temperatures with or without

silicic acid saturation and was validated by testing of Hi-Nicalon^{TM} S fiber tows at 800°C in air and silicic acid-saturated steam. The second objective was achieved by post-test analysis of the creep and tensile test data. Microstructural analysis using SEM and optical microscopy. Examination under transmission electron microscopy (TEM) was also attempted.

The experimental facility used in this effort was designed and built in the Mechanics of Advanced Aerospace Materials Laboratory of the Department of Aeronautics and Astronautics (ENY) at AFIT. Methods for testing ceramic fiber tows under monotonic tension and in creep at elevated temperature in air and in steam environments were also developed. The design of the facility and development of the methodology were influenced by the work of Armani [4], Steffens [1], and Shillig [23]. While some of the information in the following two sections describing the test facility and the test methodology has its foundations in the work of Armani, Steffens, and Shillig, the facility is significantly different and the new methodology reflects the difference.

3.1 Creep Testing of Fiber Tows

As mentioned in chapter two, it has been established that fiber bundles fail at lower stresses than the strength predicted by testing of individual filaments [115–119]. Dassios et al. [118] and Calard and Lamon [119] concluded that testing of fiber tows provided more accurate results for fiber strength and prediction of CMC performance than testing of individual filaments. Additionally, time and available resources preclude the testing of each individual fiber in the fiber tow. These observations and conclusions provide a compelling basis for testing fiber tows rather than single filaments, therefore, this work involved only the testing of fiber tows.

The creep performance of Hi-Nicalon^{TM} S fiber tows was investigated in air and steam at 800°C range, with creep run-out defined as 100 h at creep stress. Experi-

ments were conducted at various temperatures and creep stress levels in order to (1) quantify the creep activation energy, (2) establish the dependence of creep behavior on applied stress, (3) measure the steady-state creep rates, and (4) evaluate the effects of steam and silicic acid-saturated steam environments on creep behavior. After these effects were determined, the microstructure and damage/failure mechanisms were investigated. The microstructural investigation, in conjunction with the analysis of the experimental data, provided insight into the creep and the environmental degradation mechanisms present in these SiC fibers.

Creep tests were performed in air and silicic acid-saturated steam. In each test, load-displacement data was recorded during the temperature ramp up and heat-soak, during loading to the creep stress level, and during the actual creep period. Applied stress, thermal strain, total mechanical strain, and creep strain were calculated from this data. A heating rate of no greater than 1.0°C/s was used to reach the target temperature, after which the specimen was held at the target temperature for a minimum of 45 minutes in order to achieve thermal equilibrium before the application of the test load. During heat-up and heat-soak each specimen experienced a small (10-20 g) load in order to keep the fiber tow taut. This small load amounts to 1.5 - 3.5 MPa (214 - 505 psi) of stress on the fiber bundle.

A compact two-zone resistance-heated MTS 653.03A furnace, shown in Figure 20, provided the high temperature environment. The furnace has silicon carbide heating elements and non-contacting R type control thermocouples, which supply feedback to an MTS 409.83 temperature controller. The furnace has a 90 mm (3.5 in.) hot zone. A high resolution Schaevitz M12-30 linear variable differential transformer (LVDT) was used to provide accurate displacement measurements. Methods to determine strain from displacement measurements are detailed later in this section. Data was acquired using an MTS FlexTest 40 digital controller.

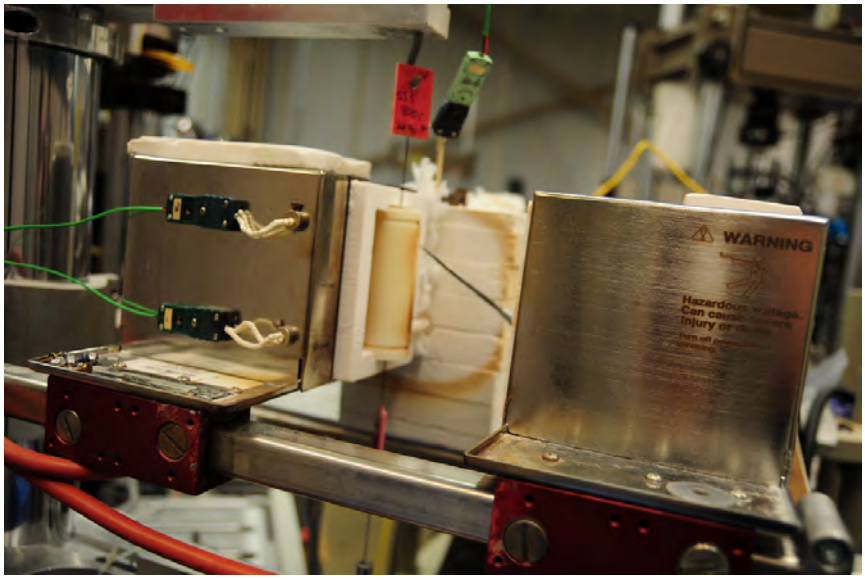


Figure 20. Two-zone resistance-heated MTS 653.03A furnace with silicon carbide heating elements, R type control thermocouples and a 90 mm (3.5 in.) hot zone

All tests employed a susceptor (test chamber) made from 99.8% pure alumina tubing with end caps, designed to fit inside the furnace. The central section of the fiber tow was inside the susceptor with the ends of the fiber tow passing through slots in the susceptor end caps. The use of a susceptor has been shown to result in a more uniform and repeatable temperature distribution along the gauge section of the fiber tow specimen [1, 23]. The susceptor provides a smaller volume for the test environment than that of the entire furnace. The temperature and steam environment is much easier to maintain in the smaller volume. Also, the susceptor prevents the heating elements from directly radiating the specimen, which would otherwise result in significant differences in temperature along the fiber depending on distance and direct line of site from the heating elements to the test specimen. Instead, the susceptor absorbs the radiant heat from the heating elements and reradiates it more uniformly to the test specimen, resulting in a more uniform temperature profile along the test specimen. Another benefit of the susceptor is that it protects the heating elements from exposure to steam, extending life and effectiveness of the heating elements and,

consequently, the life of the entire test system. As mentioned above, a supply tube delivers steam to the susceptor at the bottom of the chamber. A feeding tube supplied dry air, steam, or silicic acid-saturated steam to the susceptor.

A detailed description of the specimen mounting procedure and of the creep test procedures is given by Armani [4] and Steffens [23]. Figure 21 shows the susceptor and feeding tube assembled in one half of the furnace. Figure 22 shows a fiber tow specimen mounted in the dead weight creep testing facility.



Figure 21. Alumina susceptor and feed tube assembled in one half of the furnace, reproduced from [4]

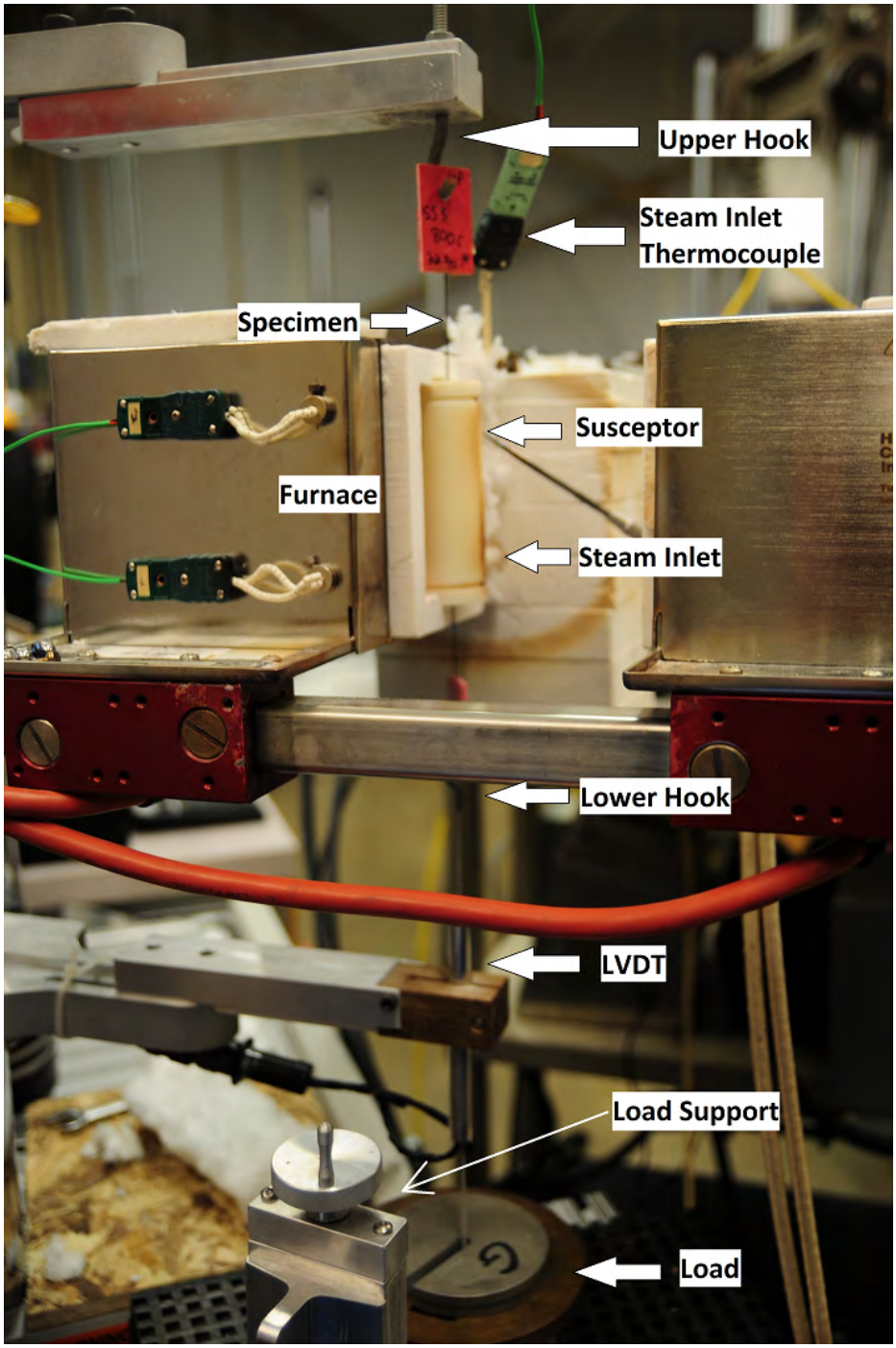


Figure 22. Fiber tow creep test setup

3.1.1 Furnace Temperature Profile.

To generate a temperature profile, temperature was measured along the entire height of the furnace using a K-type thermocouple. Temperature profiles for fiber tow testing were characterized using the same procedure as in prior work [1, 4, 23], with one exception. Rather than taking temperature readings at specific intervals vertically along the centerline of the furnace, as was done previously, temperature readings were taken during a continuous vertical sweep along the centerline of the furnace. This was accomplished by adding the required hardware to the MTS Flex Test 40 controller to record the temperature via the computer and by writing a program to collect the data while sweeping from the bottom of the furnace to the top. The sweep rate was no faster than 0.014 mm/s (5.5×10^{-4} in.) so as to minimize any latency in the thermocouple response. Temperature readings were taken with a K-type thermocouple capable of accuracy to within 2.2°C up to 1250°C. The thermocouple was attached to the ram of the servo-hydraulic machine via a magnetic fixture, allowing for controlled probing throughout the height of furnace.

To protect the upper grip and the specimen tab from the high temperatures of the furnace, a 1.27 cm (0.5 in.) thick piece of oxide insulation board was placed on top of the furnace. The setpoints of the temperature controllers were determined to ensure accurate temperature control. First, the thermocouple was positioned in the center of the furnace and the temperature was increased. Then, the thermocouple was moved up and down from the center of the furnace and the setpoints were adjusted until the desired temperature profile was achieved. Once the setpoints for the temperature controllers were determined, a detailed temperature profile was established by recording temperature values continuously along the height of the furnace starting just below bottom end cap of the susceptor and ending just above the top end cap, a total travel of 100 mm (3.937 in.). Figures 23 and 24 show the temperature profiles

determined using this method for air and steam, respectively. Individual temperature profiles for temperatures from 400 - 1000°C can be found in Appendix A.

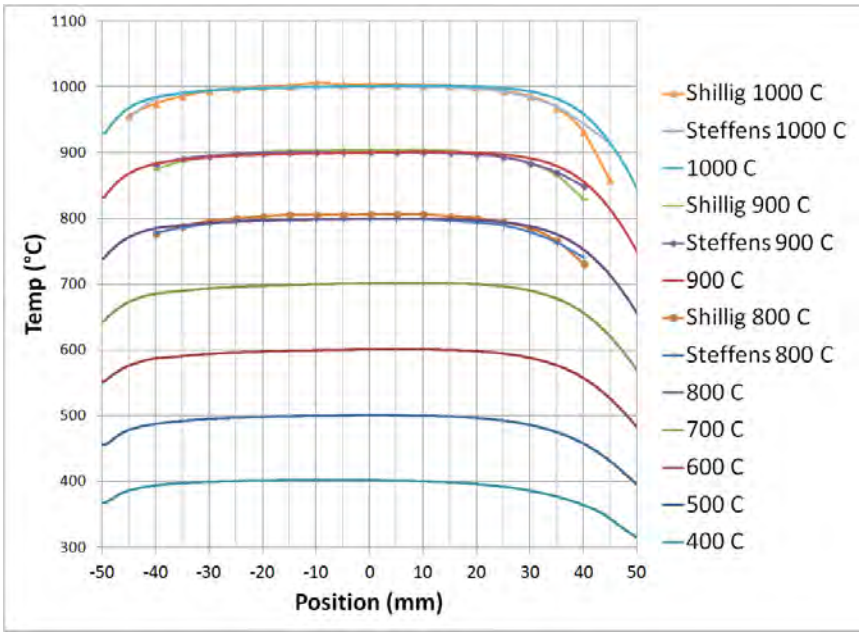


Figure 23. Temperature profiles in air for the current work with data from Steffens [1] and Shillig [23] for comparison.

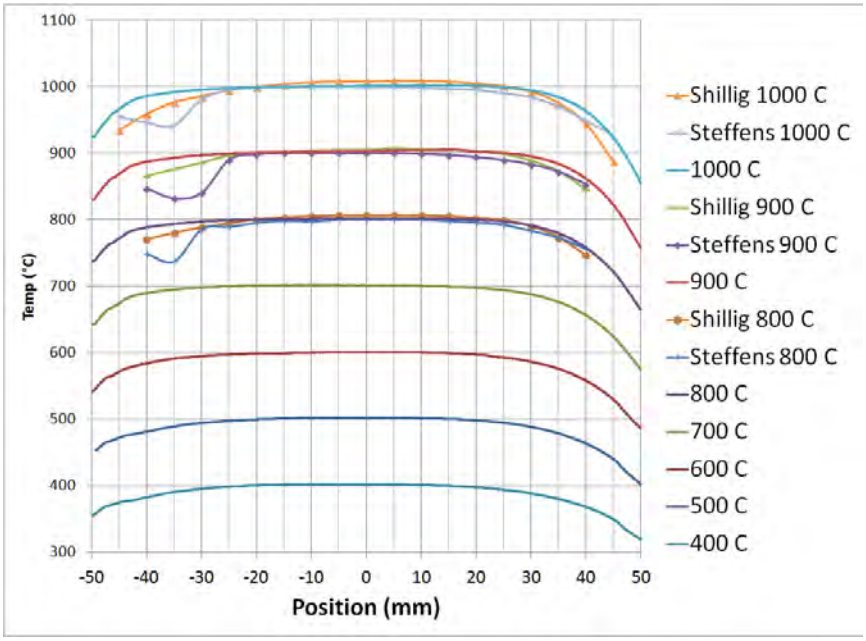


Figure 24. Temperature profiles in silicic acid saturated steam for the current work with data from Steffens [1] and Shillig [23] for comparison.

3.1.2 Strain Measurement.

It is impractical to directly measure the strain of a fiber bundle due to the difficulty in general of attaching a measuring device to the fibers and particularly within a furnace. There is no way to mount a strain gauge on the fibers due to their small size. Additionally, the use of an extensometer will not work with a fiber bundle because it relies on contact between the extensometer rods and a rigid surface. The fiber bundle is not rigid. As such, an indirect method was used to determine the strain.

Once the temperature profiles of the furnace were obtained, an effective gauge length of the test specimen was calculated for each test temperature using techniques demonstrated by Morrell [171], Kandil and Dyson [172], and DiCarlo [173] and used successfully by Armani. In these efforts, the error in strain resulting from measuring the displacement outside of the furnace was estimated and was found to be small compared to errors inherent in accurately measuring the temperature. Yun, et al. [174] calculated creep deformation another way. The majority of the creep deformation of the fiber tow was assumed to occur in a hot zone with a flat temperature profile. This flat profile was defined as a maximum temperature gradient of 6°C or less across the hot zone. Yun et al. validated this assumption using a hot grip method. Pratically speaking, this method was the same as that used by Kandil and Dyson [172]. After the effective gauge length of the heated fiber tow is determined, the measured displacements can be converted to engineering strain. Steffens [1] and Shillig [23] also employed this method successfully. This technique and Armani's method for calculating the strain was used in the current work and is reviewed here.

Consider a test specimen with a constant cross section and a length of 2L. Defining the center of the specimen gauge length as zero, creep occurs over the total length from L to L. Outside of these bounds, creep is negligible due to significantly lower

temperature. As such, the total measured strain and total measured strain rate are:

$$\varepsilon_m = \frac{\Delta l}{2L} = \int_0^t \dot{\varepsilon}_m dt \tag{5}$$

$$\dot{\varepsilon}_m = \frac{measured\, extension\, rate}{2L} = \frac{1}{2L}\int_{-L}^{L} \dot{\varepsilon} dl \tag{6}$$

Since the specimen is subject to varying temperature along its length, it follows that strain and strain rate will also vary along the specimen's length. The total measured strain and strain rate equations account for variations in strain and strain rate along the specimen length. At the hottest sections, the amount of strain or strain rate will be greater than at a lower temperature. The strain and strain rate obtained from the specimen gauge section at the desired maximum temperature at the center of the furnace are denoted by a subscript "o" and used as a reference for comparison. The strain at the center of the furnace can be obtained by calculating the time integral of the strain rate at the center of the furnace. This strain can also be described by the overall change in length of the entire specimen divided by a hypothetical length called the *effective gauge length*, $(2L)_{eff}$. This effective gauge length is akin to the gauge length of a hypothetical step-function temperature profile in which all the strain is accumulated under the peak temperature and zero strain is achieved under the lower temperature. Therefore, the strain at the desired maximum temperature can be written in terms of the effective gauge length:

$$\varepsilon_o = \int_0^t \dot{\varepsilon}_0 dt = \frac{\Delta l}{(2L)_{eff}} \tag{7}$$

And similarly, for the strain rate at the maximum temperature (i.e. strain rate at the center of the furnace):

$$\dot{\varepsilon}_o = \frac{measured\,extension\,rate}{(2L)_{eff}} = \frac{1}{(2L)_{eff}} \int_{-L}^{L} \dot{\varepsilon} dl \tag{8}$$

The ratio of Equations 6 and 8 yields:

$$\frac{\dot{\varepsilon}_m}{\dot{\varepsilon}_o} = \frac{(2L)_{eff}}{2L} \tag{9}$$

The general power-law creep equation can now be applied. Considering that the stress is uniform along the specimen and that temperature is a function of location along the fiber tow specimen:

$$\dot{\varepsilon} = A\sigma^n \exp\left(\frac{-Q}{RT(l)}\right) \tag{10}$$

Using Equations 6, 9 and 10, the ratio of the measured strain rate to the actual strain rate reduces to a function of temperature only:

$$\frac{\dot{\varepsilon}_m}{\dot{\varepsilon}_o} = \frac{1}{2L} \int_{-L}^{L} \exp\left\{\frac{-Q}{R}\left(\frac{1}{T(l)} - \frac{1}{T_o}\right)\right\} dl \tag{11}$$

Applying a numerical approach, the integral becomes a summation of increments of length h such that L = kh, where k is an integer. The ratio of the measured strain rate to the actual strain rate is

$$\frac{\dot{\varepsilon}_m}{\dot{\varepsilon}_o} = \frac{1}{2k} \sum_{i=-k}^{k} \exp\left\{\frac{-Q}{R}\left(\frac{1}{T(l)} - \frac{1}{T_o}\right)\right\} \tag{12}$$

An effective gauge length can now be calculated using this numerical approach such that:

$$(2L)_{eff} = 2L\left(\frac{\dot{\varepsilon}_m}{\dot{\varepsilon}_o}\right) \tag{13}$$

This effective gauge length enables the calculation of strain and strain rate from displacement measurements taken outside the hot zone of the furnace.

The elongation of the fiber tow specimens was measured with a Schaevitz M12-30 LVDT. For tensile creep testing, fiber tow specimens were suspended from an extendable fixture. The LVDT is connected to the bottom tab of the fiber tow specimen. A rod extending from the bottom of the LVDT core holds the dead weight, as shown in Figure 22. Slow application of the creep load is critical to preventing damage to the tow specimen during initial loading. Therefore, a hand-driven screw elevator was used to apply the load to the fiber tow specimens.

Using the method described above, the temperature profiles reported in section 3.1.1, and the activation energy reported by Gauthier and Lamon [121] of 177 kJ/mol (168 Btu), values of effective gauge length were calculated for each test temperature in air and steam. These values are listed in Table 8 and depicted Appendix A in Figures A.1 through A.14.

Table 8. Effective gauge lengths at tested temperatures in air and in steam.

Temp (°C)	**Effective Length (mm)**	
	Air	**Steam**
400	51.72	48.55
500	59.84	54.83
600	62.00	61.83
700	65.70	71.03
800	71.75	73.51
900	74.46	86.52
1000	77.58	79.08

3.2 Creep Testing in Air a Elevated Temperature

Creep tests were performed in dry air at 800°C. However, the test facility was designed and built for use at lower temperatures as well. At lower temperatures, it is possible to have some small amount of moisture in laboratory air. This moisture

can affect the fiber tow oxidation and, therefore, the creep rate and creep strain. It is important to minimize the possible effects of moisture in the air as much as possible. Therefore, the test methodology developed for this effort addressed this concern.

Compressed air has a significantly reduced amount of moisture in it, because the compression process causes the water vapor to condense out of the air and the water is siphoned out of the compressed air tank. Compressed air was introduced into the test chamber via alumina tubing passing through a set of pre-heaters that heat the air to at least two-thirds of the test temperature before the air enters the test chamber. The air flow rate was calculated by measuring the linear flow rate using a Testo 410-2 hand-held anemometer and multiplying by the cross-sectional area of the tubing. The linear flow rate was less than the resolution of the anemometer, so the volumetric flow rate was less than 301.6 ml/min (18.41 in^3/min).

3.3 Tensile Testing of Fiber Tows

The tensile strength of Hi-Nicalon^{TM} S fiber tows was investigated in air and steam at 800°C range. First, fast fracture tensile tests were conducted in order to verify the tensile strength of the fiber tows at room temperature and elevated temperature. Fast fracture tensile tests were conducted only in air because the short duration precludes any appreciable effects due to the presence of steam, rendering tests in steam unnecessary. Fast fracture tensile tests were conducted at 10 MPa/s (1.45 ksi/s).

Next, experiments were conducted at the same temperature as the fast fracture tests and applied stress rates were varied in order to (1) determine if slow crack growth (i.e. delayed failure or EACG) is a dominant failure mechanism, (2) evaluate the slow crack growth parameters, if any, and (3) evaluate the effects of steam and silicic acid-saturated steam environments on tensile behavior and slow crack growth.

The microstructure and damage/failure mechanisms were then investigated in order to provide insight into the creep and the environmental degradation mechanisms present in these SiC fibers.

Tensile tests were performed using an MTS Landmark^{TM} 370.02 servohydraulic test facility (Figure 25) fitted with an MTS force transducer, model 661.11B-02, with a test load capacity up to 500N (110 lbs). The test system is equipped with water cooled MTS 647.02B hydraulic wedge grips. A compact two-zone resistance-heated MTS 653.03A furnace, shown in Figure 20, provided the high temperature environment. An MTS FlexTest 40 digital controller provided the input signal generation and for data acquisition. Tests were conducted in air and silicic acid-saturated steam at various applied stress rates. In each test, stress was applied at a specific rate until failure of the fiber tow was achieved. Force, displacement, and time data was recorded and applied stress was calculated from this data. A heating rate of 1.0°C/s was used to reach the target temperature, after which the specimen was held at the target temperature for a minimum of 45 minutes in order to achieve thermal equilibrium before the application of the test load.

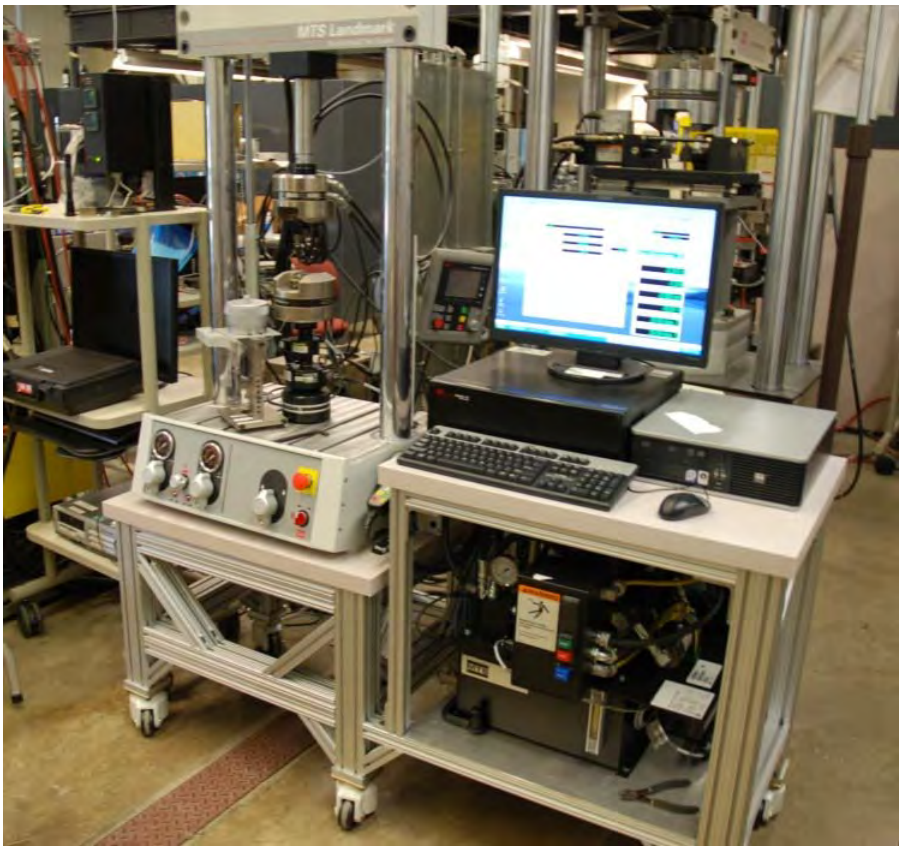


Figure 25. MTS Landmark^{TM} 370.02 servohydraulic test facility, reproduced from [4]

3.4 Test Specimen Preparation

Test specimens were prepared using the three-tab method developed by Steffens [1]. In this method, a centerline hole is punched in the fiberglass tabs so that the fiber tow specimen can be hung from the hook fixtures of the creep test facility. In preparing the fiber tow test specimens, portions of the tow that contain obvious damage, such as broken filaments and bent fibers, are discarded. Fiberglass tabs are positioned 17.78 cm (7 in.) apart on the grid of a cutting board. Each tow section is aligned over the tabs, using the grid lines, and taped onto the cutting board. The fiber tow bisects the centerline holes in each tab to ensure that only axial loading is present during testing. A two part epoxy is applied to the tow section on top of the primary tab and the secondary fiberglass tab is applied so that the tow and the

epoxy are sandwiched between the tabs. Once the adhesive has sufficiently thickened (approximately 5 minutes), the excess tow protruding beyond the tabs is folded toward the test section and the two-part epoxy is then applied to the folded tow section on top of the secondary tab. Finally, a tertiary tab is applied in order to sandwich the folded portion of the tow between the secondary and tertiary fiberglass tabs. After the adhesive has fully cured, the excess tow protruding beyond the tertiary tab is cut with a razor blade. The final length of the fiber tow specimen measured between tabs is 17.78 cm (7 in.) for all experiments. This process is presented step-by-step in Appendix A1 of Steffens [1]. The primary tab is 4.45 cm (1.75 in.) x 2.54 cm (1.0 in.), the secondary tab is 2.54 cm (1.0 in.) x 2.54 cm (1.0 in.) and the tertiary tab is 1.91 cm (0.75 in.) x 1.91 cm (0.75 in.). Figure 26 shows the steps of the specimen preparation process.

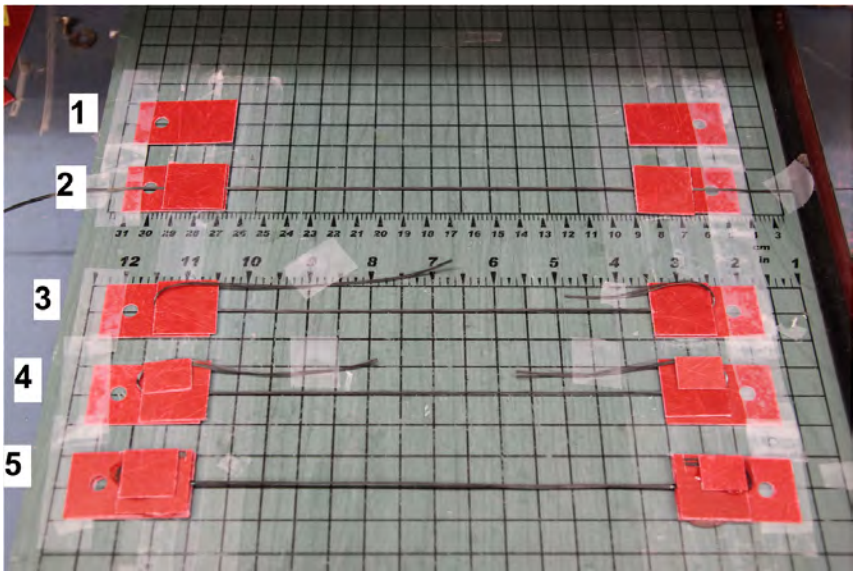


Figure 26. Fiber tow creep test specimen preparation process, reproduced from [23]

Tensile test specimens were fabricated in a similar manner, with a minor difference. Instead of the three-tab method, two of the primary tabs are used with no hole punched. The fiber tow is held in place between the two tabs, and the tabs held together using the same two-part epoxy. The fiber tow is sandwiched between the

two tabs and the epoxy allowed to cure. The primary tabs are then placed between the hydraulic grips of the loadframe and the fiber is held in place for testing.

3.5 Silicic Acid-Saturated Steam Generation

In the previous work by Armani [4], Steffens [1], and Shillig [23], steam was generated by a model HGA-H steam generator (made by MHI) (Figure 27) using deionized water. This steam was then introduced into the test chamber through a feeding tube in a continuous stream with a slightly positive pressure, expelling the dry air and creating a near 100% steam environment inside the susceptor. The susceptor enabled a more uniform heat transfer from the heating elements to the fiber tow, while protecting the interior of the furnace, including the heating elements and thermocouples, from the degrading effects of the steam environment. Due to limitations of the steam generator, steam was introduced at a temperature far below the test temperatures.

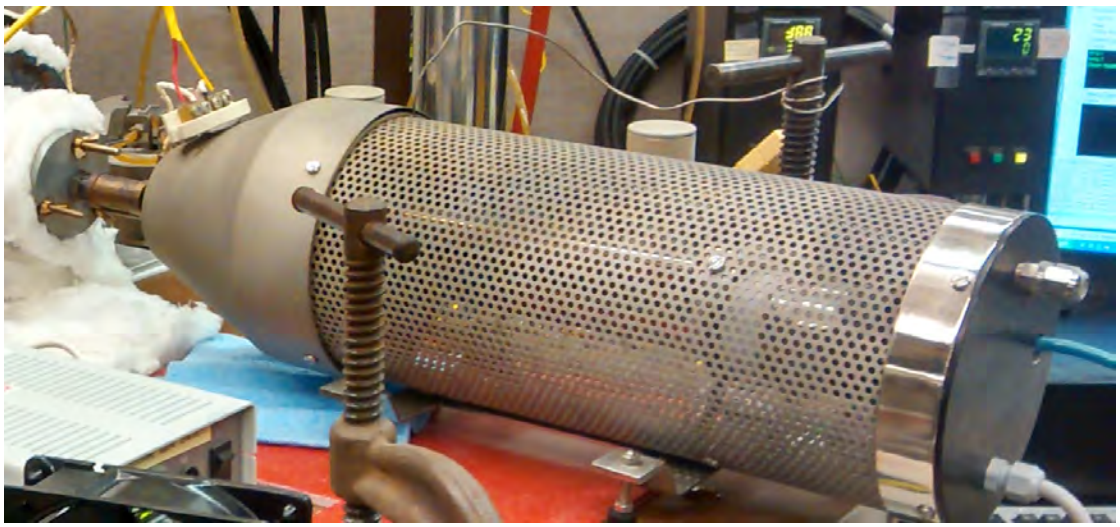


Figure 27. HGA-H (MHI) steam generator.

As mentioned in Chapter 1, Steffens reported that all of the fiber tows tested in steam failed at the same location along the fiber tow specimen, as seen in Figure 28.

This location coincided exactly with the steam entry point into the test chamber, indicating a problem with the steam delivery system. Steffens concluded that the steam impinging on the fiber tow caused the fibers to fail at that location. Such localized failures could be caused by the aerodynamic force of the steam impinging on the fiber tow generating a bending moment, but this is unlikely due to the minimal flow rate used (0.8 ml/min of water into the steam generator). It was thought that the comparatively cold steam significantly lowered the fiber tow temperature in that location, resulting in preferential failure at that point. However, it was later determined that significant active oxidation at the point of impingement was the cause.

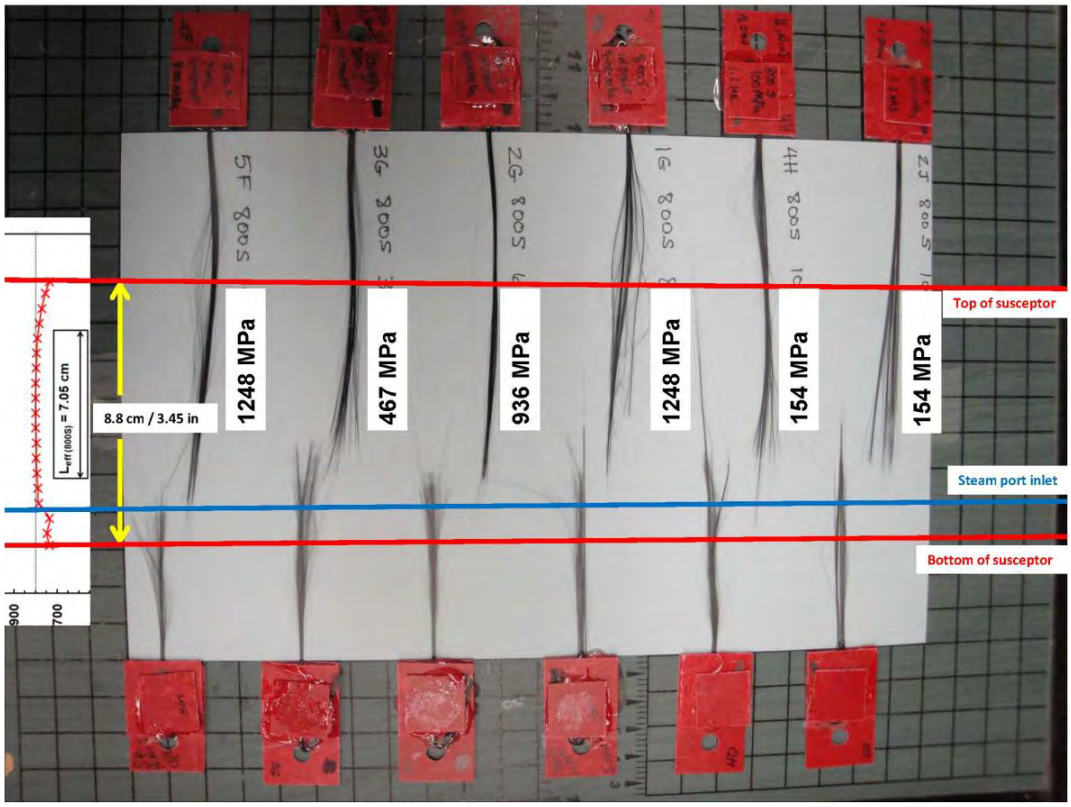


Figure 28. Effect of steam impinging on fiber tows upon entry into the test chamber, reproduced from [1]. Note that all specimens failed at the point of steam impingement.

Shillig modified the steam delivery system to deflect the steam downward as it enters the chamber, so as not to impinge directly on the fiber. While this modification

solved the problem of fiber tow failure at the steam point of entry, there was some question as to whether fiber performance is affected by the cooler steam temperature. The steam entering the test chamber was at ~100°C, effectively bathing the fiber in "cold" steam, possibly creating radial temperature gradients within the fiber. The "cold" steam could also result in a significant difference in the temperature of the individual fibers of the fiber tow. Those on the outside, exposed to the "cold" steam may be at lower temperatures than those towards the center of the fiber tow. Due to thermal expansion differences at the different temperatures, this could result in preferential loading of the outer fibers, leading to a cascading failure effect and premature tow failure.

The current effort made use of the HGA-H steam generator used in previous testing, as well as a newer model of the same steam generator, model HGA-S. The newer model includes an over-temperature thermocouple in the steam generation chamber housing that allows accurate monitoring of the temperature of the steam generator and provides that feedback to the system controller as a fail-safe against overheating. Deionized water was pumped into the steam generator using an Cole Parmer® Easy Load® peristatlic pump, model 7518-10. A Variac rheostat controlled the power input to the steam generator and determined the steam's exit temperature.

3.5.1 Reaching Desired Temperatures.

As discussed in Chapter 1, Shillig discovered that exposure to steam resulted in varying types and degrees of oxidation along the length of the fiber tows. In the test facility, the steam enters at the bottom of the test chamber and is chemically altered as it travels up through the test chamber along the fiber tow, extracting silicon from the fiber tow to become saturated with silicic acid ($Si[OH]_4$) as it reaches the top of the hot zone. This saturation process that occurs inside the test chamber resulted

in a loss of material in the fiber tow toward the bottom of the test chamber, due to active oxidation, and a growth of silica scale toward the top, due to passive oxidation that occurs once the steam has become saturated. A gradual change was observed between the bottom and the top of the fiber tow. These results were also evident in fiber tow specimens from Steffens' work, which may have contributed to fibers all failing at the same location. It is likely that the steam impinging on the fiber tows preferentially depleted silicon from that spot along the fiber tow, leading to accelerated fiber degradation and consistent failure at the point of impingement.

These tests identified an effect of the steam delivery methodology that made it difficult to interpret the results. It was not possible to separate the effect of the methodology from that of the steam environment on the fibers. This methodological effect had to be removed in order to truly evaluate the effects of the steam environment on the SiC fiber tows.

Additionally, it is thought that SiC/SiC CMCs exposed to steam would likely experience a similar phenomenon in which steam would become saturated with silicic acid as the steam moved from the surface deeper into the cracks. With the possible exception of reinforcing fibers very near the surface of the CMC, the steam would likely be saturated when making contact with fibers exposed by the crack. Therefore, it was important to investigate the specific effects of steam saturated with silicic acid on the mechanical behavior SiC fiber tows.

To avoid the chemical alteration of the fiber tow, the steam must be saturated with silicic acid at test temperature prior to entering the test chamber. A test facility had to be designed that permits pre-heating of the steam up to test temperature as well as saturation of the steam with silicic acid before it enters the test chamber. The challenges associated with this task included:

- Heating the steam safely to or above test temperature

- Maintaining the steam temperature during its travel through the pre-heater
- Introducing the steam into the test chamber at or near test temperature
- Regulating the steam flow rate
- Saturating the steam

The first challenge was to preheat the steam such that it would be at or near test temperature (800°C) upon entering the test chamber. Preheating the steam is necessary because saturation is temperature-dependent. If the saturated steam introduced into the test chamber is below the test temperature, it will be heated up to test temperature inside the test chamber. The increase in temperature increases the capacity of the steam to carry silicic acid, resulting in unsaturated steam that will extract silicon from the fiber tow in order to become saturated. This can only be avoided by introducing the steam into the test chamber at or above test temperature. However, if the steam is significantly hotter than the test temperature, it will cool in the test chamber, resulting in precipitation of silica out of the steam. This precipitated silica may deposit on the fiber tow, interfering with the scale growth. Therefore, the temperature of the saturated steam must be carefully maintained.

Steam was generated by a model HGA-S-01 steam generator, made by Micropyretics Heaters International (MHI), using deionized water. A Variac rheostat controls the power input to the HGA-S-01 steam generator and determines its temperature. The steam generator is capable of delivering steam up to approximately 500°C. A model CX1300 heating unit, also produced by MHI, was used to maintain temperature and/or heat the steam further. The CX1300 consisted of an alumina tube passing through a cylindrical insulated heating chamber where an electrically powered molybdenum disilicide resistance heating coil provided the heat. A stainless steel end plate was clamped to the end of the alumina tube and a hole in the center of the plate with

a stainless steel fitting enabled a transition to smaller tubing. The CX1300 can be set at temperatures as high as 1500°C and produce steam up to 1300°C. This steam was then passed to the test chamber via stainless steel tubing attached to the alumina.

Two problems were noted early in this effort. First, the steam very rapidly loses temperature upon exiting the CX1300 such that 1300°C steam was really only observed within the heating chamber. Even this was questionable due to the radiative effect of the heating element on the thermocouple readings. As few as 15.25 cm (6 in) downstream, even 800°C was not consistently achievable. It was clear that significant insulation would be required. Aluminosilicate blanket insulation was wrapped around the tubing, including that portion of the alumina tube protruding from the CX1300 heater. This insulation retarded the heat losses in the tubing enough that 800°C steam was achieved at maximum steam generator power settings.

The second problem involved the steam flow rate. Fiber tow testing requires a very low flow rate so as to provide the steam environment but avoid aerodynamically damaging the specimen. Too high a flow rate can cause the fiber tow to vibrate, resulting in chafing of the individual fibers against each other or even against the edge of the small opening at the to or bottom of the test chamber. Ideally the flow rate should only be high enough to induce a slightly positive pressure, ensuring that the test chamber remains completely filled with steam. Previous work by Steffens [1] and Shillig [23] used liquid water flow rates of only 0.8 ml/min (0.048 in^3/min) and 2.0 ml/min (0.122 in^3/min), respectively. Work by Armani [4], Steffens [1] and Shillig [23] reported flow rates in terms of the liquid water supply into the steam generator, as regulated by the water pump settings. In this work, flow rates are reported in terms of the *steam* flow rate. Steam flow rates are significantly higher due to volume expansion incident to the heating and vaporization of the water. A

1 ml/min (0.061 in^3/min) liquid water supply flow rate produces a steam flow rate of approximately 294 ml/min (18 in^3/min).

Although previous work was done with much lower flow rates, steam flow rates of 4700 ml/min (287 in^3/min) are required to achieve and maintain the temperatures needed for this testing. This is due to the significant losses at high temperatures. A low flow rate allowed the steam to dwell in the tubing between the heater and the furnace containing the test chamber for long enough that the temperature dropped below the required levels. A high flow rate moved the steam through the tubing fast enough to maintain temperature, but damaged the test specimen in the process.

To solve the competing need for high and low flow rates, a bleed off tube and a set of stainless steel needle valves were inserted in the stainless steel tubing, allowing control of the flow rate. One valve was placed within the bleed off tube and the other just after the junction with the bleed-off tube. By closing the valve in the bleed off tube and opening the other, all of the flow could be directed to the test chamber, and vice versa. Adjusting the two valves in combination allowed for better control of the flow rate.

The stainless steel tubing and valve design worked to control the flow rate, but could not maintain the temperatures at the reduced flow rate. Additionally, the needle valves had seals around the knobs that could not withstand the high temperatures, eventually melting and causing leaks. As if that were not bad enough, the stainless steel end cap and tubing, now well insulated, began deteriorating as well. Large amounts of metal filings and flakes were found in the test chamber, contaminating the test specimen and leading to the decision to discontinue use of metal tubing downstream of the CX1300 heater.

It was noted that the constant removal and reapplication of the blanket insulation led to questionable repeatability in the test procedure. This, in addition to the

problem with the metal tubing and valves, led to a complete redesign of the steam delivery system. The goal was to decrease the distance the steam must travel between the heater and test chamber while increasing the insulation in a repeatable way. By doing so, the heat transfer out of the system could be reduced to a level that would enable 800°C steam just prior to entering the test chamber furnace. Also, a method to bleed off some of the steam just prior to entering the test chamber was necessary.

The solution came in five developments. First, all metal tubing was replaced with 99.8% pure alumina tubing. The alumina tube that passes through the CX1300 heater was replaced with one of the same diameter, but 5.08 cm (2 in) shorter. The downstream end reduced down to just over 0.635 cm (0.25 in), negating the need for the stainless steel plate. A smaller alumina transition tube, 1.5 mm (0.590 in) outer diameter, 1 cm (0.394 in) inner diameter and 7.62 cm (3 in) in length, was placed over the reduced end of the larger tube and then the 0.953 cm (0.375 in) outer diameter alumina supply tube was inserted in the other end. The supply tube protrudes from the furnace only about 2.54 cm (1 in), half of which is inserted in the transition tube. In this small space between the transition tube and entry into the furnace, an R-type thermocouple shielded in 0.318 cm (0.125 in) diameter alumina passes through a tight fit hole in the supply tube, enabling monitoring of the steam temperature just before it enters the furnace. This completed the transition from the heater to the test chamber. In all, the length was decreased by approximately 15.25 cm (6 in).

Next, a method to bleed off steam was devised using the ceramic tubing. A 0.953 cm (0.375 in) hole was ground in the side of the transition tube half way along its length. A 0.953 cm (0.375 in) alumina bleed off tube was cut at 45° angle at the end such that the end came to a point. This end was then inserted into the transition tube. The 45° angle allowed easy redirection of the flow down the bleed off tube. Because this tube's outer diameter was nearly identical to the inner diameter of the

transition tube, the downstream flow to the furnace could be almost completely cut off. Only the very small openings left by machining defects and tolerances allowed any flow to continue past the bleed off tube. By rotating the bleed-off tube, the flow can be regulated. A 90 degree rotation would open the flow as wide as possible, leaving very little bleed off flow. This bleed-off assembly is shown in Figure 29.

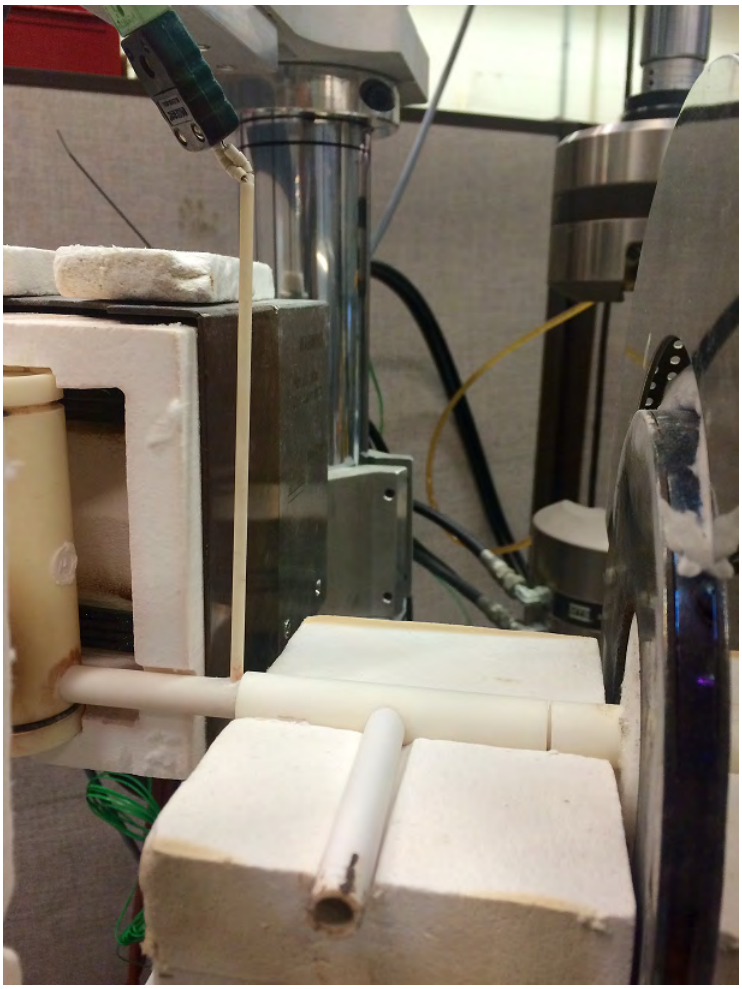


Figure 29. Bleed-off assembly between CX1300 pre-heater and test chamber inside the furnace, with steam inlet thermocouple

Experimentation showed that very little rotation (approximately $\leq 10°$) was needed to achieve the desired temperatures. With this new design, approximately 73% of the steam was removed via the bleed off tube. Flow rates for the bleed off and the test

chamber inlet were ~3388 ml/min (206.8 in^3/min) and ~1282 ml/min (78.3 in^3/min), respectively, as measured using a hand-held anemometer.

To alleviate the repeatability problem and improve the insulation, solid alumina insulation was used to replace the blanket insulation. This third development was accomplished through a layered approach. Four 2.54 cm (1 in) and two 1.27 cm (0.5 in) sheets of alumina insulation were stacked, allowing for easy removal and replacement of the insulation. An approximately 1.525 mm (0.600 in) diameter half-cylinder of material and another 0.953 cm (0.375 in) half-cylinder at ninety degrees from the first were machined out of the two center sheets to accommodate the transition and bleed off tubes. All assembled, the insulation measured 17.78 cm (7 in) high, 15.24 cm (6 in) wide, and about 11.43 cm (4.5 in) along the steam supply direction, leaving only a 0.635 cm (0.25 in) gap to allow for the steam inlet thermocouple. This gap was filled with blanket insulation. Figure 30 shows the solid alumina insulation, bleed off tube, and blanket insulation.

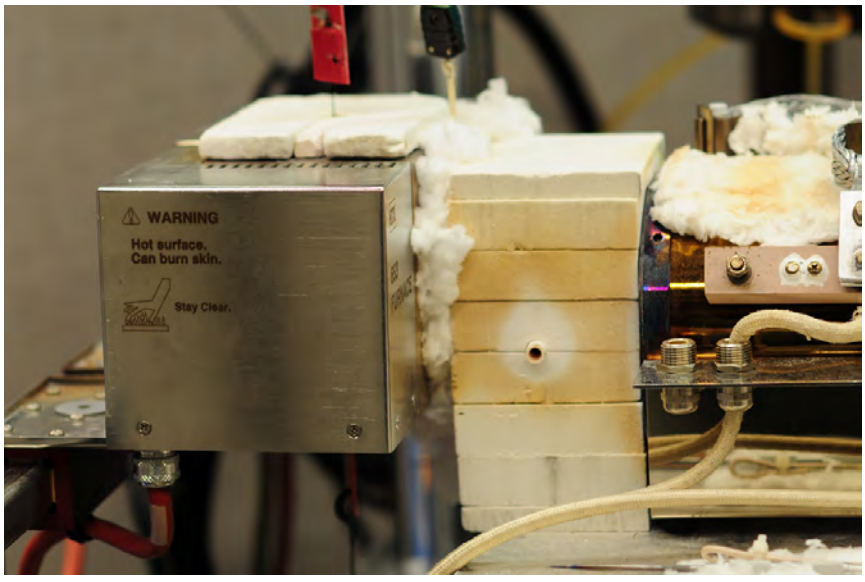


Figure 30. Layered insulation between CX1300 pre-heater and furnace, with steam bleed-off tube

The fourth development was to use two CX1300 heaters in series, rather than just one. By connecting two CX1300 heaters in series, the "heating zone of the steam, the length of tubing over which heat energy is being applied to the steam was doubled, along with length of tubing that is insulated by these heaters. This doubled length translated to twice as much time for the steam to absorb heat energy and increase in temperature. The result was that the target 800°C steam could be reached consistently and at lower settings. For example, with the steam generator set to 100% power, the CX1300 only had to be set to between 950 and 1000°C. Additionally, temperatures higher than 800°C can be achieved. Specifically, 900 and 1000°C saturated steam temperatures were demonstrated. Figure 31 shows the entire test facility.

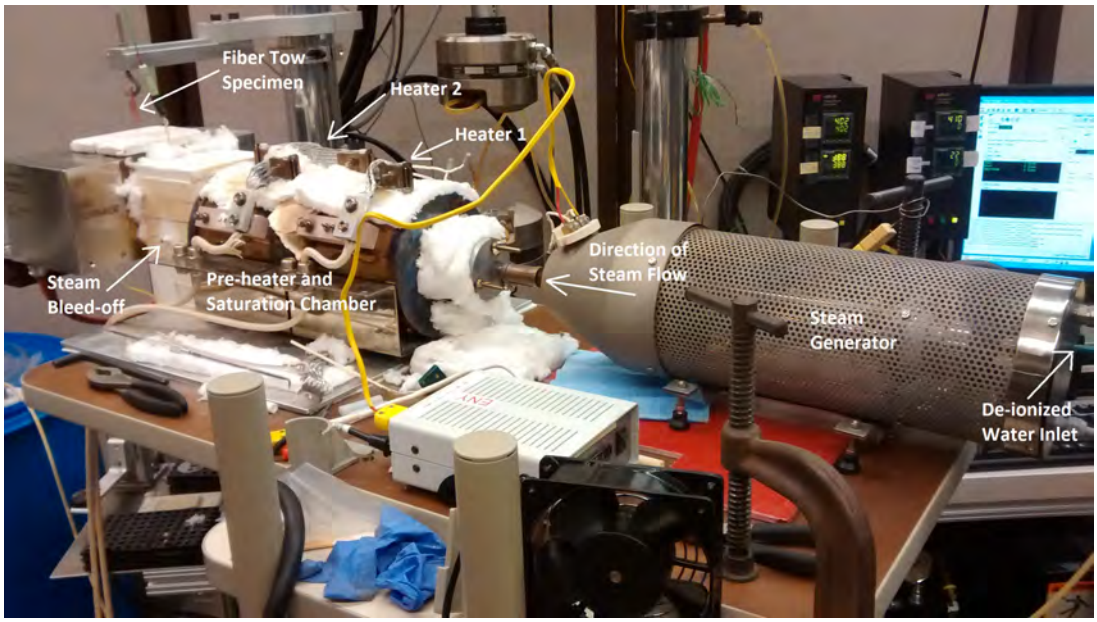


Figure 31. Saturated steam creep test facility

The original heating coils in the CX1300 heaters were slow to respond to setting adjustments and could not consistently put out enough heat to reach temperatures above 1200°C. The coils were also prone to fracture. These coils were replaced with a different design that included an additional complete turn of the coil and a

slightly smaller coil thickness, increasing the area of tubing exposed to heating. These differences enabled the new coils to produce more heat at a given power setting than the original coils. As a result, the CX1300 heaters were able to achieve desired temperatures consistently in approximately 35% of the time it took the original coils. Additionally, the new coils reached higher overall temperatures. The new coils were manufactured by I Squared R Element Company and were encased in RATH KVS 174/400 insulation prior to mounting in the CX1300 shell.

3.5.2 Saturating the Steam.

The other significant challenge was to devise a method to saturate the steam with silicic acid. This had to be done in such a way that the saturation process did not conflict with the ability to reach the desired temperature of the steam. Silica was chosen as the sacrificial supply material to generate the silicic acid. The sacrificial silica must be placed in the path of the steam, but it cannot be placed upstream of the heaters. To do so would saturate the steam at a temperature lower than the desired test temperature. Once heated to test temperature, the steam would no longer be saturated. Adding a chamber downstream of the heater, between the heater and the furnace, would likely increase the thermal losses due to an increase in the distance between the pre-heater and the furnace, jeopardizing the ability to reach the desired temperatures.

The solution to the saturation challenge was to place the silica material inside the large-diameter alumina tube that passes through the CX1300 heaters. This enables the steam to be saturated at its highest temperature. Any loss in temperature as the steam travels through the transition tube into the furnace would be accompanied by a precipitation of some of the silica out of the steam, but the steam would stay saturated. Silica wool was chosen as the silicon source material due to its high surface

area. This high surface area allows a faster reaction with the steam as it passes through, assuring steam saturation. Figure 32 shows the silica wool in the saturation chamber.

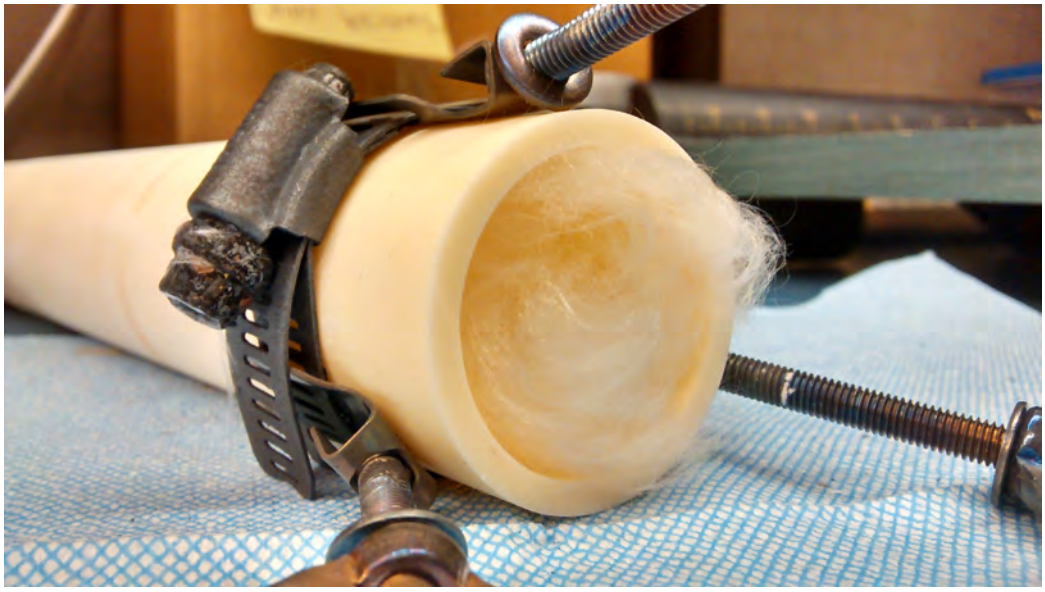


Figure 32. Saturation chamber for silicic acid-saturated steam

3.6 Post-Test Microstructural Analysis

The post-test microstructure of test specimens were examined and damage and failure mechanisms investigated via optical microscopy, and SEM. TEM analysis of the oxide layer thickness of a limited number of specimens was made possible using facilities and expertise provided by the Air Force Research Laboratory (AFRL). Personnel in the Materials and Manufacturing Directorate at AFRL prepared the specimens for TEM analysis and obtained the TEM images used in this work. The analysis of the experimental data and the microstructural investigation provide insight into the creep and the environmental degradation mechanisms occurring in these materials. Figures 33 and 34 show the Zeiss optical microscope and SEM (FEI Quanta 450) located at AFIT, respectively.



Figure 33. AFIT Zeiss optical microscope, reproduced from [4]

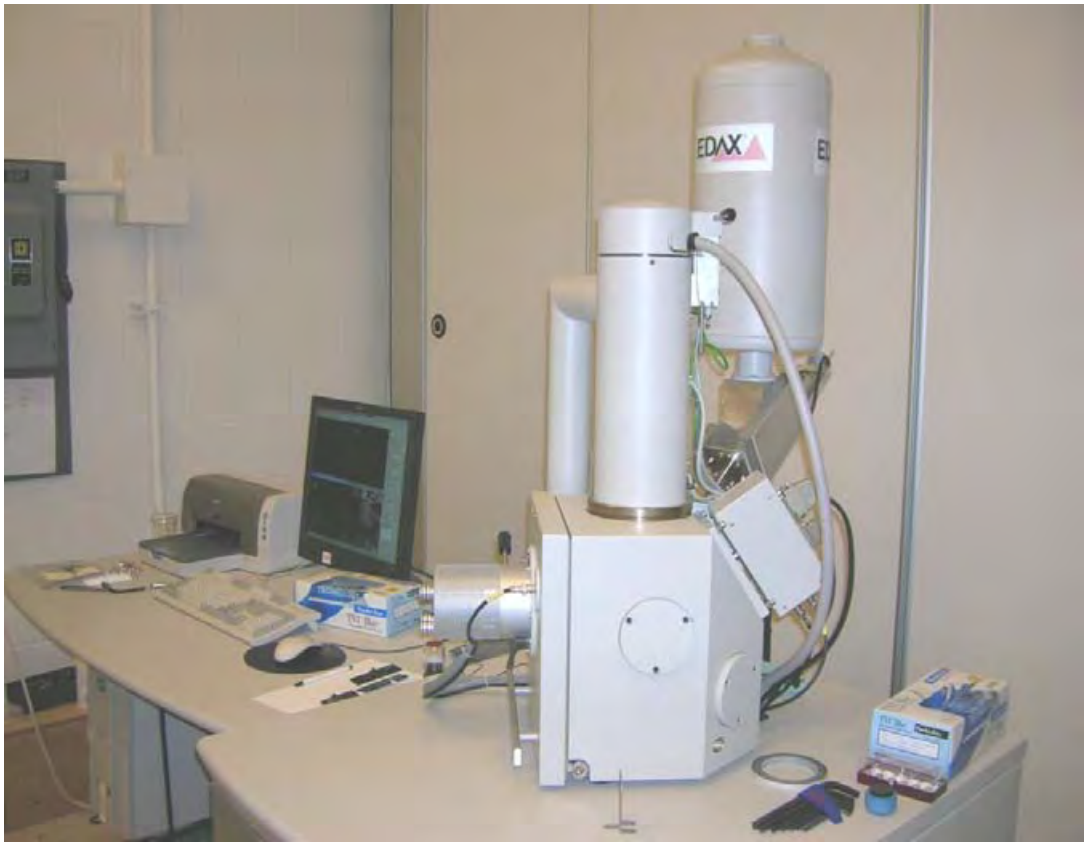


Figure 34. AFIT scanning electron microscope, reproduced from [4]

IV. Mechanical Behavior of Hi-Nicalon^{TM} S Fiber Tows

This chapter reports and discusses the mechanical behavior of Hi-Nicalon^{TM} S SiC fiber tows, specifically addressing (1) the room temperature tensile strength, (2) the influence of loading rate on tensile strength at 800°C in air and in steam and (3) the effects of steam on creep performance 800°C. Experimental results are presented and analyzed. A linear elastic crack growth model is used to predict creep lifetimes from the constant stress rate test data. Finally, the Monkman-Grant relationship is applied to creep data.

4.1 Tensile Behavior

For both oxide- and non-oxide-based CMCs and fiber tows, it has been shown that the monotonic tensile behavior and tensile properties are influenced by loading rate [4, 120, 121, 125, 175–180]. This is of concern in structural applications where loading rates vary widely, such as the aerospace applications for which oxide and non-oxide CMCs are being developed. As such, it was prudent to investigate the potential for similar influences on the non-oxide fiber tows of this study.

Tensile tests were conducted in dry air and in silicic acid-saturated steam at 800°C with applied tensile stress rates of 0.1, 0.5, 1.0, 5.0, 10.0, and 100.0 MPa/s. Results are presented in Table 9. Figures 35 and 36 show log-log plots of the tensile strength (fracture stress) as a function of loading rate (stress rate) in air and in silicic acid-saturated steam, respectively. The solid line in each figure is a regression fit to the data. Note that in both cases, the line is almost horizontal, indicating that there is very little rate dependency in the tensile strength of the Hi-Nicalon^{TM} S SiC fiber tows in either air or silicic acid-saturated steam. The average tensile strength was 1144 MPa for air, and 934 MPa for silicic acid-saturated steam. It is noteworthy that

for the oxide fibers tested by Armani, there was a range of loading rates in which the fiber tows exhibited rate dependency and above which they were independent of loading rate [4]. Although it is possible that this may be the case with Hi-Nicalon^{TM} S SiC fiber tows, it is not apparent even down to a loading rate of 0.1 MPa/s. Lower than this, the tensile test duration is long enough that the tests enter into the creep regime, rendering the results questionable. As such, it is not likely that any range of significant rate dependency can be determined. These results suggest that the rate of crack growth in Hi-Nicalon^{TM} S SiC fiber tows becomes saturated at low applied stress rates. It is known that SiC fibers and fiber tows are much less compliant, with higher elastic moduli, than oxide fibers. The lack of significant stress rate dependency noted here makes sense in light of this reduced compliance.

Table 9. Tensile Strength of Hi-Nicalon^{TM} S SiC fiber tow specimens tested under various constant stress rates at 800°C in dry air and silicic acid-saturated steam.

800°C						
Loading Rate MPa/s	**0.1**	**0.5**	**1**	**5**	**10**	**100**
Air	–	1203	972	–	1289	1137
	–	–	1017	–	1247	–
Average (MPa)	–	1203	994.5	–	1268	1137
Standard Deviation	–	–	31.8	–	29.7	–
Steam	787	1018	805	1040	1130	775
	–	–	–	–	1034	879
Average (MPa)	787	1018	805	1040	1082	827
Standard Deviation	–	–	–	–	67.9	73.5

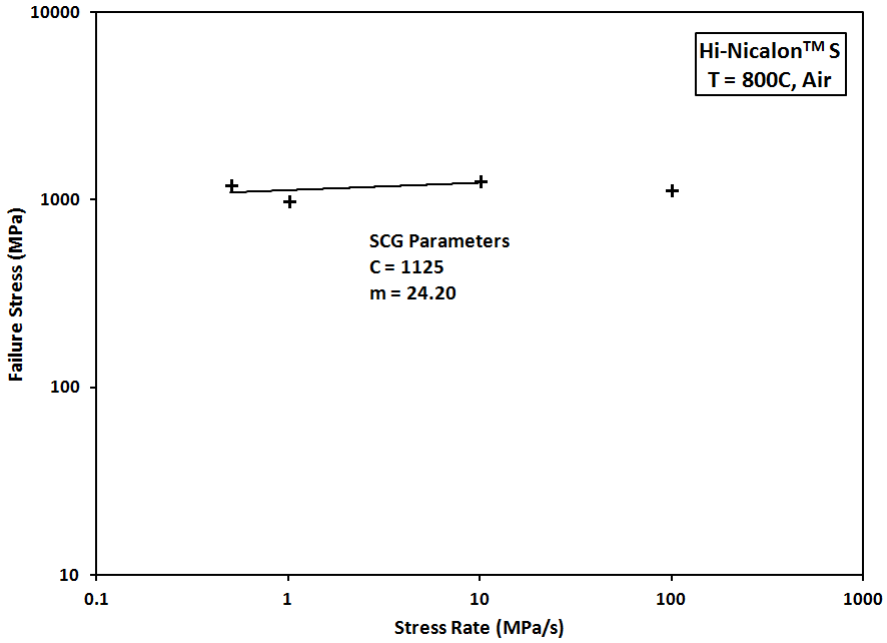


Figure 35. Failure Stress of Hi-Nicalon^{TM} S fibers at 800°C in air as a function of stress rate. The effect of loading rate is minimal.

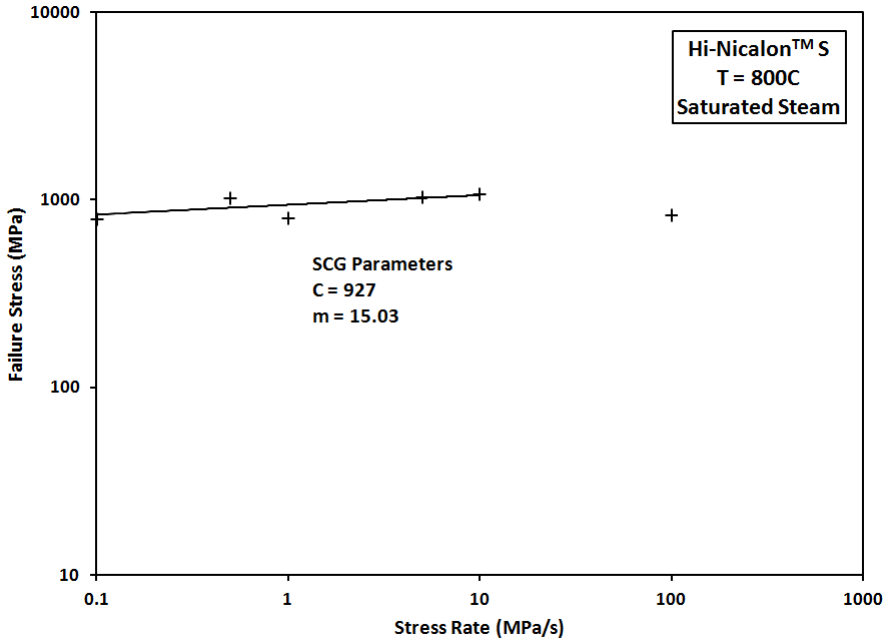


Figure 36. Failure Stress of Hi-Nicalon^{TM} S fibers at 800°C in silicic acid-saturated steam as a function of stress rate. The effect of loading rate is minimal.

Choi et al [176, 177] reported a rate dependence in air, however, there were several significant differences. First, only CMCs were tested, not fiber tows. Second the CMCs were reinforced with Nicalon^{TM} and Hi-Nicalon^{TM}, not Hi-Nicalon^{TM} S fiber tows. Third, the CMCs were not purely SiC, but also aluminosilicate-based CMCs. Lastly, the tests were conducted at 1100 - 1200°C, in contrast to the 800°C of the this work. Environmentally assisted (subcritical) crack growth (EACG) is founded upon a bedrock of adsorption. The four differences listed above all affect the chemical environment and it's potential for reactions to occur. In isolation, fiber tows will behave differently than they do when incorporated into CMCs. Hi-Nicalon^{TM} S fiber tows are nearly stoichiometric, whereas Nicalon^{TM} and Hi-Nicalon^{TM} contain more substantial amounts of oxygen and free carbon, making them more susceptible to the adsorption of EACG. The presence of other elements (calcium, magnesium, barium, and aluminum in the case of Choi et al) creates a completely different kind of chemical environment and, therefore, chemical reactions. In the case of Choi et al, these other elements are also known to significantly increase oxidation of SiC by acting as nucleation sites for oxide growth, particularly crystallized growth. Additionally, the higher temperature of experiments conducted by Choi et al translates to higher rates of reaction due to more available energy to activate. For these reasons, it is not surprising that the results of this study differ from those of Choi et al. It is possible that a greater rate dependency would be apparent for Hi-Nicalon^{TM} S fiber tows at higher temperatures or when incorporated into CMCs of various matrix materials. Further work in this area should be accomplished.

Through additional analysis, the subcritical crack growth parameters can be determined from failure stress and stress rate data and creep lifetimes can be predicted based on the monotonic tensile tests. The subcritical crack growth parameters are de-

termined in the next section and predictions of creep lifetime are presented in Section 4.3.

4.1.1 Subcritical Crack Growth Parameters.

The dependence of tensile strength on stress rate observed by Ruggles-Wrenn et al. [178–180] for CMCs and the failure of fibers at lower stresses and temperatures than expected (delayed failure) noted by Forio, Gautier, and Lamon [120, 121, 125] for Hi-Nicalon^{TM} S fiber tows are related and akin to that observed for the monolithic ceramics at elevated temperatures [181–183]. For monolithic ceramics, these phenomena have been shown to proceed by environmentally assisted subcritical crack growth (or slow crack growth) [184]. A model has been developed by which delayed failure can be predicted. Parameters that account for the material and environment in the model can be determined from experimental data. Armani [4] successfully demonstrated a method for determining the subcritical crack growth parameters. This method was used in the current work and is explained here:

The subcritical crack growth rate can be expressed by the empirical power-law relation [48, 181]:

$$v = \frac{da}{dt} = M \left[\frac{K_I}{K_{IC}} \right]^m \tag{14}$$

where v is crack velocity, a is crack size, t is time, K_I is the mode I stress intensity factor, K_{IC} is the critical stress intensity factor (i.e. fracture toughness) under mode I loading, and M and m are the slow crack growth parameters associated with the material and environment.

By definition, the relationship between the mode I stress intensity factor and the applied stress is:

$$K_I = Y\sigma\sqrt{a} \tag{15}$$

where Y is a geometry factor based on flaw size, shape, and orientation to the applied stess, and σ is the applied stress.

Equations 14 and 15 can be combined to determine a relationship between the degraded fracture strength under slow crack growth, σ_f, and the inert strength, σ_i, as seen in Equation 16

$$\sigma_f^{m-2} = \sigma_i^{m-2} - \frac{1}{B}\int_0^t [\sigma(t)]^m \, dt \tag{16}$$

where B is a parameter accounting for the material/environment and is defined as:

$$B = \frac{2K_{IC}^2}{AY^2(m-2)} \tag{17}$$

In the case of constant rate testing, the applied stress can be written as:

$$\sigma(t) = \dot{\sigma}t \tag{18}$$

Substituting Equation 18 into Equation 16 gives a fracture strength of:

$$\sigma_f = \left[B(m+1)\sigma_i^{m-2}\right]^{\frac{1}{(m+1)}} \dot{\sigma}^{\frac{1}{(m+1)}} \tag{19}$$

which reduces to:

$$\sigma_f = C\dot{\sigma}^{\frac{1}{(m+1)}} \tag{20}$$

where C is a slow crack growth parameter:

$$C = \left[\frac{2(m+1)K_{IC}^2\sigma_i^{m-2}}{AY^2(m-2)}\right]^{\frac{1}{(m+1)}} \tag{21}$$

The subcritical (slow) crack growth parameters, m and C, can be determined through linear regression analysis by taking the logarithm of both sides of Equation 20 and

plotting the result:

$$log\sigma_f = \frac{1}{m+1} log\dot{\sigma} + logC \tag{22}$$

For the Hi-Nicalon^{TM} S fiber tows studied in this work, the subcritical crack growth parameters are listed for air and steam in Table 10.

Table 10. Subcritical crack growth paramters for Hi-Nicalon^{TM} S SiC fiber tow specimens tested at 800°C in dry air and in silicic acid-saturated steam.

800°C		
Parameter	**Air**	**Steam**
m	24.20	18.43
C	1125	940

4.2 Creep Behavior

Before conducting extensive creep tests, the functionality of the newly designed creep test facility had to be verified. A temperature profile was measured in the test chamber, and a static creep test was performed. A Hi-Nicalon^{TM} S SiC fiber tow specimen, fabricated from the same spool used by Steffens [1] and Shillig [23], consisting of approximately 500 fibers with an average cross-sectional diameter of 13 microns, was subjected to the saturated steam environment at 800°C and to a load of 2.96 MPa (429.3 psi). The load was provided by a 20 g (0.044 lbm) weight hung from the bottom of the specimen and was applied only to keep the specimen taught during the test. Creep run-out was defined as 100 hrs in the test conditions without failure of the specimen and was achieved. As expected, the measured creep rate was extremely small: 1.59 x 10^{-10} s^{-1}. A second creep test was conducted at 800°C with a load of 154 MPa (22.3 ksi) and also went to run-out, exhibiting a similarly negligible creep rate of 3.63 x 10^{-10} s^{-1}. Lifetimes were consistent with literature [121]. It should be acknowledged that these results may be due to progressive failure

of individual fibers within the fiber tow, causing the remaining fibers to be subject to a higher load resulting in additional elastic strain.

Maintaining a steady steam input temperature is challenging. There are many factors to control, and superheated steam is quite reactive. Though the test chamber was maintained at 800°C at all times throughout the testing, the steam inlet temperature fluctuated as much as ± 25°C on a regular basis. A method was developed to address the thermal expansion/contraction associated with these steam inlet temperature fluctuations. Three steam tests conducted early in the development of the experimental methodology experienced a total of six instances of near-instantaneous spikes or drops in the steam inlet temperature, usually due to adjustment of the bleed-off tube. These near-instantaneous changes in temperature happened over such a short time period that an associated change in length of the fiber tow could not be due to creep, therefore any associated change in length must only be due to thermal effects. At these points of near-instantaneous changes in temperature, the total change in steam inlet temperature and the total change in strain was recorded. Using these data and applying principles of linear thermal strain, a pseudo-Coefficient of Thermal Expansion (CTE) was calculated. The thermal strain equation is:

$$\Delta\epsilon = \alpha\Delta t \tag{23}$$

where α is the CTE. For each spike or near-instantaneous drop in steam inlet temperature, the change in temperature (Δt) and associated change in strain ($\Delta\epsilon$) were applied and a pseudo-CTE calculated. All instances produced a pseudo-CTE in the range of $3.13 - 3.52\ x\ 10^{-6}$ mm/mm-K, with an average value of $3.32\ x\ 10^{-6}$ mm/mm-K. Although this is not a true CTE for SiC fiber tows, it is in good agreement with literature. The CTE of SiC fiber tows has not been widely studied or documented, however, data from testing conducted by Rashad on bulk SiC at 800°C gives a CTE

value of 4.18 μm/m-K [185], which is equivalent to 4.18 x 10^{-6} mm/mm-K . Using this pseudo-CTE, the thermal effects on the measured creep strain due to changes in the steam inlet temperature was estimated at each data point and accounted for in the calculation of the creep strain. In certain limited instances, this average pseudo-CTE did not adequately account for the thermal effects of a particular large spike or drop. Upon further investigation, it was found that the pseudo-CTE specific to that point was different enough from the average to warrant the use of the specific pseudo-CTE in place of the average. In each case where this was done, the specific pseudo-CTE was adequate. Table 11 summarizes the results of creep testing at 800°C.

Table 11. Creep results for Hi-Nicalon^{TM} S SiC fiber tow specimens tested at 800°C in dry air and silicic acid-saturated steam.

800°C					
Specimen ID	**Test Env.**	**Creep Stress (MPa)**	**Creep Lifetime (h)**	**Steady-State Creep Rate (s^{-1})**	**Creep Strain (%)**
A11	Air	1250†	-	-	-
A16	Air	1023	16.89	1.77E-09	0.135
A17	Air	980	17.40	1.83E-09	0.178
A12	Air	937	84.29	1.47E-09	0.323
A21	Air	960	100‡	1.08E-09	0.218
A18	Air	937	100	2.17E-09	0.221
A15	Air	798	100	5.32E-10	0.153
SS3	SS	798†	-	-	-
SS25	SS*	798	12.94	5.87E-09	0.128
SS24	SS	748	40.13	3.48E-09	0.203
SS18	SS	700	90.17	1.87E-09	0.205
SS13	SS	538	76.83	6.83E-10	0.136
SS17	SS	625	100	1.13E-09	0.181
SS16	SS	557	100	1.12E-09	0.162
SS12	SS	450	100	4.19E-10	0.112
SS11	SS	425	100	5.20E-10	0.167
SS9	SS	400	100	5.10E-10	0.159
SS1	SS	2.96	100	7.45E-11	0.013

*Silicic acid-saturated steam
†Broke on loading
‡Creep run-out defined as 100h at creep stress. Failure did not occur before test termination.

Recall that Steffens reported values of the stress exponent, n, for Hi-Nicalon^{TM} S fiber tows at 800°C in air and in steam. For comparison, the stress exponents reported in this effort were also determined by fitting the data to the temperature-independent

Norton-Bailey form of the power law creep equation shown in Equation 3. The values of stress exponents for the current effort were $n \approx 5.0$ and $n \approx 4.1$ for air and steam, respectively, which is consistent with climb-controlled dislocation creep in air and grain boundary sliding, with cavity nucleation and growth. The results match well with those of Steffens [23], who reported similar values for the stress exponent. It is significant to note, however, that though the creep exponent for steam was comparable, the fiber tows were capable of maintaining stresses as much as five times higher than those in unsaturated steam. Creep run-out was obtained at stress 625 MPa in saturated steam, whereas Steffens reported creep run-out at 139 MPa in unsaturated steam and Shillig's longest test in unsaturated steam was at 154 MPa and lasted 72 h. Creep rates were an order of magnitude lower than those reported by Steffens and Shillig for the same applied stress. Figure 37 shows the creep strain rate data.

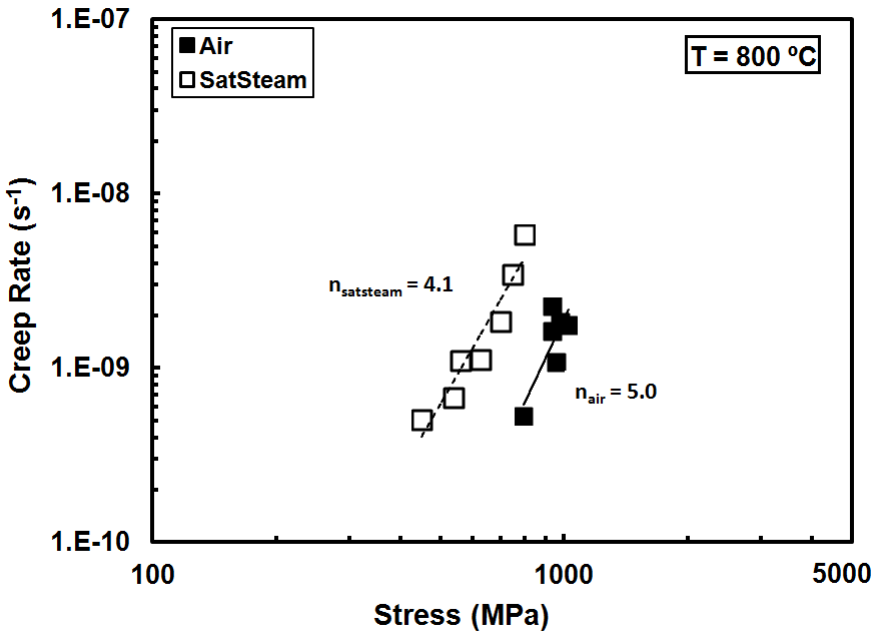


Figure 37. Creep strain rate vs. applied stress for Hi-Nicalon^{TM} S fibers tows at 800°C in air and in steam, with associated creep exponents

The difference in creep rates and fiber tow strength in the current work as compared to Steffens' and Shillig's results is readily explained by the saturating of the steam. As will be discussed in Chapter 5, the saturating of the steam was successful in eliminating the variations along the length of the fiber tows. In fact, there were no signs of active oxidation in any of the specimens, only passive oxidation. It would seem evident that the effect of silicic-acid saturation is to significantly inhibit the deleterious effects of steam. Hence, the slightly lower creep rates and higher strength. It is also possible that the higher creep rates reported by Steffens and Shillig were due, in part, to progressive failure of the fibers within the fiber tow as a result of any or all of the following: direct impingement of the steam on the fiber tow, "cold" steam, and lack of pre-saturation.

The creep rates and creep strain reported here are quite small. It is acknowledged that many of these rates and strains are within the accuracy tolerances of the LVDT used to measure strain. These may very well be within the "noise" of the system. The accuracy of these numbers is, therefore, questionable, but it is clear that there is very little creep taking place. In addition to the accuracy concerns, other factors may account for the apparent creep. Oxidation causes a change in the elastic modulus of the fibers, causing them to become more compliant. This is due, in part, to the reduction in the cross-section of the fibers due to the oxidation. This increase in compliance over time is usually small compared to creep, but could be the cause of the apparent creep here, since the reported creep strains are small. Since oxidation is faster in steam, this could also explain the apparent increase in the rates (though still very small) for tests in steam.

Figure 38 shows the creep lifetimes for tests conducted in air and steam. As expected, the performance of Hi-Nicalon^{TM} S fiber tows is better in air than in steam, with the fiber tows capable of sustaining stresses as much as 250 MPa higher than

in saturated steam for considerable time. Of note is that in both air and saturated steam, the transition from fast fracture to run-out is fairly sharp, though less so for saturated steam. Figures 39 - 42 show selected creep curves for air and silicic acid-saturated steam, respectively, that are representative of the tested specimens.

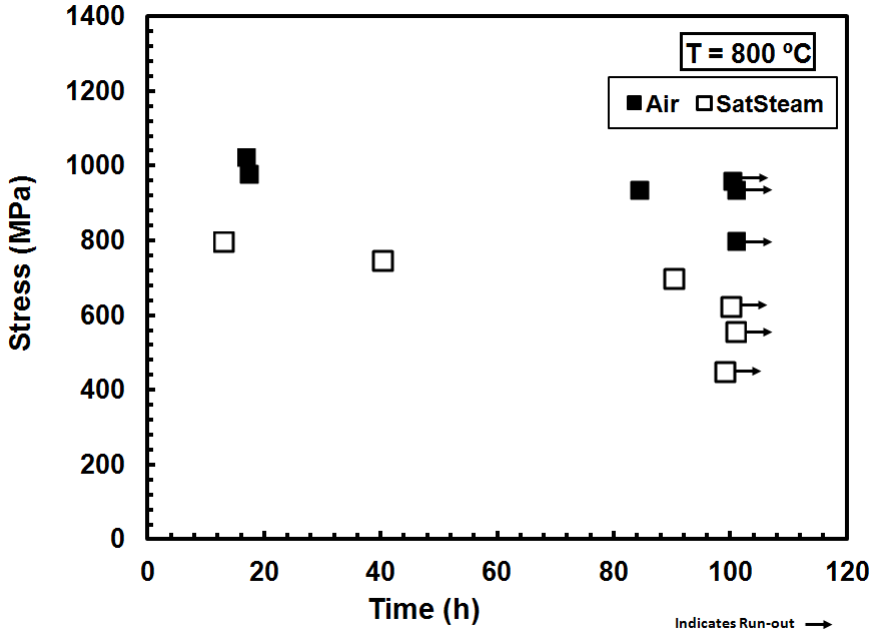


Figure 38. Creep Lifetimes of Hi-Nicalon^{TM} S fibers at 800°C in air and in steam

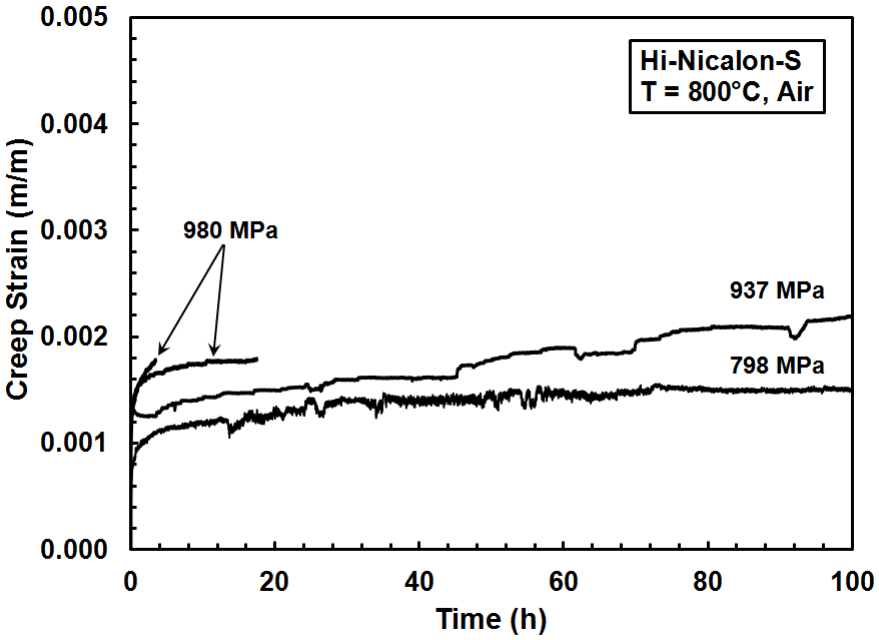


Figure 39. Representative creep curves for Hi-Nicalon^{TM} S fibers at 800°C in air

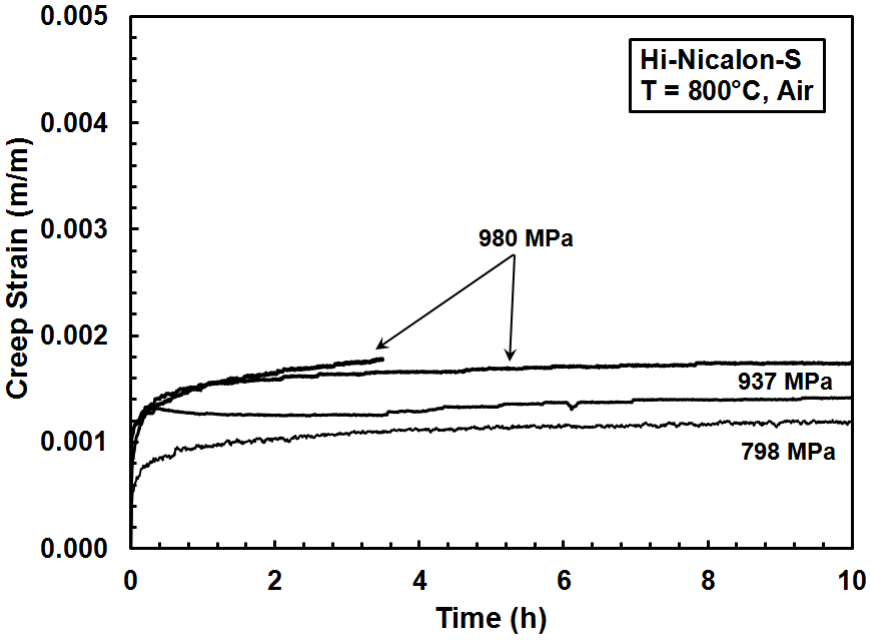


Figure 40. Representative creep curves for early stages of creep of Hi-Nicalon^{TM} S fibers at 800°C in air

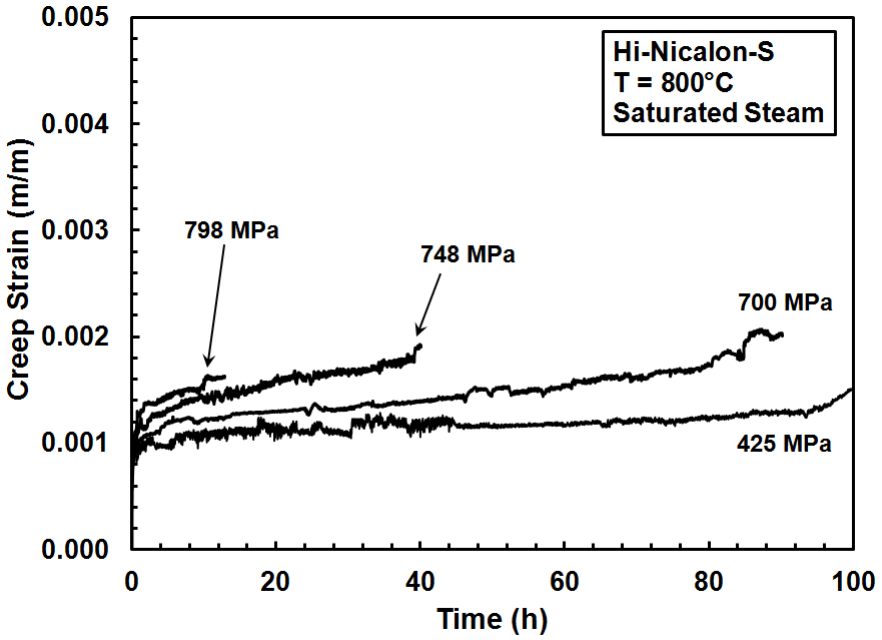


Figure 41. Representative creep curves for Hi-Nicalon^{TM} S fibers at 800°C tested in silicic acid-saturated steam

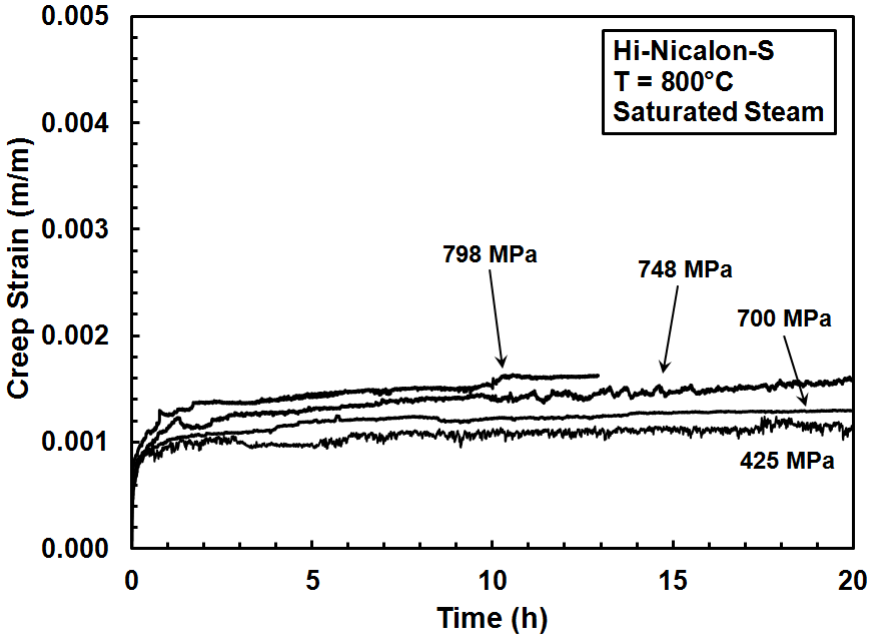


Figure 42. Representative creep curves for early stages of creep of Hi-Nicalon^{TM} S fibers at 800°C tested in silicic acid-saturated steam

4.3 Predicting Creep Lifetime

Many glasses and ceramics exhibit subcritical crack growth, also known as slow crack growth or environmentally assisted crack growth. Linear Elastic Fracture Mechanics (LEFM) assumes that cracks are pre-existing in brittle materials and that these cracks grow due to the constant stress. Once the cracks grow to a critical size, spontaneous crack growth occurs, causing sudden brittle failure. When subcritical crack growth is the dominant time-dependent failure mechanism, a model can be developed to predict creep lifetime (time-to-failure) under constant stress. This model is based on the LEFM work of Griffith and uses the subcritical crack growth parameters determined as described in section 4.1.1. This model was successfully used by Armani [4] to predict subcritical crack growth in oxide fibers, and the model development is reproduced here.

The time to failure under a constant tensile stress can be derived from the stress intensity factor given in Equation 15. By taking the derivative of Equation 15 with respect to time and substituting the subcritical crack velocity from Equation 14, the following expression is obtained:

$$\frac{dK_I}{dt} = v\left(\frac{\sigma^2 Y^2}{2K_I}\right) \tag{24}$$

Solving for dt and integrating yields the time to failure, t_f:

$$t_f = \frac{2}{\sigma^2 Y^2}\int_{K_{Ii}}^{K_{IC}} \left(\frac{K_I}{v}\right) dK_I \tag{25}$$

where the initial stress intensity factor, K_{Ii}, is:

$$K_{Ii} = \frac{\sigma}{\sigma_i} K_{IC} \tag{26}$$

Now substitute Equation 14 into Equation 25 and integrate to get the time to failure as:

$$t_f = \frac{2K_{IC}^m}{\sigma^2 Y^2 M(m-2)} \left(K_{Ii}^{2-m} - K_{IC}^{2-m}\right) \tag{27}$$

For ceramic materials, literature reports values for m that are > 2, therefore $K_{IC}^{2-m} \ll K_{Ii}^{2-m}$. With this in mind, and using Equation 26, t_f, becomes:

$$t_f = \left[\frac{2K_{IC}^m \sigma_i^{m-2}}{MY^2(m-2)}\right] \sigma^{-m} \tag{28}$$

which, using Equation 21, reduces to:

$$t_f = \left[\frac{C^{m+1}}{m+1}\right] \sigma^{-m} \tag{29}$$

This is the time to failure under a constant tensile stress and represents the time for a subcritical crack to grow to a critical size that causes sudden brittle failure. This form of the time to failure is in terms of the subcritical crack growth parameters m and C determined in section 4.1.1 using the data from constant stress rate tensile tests.

Using the subcritical crack growth parameters determined in section 4.1.1, the creep lifetime of Hi-Nicalon^{TM} S fiber tows in air and steam was predicted and compared to the experimental creep lifetimes reported in section 4.2. Table 12 lists the predicted lifetimes for stresses from 450 - 1250 MPa (65.3 - 181.3 ksi), and these values are plotted with the actual creep lifetime data in Figure 43.

Table 12. Predicted Creep Lifetimes for Hi-Nicalon^{TM} S SiC fiber tow specimens tested at 800°C in dry air and in silicic acid-saturated steam.

800°C		
Stress	Lifetime (h)	
(MPa)	Air	SatSteam
450	-	10598
538	-	394
575	-	116
625	-	24.9
700	1197	3.1
798	50.2	0.28
937	1.03	0.014
960	0.57	-
980	0.35	-
1023	0.12	-
1250	0.001	-

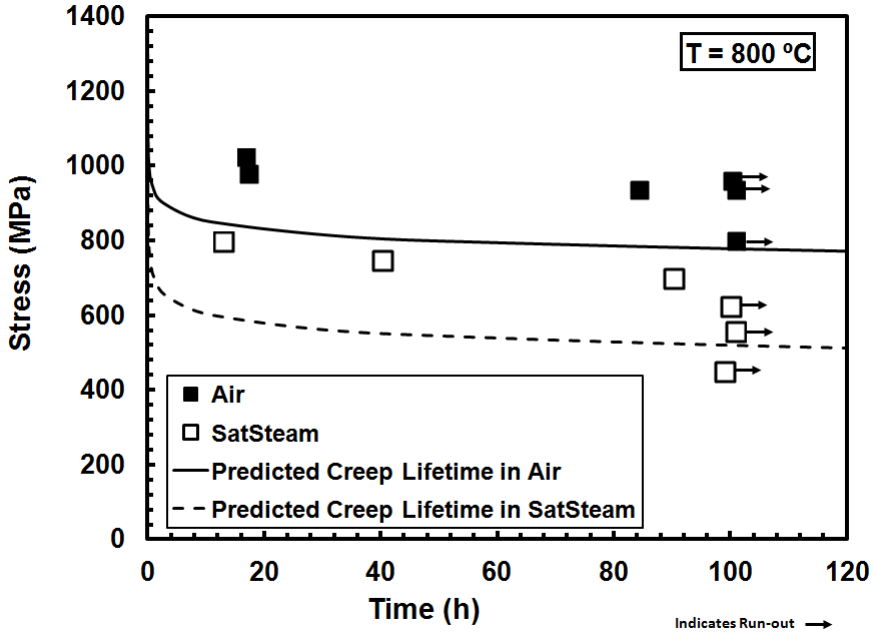


Figure 43. Model predictions of creep lifetime compared to actual creep lifetime data for Hi-Nicalon^{TM} S SiC fiber tow specimens tested at 800°C in dry air and in silicic acid-saturated steam.

The predictions for both air and silicic acid-saturated steam under-predict the experimental data. The shape of the curve matches fairly well in both cases, capturing

the rapid transition from fast fracture to run-out, however the predicted stresses are 80 - 85% of the experimental values for both air and silicic acid-saturated steam. This under-prediction indicates that EACG is not the dominating failure mechanism in creep of Hi-Nicalon^{TM} S SiC fiber tows. This is consistent with the minimal dependence on stress rate reported earlier, and is also consistent with Gauthier and Lamon's observation that Hi-Nicalon^{TM} S fibers are more resistant to EACG than other SiC fibers [121]. Additionally, this is consistent with expectations that exposure to the silicic acid-saturated steam would create a layer of protective amorphous oxide, effectively sealing off the surface from the effects of EACG.

It is important to note that these results, observed at 800°C, are at a single temperature. This temperature is at the low end of the temperature regime where Hi-Nicalon^{TM} S SiC fiber tows exhibit significant creep, therefore creep is minimal at this temperature. Also, this temperature is at the high end of the temperature regime in which EACG is typically a concern. Further testing at higher and lower temperatures would provide a more complete picture of the effects of EACG and would elucidate any loading rate dependency that may exist.

4.4 Creep Rupture and the Monkman-Grant Relationship

In 1956, Monkman and Grant [186] published their seminal work detailing an empirical relationship between the steady-state creep rate and the creep-rupture lifetime (time to failure) of metals. In more recent times, this same relationship has been shown to apply to creep of ceramic materials as well [4, 46, 187–190]. The Monkman-Grant relationship, shown in Equation 30, is a useful tool in the study and design of fiber-reinforced CMCs because it eliminates the need for long-term creep tests to failure. Once the parameters of the relationship are determined for a given material, all that is needed to predict creep-rupture lifetimes is the steady-state creep rate.

Generally, ceramics and CMCs reach secondary creep, where the steady-state creep rate is apparent, in a fairly short period of time (a few hours or less). Rather than conducting creep tests all the way to failure, short creep tests can be conducted to obtain the steady-state creep rate and then creep-rupture lifetime can be predicted. This is significant, since creep-rupture can occur at very long times. The Monkman-Grant relationship is:

$$t_f \dot{\varepsilon}^q = G \tag{30}$$

where t_f is the time to failure, $\dot{\varepsilon}$ is the strain rate, and q and G are Monkman-Grant parameters and are constants.

Ferber and Jenkins [190] investigated the creep performance of hot isostatcially pressed silicon nitride at temperatures from 1150 to 1370°C. They found that, for the temperature range of 1150 to 1370°C, the secondary creep strain rate controlled creep-fatigue life according to the Monkman-Grant relationship. Menon et al [189] examined the applicability of the Monkman-Grant relationship to NT154 silicon nitride and found that it was applicable with evidence of a temperature dependence. DiCarlo et al successfully predicted the creep lifetime of various oxide and non-oxide composites using the Monkman-Grant relationship based on data from single filament creep test results [46, 187, 188]. In 2004, they did so for SiC/SiC minicomposites [46] reinforced with various types of first and second generation SiC fibers, including Hi-Nicalon^{TM}. Data was used from creep tests of these CMCs at 1200 - 1400°C in air. Monkman-Grant plots, log-log plots of creep rupture time vs creep rate, showed the characteristic parallel lines at different temperatures and closely matched empirical creep rupture data of SiC/SiC composites from Zhu et al [191, 192] and others. Armani [4] applied the Monkman-Grant relationship to creep data collected for Nextel^{TM}610 and 720 aluminosilicate fiber tows in air and in steam at temperatures of 1100°C and 1200°C, respectively. The Monkman-Grant plot based on this data

was in good agreement with oxide-oxide CMC creep data gathered from literature, showing that the Monkman-Grant relationship can be used to successfully predict creep lifetime of CMCs reinforced with Nextel^{TM}610 and 720 fiber tows.

Due to the benefits of using the Monkman-Grant relationship, it is worthwhile to investigate whether it applies to Hi-Nicalon^{TM} S fiber tows and can be used to predict their creep lifetime. In this section, the Monkman-Grant relationship is evaluated for Hi-Nicalon^{TM} S fiber tows in air, steam, and silicic acid-saturated steam environments at temperatures in the range of 800 - 1100°C using data from Steffens [1], Shillig [23], and the current work. Figure 44 shows creep lifetime data as a function of steady-state strain rate on a log-log plot. Note that the data obtained for air and silicic acid-saturated steam at 800°C fall along a common line. This indicates that the Monkman-Grant relationship given in Equation 30 applies to Hi-Nicalon^{TM} S fiber tows and is consistent with results found in literature for ceramics [4, 94, 193, 194]. DiCarlo et al noted that for ceramic materials, the Monkman-Grant log-log plots "typically fall on one straight-line master curve" [94] and this is the case for Hi-Nicalon^{TM} S fiber tows. Furthermore, the fact that the data for both air and silicic acid-saturated steam fall on the same line indicates that the Monkman-Grant parameters, q and G are independent of environment. The solid line in Figure 44 represents the fit of the experimental data to Equation 30. The fit was good, with a regression coefficient of 0.945. The Monkman-Grant parameters determined by this regression analysis are $q = 1.20$ and $G = 5.77x10^{-5}$.

The evidence that the Monkman-Grant relationship for Hi-Nicalon^{TM} S fiber tows is independent of environment is further supported by a review of the data for air and steam (unsaturated) from Steffens and Shillig. Note that although there is greater scatter, the data from Steffens and Shillig agrees fairly well with that of the current work and seems to also fall approximately along the same line. Figure 45 shows

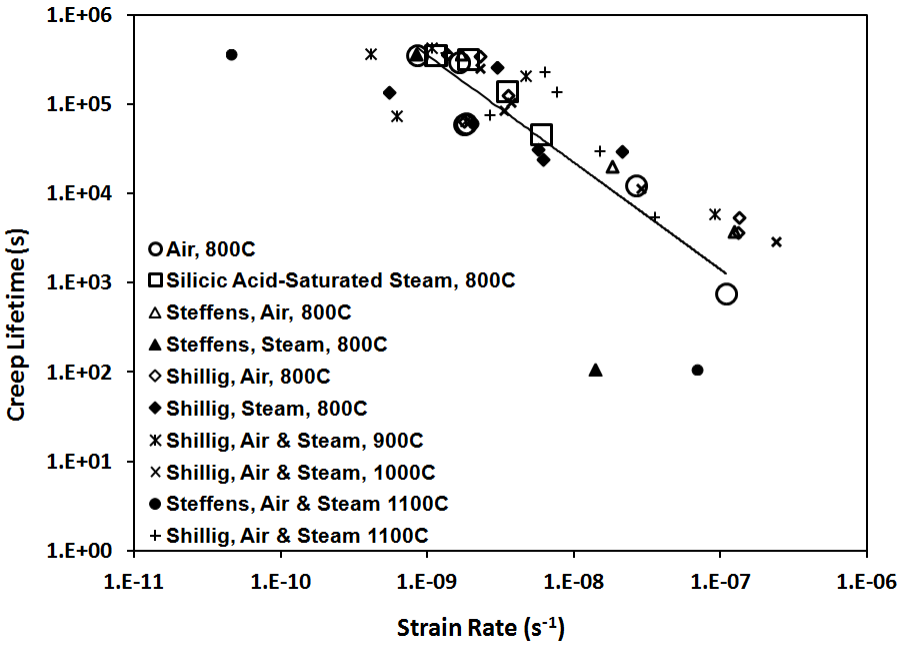


Figure 44. Monkman-Grant plot of creep lifetime vs. steady-state strain rate for Hi-Nicalon^{TM} S SiC fiber tow specimens tested at 800°C in dry air, in steam, and in silicic acid-saturated steam. Data is from the current work and reproduced from Steffens [1] and Shillig [23]

the same data as Figure 44 with regression fits for the 1100°C data from Steffens and Shillig. Note that each is parallel to the fit for the current work, indicating that the Monkman-Grant parameter q is the same. As DiCarlo et al noted [94], at higher temperatures, the slope remains the same but the creep lifetime (creep rupture time) is higher for a given creep rate. Although the data from Steffens does not demonstrate this increase in lifetime, this is easily explained by the test methodology issues described by Steffens [1] and corrected by Shillig [23] wherein steam impinged on the fibers, causing premature failure. It is also important to note the paucity of data collected (only three data points at 1100°C) may be a further cause of this discrepancy. Data for the other temperatures noted were also too few to provide meaningful results on a temperature by temperature basis, however taken as a whole the data supports the conclusion that the Monkman-Grant relationship is applicable to Hi-Nicalon^{TM} S fiber tows.

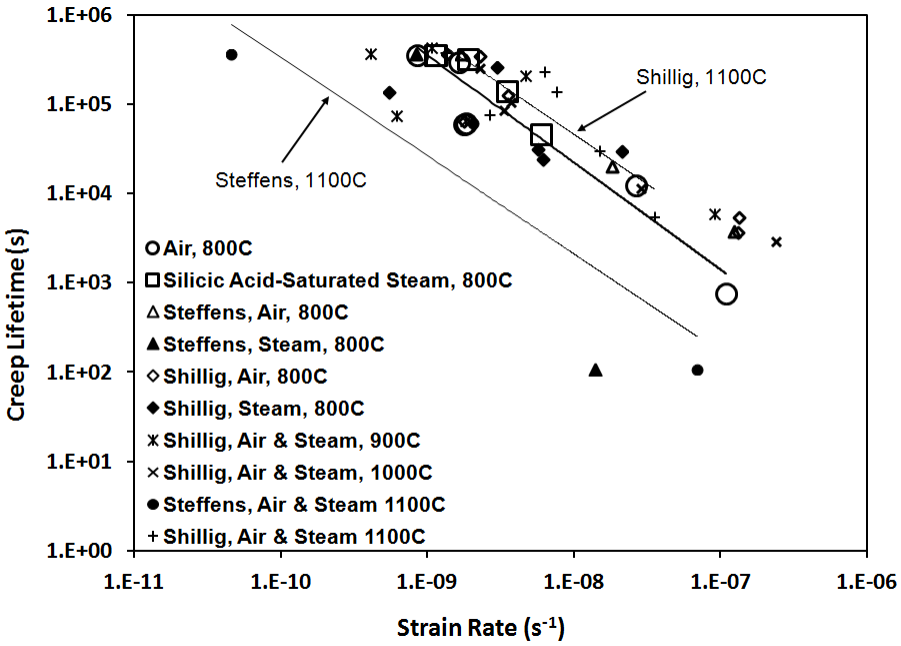


Figure 45. Monkman-Grant plot of creep lifetime vs. steady-state strain rate for Hi-Nicalon^{TM} S SiC fiber tow specimens tested at 800°C in dry air, in steam, and in silicic acid-saturated steam with regression fits for 1100°C data. Data is from the current work and reproduced from Steffens [1] and Shillig [23]

Because the performance of CMCs is predominantly dependent on the performance of their fiber reinforcements, it would seem to follow that if Hi-Nicalon^{TM} S fiber tow creep lifetime can be successfully predicted by the Monkman-Grant relationship, then the creep lifetime of CMCs reinforced with Hi-Nicalon^{TM} S fiber tows may also be predicted by the Monkman-Grant relationship. This has been demonstrated for various oxide fibers and oxide-oxide CMCs [4] and for SiC fibers and SiC-based CMCs [46, 94, 195, 196], however these studies were conducted at temperatures of 1100 - 1400°C, where creep is known to occur, as opposed to the current work at 800°C where creep is minimal. Additionally, use of fiber tow Monkman-Grant data to predict creep lifetimes of CMCs is problematic due to differences in load sharing. The presence of the matrix in a CMC changes the way the applied load is shared by the fibers in the tow. Fibers in a free fiber tow will be loaded non-uniformly, with some carrying high stresses and others very little. When one breaks, all of its load is

passed to the surrounding fibers. In a CMC, the load is applied to the matrix, which transfers the load to the fibers. Except, possibly for a porous matrix CMC, since the matrix encompasses the entire tow and all of its fibers, the load is transferred more evenly across the fibers in the tow. This makes drawing conclusions for CMC creep lifetimes from fiber tow data challenging.

Unfortunately, there is insufficient published data in literature at this time for CMCs reinforced with Hi-Nicalon^{TM} S fiber tows for comparison with the fiber tow data of this work. Therefore, no conclusions can be made at this time as to whether creep lifetimes of CMCs reinforced with Hi-Nicalon^{TM} S fiber tows can be successfully predicted by the Monkman-Grant relationship derived from creep data of Hi-Nicalon^{TM} S SiC fiber tows. However, Figure 46 compares data from various SiC fibers and SiC/SiC CMCs tested in air at 1200 - 1400°C to that of the current work. Data for CMCs at 800°C could not be found in literature. The SiC/SiC CMCs with data shown in Figure 46 were reinforced with Nicalon^{TM} (Zhu et al, 1997) and Hi-Nicalon^{TM} fiber tows (Zhu et al, 1999).

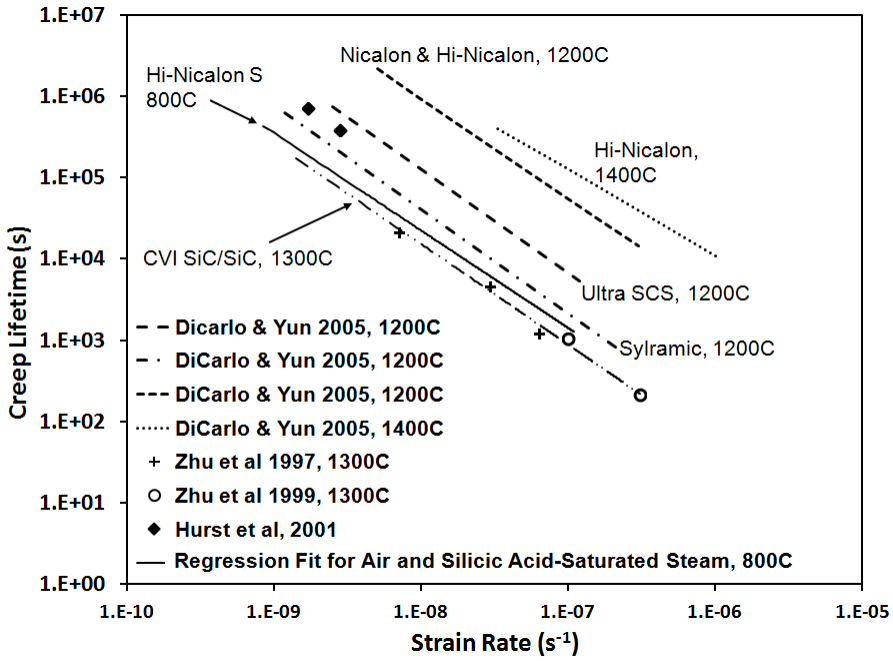


Figure 46. Monkman-Grant plot of creep lifetime vs. steady-state strain rate for Hi-Nicalon^{TM} S SiC fiber tow specimens tested at 800°C in dry air and in silicic acid-saturated steam compared with data for various other SiC fibers and SiC/SiC CMCs. Data is from the current work and reproduced from DiCarlo et al [46], Zhu et al [191, 197], and Hurst et al [196]

The Monkman-Grant relationship for Hi-Nicalon^{TM} S fiber tows tested in air and silicic acid-saturated steam agrees well with that of other SiC fibers and SiC fiber-reinforced CMCs. With the exception of Hi-Nicalon^{TM} at 1400°C, which has a Monkman-Grant exponent, q, value of less than one, the value of q is ~1.2 for each of the lines. Recall that for this work, q was found to be 1.20, which is why the Monkman-Grant line is parallel to that of the other fibers and CMCs. Note that the master line for Nicalon^{TM} and Hi-Nicalon^{TM} fiber tows tested at 1200°C in air is shifted higher than that of the current work. This is consistent with the observations of DiCarlo et al, mentioned earlier, that as temperature increases, the slope remains the same but the creep lifetime is higher for a given creep rate. DiCarlo et al suggested that the discrepancy for Hi-Nicalon^{TM} at 1400°C may be due to the long term effects of oxidation, causing rupture at a reduced strain and longer rupture times [46].

The above results indicate that the Monkman-Grant relationship for Hi-Nicalon^{TM} S fiber tows is independent of environment and agrees well with previous Monkman-Grant analyses for earlier generation SiC fiber tows and CMCs. The Monkman-Grant relationsip can be used with confidence to predict creep lifetime of Hi-Nicalon^{TM} S fiber tows and, with caution, may be useful in predicting that of CMCs reinforced with Hi-Nicalon^{TM} S fiber tows. However, data should be collected for Hi-Nicalon^{TM} S fiber tows at temperatures in the range of 1200 - 1400°C and for CMCs reinforced with Hi-Nicalon^{TM} S fiber tows in order to confirm the usability of the Monkman-Grant relationship.

V. Oxidation Kinetics of Hi-Nicalon^{TM} S Fiber Tows

5.1 Verification of Silicic Acid Saturation of Steam

To determine whether the redesigned test facility had eliminated the variations in oxidation along the length of the fiber tows, various microscopic analysis were employed to observe the fibers and any oxide scale that formed. Optical microscopy and scanning electron microscopy (SEM), with Energy Dispersive Spectroscopy (EDS), were attempted. The data collected indicated that the new facility had, indeed, solved the problem. The following sections discuss these analysis methods and their results.

5.1.1 Optical Microscopy.

One method of post-test analysis of oxide growth involves inspecting a fiber tow specimen via optical microscopy. A specimen is placed under an optical microscope, such as the one depicted in Chapter 3, Figure 33, with a light shining from the same side of the specimen as the lenses capturing the images so as to provide reflected light to the lenses, rather than transmitted light. If a sufficient thickness of oxide layer has developed on the surface, colored bands of light will be visible, as though transmitting the light through a prism. These colored bands are called interference fringes.

This phenomenon can often be observed in pools of water in a parking lot. Oil from cars floats on the surface of the water. As the sunlight hits the pool, some of the light reflects off the surface of the oil while other light continues through the oil and reflects off of the surface of the water. As we know, visible light has different wavelengths associated with different colors. When all wavelengths are together, the light appears to have no color. However, the slightly longer distance traveled by light that goes

through the oil and reflects off of the water causes those wavelengths of light to be out of phase with the same wavelengths of light that reflected off of the oil surface. When all of the light recombines, the light that traveled the longer distance constructively and destructively interferes with the rest of the light, causing some wavelengths to increase in amplitude (get stronger) and others to decrease in amplitude (get weaker), or even annihilate each other completely, causing the appearance of the colored bands and their name: interference fringes. This phenomenon is depicted schematically in Figure 47.

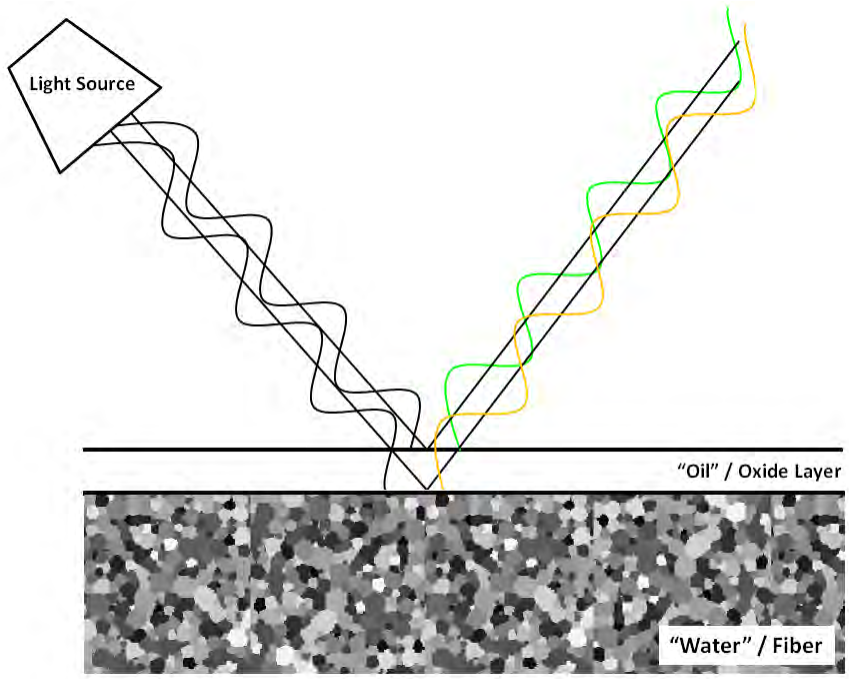


Figure 47. Schematic of constructive and destructive interference of light that causes interference fringes to be present during optical microscopy of oxidized fiber tows

The same principle occurs with oxide layers that grow on the surface of fiber tow specimens. In this case, the "oil on the surface of the water" is the oxide layer on the surface of the fiber. Early analysis using this method showed no interference fringes at all along the length of the fiber tow. This was a positive result because it was the first indicator saturating the steam with silicic acid had successfully corrected the problem

with variations in oxidation along the length of the fiber tow. However, it also meant that analysis via optical microscopy would not provide more useful information, so no further optical microscopy was conducted and analysis via SEM was pursued and is discussed in the next section and in Section 5.2. It is important to note that the absence of interference fringes did not suggest that no oxidation had occurred. In order for interference fringes to appear, the oxide layer must be of sufficient thickness that the light traveling through it goes far enough to create enough of an offset (phase lag) to result in the constructive and destructive interference. For SiC, the thickness must be approximately 60 nm before the interference fringes begin to appear. In this case, the oxide layers that developed were too thin to create such interference.

5.1.2 Scanning Electron Microscopy.

An analysis of the HiNicalon^{TM} S fiber tow specimens was conducted using EDS and SEM and compared to the results produced by Steffens [1] and Shillig [23]. The fiber tow was cut at three locations within the gauge section: near the center, and approximately one inch below and above so as to be near the bottom and the top of the hot zone. These three sections of fiber tow were mounted and observed under SEM. Whereas fiber tows tested using previous methods had shown signs of significant differences in chemical composition of the fiber tow from the bottom to the top of the test chamber, this fiber tow showed no significant variation. Silica scale growth due to oxidation of the fibers was minimal and relatively uniform along the length of the fiber tow. Additionally, the appearance of the silica scale was fairly smooth, with no pitting and very few deposits that would result from silica precipitation out of the saturated steam and showed no signs of a crystallized oxide layer. Figure 48 shows examples of the active and passive oxidation found at different locations along the fiber tow length in Shillig's work [23]. Figures 49-51 are SEM images of the Hi-

Nicalon^{TM} S SiC fiber tow specimen subjected to the saturated steam environment at 800°C and to a load of 2.96 MPa (429.3 psi), taken at the three locations along the length of the fiber tow.

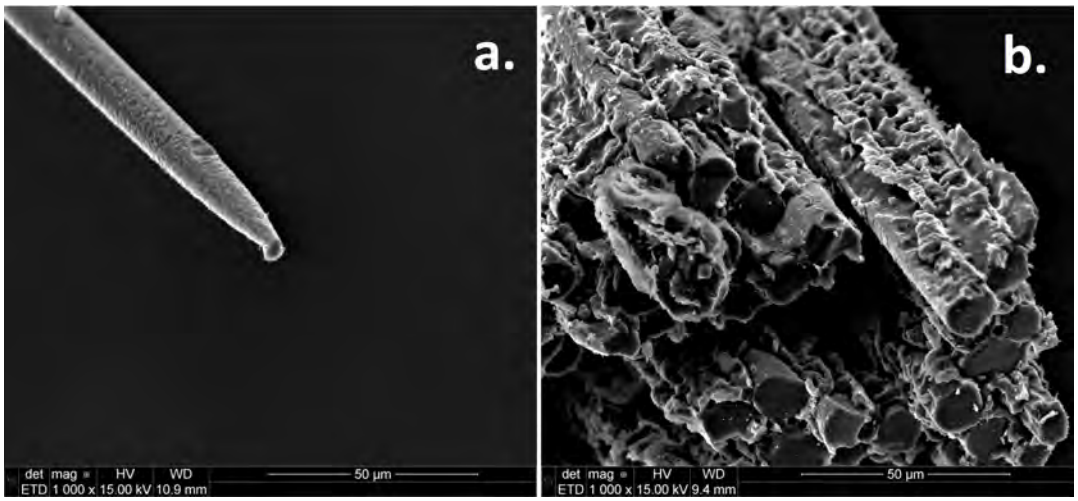


Figure 48. Variations along the fiber tow due to testing in unsaturated steam. a.) Fiber degradation due to active oxidation, typically found in sections of the fiber tow near the bottom of the test chamber. b.) Silica (SiO_2) scale growth typically found in sections of the fiber tow near the top of the test chamber. Reproduced from [23]

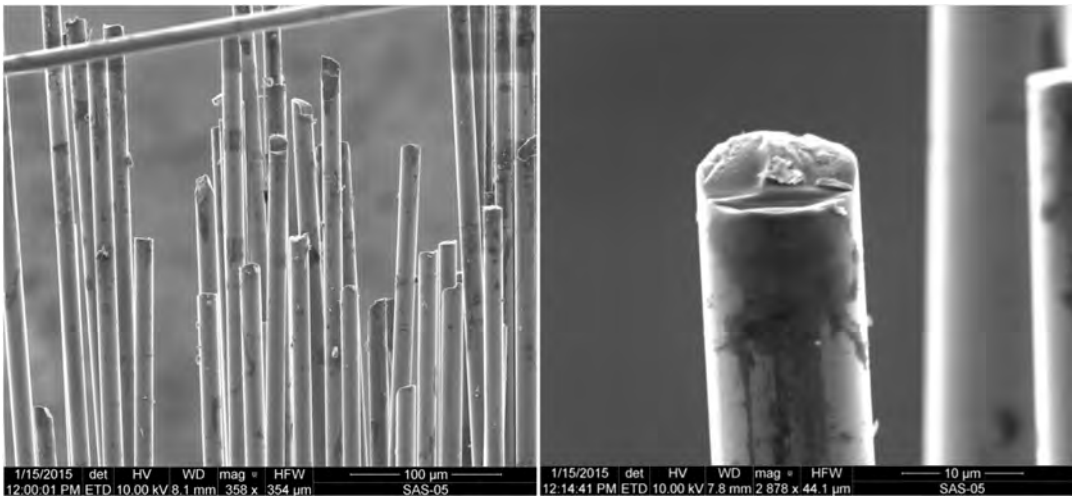


Figure 49. Lower section of Hi-Nicalon^{TM} S SiC fiber tow specimen subjected to the saturated steam environment at 800°C and to a load of 2.96 MPa (429.3 psi)

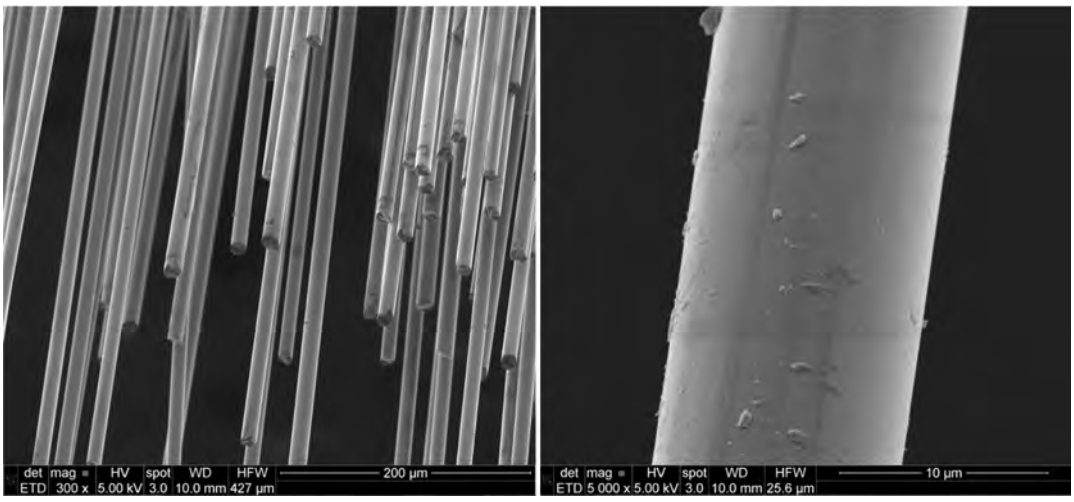


Figure 50. Center section of Hi-Nicalon^{TM} S SiC fiber tow specimen subjected to the saturated steam environment at 800°C and to a load of 2.96 MPa (429.3 psi)

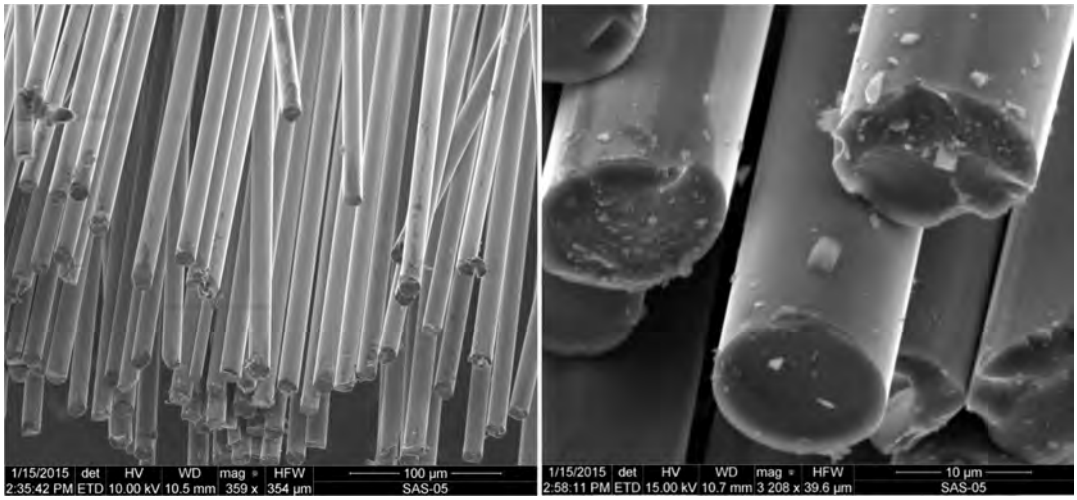


Figure 51. Upper section of Hi-Nicalon^{TM} S SiC fiber tow specimen subjected to the saturated steam environment at 800°C and to a load of 2.96 MPa (429.3 psi)

The various features evident in Figures 49-51 are characteristic of the fibers at all locations studied. The most prominent feature is the smooth, somewhat mottled surface, which has a thin layer of oxidation. Areas that appear lighter in the SEM images have decreased carbon content with an accompanying increase in silicon and oxygen, as shown in the representative spectrograph shown in Figure 52. The decreased carbon content is attributable to the release and vaporization of the carbon

during the oxidation process. The darker areas showed less oxygen content and a more stoichiometric SiC composition, as seen in Figure 53. Figure 54 shows a representative spectrograph for the interior of the fibers, obtained in the cross-section of a cut fiber, where very little oxygen is present and the SiC is near-stoichiometric.

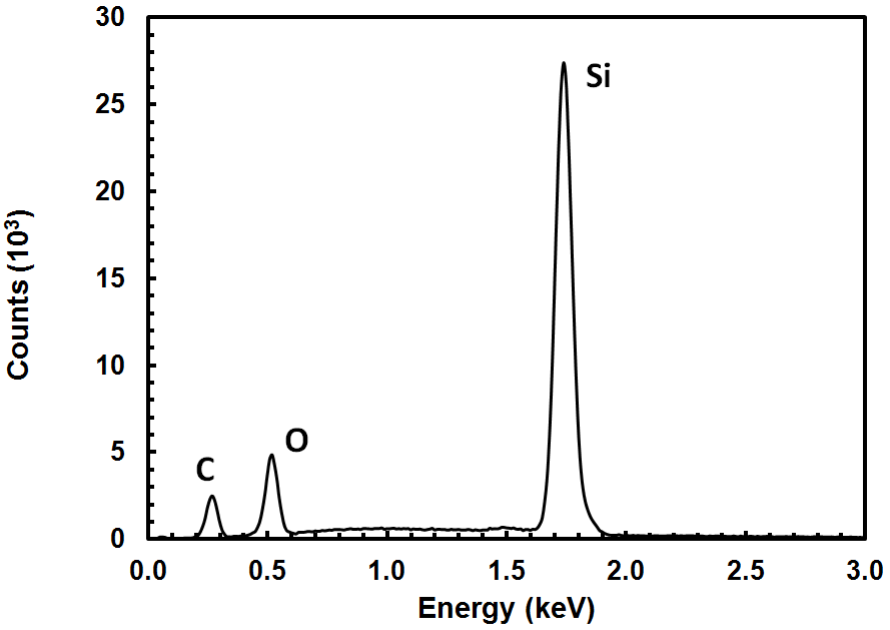


Figure 52. Energy dispersive spectrograph representative of the lighter areas of the surface of Hi-Nicalon^{TM} S SiC fiber tow specimen subjected to the saturated steam environment at 800°C and to a load of 2.96 MPa (429.3 psi). The composition shows in increase in silicon content from stoichiometric SiC, an accompanying decrease in carbon, and some oxygen. The content was 72.96% silicon, 16.29% carbon, and 9.72% oxygen by atomic percent.

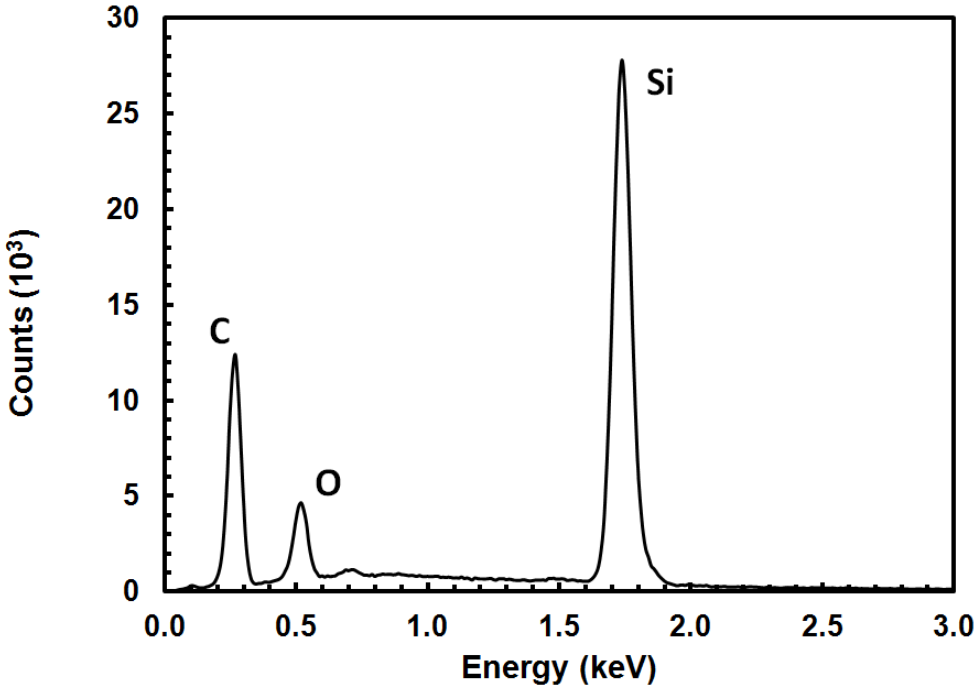


Figure 53. Energy dispersive spectrograph representative of the darker areas of the surface of Hi-Nicalon^{TM} S SiC fiber tow specimen subjected to the saturated steam environment at 800°C and to a load of 2.96 MPa (429.3 psi). The composition is near stoichiometric SiC and a smaller amount of oxygen than the lighter areas. The content was 46.53% silicon, 45.25% carbon, and 7.06% oxygen by atomic percent.

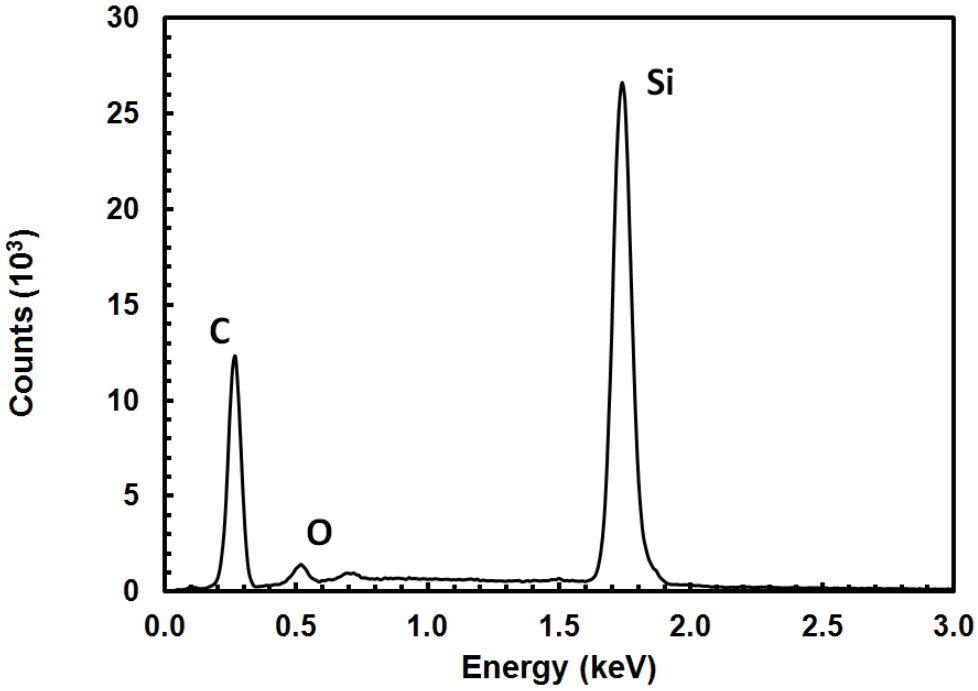


Figure 54. Energy dispersive spectrograph representative of the darker areas of the surface of Hi-Nicalon^{TM} S SiC fiber tow specimen subjected to the saturated steam environment at 800°C and to a load of 2.96 MPa (429.3 psi). The composition is near stoichiometric SiC and a very small amount of oxygen. The content was 48.87% silicon, 49.09% carbon, and 1.51% oxygen by atomic percent.

It was noted in the SEM analysis that the dark areas tend to be axial in nature, running along the fibers in fairly straight lines, suggesting areas of contact between neighboring fibers. The composition difference between the light and dark areas of the surface indicates that less oxidation took place in the dark areas. This is likely a result of less exposure to the steam environment than the lighter areas due to contact between fibers. The common features observed on the fibers subjected to the saturated steam environment at 800°C and to a load of 2.96 MPa (429.3 psi) can be seen in Figure 55.

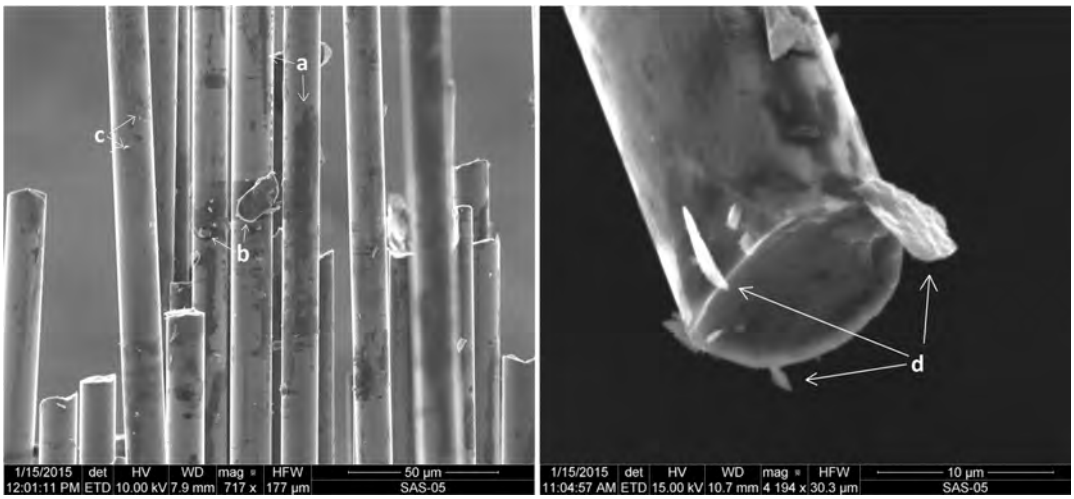


Figure 55. Common surface features of Hi-Nicalon^{TM} S SiC fiber tow specimens subjected to the saturated steam environment at 800°C and to a load of 2.96 MPa (429.3 psi). Note the a) smooth, mottled surface, b) large chunks of fiber, c) small precipitates of silica, and d) small flakes of the silica oxide layer.

Large chunks of fiber and small flakes, primarily found near the cut end of the fiber were common. The large chunks had the same appearance as the fibers and showed the same composition. The small flakes were similar in appearance and composition to the lighter areas of the fiber surface, suggesting flakes of oxide layer. The concentration of the fiber chunks and flakes of oxide layer near the cuts supports the conclusion that the chunks and flakes are generated when the fibers that have not failed are mechanically cut during SEM specimen preparation.

Another common feature was bits of crystalline material scattered along the lengths of the fibers. These bits tended to have compositions high in silicon and oxygen and a crystalline appearance. It is likely that these are small precipitates formed on the surface of the fiber as a result of slight localized cooling of the silicic acid-saturated steam. This cooling would cause a small decrease in the capacity of the steam to carry the dissolved silicic acid, resulting in small amounts of silica precipitating out of the steam. This conclusion is supported by a small, but noticeable increase in the number of these small bits that appear on the fibers near the top of

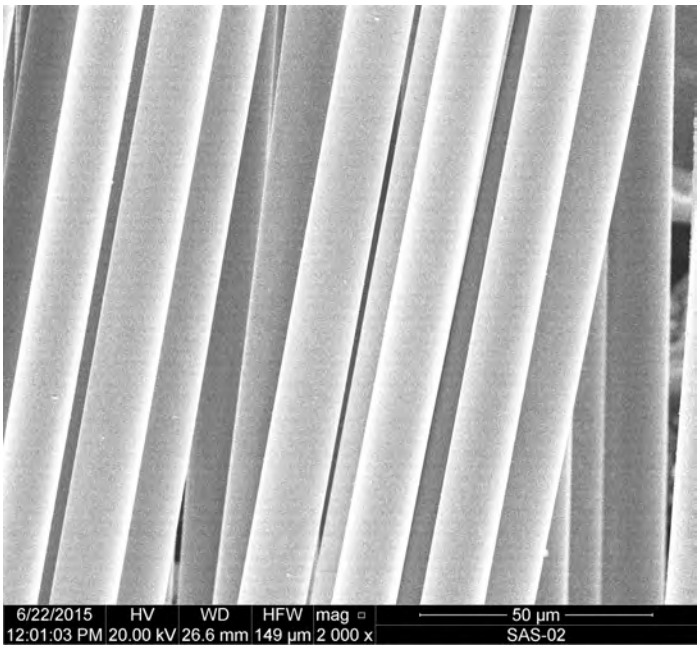
the hot zone, where the temperature drops off. The presence of a small amount of precipitation both supports the conclusion that the steam is saturated and highlights the need to closely control the steam temperature.

Yet another indicator that the steam was saturated is that the 154 MPa (22.3 ksi) test went to run-out. This is consistent with creep lifetimes reported by Gauthier and Lamon [121], whose results predicted the lifetime at loads below 300 MPa (43.5 ksi) to be on the order of one to two months. None of the previous tests conducted by Steffens [1] and Shillig [23] in unsaturated steam resulted in run-out at this load level. Steffens' test at 154 MPa (22.3 ksi) lasted only 0.03 hrs [1]. Shillig's two tests at 154 MPa (22.3 ksi) lasted 37.89 hrs and 71.69 hrs.

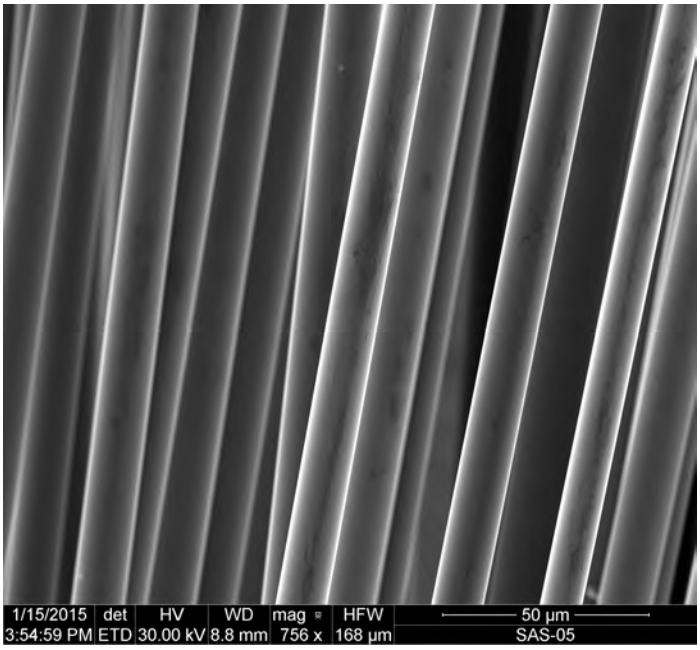
5.2 Common Features of Oxidized Fibers

More extensive analysis of specimens via SEM revealed common features of the oxidized fibers and other features of interest. The following is a brief review and discussion of the features of interest as observed via SEM. The SEM images presented here are representative of what was seen on all of the specimens. The complete set of images captured via SEM is found in Appendix B.

The most common feature among all of the specimens is the smooth surface and light hue of the fibers. As can be seen in the representative images shown in Figure 56, the fibers appear smooth, but not glassy. Areas of darker hue are evident, but not ubiquitous, and often have a linear appearance, as noted in Section 5.1.2.



(a)



(b)

Figure 56. Hi-Nicalon^{TM} S SiC fibers have a smooth surfce and light hue that is still readily observable after being subjected to air or a saturated steam environment at 800°C.

Those fibers that experienced fracture during the creep test (creep rupture) displayed a classic brittle fracture behavior, as can be seen in Figures 57 and 58. The fracture surface is perpendicular to the surface and long axis of the fibers. A clear progression of the fracture can be seen in most fibers as represented by Figure 57. The fracture initiated on the right of the fiber, as indicated by the arrow, likely due to a surface flaw created by the fabrication process, to specimen preparation or handling, or to oxidation of the fiber. The crack grew radially outward from that spot for a period of time until reaching the critical crack size, after which the crack grew rapidly to failure, as evidenced by the more rough fracture surface toward the left side.

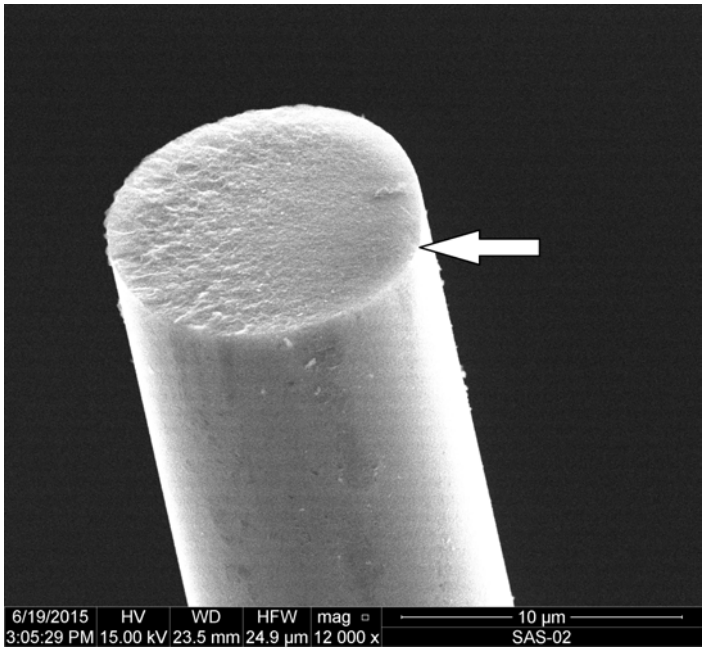


Figure 57. Brittle fracture of Hi-Nicalon^{TM} S fiber tow specimens after creep rupture in air at 800°C.

The SEM images of brittle fracture surfaces do not show significant signs of cavity nucleation and growth as the cause of fracture. The crack initiation point is clearly at the edge, due to oxidation or a surface defect. This suggests that a conclusion of grain boundary sliding with cavity nucleation and growth as the dominant damage mech-

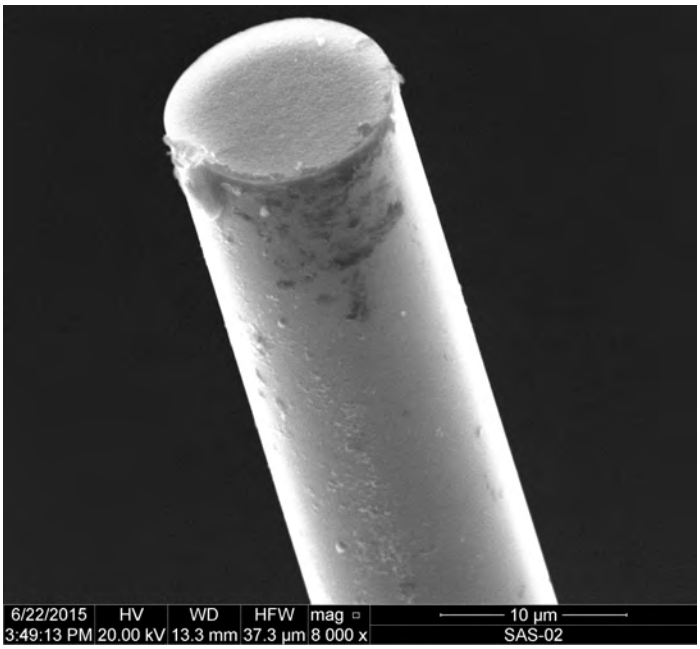
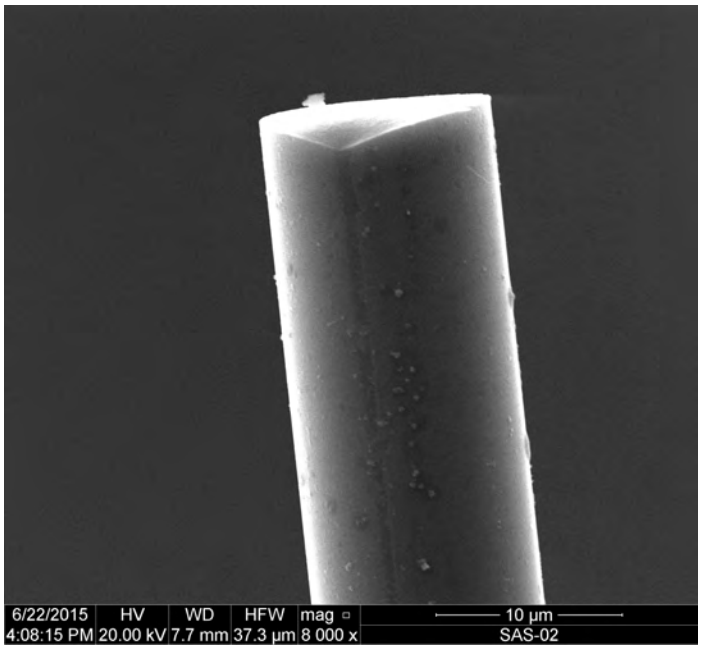


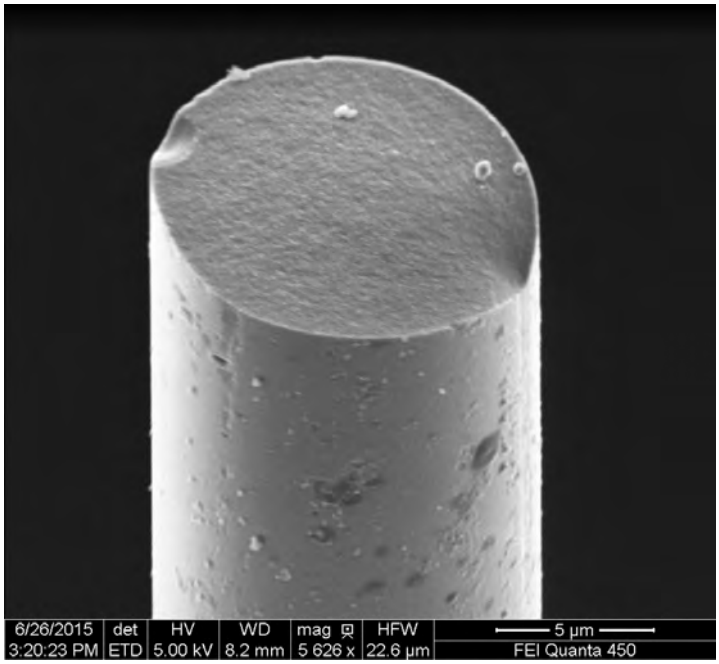
Figure 58. Brittle fracture of Hi-Nicalon^{TM} S fiber tow specimens after creep rupture in silicic acid-saturated steam at 800°C.

anism in saturated steam may be premature. SEM images at higher magnification and resolution would be helpful in determining this definitively.

Some brittle fractures clearly initiated at points of interaction with other fibers. Figure 59 shows examples of two such fibers. Note the initiation site of the fracture coincides with the axial line of darker (a) or recessed (b) portion of the fiber. Figure 60 shows two fibers still bonded together and the line of interaction where a portion of on of the fibers has been dislodged. It is instructive to note that the fiber interactions that were not simply incidental, i.e. interactions that "cemented" fibers together and that caused fracture, occurred mostly in specimens subjected to silicic acid-saturated steam. This is likely due to the increased oxidation as compared to specimens tested in air.

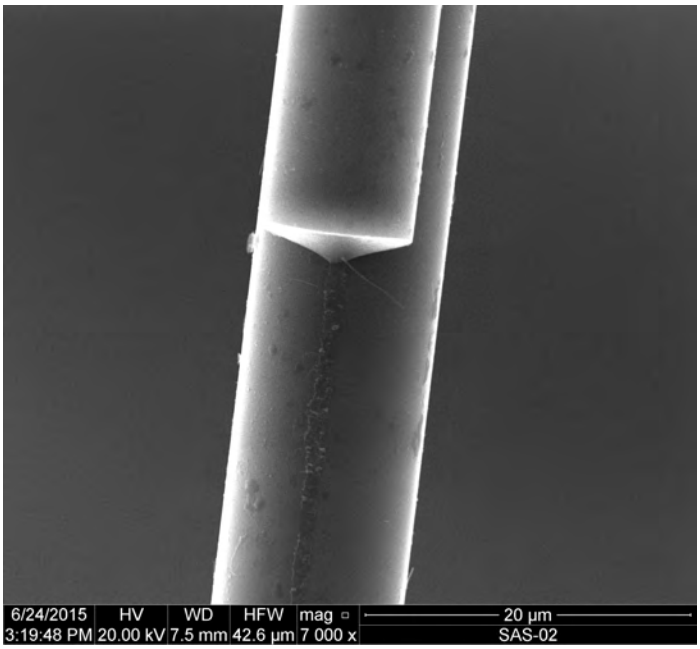


(a)

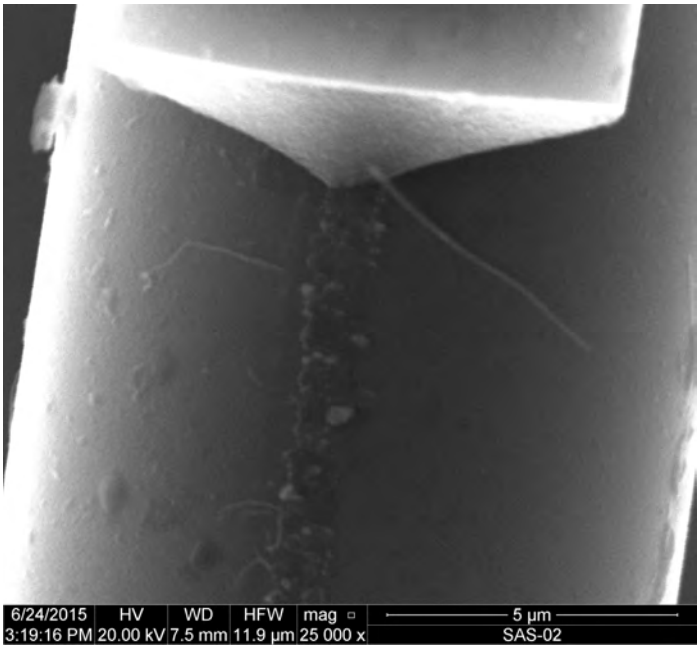


(b)

Figure 59. Evidence of fiber interactions as a cause of crack initiation in Hi-Nicalon^{TM} S fiber tow specimens subjected to creep in silicic acid-saturated steam at 800°C.



(a)



(b)

Figure 60. Evidence of fiber interactions of Hi-Nicalon^{TM} S fiber tow specimens after being subjected to creep in silicic acid-saturated steam at 800°C.

Some less common but noteworthy features were also seen among the fiber tow specimens. Rough, dark areas were observed occasionally on the surface of the fibers and tended to be concentrated in areas around fractures. These areas are likely areas of greater oxidation. This increased oxidation may be a a result of exposure to a contaminant or due to greater exposure to the oxidizing species in the environment. It is possible that these fibers were near the outer edges of the fiber tow, causing them to react more quickly than fibers toward the center of the tow. Figures 61 and 62 are representative of the fibers observed with this feature.

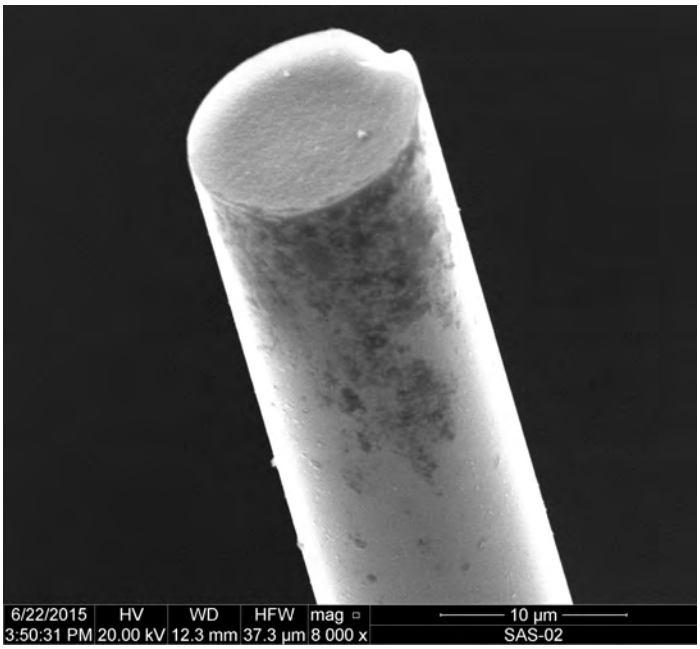


Figure 61. Rough, dark areas seen around fractures of Hi-Nicalon^{TM} S fiber tow specimens subjected to creep in silicic acid-saturated steam at 800°C are likely the crack initiation sites.

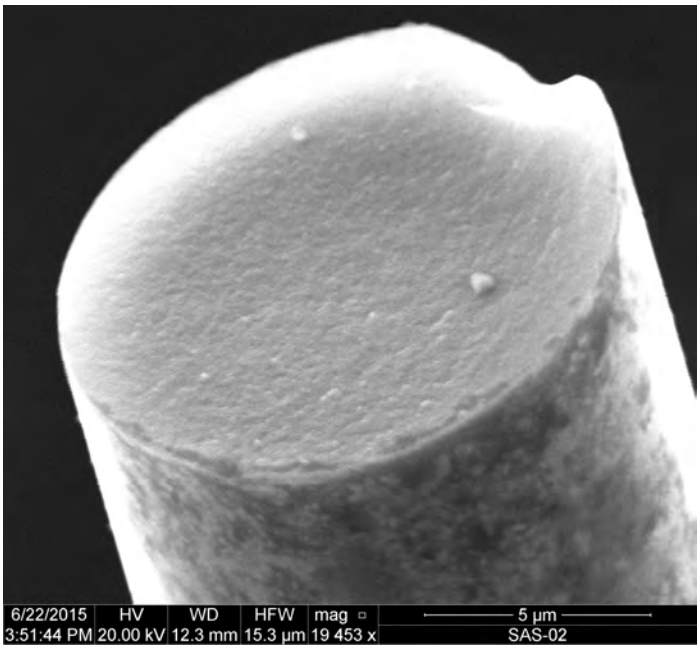
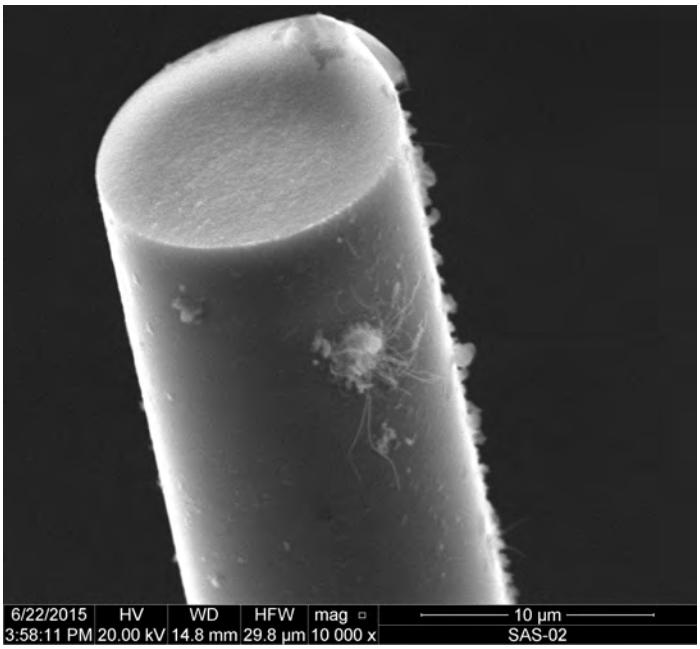
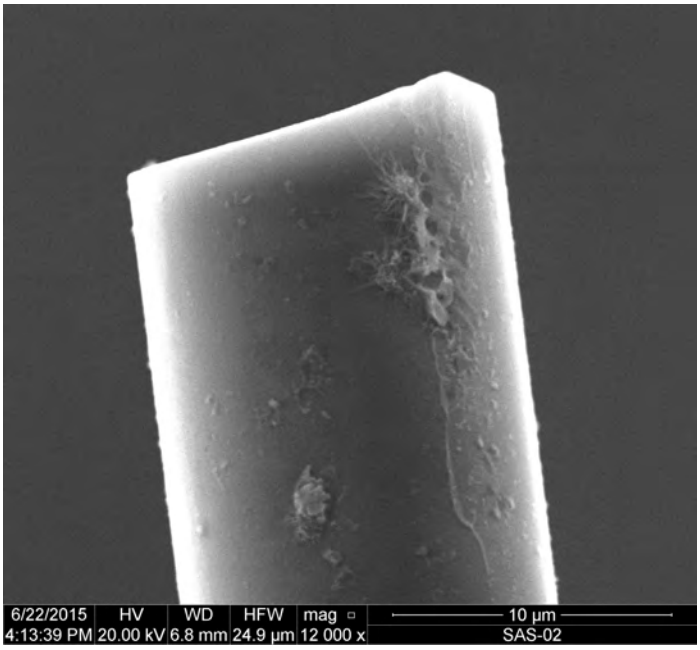


Figure 62. Rough, dark areas seen around fractures of Hi-Nicalon^{TM} S fiber tow specimens subjected to creep in silicic acid-saturated steam at 800°C are likely the crack initiation sites.

In section 5.1.2, it was mentioned that there was evidence of small particles on the surface of the fibers. It is assumed that these are precipitates of silica left behind as the steam cools. These were fairly common. Spidery tendrils, as seen in Figure 63, and crystalline growths, as seen in Figure 64, were not frequent but were noted on some fibers tested in silicic acid-saturated steam. These are also likely to be silica precipitation from the steam. These features were not observed on specimens tested in air.



(a)



(b)

Figure 63. Spidery tendrils of deposits of silica likely precipitated out of the silicic acid-saturated steam environment during creep tests of Hi-Nicalon^{TM} S fiber tow specimens at 800°C.

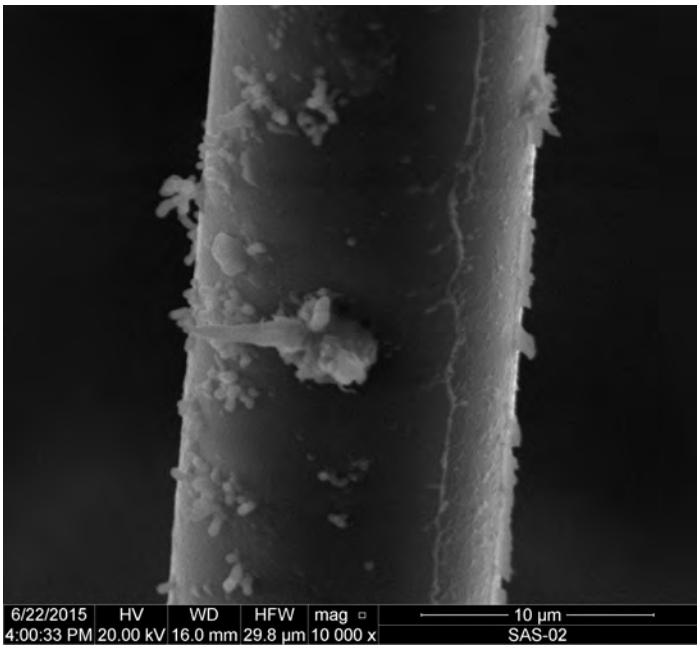
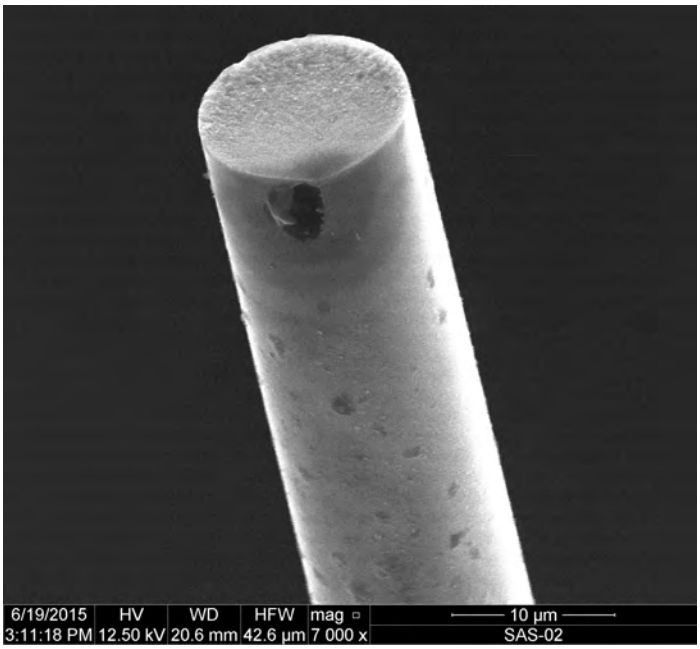
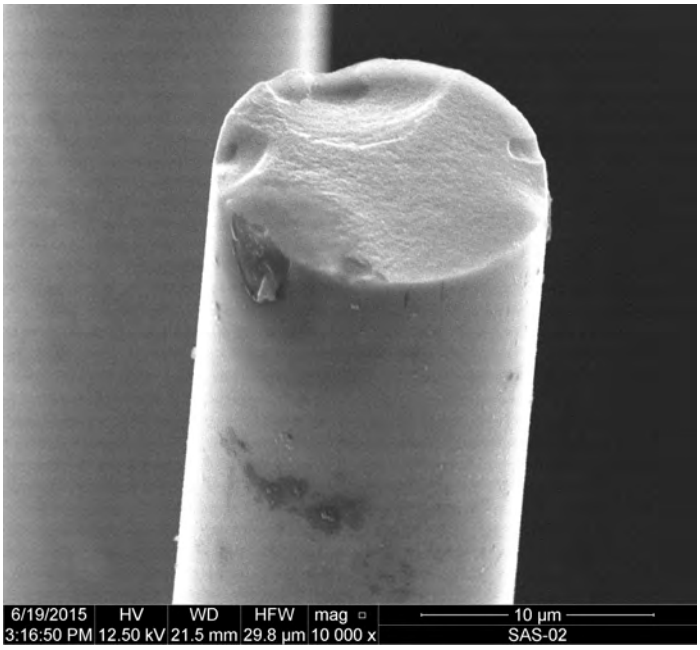


Figure 64. Crystalline deposits of silica likely precipitated out of the silicic acid-saturated steam environment during creep tests of Hi-Nicalon^{TM} S fiber tow specimens at 800°C.

Another less common, but noteworthy feature was evidence of contaminants or inclusions. A contaminant is a foreign substance not intended to be part of the fiber. An inclusion is a contaminant that becomes part of the crystal structure of the fiber, typically during the manufacturing process. Figures 65 and 66 show examples of possible inclusions or contaminants in fiber tow specimens tested in air that were at or near the fracture surface of the fiber, likely causing the fracture, while Figure 67 shows an example in a specimen tested in silicic acid-saturated steam. Note the concentric rings of discoloration in the fiber surface and similar discoloration in the fracture surface. This discoloration is an indication of the change in the crystal structure of the fiber caused by the inclusion or contaminant. Inclusions and contaminants can accelerate oxidation by acting as nucleation sites where the chemical energy necessary to break bonds and conduct the oxidation reaction is less than the surrounding area.

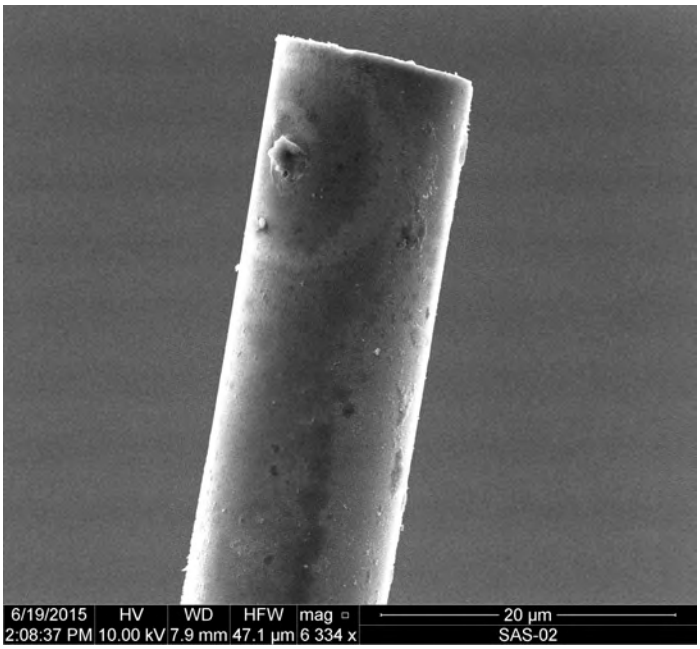


(a)

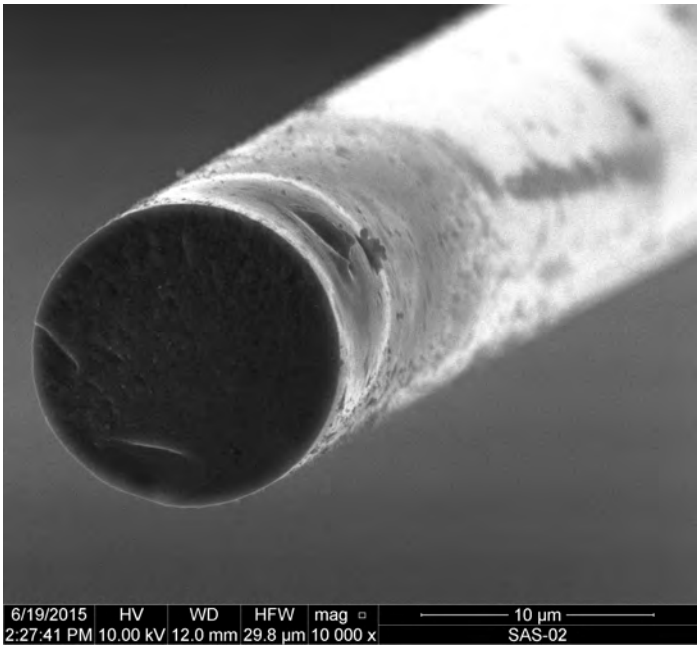


(b)

Figure 65. Contaminants introduced during fabrication, preparation, or testing of Hi-Nicalon^{TM} S fiber tow specimens subjected to creep in air at 800°C can cause increased localized oxidation, often resulting in failure of the fiber at or near the location of the contaminant. Here the fracture surface clearly shows that the crack formed at the site of the contaminant.



(a)



(b)

Figure 66. Contaminants introduced during fabrication, preparation, or testing of Hi-Nicalon^{TM} S fiber tow specimens subjected to creep in air at 800°C can cause increased localized oxidation, often resulting in failure of the fiber at or near the location of the contaminant.

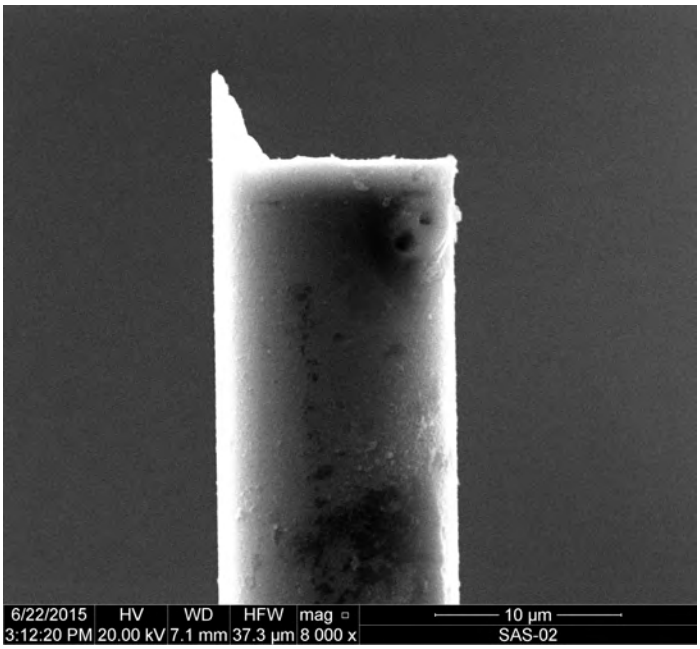
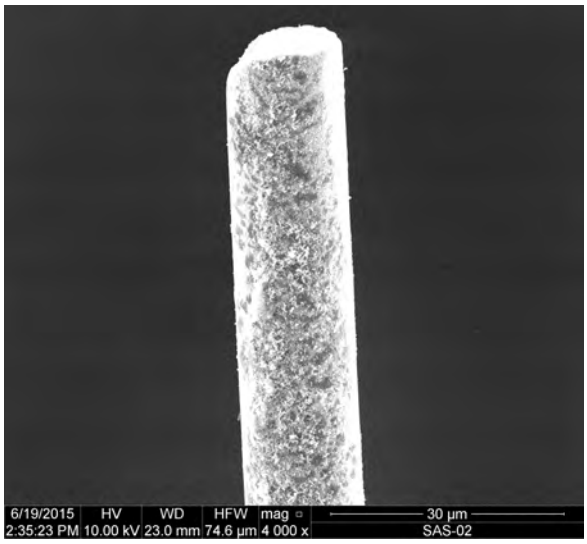


Figure 67. Contaminants introduced during fabrication, preparation, or testing of Hi-Nicalon^{TM} S fiber tow specimens subjected to creep in silicic acid-saturated steam at 800°C can cause increased localized oxidation, often resulting in failure of the fiber at or near the location of the contaminant.

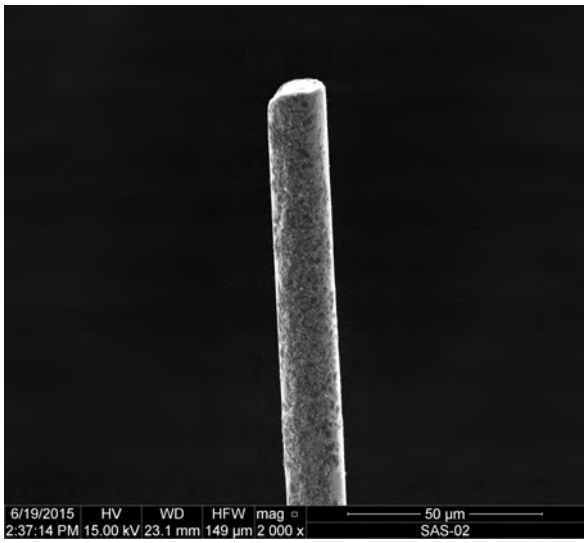
As part of the manufacturing process, Hi-Nicalon^{TM} S SiC fiber tows have a Polyvinyl Alcohol (PVA) coating applied to decrease damage due to handling. For this study, this coating was allowed to burn off during the warm up portion of the test. It is likely that the byproducts of this coating burning off were a source of the contamination observed in the specimens. The evidence of contamination was minimal and effects like those seen in Figures 65 - 67 were not commonplace. Though removal of the sizing prior to testing in future efforts would reduce these occurrences, oxidation results were qualitatively consistent with work done by Hay in which sizing was removed prior to testing. This indicates that the sizing may not be a critical factor.

One of the most interesting and inexplicable features was also the least common. In most of the saturated steam specimens analyzed via SEM, and in one air specimen, there was one or two "rogue" fibers that had an extremely rough surface similar to

that of a crystallized oxide layer, as shown in Figures 68 - 69. This layer is clearly thicker than any other observed oxide layer. It is unclear what causes these "rogue" fibers to exhibit this morphology, but it has been noted in other oxidation tests [198].

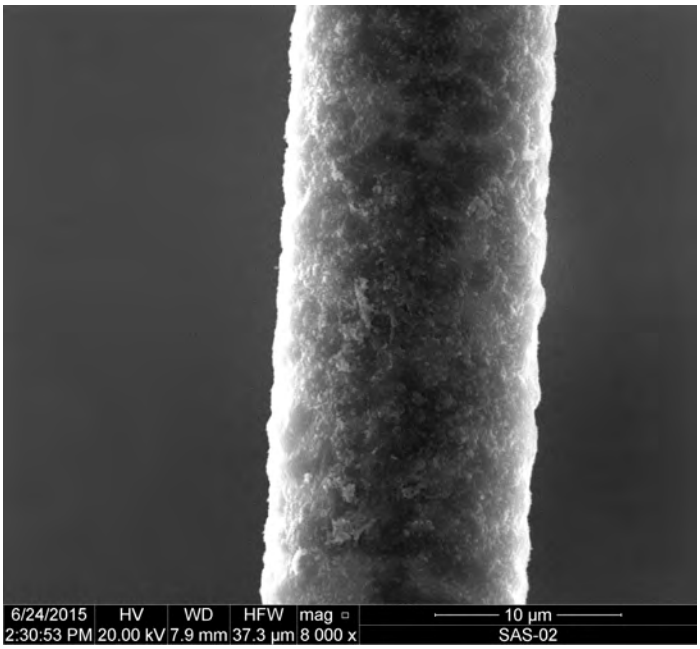


(a)

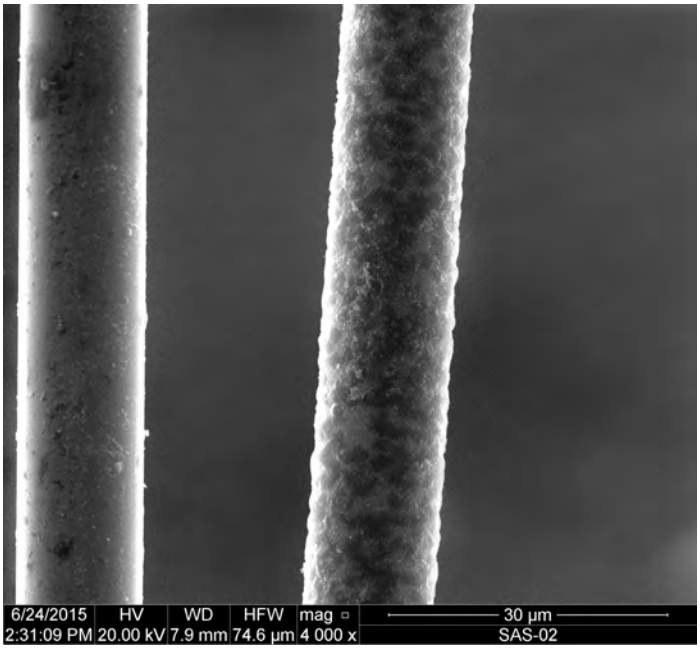


(b)

Figure 68. One or two "rogue" fibers with excessive oxide scale growth were observed in most specimens of Hi-Nicalon^{TM} S fiber tow specimens subjected to creep in air at 800°C. Though difficult to say definitively, these appeared to always be on the outer edge of the fiber tow.



(a)



(b)

Figure 69. One or two "rogue" fibers with excessive oxide scale growth were observed in most specimens of Hi-Nicalon^{TM} S fiber tow specimens subjected to creep in silicic acid-saturated steam at 800°C. Though difficult to say definitively, these appeared to always be on the outer edge of the fiber tow.

The preponderance of evidence in the SEM images of Hi-Nicalon^{TM} S fiber tows tested as part of this research effort indicates that oxide scale growth for air and silicic acid-saturated steam is very small. It was possible to see what appeared to be a thin layer of oxide growth on most specimens, but difficult to separate it from edge effects of the SEM. As mentioned in Section 5.1.2, Electron Dispersive Spectroscopic analysis of various surfaces showed that an oxide layer does exist. However, the oxide layer was too thin to be measured via SEM. A limited number of specimens was analyzed via Transmission Electron Microscopy (TEM) and the results are discussed in the next section.

5.3 Oxidation in Air and Silicic Acid-Saturated Steam

Oxidation is controlled by the rate of delivery of oxygen to the surface of the oxidizing material and the rate of reaction of the oxygen with that material. Whichever rate is slower will drive the oxidation rate. However, this is only true for a very brief time at the outset of oxidation. As oxidation proceeds, a layer of oxide forms over the surface of the material, causing the oxidation rate to become a function of the rate of diffusion of oxygen through the oxide layer to the oxide-material interface where further oxidation can occur in addition to the rate of transport to the surface and the reaction rate. Over time, as the oxide layer gets thicker the time required for diffusion of the oxygen through the oxide layer increases. Regardless of the rate of transport to the surface and the oxidation reaction rate, eventually, the oxide layer will become thick enough (assuming sufficient size of the oxidizing material) that the diffusion rate will be lower than the other rates and will be the driving factor in the overall oxidation rate of the material. This diffusion-dependent oxidation rate continues to decrease as the oxidation layer, or scale, grows thicker. Figure 70 shows a schematic of this oxidation process.

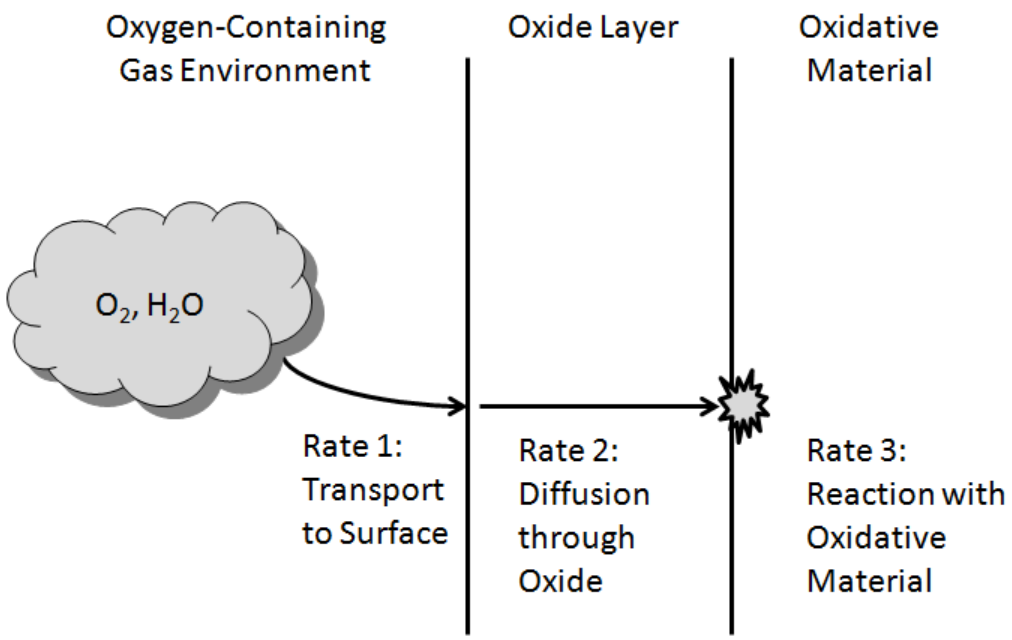


Figure 70. Schematic of oxidation dependence on mass transport, diffusion, and reaction rates.

Deal and Grove developed a mathematical relationship describing this oxidation process for silicon [28] and it is reviewed here. Rates one, two, and three depicted in Figure 70 are denoted as fluxes F_1, F_2, F_3, respectively.

The rate of transport of the oxygen from the environment is:

$$F_1 = h\,(C^* - C_0) \tag{31}$$

where h is a transport coefficient specific to the gaseous environment and the oxide surface, C_0 is the concentration of the oxidant on the oxide surface at any point in time, and C^* is the equilibrium concentration of the oxidant in the oxide. In other words, C^* is the oxide surface concentration at which no transport from the environment will occur and is related to the partial pressure of the oxidant in the gaseous environment.

The rate of diffusion through the oxide layer is given by Fick's Law and assumed to be steady state and, therefore, linear:

$$F_2 = -D_{eff}\frac{C_0 - C_i}{x_0} \tag{32}$$

where D_{eff} is the effective diffusion coefficient, C_i is the concentration of the oxidant near the boundary of the oxide layer and the oxidizing material, and x_0 is the oxide layer thickness.

The oxidation reaction rate is:

$$F_3 = kC_i \tag{33}$$

where k is a rate coefficient specific to the interface between the oxide layer and the oxidizing material.

Noting that for steady-state conditions $F_1 = F_2 = F_3 = F$, and assuming that $D_{eff} \ll k$ and h, then C_0 and C_i can be eliminated and the flux, F, becomes:

$$F = \frac{kC_i}{1 + \frac{k}{h} + \frac{kx_0}{D_{eff}}} \tag{34}$$

Deal and Grove go on to state that the rate of oxide growth can be written as:

$$\frac{dx_0}{dt} = \frac{F}{N_1} \tag{35}$$

where N_1 is the number of oxidant molecules in a unit volume of the oxide layer.

Using the boundary condition that x_0 is equal to an initial oxide layer thickntess, x_i, at $t = 0$, the solution to this differential equation is:

$$x_0^2 + Ax_0 = B(t + \tau) \tag{36}$$

where τ is a time shift that accounts for the presence of the initial oxide layer and is:

$$\tau = \frac{x_i^2 + Ax_i}{B} \tag{37}$$

and A and B are:

$$A = 2D_{eff}\left(\frac{1}{k} + \frac{1}{h}\right) \tag{38}$$

$$B = 2D_{eff}\frac{C^*}{N_1} \tag{39}$$

Lastly, solving Equation 36 for x_0 yields a relationship for the oxide thickness as a function of time:

$$x_0 = \frac{A}{2}\left[\left(1 + \frac{t+\tau}{\frac{A^2}{4B}}\right)^{\frac{1}{2}} - 1\right] \tag{40}$$

which, for long times, becomes:

$$x_0 \approx (Bt)^{\frac{1}{2}} \tag{41}$$

where B becomes the parabolic rate constant.

These equations can be applied to a number of different oxidants and oxide layers for various materials, with the values of C^*, C_0, h, k, and D_{eff} depending on the species of oxidant, the oxidizing material, and the oxide that forms. Deal and Grove applied this model to O_2 as the oxidant, Si as the oxidizing material, and SiO_2 as the oxide layer.

Song et al modified the Deal-Grove model for oxidation of SiC [165]. The model took into account the effect of the CO oxidation reaction byproduct and its diffusion out through the SiO_2 oxide layer. This results in an additional flux equation for mass transport (F_1) and diffusion (F_2) and an added term in the reaction flux equation (F_3) each for the CO. The F_1 and F_2 equations take the same form with values for

C^*, C_0, h, k, and D_{eff} for CO. The modified oxidation reaction rate, F_3, is:

$$F_3 = k_f C_{O_2} - k_r C_{CO} \tag{42}$$

where k_f is the forward reaction rate coefficient and k_r is the reverse reaction rate coefficient.

The inclusion of the CO out-diffusion effects and subsequent adjustment of the flux equations results in a slightly different definition for the parameters A and B:

$$A = \frac{1 + \frac{1.5k_f}{h_{O_2}} + \frac{k_r}{h_{CO}}}{\frac{1.5k_f}{D_{O_2}} + \frac{k_r}{D_{CO}}} \tag{43}$$

$$B = \frac{k_f C^*_{O_2} - k_r C^*_{CO}}{N_i \left(\frac{1.5k_f}{D_{O_2}} + \frac{k_r}{D_{CO}} \right)} \tag{44}$$

where B is also the parabolic rate constant and the linear rate constant, B/A, becomes:

$$\frac{B}{A} = \frac{k_f C^*_{O_2} - k_r C^*_{CO}}{N_i \left(1 + \frac{1.5k_f}{h_{O_2}} + \frac{k_r}{h_{CO}} \right)} \tag{45}$$

Song et al also note that this formulation of the Deal-Grove relationship can be applied to oxidation in wet air (steam) with H_2 as the out-diffusing species, rather than CO. The flow of oxidant to the surface, the mass transport flux, is rarely the rate-limiting part of the oxidation process and Song et al assume that it is not. However, in a tightly packed fiber tow, the fibers towards the center of the tow experience a lower mass transport flux of oxidant to their surfaces than the outer fibers experience due to physical barrier of other fibers past which the oxidant must flow. Additionally, fiber tows encased in the matrix of a CMC will only be significantly exposed to an oxidant through cracks in the matrix. As these cracks are small and tend to passivate, the mass transport flux through the cracks is significantly lower than at the surface

of the CMC. These factors make it conceivable for the mass transport flux to be more of a limiting factor in certain cases. One possible evidence of a mass transport flux driving the oxidation might be evidence of significantly thicker oxide scales in fibers towards the outside of the fiber as compared to those in the center of the fiber. This question remains largely unexplored in literature, possibly due to the difficulty in maintaining the "inner" vs. "outer" status of a given fiber during testing and due to the difficulty of determining which fibers are outer fibers and which are inner fibers during post-test analysis.

Based on the assumption that the mass transport flux is not the limiting factor, i.e. that $h \gg k$, and the fact that during steady-state oxidation $C^*_{O_2} \gg C^*_{CO}$, the linear and parabolic rate constants become:

$$\frac{B}{A} = \frac{k_f C^*_{O_2}}{N_i} \tag{46}$$

$$B = \frac{k_f C^*_{O_2}}{N_i \left(\frac{1.5 k_f}{D_{O_2}} + \frac{k_r}{D_{CO}} \right)} \tag{47}$$

and B may be further reduced depending on whether the O_2 diffusion or the CO out-diffusion is the controlling process.

As reported in chapter two, Hay et al showed that the Deal-Grove model, using the definition of A and B modified by Song, applies to amorphous oxidation growth on SiC fiber tows in dry and wet air [153, 155]. Hay et al compared the model to one for the cylindrical geometry of fibers. Using this cylindrical version of the model, Hay et al found that the oxidation kinetics of fibers very closely matches that of a flat plate up to a certain oxide thickness. For fibers of approximately 12 μm diameter, such as Hi-Nicalon^{TM} S, the point of deviation from the flat plate oxidation kinetics was four to five μm. For oxide layers (scale) that crystallize at or below this thickness, the flat plate version of the model is sufficiently accurate and is simpler to employ.

Since the fibers used in the current study have an average diameter of 13 μm, very near that reported by Hay et al, the same approach may be taken here. Although it is unrealistic to measure the scale thickness in the SEM images taken for the current work, it is evident that oxide scale is very thin and definitely less than one-third the diameter of the fibers, so the flat plate version of the model is adequate for this study.

Using Equations 36 and 41, experimental creep lifetime data, and scale thickness measurements obtained via microscopy, the linear and parabolic rate constants, B/A and B, respectively can be determined. It is assumed that oxidation at room temperature during the storage of specimens prior to and after testing is negligible. Specimens that achieved run-out, 100 h at test temperature in the oxidizing environment, meet the criterion for long time ($t \gg \tau$) that yields Equation 41, since the heat-up and soak step is only 1.5 h. Using Equation 41 and the measured scale thickness for specimens that achieved run-out, an average value for the parabolic rate constant, B, can be found for air and saturated steam. This value for B can then be used with Equation 36 to determine the parameter A and, thereby, the linear rate constant B/A.

It is impractical to directly measure the scale thickness formed during the heat-up and soak step prior to continuing testing. Conducting a test that only undergoes heat-up, soak, and cool-down would provide the opportunity to directly measure the scale thickness due to these steps, but the scale growth due to heat-up and soak would be indistinguishable from that of cool-down. As such, it is problematic to experimentally determine a value for the initial oxide layer and the associated time shift, τ. It is possible to calculate this value using the methods described by Hay et al (see [153], Eq 11), but this method requires the determination of the activation energies, Q_a and Q_b, associated with the parameters A and B, respectively, which requires experimental data at multiple temperatures. Because the current work was limited to 800°C only, determination of these activation energies was not possible. As

such, it is assumed for the current study that any oxide growth due to heat up, soak, and cool down is negligible compared to that due to the test period and that $\tau = 0$ as a result of this assumption. It is acknowledged that this assumption is questionable at shorter test times, such as in the case of fast fracture, therefore, calculation of the rate constants should be accomplished using tests at least one order of magnitude longer than the heat up and soak period. Heat up and soak periods ranged from 1 - 1.7 hours and test times ranged from 14.3 - 100 hours.

With the values calculated for B using Equation 41 and the long-term test data at each stress level, a value for A can also be calculated for using Equation 36 and short-term test data at the same stress level. These values can then be used with their respective B values for the same stress to determine the linear rate constant, B/A. An average of these values for a given stress can then be taken as the overall linear rate constant. As a secondary check, scale thicknesses and growth times can be plotted and a quadratic regression fit used to determine the linear and parabolic rate constants. With $\tau = 0$, Equation 36 can be rearranged such that:

$$t = \frac{1}{B}x_0^2 + \frac{A}{B}x_0 \tag{48}$$

By plotting scale thickness on the abscissa and time on the ordinate and fitting a quadratic regression, the coefficients of the x_0 terms may be found. The coefficient of the first term is the inverse of the parabolic rate constant and the coefficient of the second term is the inverse of the linear rate constant.

As scale thickness measurements could not be accomplished via available optical or scanning electron microscopy, the test specimens were delivered to the Materials and Manufacturing Directorate of the Air Force Research Laboratory, Wright-Patterson Air Force Base, OH, for preparation and imaging under TEM. Fiber tows are encased in an epoxy resin for ease of handling. The fiber tows are then cut into thin cross-

sections suitable for mounting in a TEM and polished to remove debris from the sectioning. Figure 71 is a schematic of a typical TEM image of a fiber tow. A portion of the fiber cross-section is selected and an image is taken at high magnification, as indicated by the colored box. The magnified image, as depicted at the bottom of the schematic, clearly shows the fiber cross-section, the oxide layer, and the epoxy. The oxide scale appears as a layer between the epoxy and the fiber cross section and can be measured directly while imaging, or at a later time using a scale bar saved with each image. Multiple measurements are taken, as depicted by the arrows in the schematic, at different locations in order to get a more accurate idea of the scale thickness. The measurements can then be averaged to determine an overall scale thickness for a given fiber tow specimen. Preliminary results of TEM analysis are shown below in Table 13, however, there was an insufficient number of data points to calculate the rate constants with any confidence.

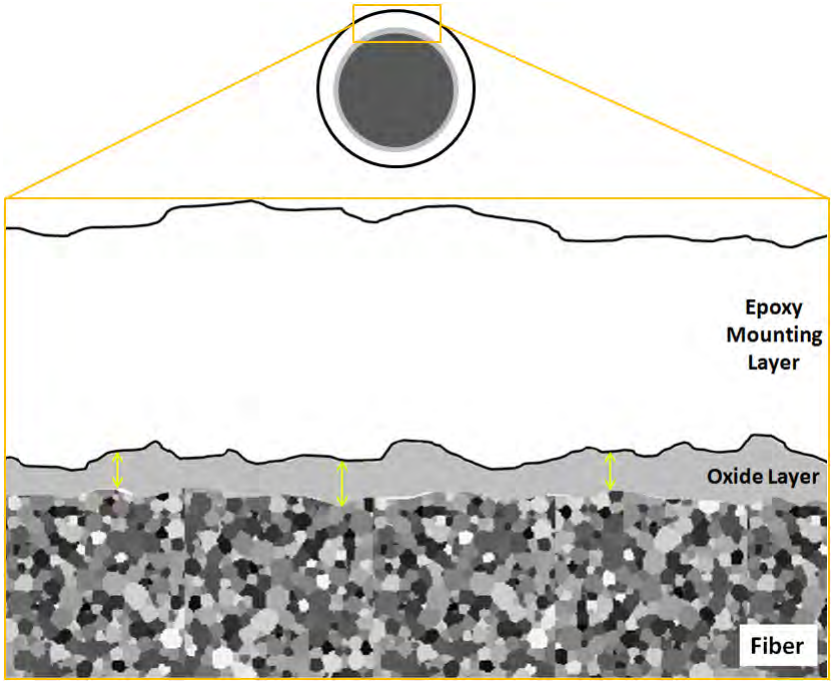


Figure 71. Schematic of a typical TEM image. Yellow arrows indicate multiple measurements taken and averaged to determine oxide thickness.

Table 13. Preliminary oxide scale thickness measurements obtained under TEM for Hi-Nicalon^{TM} S SiC fiber tow specimens tested at 800°C in dry air and in silicic acid-saturated steam.

800°C		
Stress	**Scale Thickness (nm)**	
(MPa)	**Air**	**SatSteam**
2.96	14.4	-
625	-	21.7
798	31.1	-
960	31.8	-

The Deal-Grove model was developed for oxidation of unstressed silicon. In cases of stressed oxidation, as with SiC fiber tows used to reinforce CMCs, the oxidation rate is significantly affected by the presence of the stress. For tensile stresses, the rate increases [125, 199, 200], whereas compressive stresses tend to decrease the rate. This is due, in part, to the effect of stress on crack growth.

Cracks in the fibers and in the oxide layer provide a path of least resistance for the environmental species that causes oxidation, since the energy required to deliver oxygen through the open environment of the crack is much lower than that required to diffuse through the oxide layer. To use an electrical analogy, the resistance is much lower in the crack, and a "short circuit" is formed. This "short circuit" significantly increases the rate of oxidation.

As oxidation occurs on the surface of the SiC fibers, an oxide layer grows with an associated volume increase. This volume increase is constrained by the surface of the fiber tow and causes compressive stresses on the scale. This large compressive stressed is relaxed by radial viscous flow, causing the oxide layer to get thicker [142]. For an amorphous or glassy oxide layer, relaxation and flow take place quickly. As

the active oxidizing species diffuses through the oxide layer and continues to react with the fiber at its surface, new oxide is formed and pushes the already formed oxide radially outward. When a crystalline oxide scale forms, it can increase the oxidation rate in two ways. The crystalline scale begins to form at the surface of the oxide layer. It then proceeds to grow, more rapidly tangent to the surface than through the thickness, consuming the amorphous oxide layer. This formation of a crystalline oxide scale causes a hydrostatic tension to develop [142], which causes the oxidation driving force to increase. Additionally, the crystalline scale cannot flow like an amorphous oxide layer. As the oxidation continues and the now crystalline scale is pushed radially outward, a tensile hoop stress is generated and the crystalline scale can crack, creating a "short circuit" and increasing the rate of oxidation.

Yen and Hwu [199, 200] found that tensile stress strongly enhances the oxidation rate of silicon and that the parabolic rate constant was stress dependent. Hay noted that SiC oxidation is very similar to that of silicon [142]. Gauthier et al [125] investicated stressed oxidation of SiC fiber tows and reported a significant increase in oxide layer thickness for Hi-Nicalon^{TM} single filaments and fiber tows as well as an increase in the parabolic rate constant with an increase in applied stress. However, for Hi-Nicalon^{TM} S, there was a much smaller increase in the parabolic rate constant. The parabolic rate constant for Hi-Nicalon^{TM} changed from 0.49 to 0.76 nm^2/s with an increase in stress from 800 MPa to 1276 MPa, whereas the increase for Hi-Nicalon^{TM} S was from 0.01 to 0.04 nm^2/s for the same change in applied stress. It is also notable that value of the parabolic rate constant for Hi-Nicalon^{TM} S at 1276 MPa, 0.04 nm^2/s, was the same value for Hi-Nicalon^{TM} at zero applied stress.

In accordance with the discussion above, the oxidation rate and, therefore, the oxide thickness should increase with stress for a given oxidation time. Multiple tests conducted in both air and steam as a part of this work achieved run-out, enabling

a comparison of oxide growth (scale thickness) at various stress levels in both air and steam at 100 hours oxidation time. The preliminary results listed in Table 13 show a clear correlation between the applied stress and the oxide thickness and agree with the parabolic rate constants presented by Gauthier et al that indicate that the increase for Hi-Nicalon^{TM} S fiber tows should be small.

5.3.1 Evidence of Preferential Oxide Growth and Crystallization.

During optical imaging conducted at AFRL, an interesting phenomenon became apparent and can be seen in Figure 72. Inside the indicated area, note the fibers that from a hexagonal pattern, and a few others around them, that exhibit significant oxidation. All the rest of the fibers show no sign of oxidation in the optical micrograph. These few fibers, out of the entire tow of approximately 500 fibers, exhibit this phenomenon. Figures 73 - 75 show these fibers at greater magnification. A clear ring of oxide scale can be seen surrounding each of the fibers, and the fibers appear to be degraded.

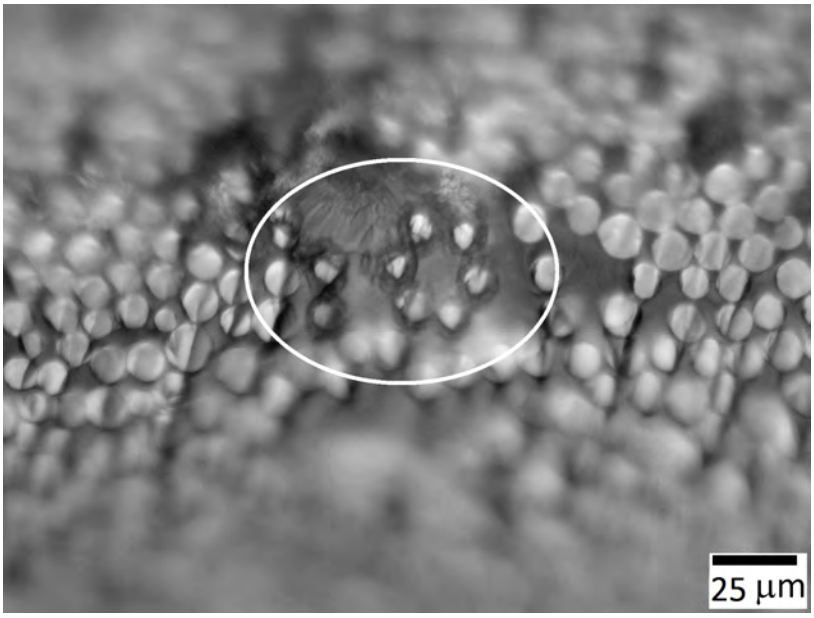


Figure 72. Optical micrograph of Hi-Nicalon^{TM} S fiber tow specimens subjected to creep in silicic acid-saturated steam at 800°C and 625 MPa. Note the region in the center with a few fibers showing very large oxide scale.

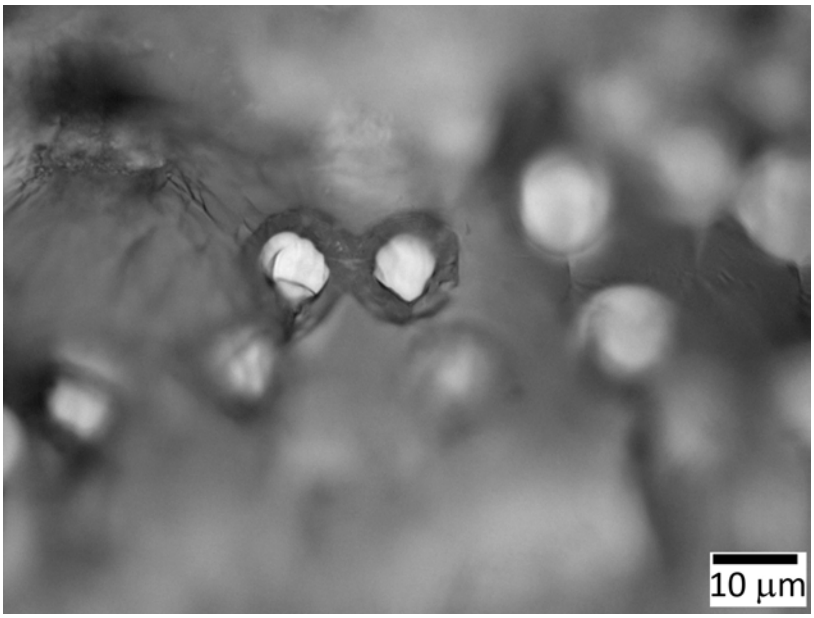


Figure 73. Optical micrograph of Hi-Nicalon^{TM} S fiber tow specimens subjected to creep in silicic acid-saturated steam at 800°C and 625 MPa.

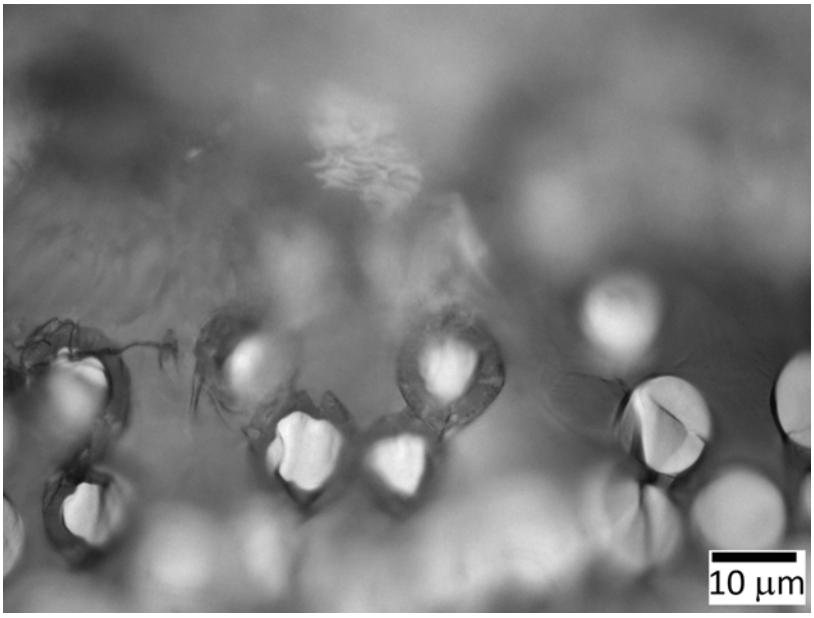


Figure 74. Optical micrograph of Hi-Nicalon^{TM} S fiber tow specimens subjected to creep in silicic acid-saturated steam at 800°C and 625 MPa.

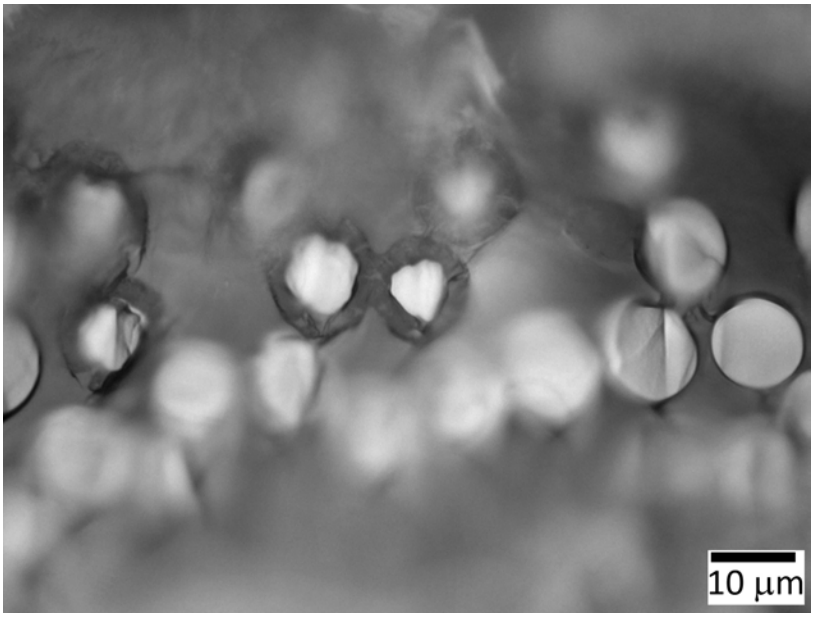


Figure 75. Optical micrograph of Hi-Nicalon^{TM} S fiber tow specimens subjected to creep in silicic acid-saturated steam at 800°C and 625 MPa.

Recall the "rogue" fibers discussed previously and shown in Figures 68 and 69. The surface morphology of these fibers is consistent with that of a thick crystallized scale. Though unclear at this time, it is possible that these are the same "rogue"

fibers seen in the SEM images. However, this phenomenon is not isolated to the present work. Ongoing studies of oxidation of Hi-Nicalon^{TM} S fiber tows by Hay at AFRL have also shown evidence of this phenomenon [198]. The AFRL tests were also conducted in silicic acid-saturated steam, based on the design developed for this research effort, with the key difference that specimens were not tested under load. All specimens were laid horizontally in a quartz tube and exposed to an oxidizing environment. Figures 76 and 77 are optical micrographs of specimens exposed to silicic acid-saturated steam for 100 hours. Note the similar ring of oxide and, in the 800°C specimens, similar fiber degradation. In these specimens, it was confirmed via TEM that the thick oxide was crystallized SiO_2 [198]. It was also observed that the other fibers had 1 - 2 nm of scale growth at most for the 700°C test specimens, with many having no measurable scale at all, and only nominally thicker scales at 800°C. Also of interest in the 800°C specimens is the evidence of the oxide wicking to one side of the fiber, leaving almost no oxide elsewhere. Though this was not captured in the limited optical and TEM images of specimens from the current work, SEM analysis did show fibers exhibiting the morphology of the "rogue" fibers on only one side or a limited portion of the fiber. An example of this can be seen in Figures B.91c and B.91d in Appendix B. This may be the same kind of wicking phenomenon, though the evidence is insufficient at this time to say definitively one way or the other.

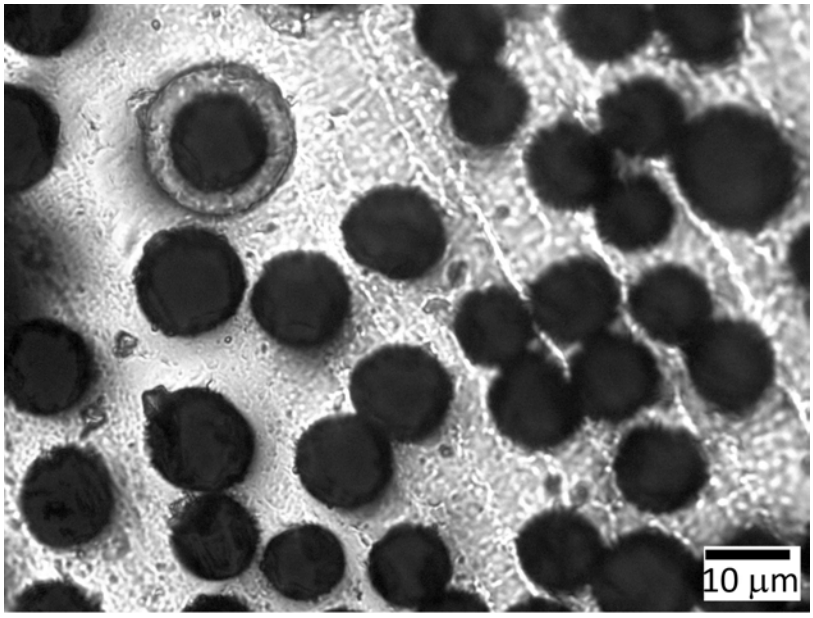


Figure 76. Optical micrograph of Hi-Nicalon^{TM} S fiber tow specimen subjected to oxidation for 100 h at 700°C [198], used with permission.

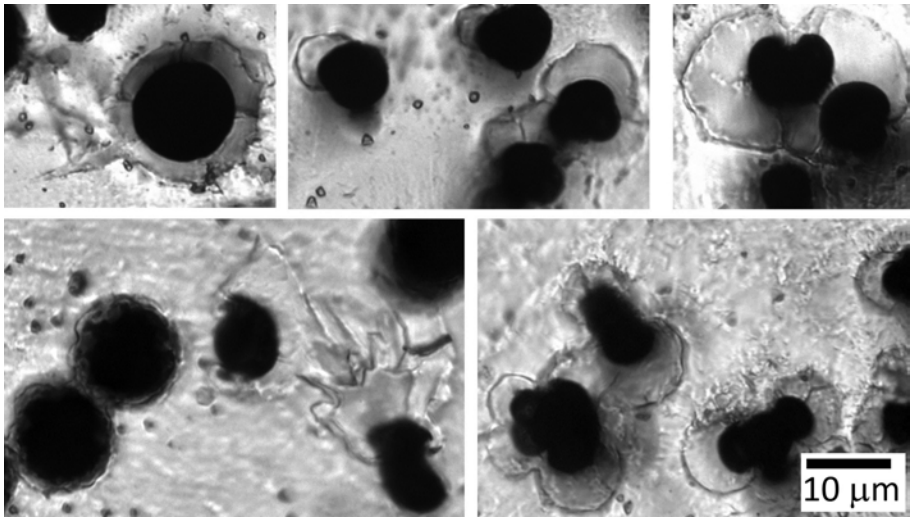


Figure 77. Optical micrograph of Hi-Nicalon^{TM} S fiber tow specimen subjected to oxidation for 100 h at 800°C [198], used with permission.

One possible explanation for this phenomenon is that the majority of the fibers did have a large crystallized scale growth, but it was lost prior to analysis. It is known that crystallization can cause large radial stresses in the scale, causing it to de-bond or separate from the surface of the fiber. It is also known that crystallized scale tends

to crack. It is possible that as the scale separated from the surface of the fibers, the flowing gaseous environment blew it off of the fibers. A fine dust found inside the test facility after testing may support this hypothesis, but there are several problems with it. Loss of the scale should expose the SiC more readily to the oxidizing environment. Therefore, one would expect the fibers without scale to be smaller than "rogue" fibers, yet they are similar size or smaller. It is possible that the scale happened to fall off right at the end of the test. This seems unlikely, especially since the same phenomenon is seen in two different test facilities, with separate procedures. While it is possible that specimen handling could be responsible for this, it is unlikely that handling would have so cleanly and preferentially removed scale and this does not account for the smaller, degraded "rogue" fibers. A more likely explanation is that the difference in the coefficient of thermal expansion between the fiber and the silica scale caused the scale to de-bond from the fiber during post-test cool down. However, one would expect to find a large amount of scale left behind in the test chamber, and this was not the case.

Another possibility is that these "rogue" fibers exhibit such oxidation because they are on the outside of the fiber tow and, therefore, have greater exposure to the oxidizing environment. These outer fibers might take more of the "brunt" of the effects of the oxidizing environment, protecting inner fibers. The presence of oxide scale growth on only one side of some fibers suggests that these were outer fibers, but more tightly packed so as to be exposed on one side and not so much on the other. However, this does not seem likely, either. If this were the case, one would expect a larger number of fibers to exhibit this morphology. Based on calculations of the area and circumference of the tow as compared to the diameter of the fibers, a tow of 500 fibers would have approximately 70 fibers making up the circumference of the tow, yet only a few of these were observed in each specimen.

Contaminants and inclusions are known to act as nucleation sites for scale growth, and have been seen to cause crystallization at temperatures below the normal for crystallization. The "rogue" fibers may have been been exposed to contaminants or developed inclusions during the manufacturing process, causing them to be preferentially susceptible to this crystalline oxide formation. This idea is supported by the observation that these "rogue" fibers appear in close proximity to one another within the fiber tow, as can be seen in Figures 72 through 75. Similar groupings were observed in SEM analysis.

Alternatively, contaminants may have been introduced during testing due to test conditions and or degradation of test equipment. If these "rogue" fibers are outer fibers, they were more readily exposed to these contaminants. Small amounts of contaminants introduced into the test chamber could come into contact with a few of the outer fibers, nucleating the crystallized oxide growth. However, as mentioned before, the "rogue" fiber phenomenon was observed in specimens from experiments conducted by Hay [198] as well as those from the current work. The test facility used by Hay employed all quartz tubing, whereas the test facility designed for this effort used all alumina tubing. Additionally, the two facilities used different models of steam generator. Another difference is that specimens used in Hay's experiments had the fiber tow sizing removed by boiling in de-ionized water, whereas sizing was not removed prior to testing in this work. These differences suggest that any contaminants introduced by the test facility and any associated effects would be unique to that test facility, yet the same phenomenon appears in both cases. One difference is that the "rogue" fibers of this work appear to be more degraded than those tested by Hay. This may be due to contamination from the sizing that burned off during heat up. In an effort to investigate this, EDS was conducted on some of the "rogue" fibers to determine their composition and identify any contaminants that may be present.

Spectrographs of the rough crystalline surface confirmed that the scale was silica but did not show significant amounts of any possible contaminants. Figure 78

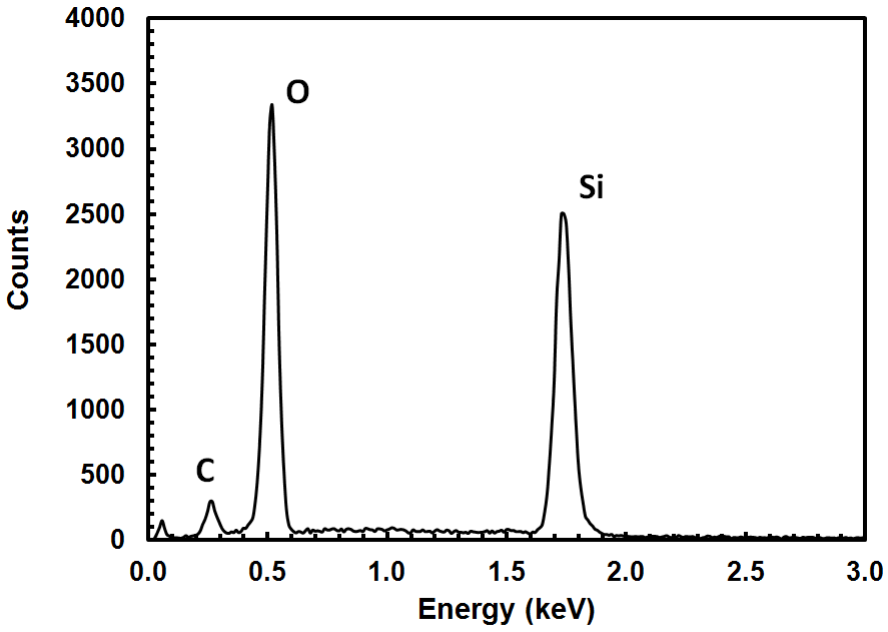


Figure 78. Energy dispersive spectrograph of the surface of "rogue" fiber from a Hi-Nicalon^{TM} S SiC fiber tow specimen subjected to the saturated steam environment at 800°C and to a load of 450 MPa (65.3 ksi). The composition is representative of all EDS conducted on this morphology and is consistent with significant oxidation of the fiber to form a silica scale. The content was 42.86% silicon, 10.68% carbon, and 45.81% oxygen by atomic percent.

At 800°C and about 1 atm, the conditions for the tests conducted in this research and in that of Hay, the formation of such a crystallized scale is unusual in air, but not in steam. Under steam environments at these conditions, published phase data for silica in the presence of water indicates that any silica formation should be in the form of quartz, a crystallized silica. Therefore, it is likely that the scale noted on the "rogue" fibers is quartz. This phase data was gathered from Tuttle and England [201] and is depicted in Figure 79. Note that the conditions for this testing are fairly close to the transition to tridymite, another crystallized scale, making that a secondary possibility.

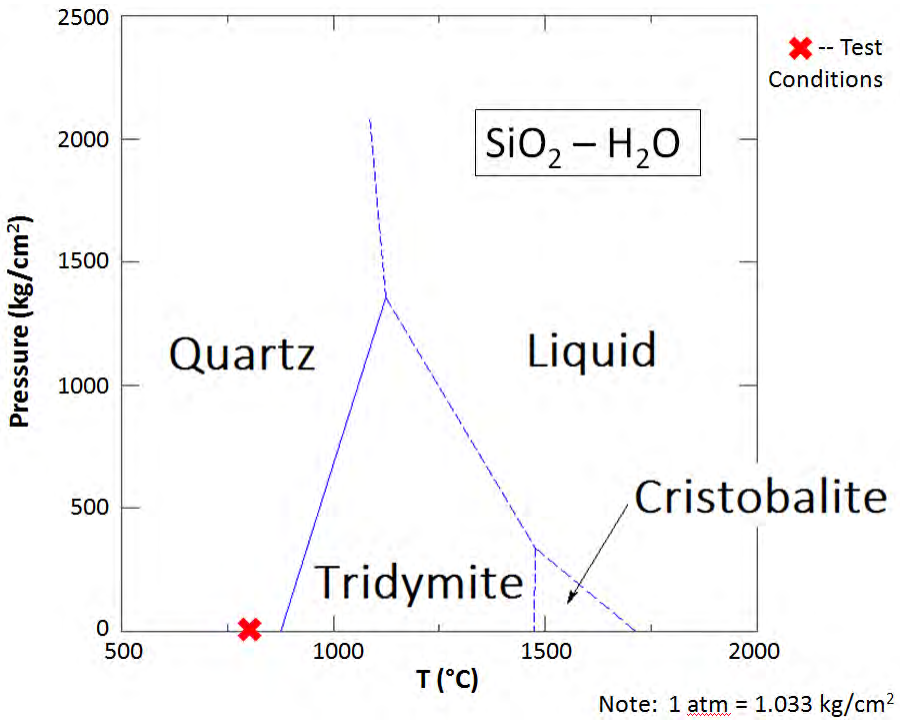


Figure 79. Phase Diagram for silica formation in a water environment. Note the red X depicting the test conditions during this research effort. Data reproduced from [201].

As mentioned in Chapter 2, Opila [152, 157] studied the effects of water vapor partial pressure on the oxidation of SiC. Recall that the experiments were conducted H_2O/O_2 and H_2O/Ar environments with 10-90 vol% water vapor and a total pressure of 1 atm. It was found that oxidation rates increased with increased water vapor partial pressure. Opila also found that an equilibrium point existed at which the rate of formation of the silica oxide equals the rate of volatization, causing the scale thickness to become constant. It is thought that quartz, tridymite, and cristobalite have similar values of equilibrium partial pressure. If, in fact, the equilibrium partial pressures are significantly different, especially between the amorphous quarts and its crystallized counterparts, another possible explanation for the "rogue" fiber emerges. Assuming the equilibrium partial pressures are different, it is possible that the quartz which was expected to form at 800°C had reached the equilibrium point very early, resulting in the thin scales, while the crystalline scale, nucleated by a contaminant or

inclusion, formed and grew on the "rogue" fibers because the environment was not at its equilibrium partial pressure. Figure 80 shows the equilibrium partial pressure of $Si(OH)_4$ over various morphologies of solid SiO_2 in a water vapor environment based on data from Jacobson et al [202] and prepared by Mogilevsky [203]. This data is applicable to the test facility used by Hay, with its quartz tubing, and would be different for the current work due to the use of alumina tubing. It is noteworthy that the equilibrium partial pressures are not significantly different.

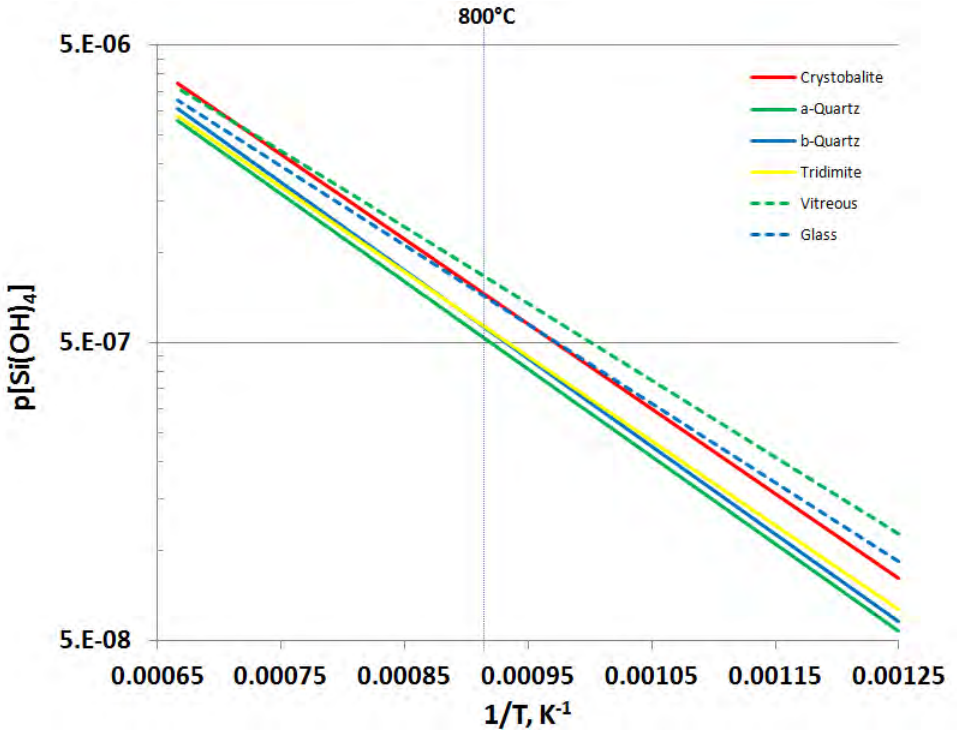


Figure 80. Equilibrium partial pressures of silicic acid in steam over various morphologies of silica. Data reproduced from [202] by Mogilevsky [203].

These hypotheses are complicated by the fact that in the current work, tests were conducted in 100% water vapor saturated with silicic acid. This is a different chemical environment, with different reactions, from those studied by Opila and others and reported in literature. The chemical reaction $SiO_2+H_2O \longrightarrow Si(OH)_4$ takes place inside the pre-heater chamber prior to delivery of the steam to the test chamber and exposure of the SiC fiber tow, in contrast to the work by Opila, in which the reaction

took place within the test chamber. As a result, the work by Opila is instructive, but these differences make it challenging to gain a clear picture of what should be expected. For these reasons, further investigation of this "rogue" fiber phenomenon and the associated chemical reactions ought to be pursued in future work.

VI. Conclusions and Recommendations

6.1 Summary

Aerospace structural materials are designed for use under very challenging conditions including large and dynamic stresses, high temperatures, harsh environments, and long service periods. These materials must have excellent mechanical properties and be capable of maintaining these properties under these conditions. As structural metal alloys have reached the limits of their capabilities, the future appears to be in CMCs, and this future appears very bright. It is anticipated that the use of CMCs in aerospace applications will result in significant weight savings, increased efficiency and capability of engines, reduce harm to the environment, and make attainable capabilities that currently are not, such as hypersonic aircraft. These benefits will result in an improvement in cost, performance, and lifetime of aerospace applications.

CMC development has been and continues to be driven by the desire to harness the positive attributes of ceramics while limiting or eliminating the drawbacks. In particular, designers would like to capture the high strength, creep resistance, and temperature capabilities of ceramics while still maintaining the graceful failure of metal alloys, rather than the typical sudden catastrophic failure common to ceramics. To accomplish this, CMCs must be developed that exhibit superior toughness, damage tolerance, and graceful modes of failure. CMCs must also maintain these characteristics at high temperatures and in harsh, oxidizing environments. Thermodynamic stability and oxidation resistance are vital issues. SiC fibers and CFCCs have shown superior strength, creep resistance, high temperature capabilities, toughness, damage tolerance, and graceful modes of failure, making them an attractive alternative to metal super-alloys. However, SiC CMCs have shown poor oxidation resistance, made significantly worse by the presence of water. In order to improve

the performance of SiC CMCs, the performance of the constituents must first be improved. Methods such as environmental barrier coatings Environmental Barrier Coating (EBC) applied to fibers are being developed to mitigate the oxidation problem, but these solutions can only succeed based on a thorough knowledge of the damage and failure mechanisms of these constituents.

This research effort delivered the only known facility for testing creep of SiC fiber tows in steam and silicic acid-saturated steam. It solved the facility and methodology problems identified in preliminary efforts to study SiC fiber tows, making meaningful creep data obtainable. Using this facility, the creep performance of Hi-Nicalon^{TM} S SiC fibers in air and in steam at elevated temperatures was investigated. This effort added to the incomplete body of knowledge regarding the damage and failure mechanisms of SiC fibers operating under a combination of mechanical load, high temperature and oxidizing environment and paved the way for future testing of SiC fiber tows. This knowledge enables designers to develop CMCs that meet the current and future needs of aerospace applications.

6.2 Conclusions

A unique facility and methodology were developed to conduct creep and tensile tests of fiber tows at temperatures up to 1000°C in preheated steam saturated with silicic acid, as well as in unsaturated steam and in dry air. The challenges of chemical and temperature control of the steam environment identified in preliminary SiC test efforts were overcome. Chemical variability due to test methodology was eliminated, resulting in oxidation effects being independent of location within the test chamber. Steam was successfully preheated to test temperature and saturated prior to introduction into the test chamber. As a result, meaningful, repeatable test results were obtained. The effects of silicic acid-saturated steam on the mechanical performance

of Hi-Nicalon^{TM} S SiC fiber tows were studied. Creep and monotonic tension tests were conducted in air and in silicic acid-saturated steam at 800°C and compared with previous tests conducted in steam to elucidate the performance of the fiber tows.

Creep results revealed that silicic-acid saturated steam had a degrading effect on the creep lifetime and steady-state creep rate, as compared to air. However, the degrading effect was much less pronounced than tests previously conducted in steam that was not preheated and saturated. Creep lifetimes were an order of magnitude lower for a given stress level in silicic acid-saturated steam than in dry air, but an order of magnitude higher than creep lifetimes in unsaturated, unheated steam. Likewise, creep rates were an order of magnitude higher in silicic acid-saturated steam than in dry air, but an order of magnitude lower than creep rates in unsaturated, unheated steam. Also, Hi-Nicalon ^{TM} S fiber tows exhibited five times the load carrying capacity in silicic acid-saturated steam as in unsaturated, unheated steam. This is a direct result of the uniform oxide layer sealing the surface of the fiber. Load carrying capacity in silicic acid-saturated steam was two-thirds that of fiber tows tested in dry air, as measured by the highest stress at which the fiber tows attained creep run-out. As discussed in chapter four, there are other possible explanations for the behavior referred to herein as creep. If it truly is creep, then the stress exponents for air and silicic acid-saturated steam were determined to be $n \approx 5$ for air, indicating climb-controlled dislocation creep as the driving creep failure mechanism in air, and $n \approx 4$ for silicic acid-saturated steam, indicating a creep failure mechanism of grain boundary sliding with cavity nucleation and growth. However, little evidence of cavity nucleation and growth was seen in SEM images of fracture surfaces. Further microstructural analysis is required to definitively say what the dominant failure mechanism is. The Monkman-Grant relationship was shown to be applicable to Hi-Nicalon ^{TM} S fiber tows, successfully predicting creep lifetime of the fiber tows.

Though lack of data in the literature for CMCs reinforced with Hi-Nicalon ^{TM} S fiber tows precluded a determination on the use of the Monkman-Grant relationship to predict creep lifetimes of these CMCs, it possible that such predictions could be successful, and limitations were discussed.

The results of monotonic tensile tests showed that the ultimate tensile strength of Hi-Nicalon ^{TM} S fiber tows had little to no dependence on stress rate at 800°C. Subcritical crack growth parameters were calculated from the experimental results of these tensile tests and a linear-elastic fracture mechanics model was used to predict creep lifetimes. Though the model successfully predicted the sharp transition from fast fracture to creep run-out seen in the experimental creep data, it underpredicted the creep lifetimes of Hi-Nicalon ^{TM} S fiber tows in both air and silicic-acid saturated steam. This underprediction, and the lack of stress rate-dependency, are evidence that subcritical crack growth is not the governing failure mechanism for Hi-Nicalon ^{TM} S fiber tows, though it may contribute somewhat. This is consistent with literature.

Scale thicknesses were measured for a limited set of specimens using images obtained via transmission electron microscopy. Scales were found to be approximately half those found in previous testing of Hi-Nicalon ^{TM} S fiber tows. This is due to the saturating of the steam with silicic acid prior to fiber tow exposure, which eliminated the variations along the length of the fiber tow, and to the passivating effect of the now uniform amorphous oxide layer.

6.3 Contributions

Mechanical testing of SiC fiber tows in steam at elevated temperatures is not a trivial matter. Control of the temperature and containment of the corrosive high-temperature steam are problematic. The unique test facility and methodology developed in this effort successfully controlled and contained the steam to provide a

steam environment with preheated and silicic acid-saturated steam up to 1000°C for mechanical testing of SiC fiber tows, while also providing unsaturated steam and dry air options. Previous work with steam did not preheat or saturate the steam. This is the first and only known test facility to achieve this.

Previous testing in unheated, unsaturated steam produced inconclusive results due to problems with contamination, temperature control, and test methodology that resulted in variability within each test specimen based on location within the test chamber [1, 23]. As a result, creep results were suspect and inconsistent. This research effort developed a new methodology, successfully reducing contamination and eliminating the variability. Consequently, test results were more consistent and repeatable, making test data more reliable.

Furthermore, testing in silicic acid-saturated steam has produced very promising results. It is significant that fiber tows tested in steam saturated with silicic acid showed significantly less creep, lower creep rates and more than five times the load carrying capacity at creep run-out than any previous test in unsaturated steam. This study shows that SiC fiber tows are much less susceptible to damage due to oxidation and to subcritical crack growth when exposed to silicic-acid saturated steam. This is due to the fact that the steam is already saturated with silicic acid, so it does not leech the silicon from the fiber tows and actively degrade them. Instead, a thin passivating layer of silica is formed which slows oxidation. Since the performance of a CMC is largely dependent on the performance of the reinforcing fibers, this suggests that a silicon-rich matrix in a CMC, like a SiC-SiC CMC, would be ideal for reducing the effects of oxidation on the reinforcing fibers, prolonging the life and structural integrity of the CMC. This study shows that when the surface of the fibers is protected from the active oxidizing species in steam, the properties are very close to those in air.

This effort determined the stress rate dependency of the failure stress of Hi-Nicalon^{TM} S fiber tows in dry air and in silicic acid-saturated steam and calculated slow crack growth parameters for these environments. This has not been extensively investigated in air and has not been done in any steam environment. This is the first study to produce the slow crack growth parameters in air or in any steam environment.

The use of the Monkman-Grant relationship for creep lifetime predictions of fiber tows and CMCs has been widely explored, but has not been investigated for Hi-Nicalon^{TM} S fiber tows or CMCs reinforced with them. In this study, the Monkman-Grant relationship was shown to apply to Hi-Nicalon^{TM} S fiber tows and agree well with published work on similar fibers. This work is the first to investigate the Monkman-Grant relationship for Hi-Nicalon^{TM} S fiber tows. This will allow future efforts to avoid long-duration creep testing of fiber tows by applying the Monkman-Grant relationship to predict the results of such tests. This may also be possible for CMCs reinforced with Hi-Nicalon^{TM} S fiber tows, but the application to CMCs is problematic for the reasons discussed.

6.4 Recommendations for Future Work

There are multiple aspects of this body of work that can be investigated further. Each of these areas should be pursued in future work:

- Oxidation of Hi-Nicalon^{TM} S non-oxide SiC fiber tows at temperatures in the range of 400 - 700°C
- The effects of silicic acid-saturated steam on strength and creep performance of Hi-Nicalon^{TM} S fiber tows at temperatures greater than 800°C, as well as oxidation of the fibers at higher temperatures

- The effects of sizing (a byproduct of manufacturing that coats the fiber surface) on the creep performance of Hi-Nicalon^{TM} S fiber tows at elevated temperatures
- Evaluate and guide the Deal-Grove oxidation kinetics model for use with SiC fibers using post-test microstructural examination and analysis
- Investigate the "rogue" fiber phenomenon of limited but thick crystallized scale growth
- The effects of silicic acid-saturated steam on SiC fiber-reinforced CMCs

6.4.1 Oxidation at Lower Temperatures.

Current manufacturing techniques for SiC fibers tows and SiC-based CMCs include processing at temperatures in the range of 400 - 800°C. It is also known that oxidation can cause significant degradation of SiC fibers in this temperature range. Much work has been done in wet and dry air to characterize the oxidation kinetics of SiC fibers in this temperature range. For comparison with the body of work to date, conducting tests in silicic acid-saturated steam in the range of 400 - 700°C could provide greater inside into the oxidation kinetics of SiC fiber tows and guide the development of future manufacturing and processing methods for fiber tows and SiC-based CMCs.

6.4.2 Creep and Oxidation at Higher Temperatures.

The investigation into the behavior of Hi-Nicalon^{TM} S fiber tows at elevated temperature should be continued by conducting creep tests at higher temperatures such as 900-1200°C. The test facility has been shown to be capable of producing steam and silicic acid-saturated steam at temperatures up to 1000°C. It is likely that the facility is capable of temperatures higher than that without significant alteration. The

CX1300 heaters are capable of reaching temperatures up to 1500°C. The alumina tubing and the test chamber furnace are both capable of temperatures well above that. One possible challenge is that silica begins to soften at about 1300°C and melt at about 1600°C. Testing above 1300°C may experience difficulties with the silica wool flowing or partially melting and pooling. This would reduce surface area of the wool and possibly reduce the ability to completely saturate the steam.

Additionally, most of the body of work in literature that investigated the Monkman-Grant relationship for SiC fiber tows was done in the range of 1100 - 1300°C [46, 191, 196, 197]. Further work at higher temperatures would enable a more direct comparison of the Monkman-Grant relationship for Hi-Nicalon^{TM} S fiber tows with the larger body of work.

6.4.3 Removal of Sizing.

Hi-Nicalon^{TM} S fiber is coated by the manufacturer with a polyvinyl alcohol (PVA) sizing to reduce damage to the fibers during handling. PVA is a synthetic polymer resin with a chemical formula of $[CH_2CH(OH)]_n$. It is a common textile coating and is water soluble. Sizing typically burns off at temperatures in the range of 200-500°C in argon or air [116], such that it is not present during tests at elevated temperature. In the previous work of Steffens [1] and Shillig [23], it was assumed that the sizing burned off during the temperature ramp up and heat soak prior to application of the load for creep testing. However, microstructural investigation showed some evidence of contamination, possibly due to products of the sizing burn off.

In order to determine the effect of the sizing and its possible contribution to these observed contaminants, tests should be conducted on fiber tows with and without sizing. Tests would be conducted on fiber tows with sizing, as in previous efforts, while others would be conducted on desized fiber tows. Sizing can be removed by

boiling in de-ionized water [153, 155]. It is also possible to burn off the sizing in an inert atmosphere, namely argon, prior to testing. Both methods should be thoroughly investigated.

6.4.4 Oxidation Kinetics Model.

Only preliminary results were available at the completion of this study, which were insufficient to confidently determine the linear and parabolic rate constants used to model oxidation kinetics. Further analysis of the test data and that of tests in the temperature ranges recommended above would provide greater insight into how well the Deal-Grove model predicts oxidation of SiC fibers in silicic acid-saturated steam. Although it is possible to calculate the Deal-Grove linear and parabolic rate constants from short and long-term scale thickness data, additional data from different temperatures would enable the calculation of activation energies as well. Also the linear and parabolic rate constants could be determined with greater confidence from a larger body of data and the model predictions compared with the experimental data.

6.4.5 "Rogue" Fiber Phenomenon.

An unexplained phenomenon of thick crystallized scale growth was observed on a very small percentage of the fibers in most fiber tow specimens. This phenomenon should be investigated further. Samples of the saturated steam could be collected and analyzed to determine chemical composition, verify saturation, and identify contaminants, if any. Additionally, tests at different partial pressures of silicic acid could be conducted to determine whether there is a correlation between the appearance of the "rogue" fibers, the thickness and structure of the crystallized scale, and the partial pressure. Lastly, a thorough examination of the "rogue" fibers could be conducted

via SEM and TEM to identify differences from other fibers in chemical makeup and determine the presence, if any, of inclusions or contaminants.

6.4.6 SiC Fiber-Reinforced CMCs.

A next logical step is to investigate the behavior of CMCs reinforced with Hi-Nicalon^{TM} S fiber tows, particularly SiC-SiC CMCs. As mentioned earlier, it is thought that steam moving along a crack in a CMC with a silicon-based matrix would become saturated with silicic acid prior to reaching the reinforcing fibers. Conducting tests in air, steam saturated with silicic-acid, and unsaturated steam would provide great insight into the efficacy of this idea. For example, if results were similar in saturated and unsaturated steam, it would indicate that this thought process may be correct. These results could be compared with those of SiC fiber-reinforced CMCs with an oxide matrix, also. CMCs with an oxide matrix would not saturate with silicic acid, providing yet another comparison. Creep performance and oxidation of these CMCs in silicic acid-saturated steam should be investigated.

Appendix A. Effective Gauge Lengths

A.1 Air

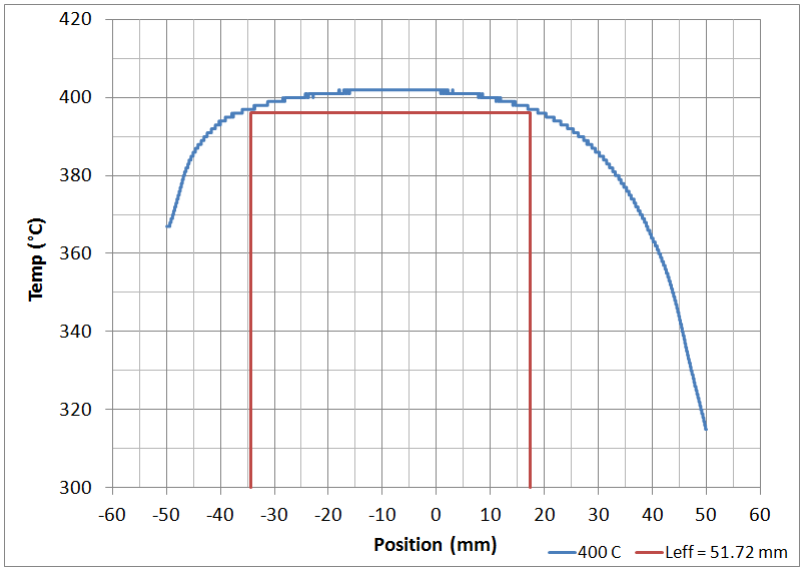


Figure A.1. Effective gauge length and temperature profile in Air for $400°C$.

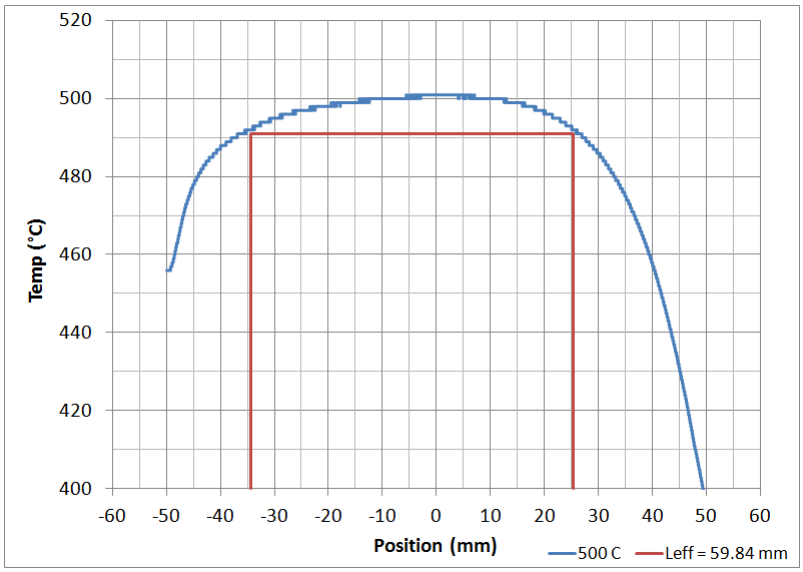


Figure A.2. Effective gauge length and temperature profile in Air for $500°C$.

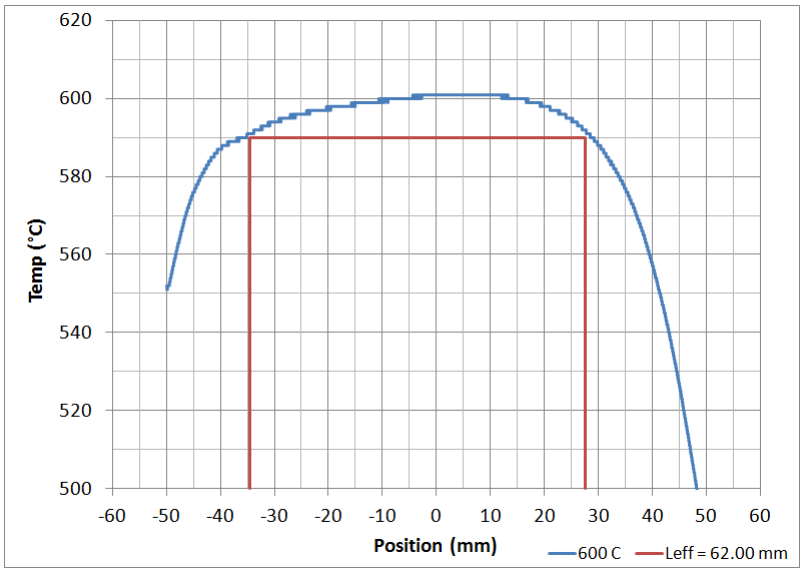


Figure A.3. Effective gauge length and temperature profile in Air for 600°C.

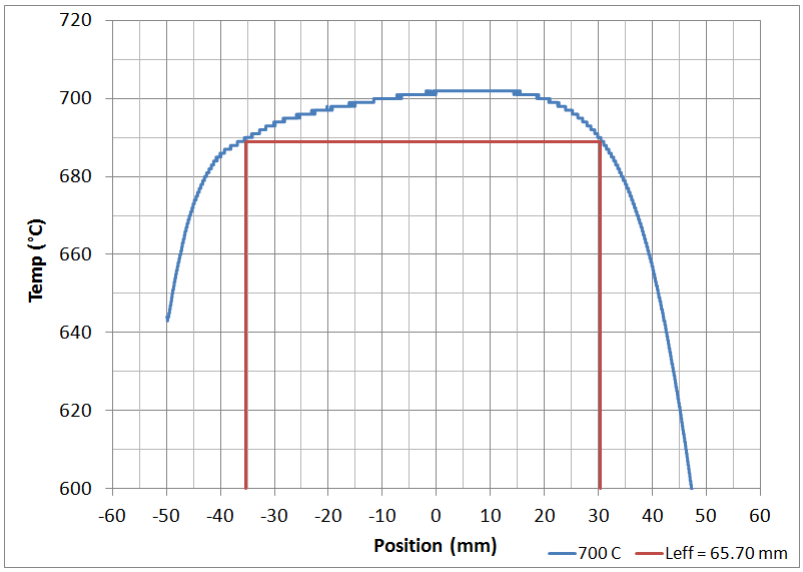


Figure A.4. Effective gauge length and temperature profile in Air for 700°C.

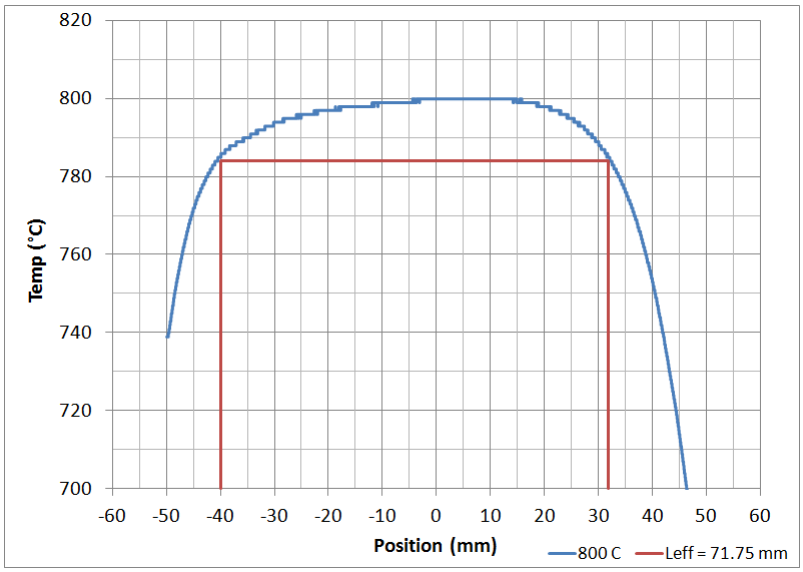


Figure A.5. Effective gauge length and temperature profile in Air for 800°C.

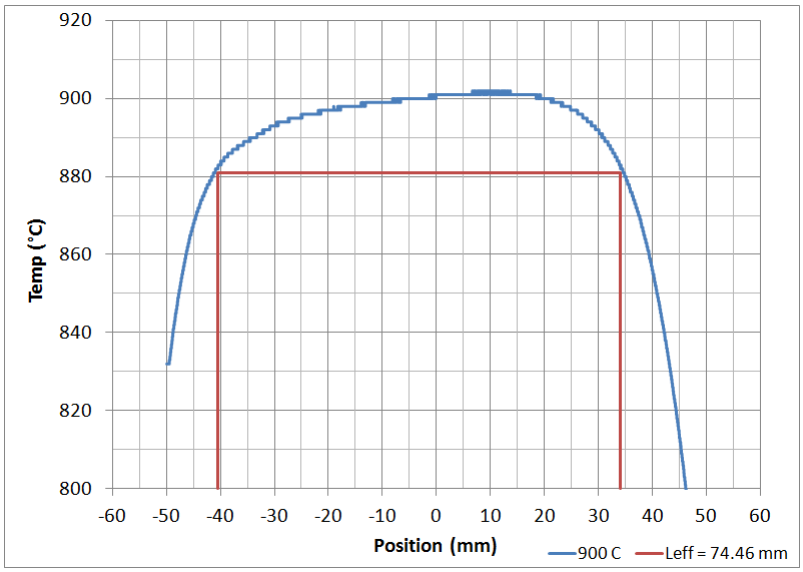


Figure A.6. Effective gauge length and temperature profile in Air for 900°C.

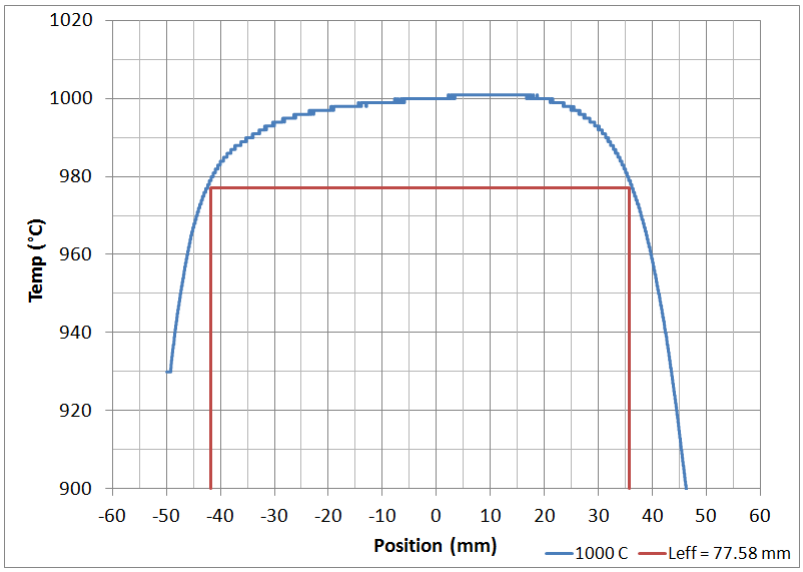


Figure A.7. Effective gauge length and temperature profile in Air for $1000°C$.

A.2 Steam

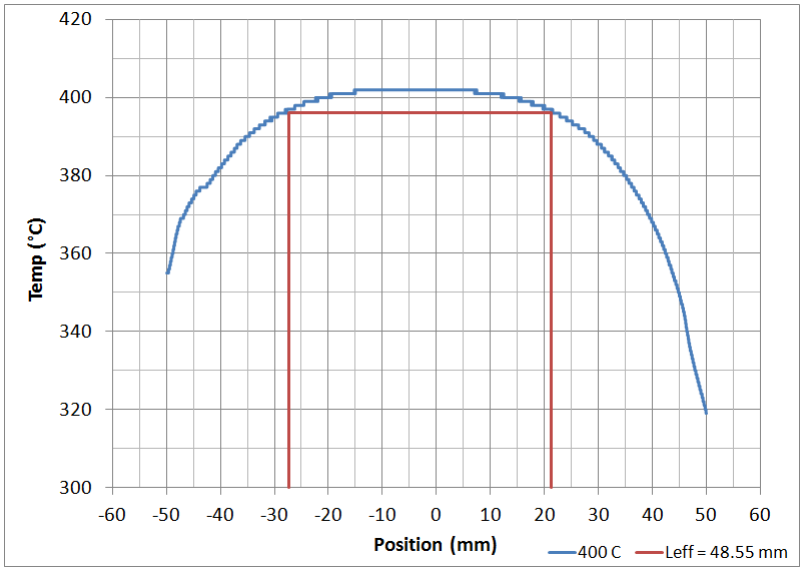


Figure A.8. Effective gauge length and temperature profile in silicic acid saturated steam for $400°C$.

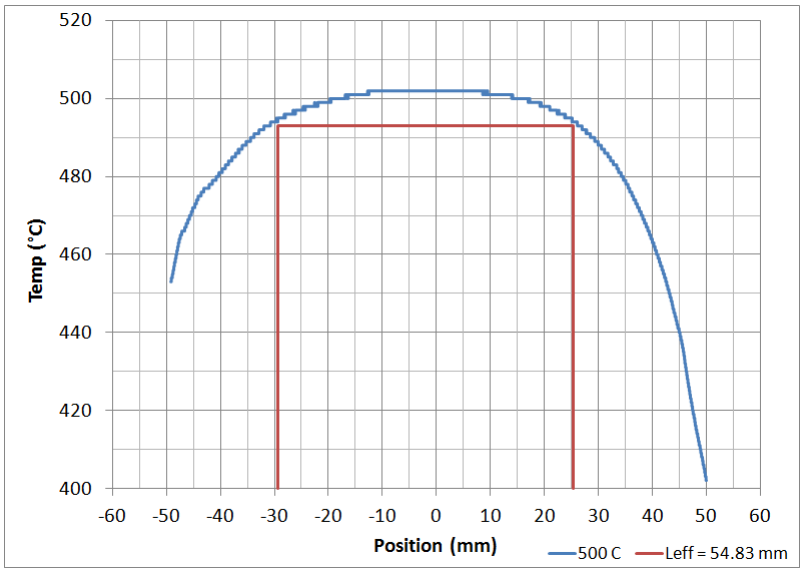


Figure A.9. Effective gauge length and temperature profile in silicic acid saturated steam for $500°C$.

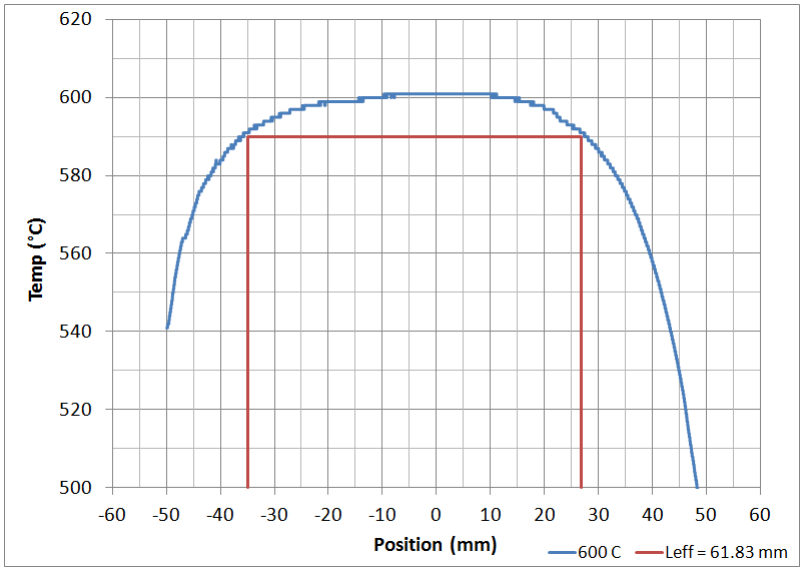


Figure A.10. Effective gauge length and temperature profile in silicic acid saturated steam for $600°C$.

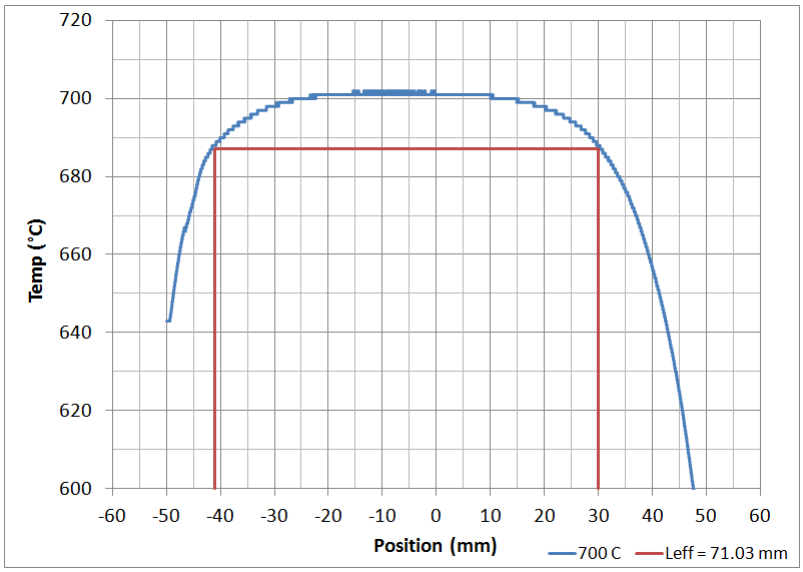


Figure A.11. Effective gauge length and temperature profile in silicic acid saturated steam for 700°C.

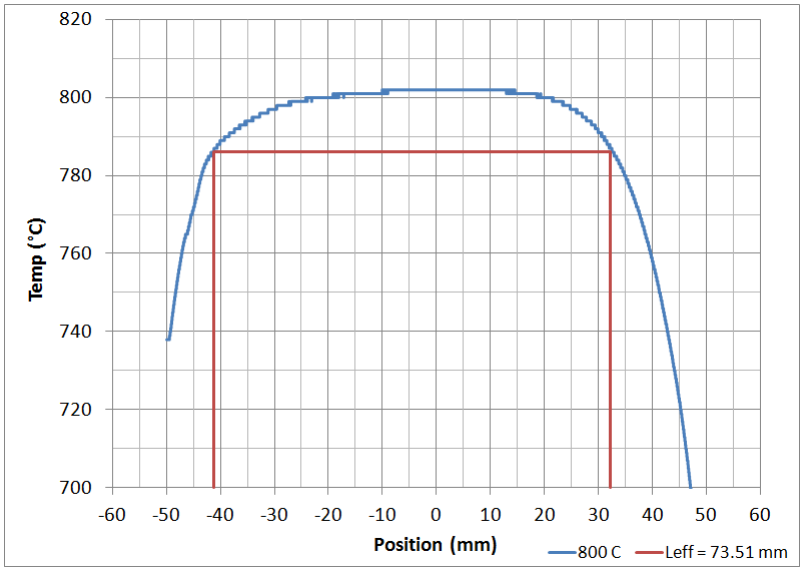


Figure A.12. Effective gauge length and temperature profile in silicic acid saturated steam for 800°C.

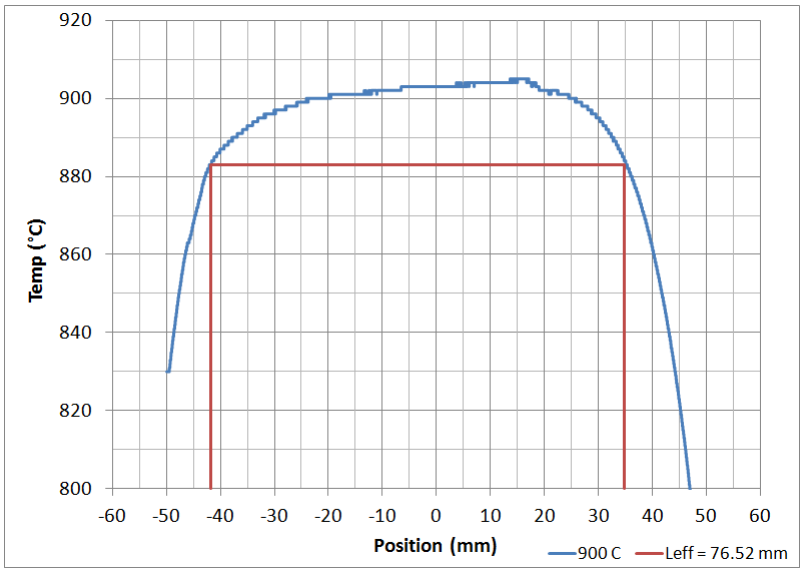


Figure A.13. Effective gauge length and temperature profile in silicic acid saturated steam for 900°C**.**

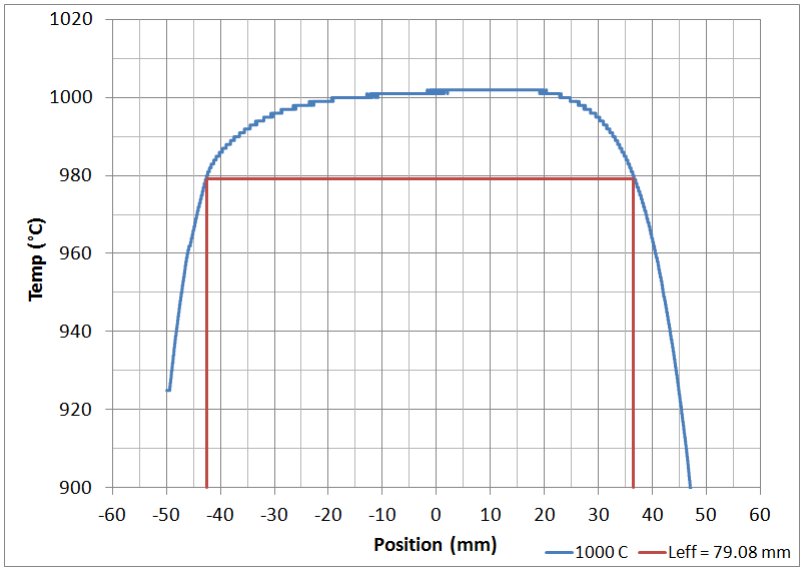
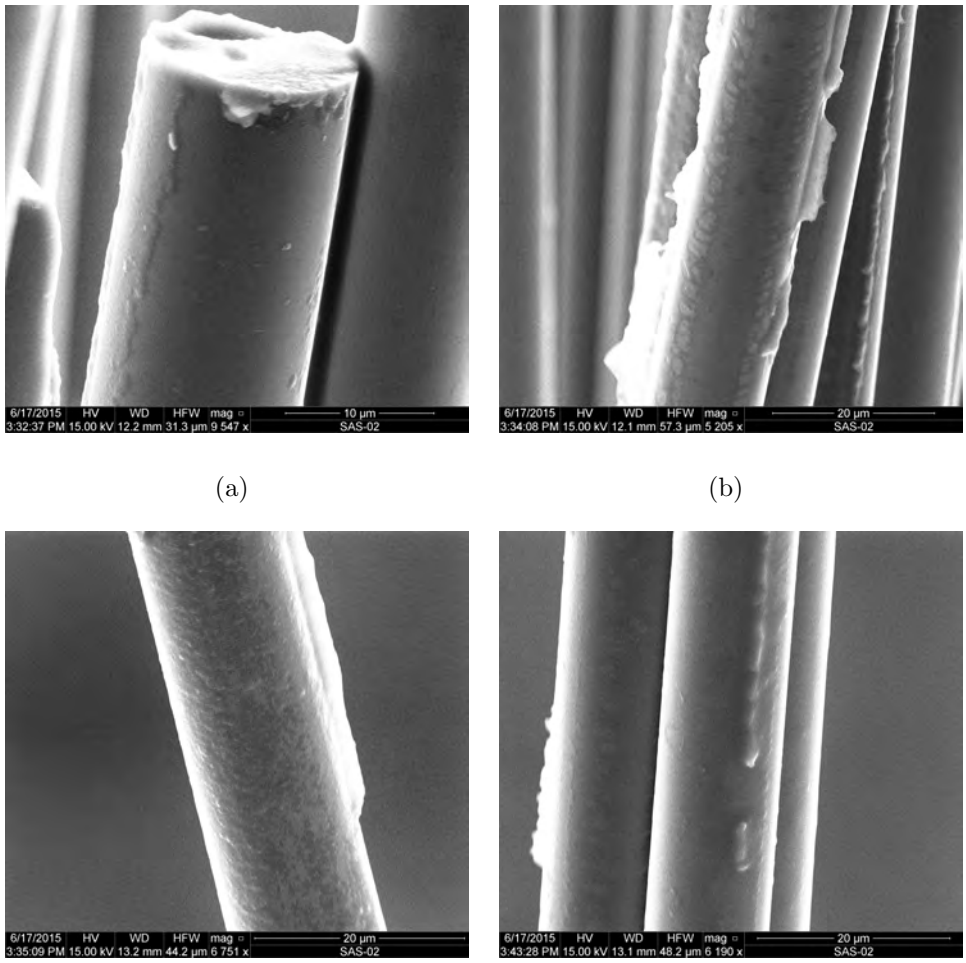


Figure A.14. Effective gauge length and temperature profile in silicic acid saturated steam for 1000°C**.**

Appendix B. SEM Images

B.1 Air



(a) (b)

(c) (d)

Figure B.1. Hi-Nicalon^{TM} S fiber tow untested specimen

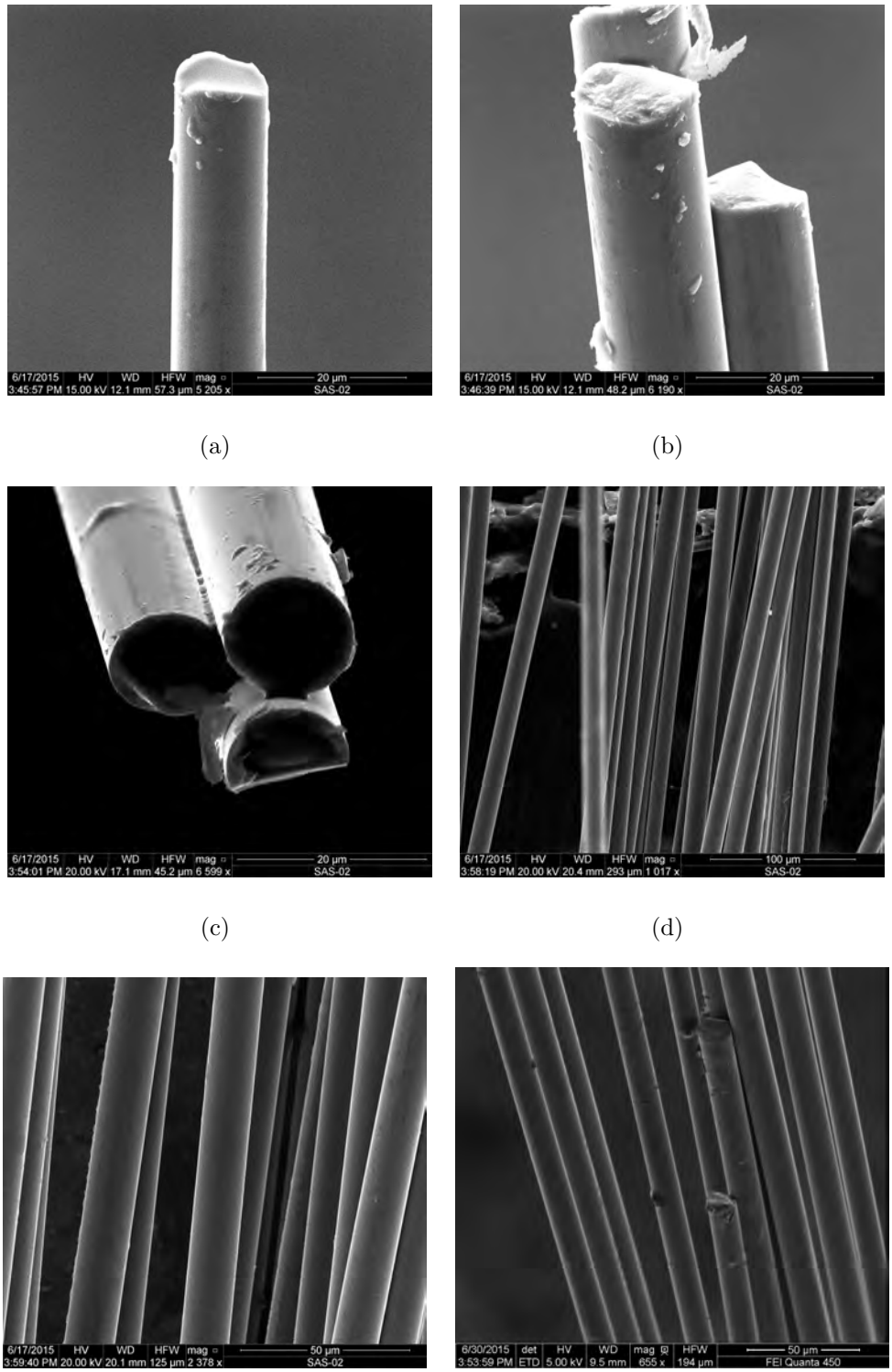
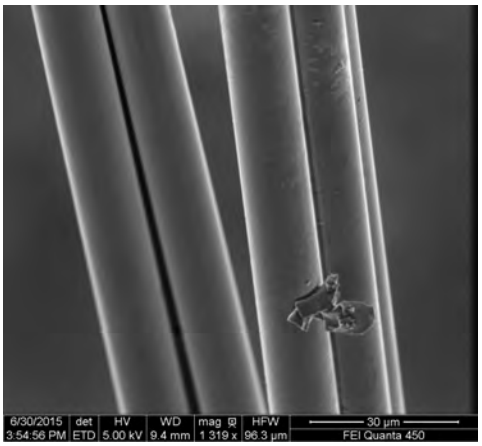
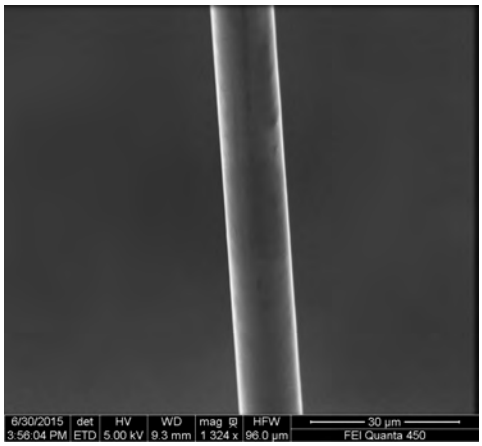


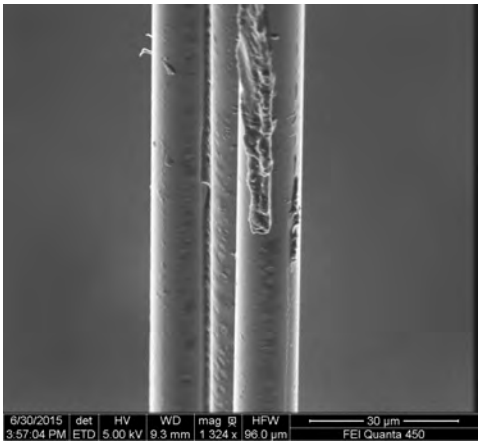
Figure B.2. Hi-Nicalon^{TM} S fiber tow untested specimen



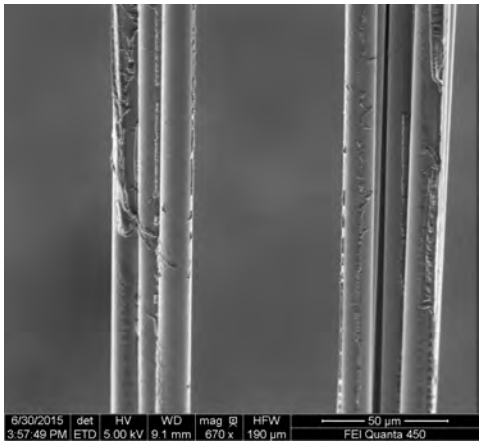
(a)



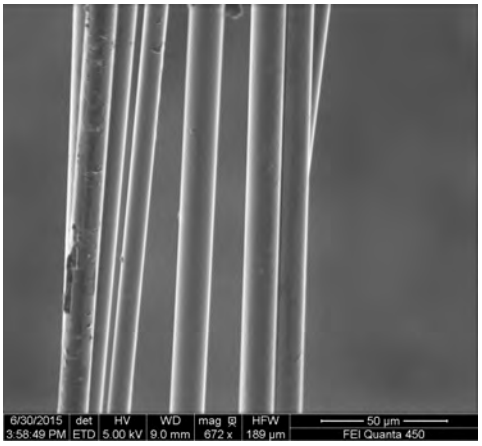
(b)



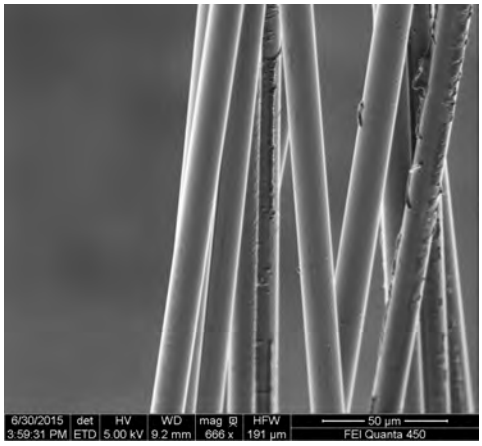
(c)



(d)

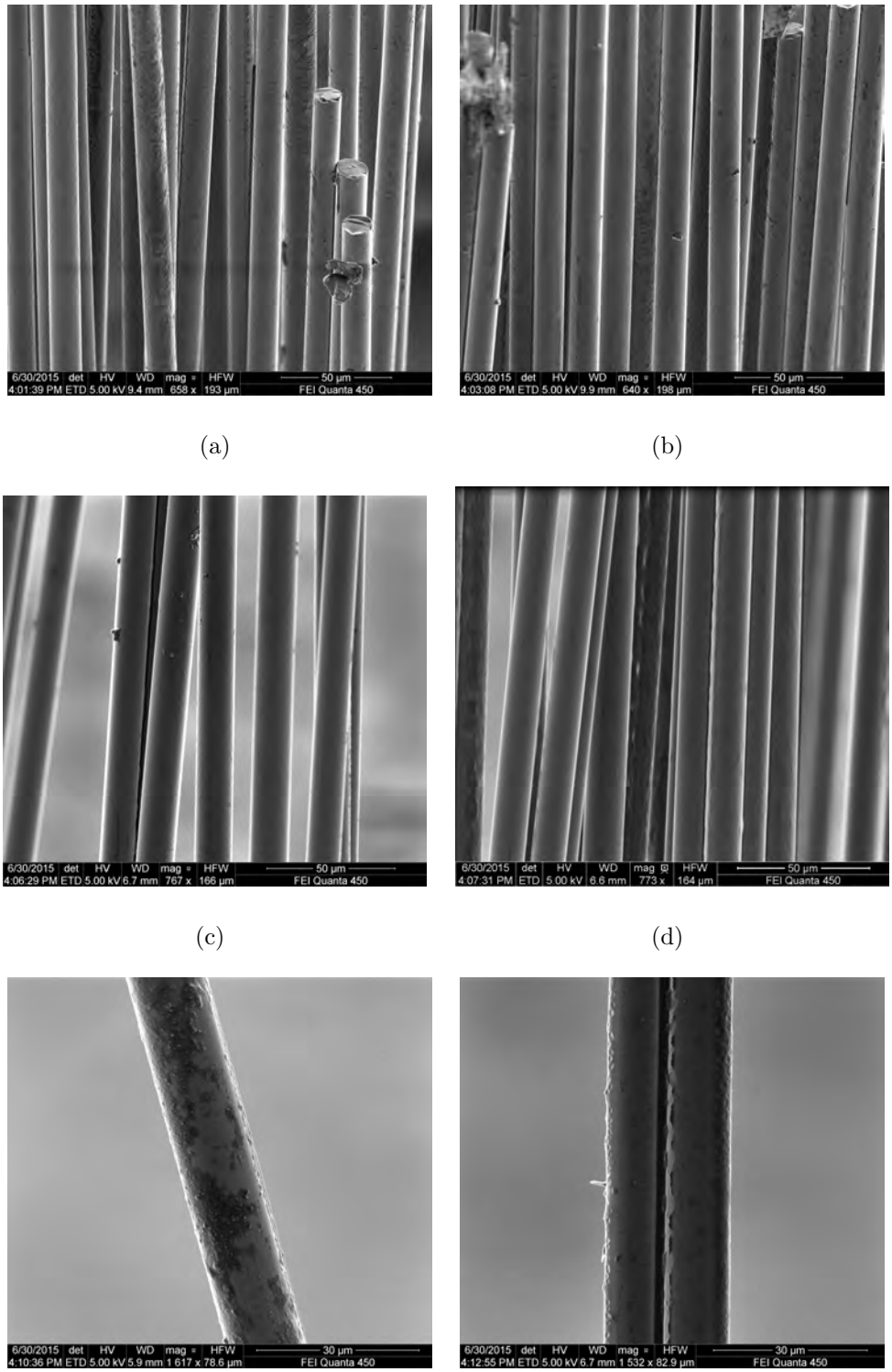


(e)



(f)

Figure B.3. Hi-Nicalon^{TM} S fiber tow untested specimen

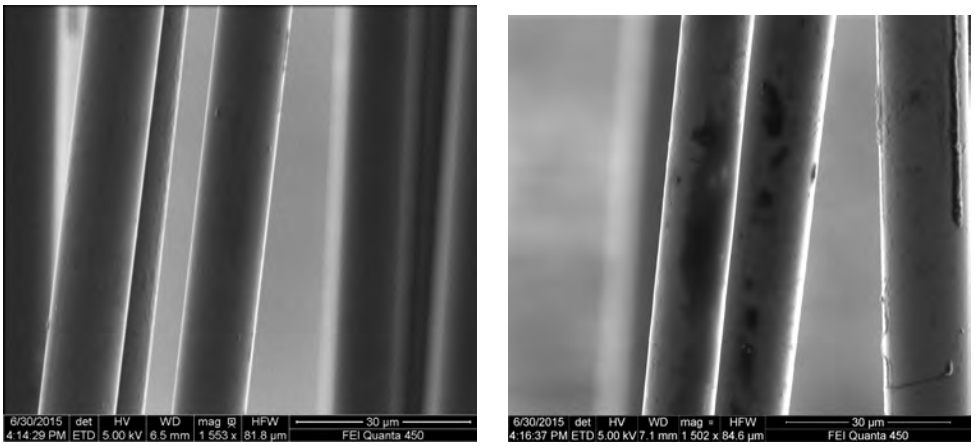


(a) (b)

(c) (d)

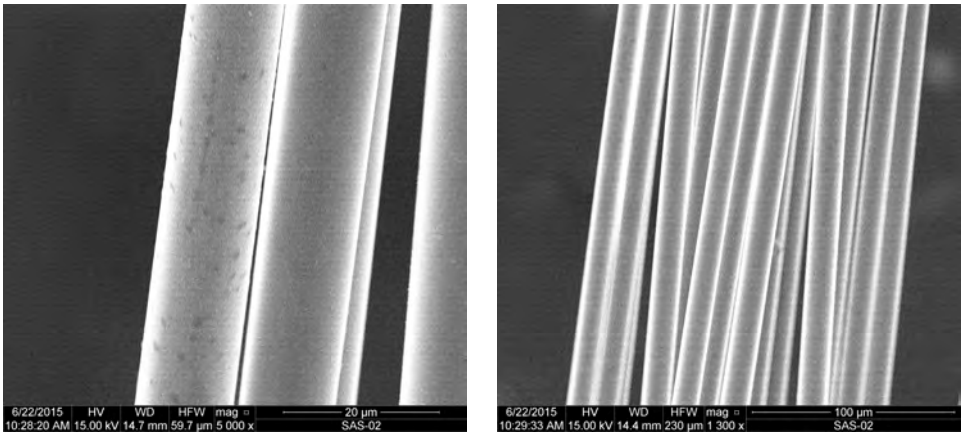
(e) (f)

Figure B.4. Hi-Nicalon^{TM} S fiber tow untested specimen



(a) (b)

Figure B.5. Hi-Nicalon^{TM} S fiber tow untested specimen



(a) (b)

Figure B.6. Hi-Nicalon^{TM} S fiber tow specimen A12, center section, (800°C, σ = 937 MPa, t = 84.3 h)

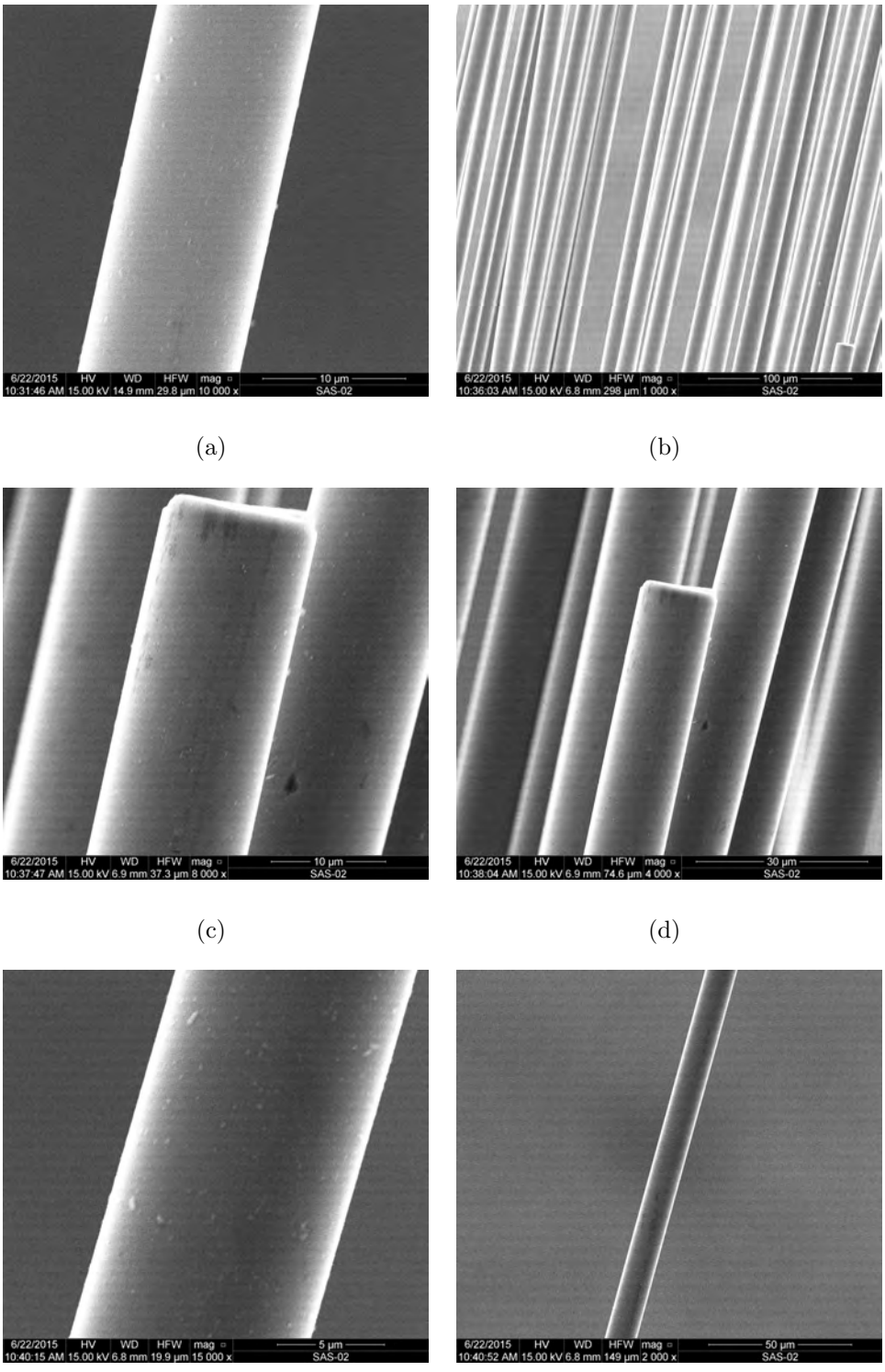
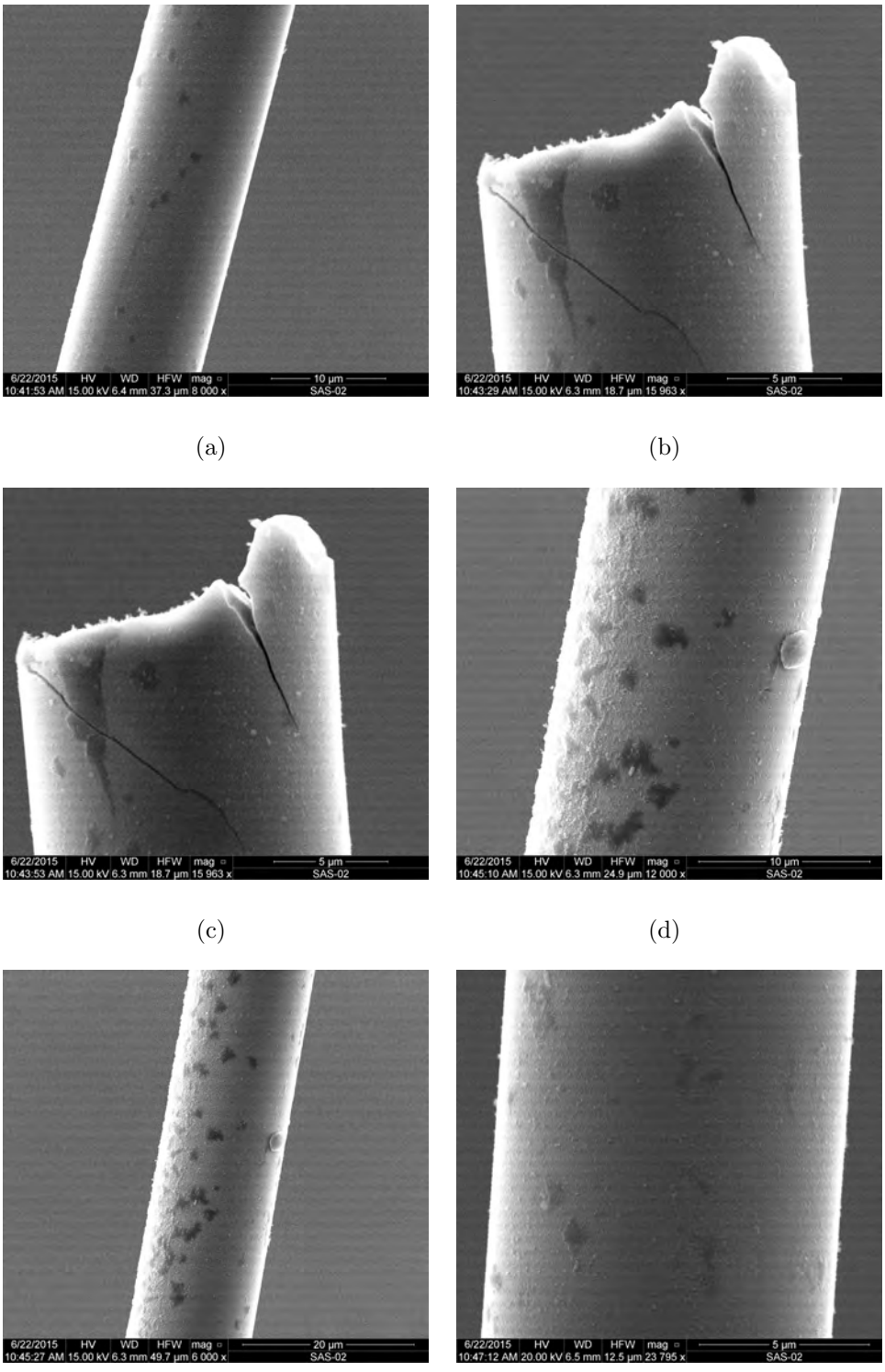


Figure B.7. Hi-Nicalon^{TM} S fiber tow specimen A12, center section, (800°C, σ = 937 MPa, t = 84.3 h)



(a) (b)

(c) (d)

(e) (f)

Figure B.8. Hi-Nicalon^{TM} S fiber tow specimen A12, center section, (800°C, σ = 937 MPa, t = 84.3 h)

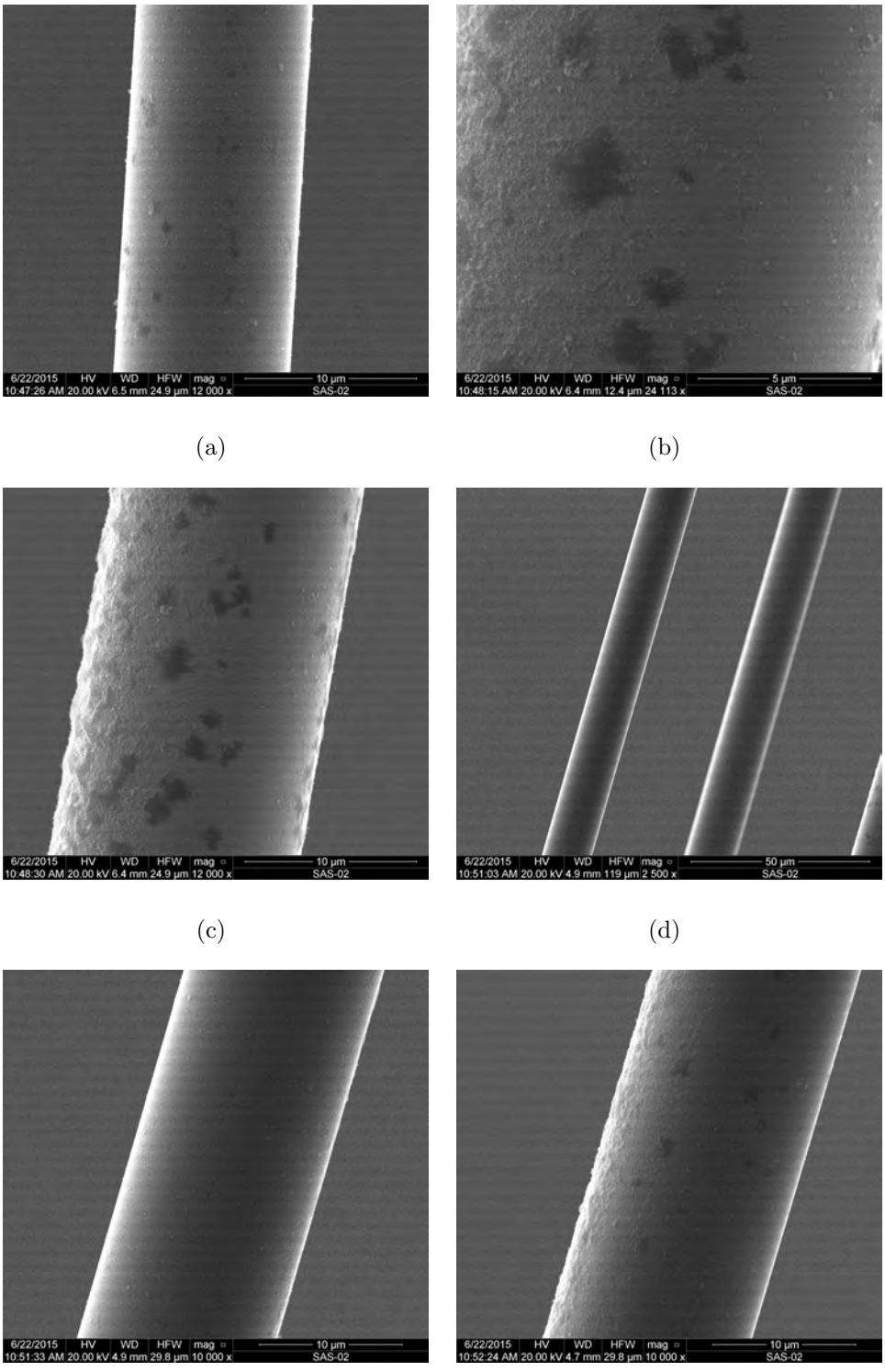
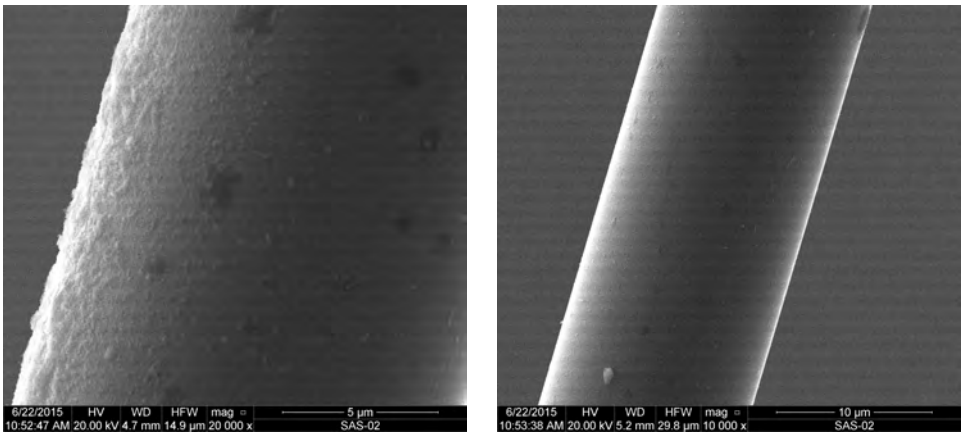
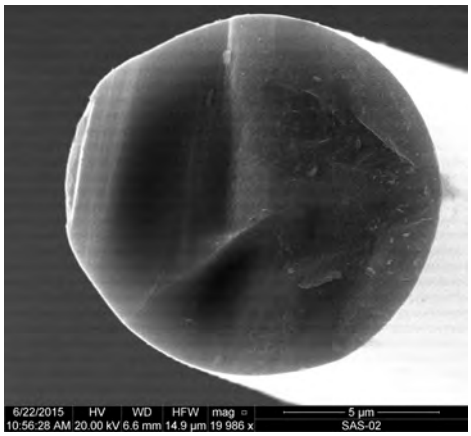


Figure B.9. Hi-Nicalon^{TM} S fiber tow specimen A12, center section, (800°C, σ = 937 MPa, t = 84.3 h)

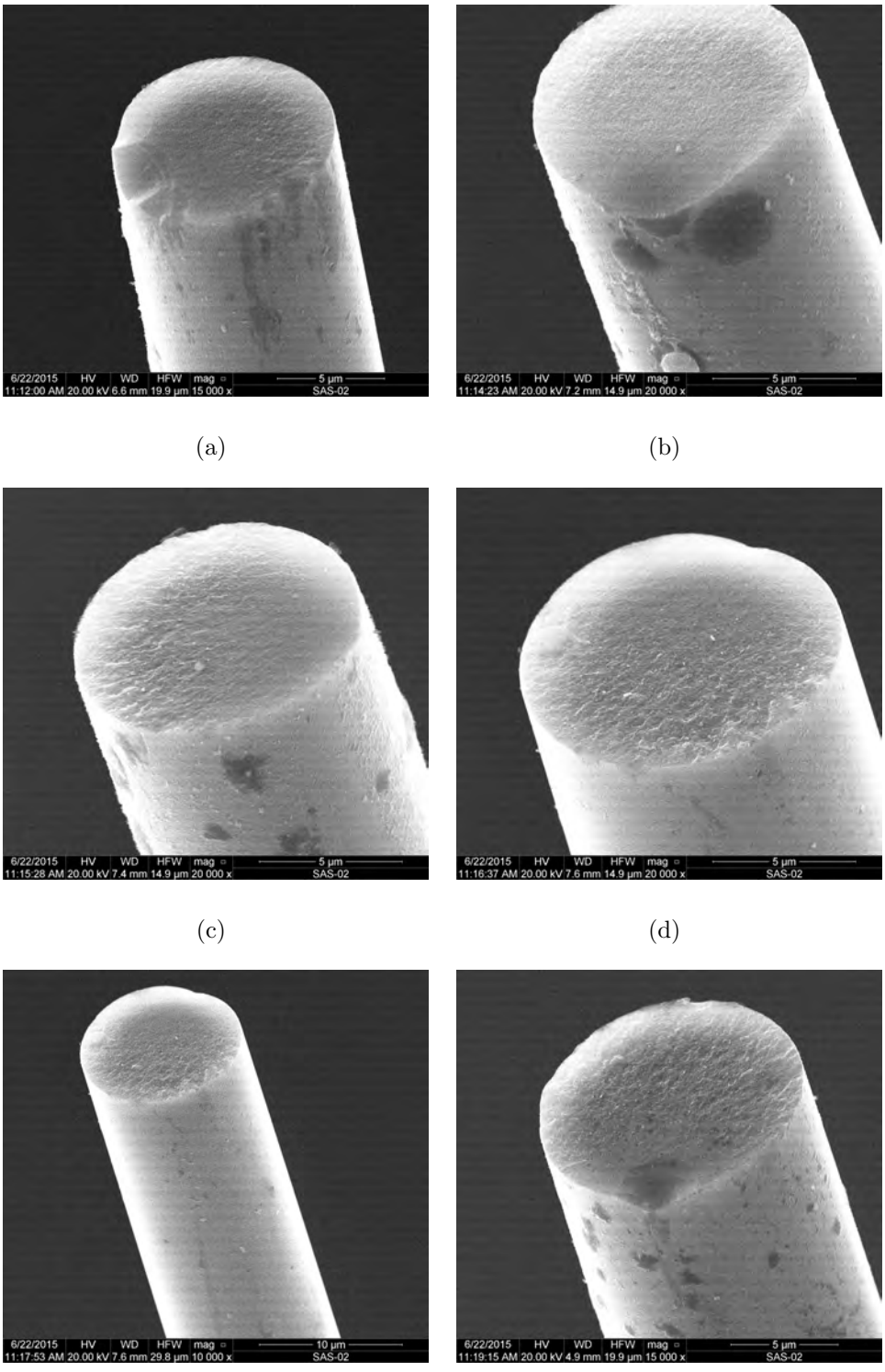


(a) (b)



(c)

Figure B.10. Hi-Nicalon^{TM} S fiber tow specimen A12, center section, (800°C, σ = 937 MPa, t = 84.3 h)



(a) (b)

(c) (d)

(e) (f)

Figure B.11. Hi-Nicalon^{TM} S fiber tow specimen A12, fracture surfaces, (800°C, σ = 937 MPa, t = 84.3 h)

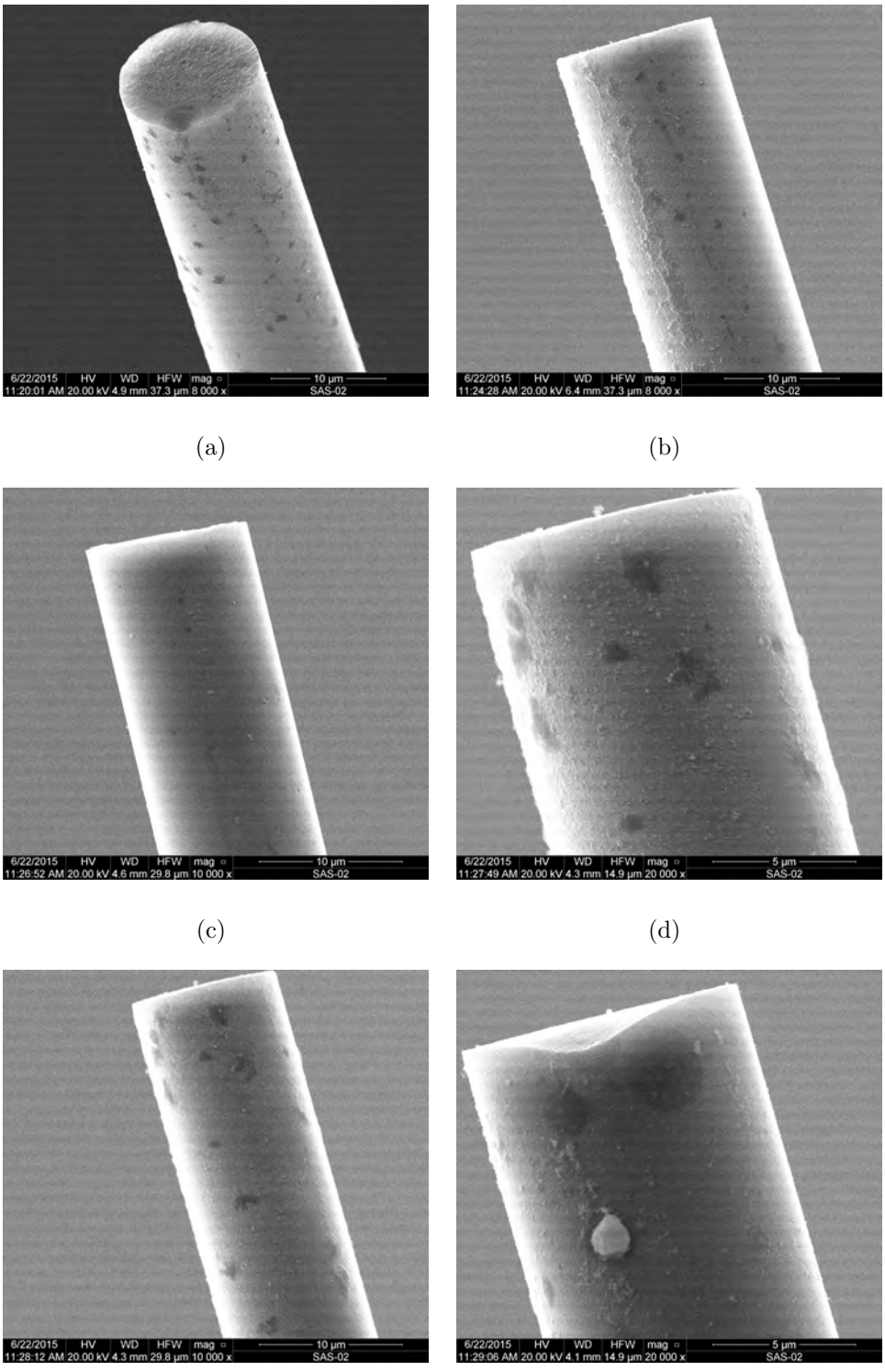
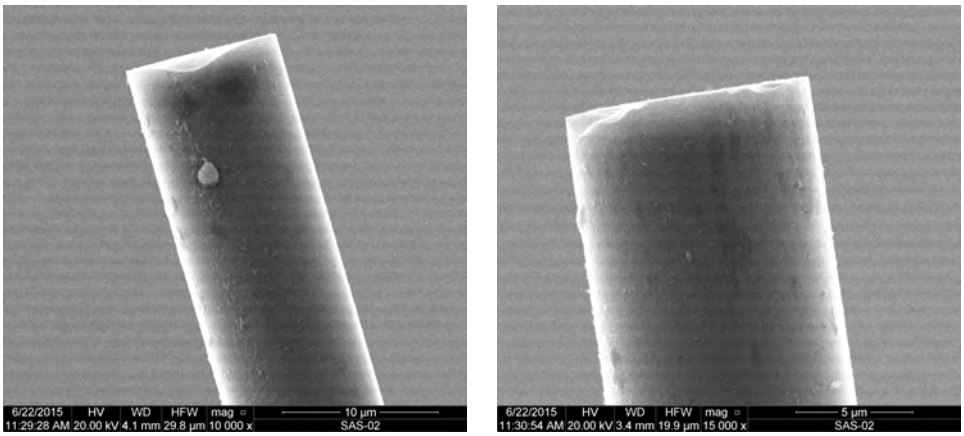
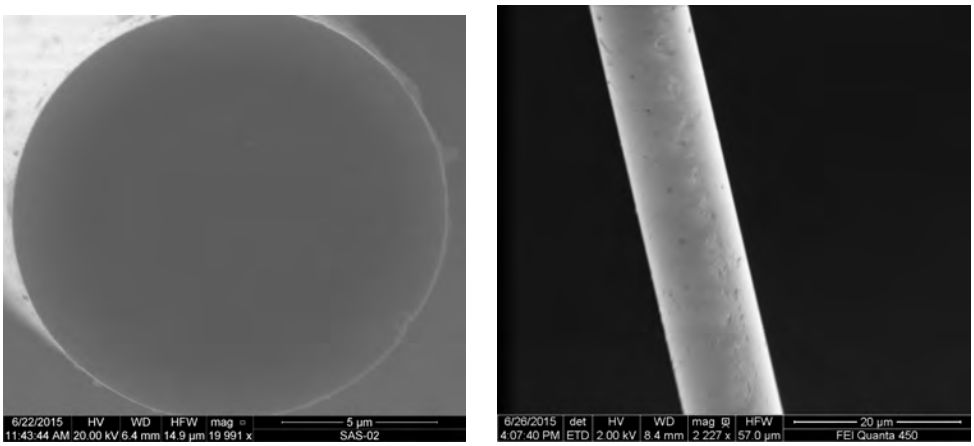


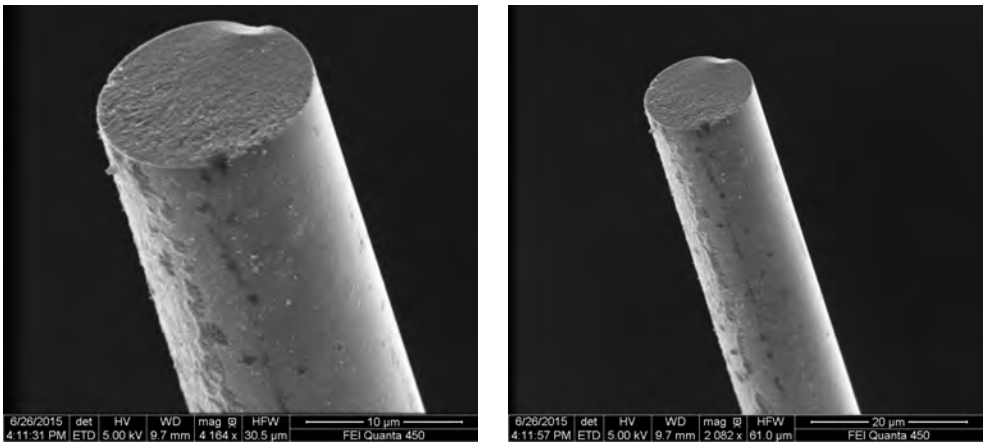
Figure B.12. Hi-Nicalon^{TM} S fiber tow specimen A12, fracture surfaces, (800°C, σ = 937 MPa, t = 84.3 h)



(a) (b)



(c) (d)



(e) (f)

Figure B.13. Hi-Nicalon^{TM} S fiber tow specimen A12, fracture surfaces, (800°C, σ = 937 MPa, t = 84.3 h)

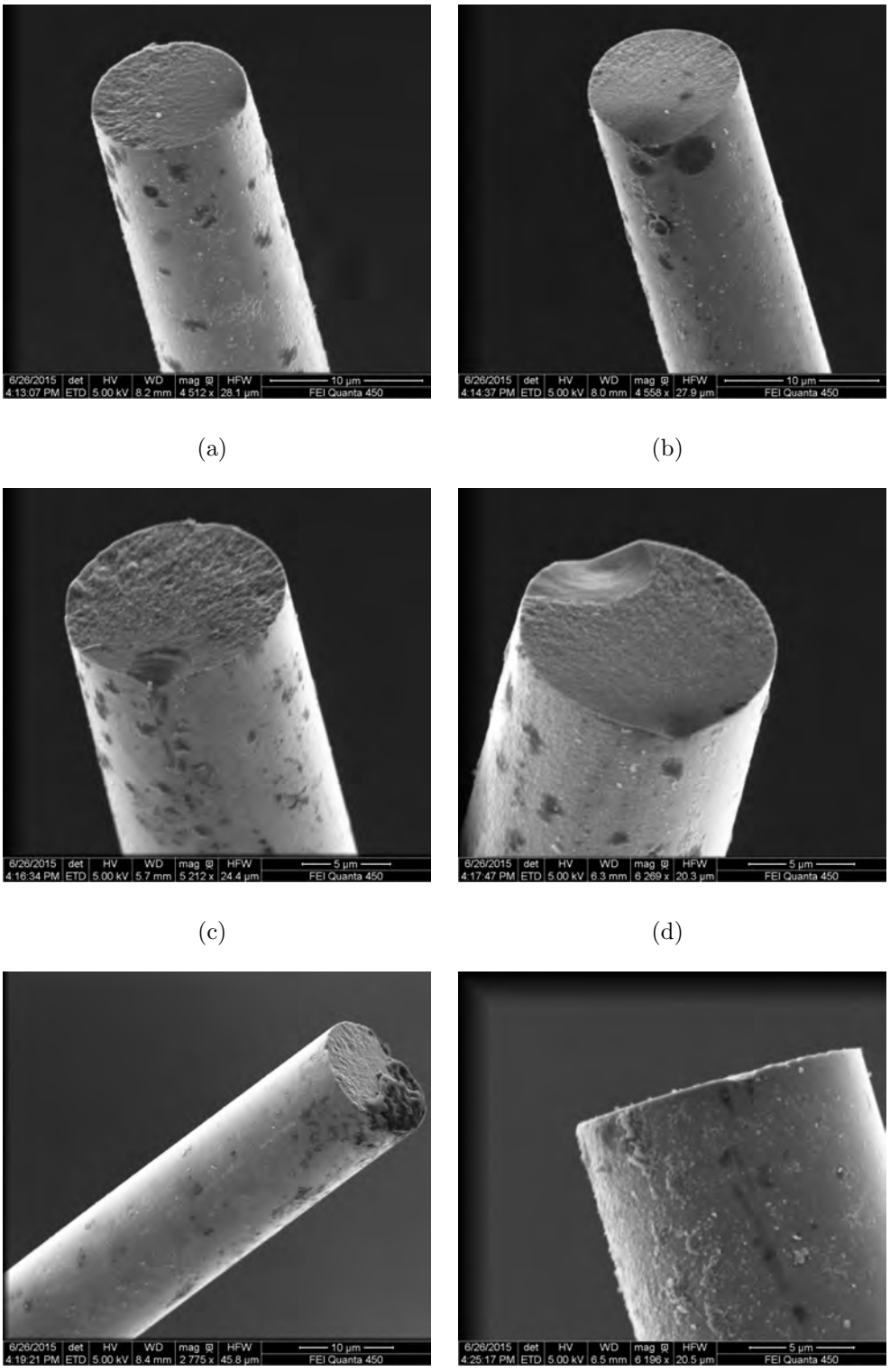
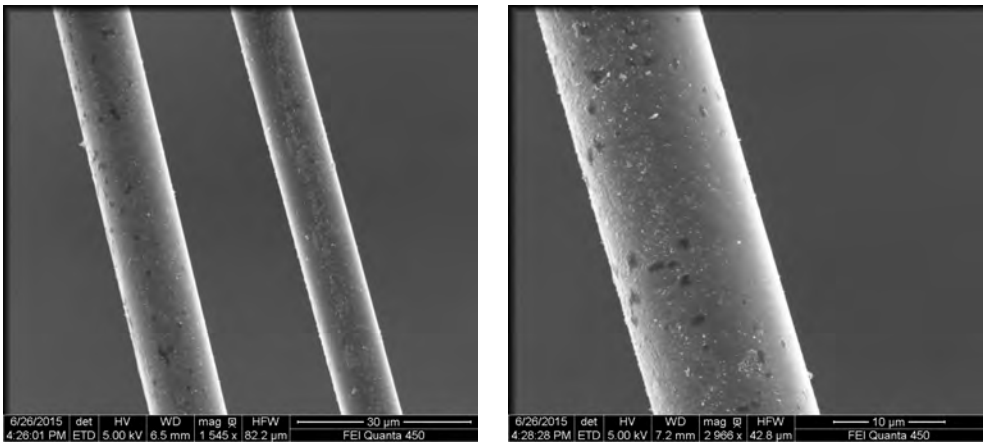
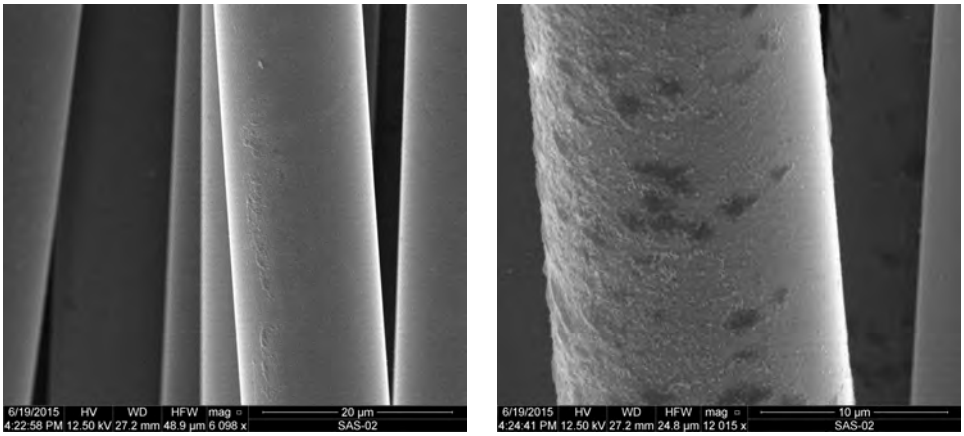


Figure B.14. Hi-Nicalon^{TM} S fiber tow specimen A12, fracture surfaces, (800°C, σ = 937 MPa, t = 84.3 h)



(a) (b)

Figure B.15. Hi-Nicalon^{TM} S fiber tow specimen A12, fracture surfaces, (800°C, σ = 937 MPa, t = 84.3 h)



(a) (b)

Figure B.16. Hi-Nicalon^{TM} S fiber tow specimen A15, center section, (800°C, σ = 798 MPa, t = 100 h)

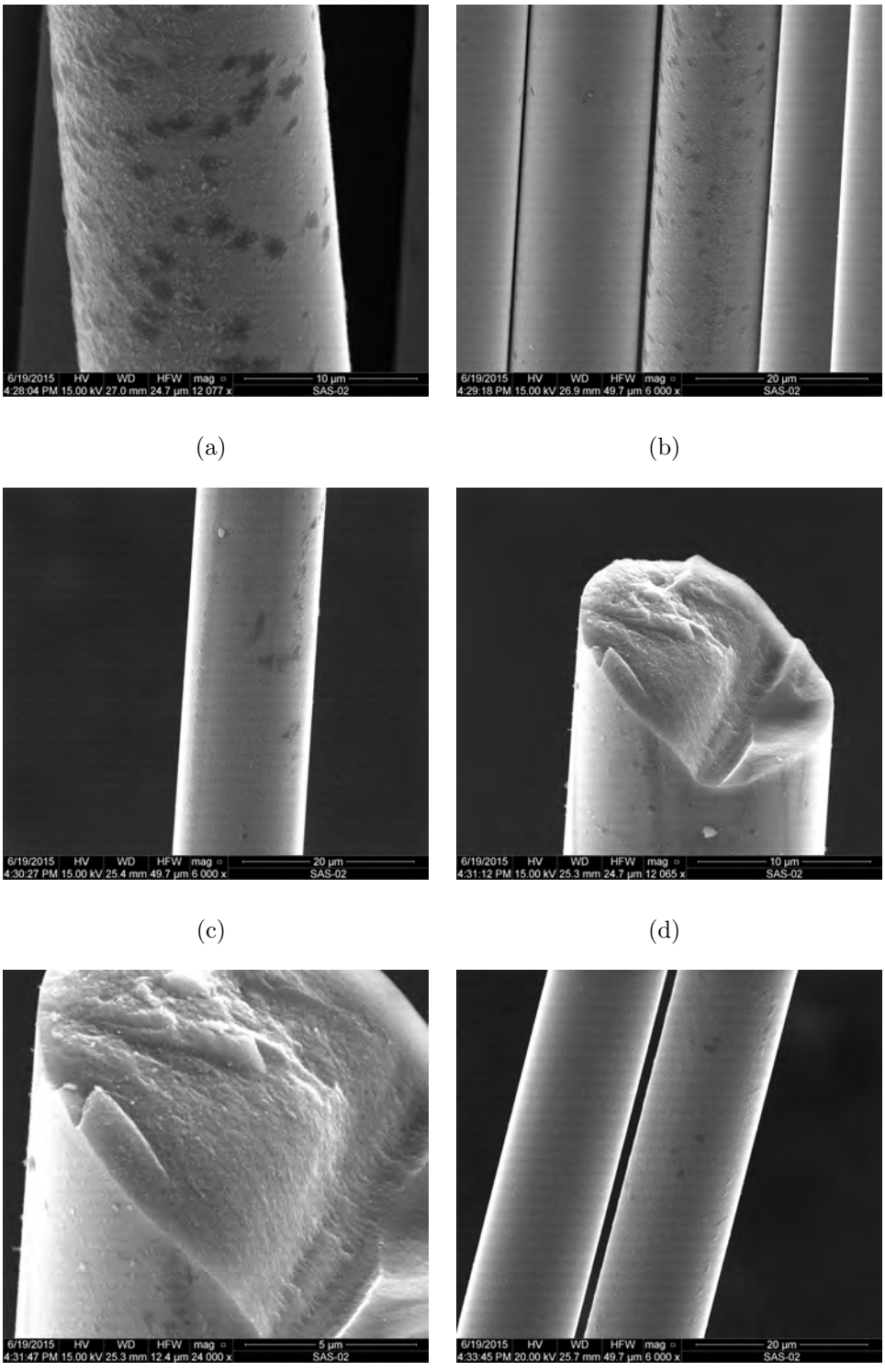
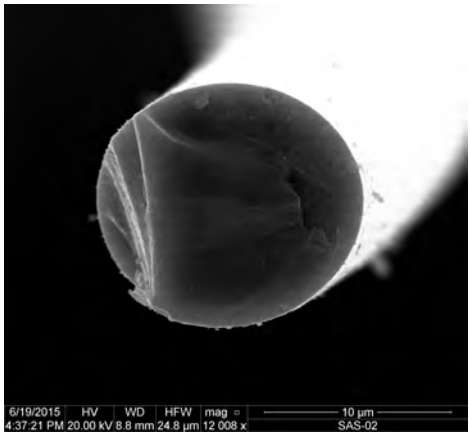
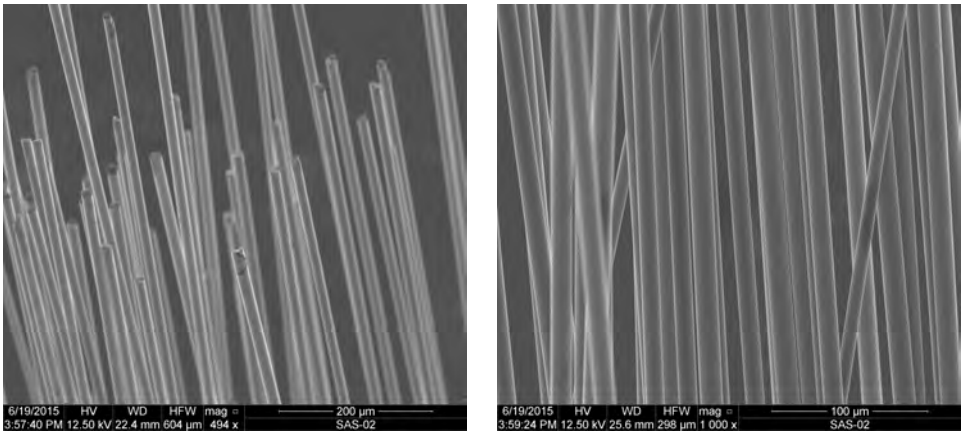


Figure B.17. Hi-Nicalon^{TM} S fiber tow specimen A15, center section, (800°C, σ = 798 MPa, t = 100 h)



(a)

Figure B.18. Hi-Nicalon^{TM} S fiber tow specimen A15, center section, (800°C, σ = 798 MPa, t = 100 h)



(a) (b)

Figure B.19. Hi-Nicalon^{TM} S fiber tow specimen A16, center section, (800°C, σ = 1023 MPa, t = 16.9 h)

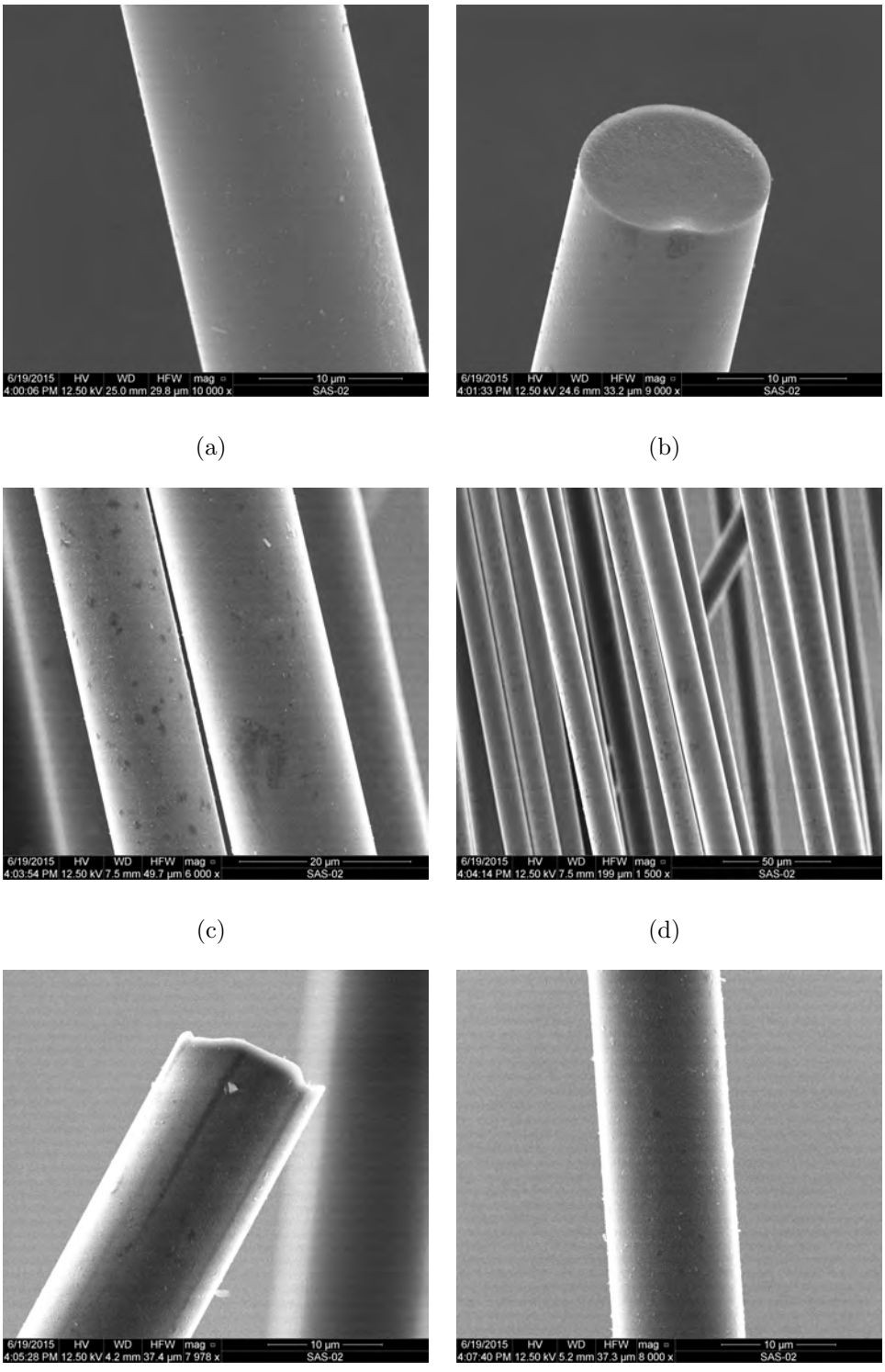
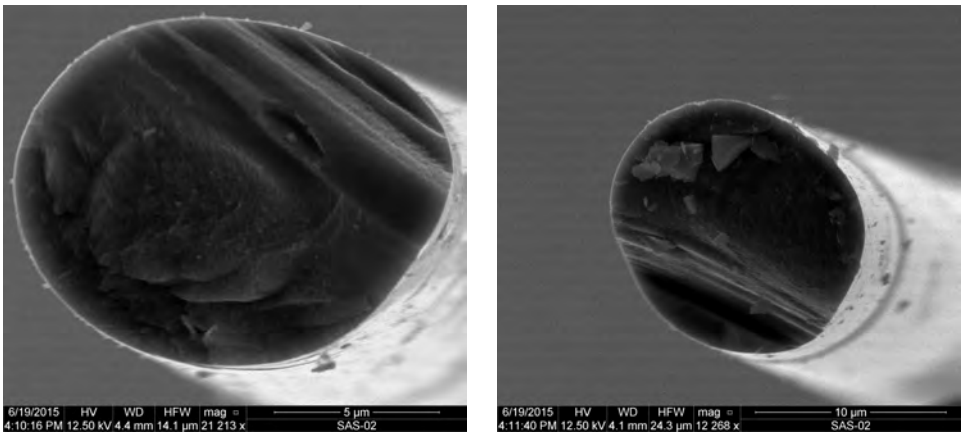
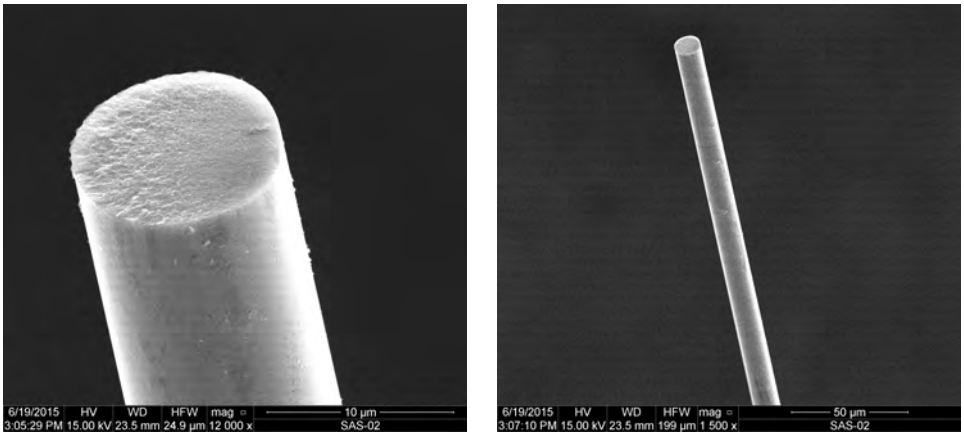


Figure B.20. Hi-Nicalon^{TM} S fiber tow specimen A16, center section, (800°C, σ = 1023 MPa, t = 16.9 h)



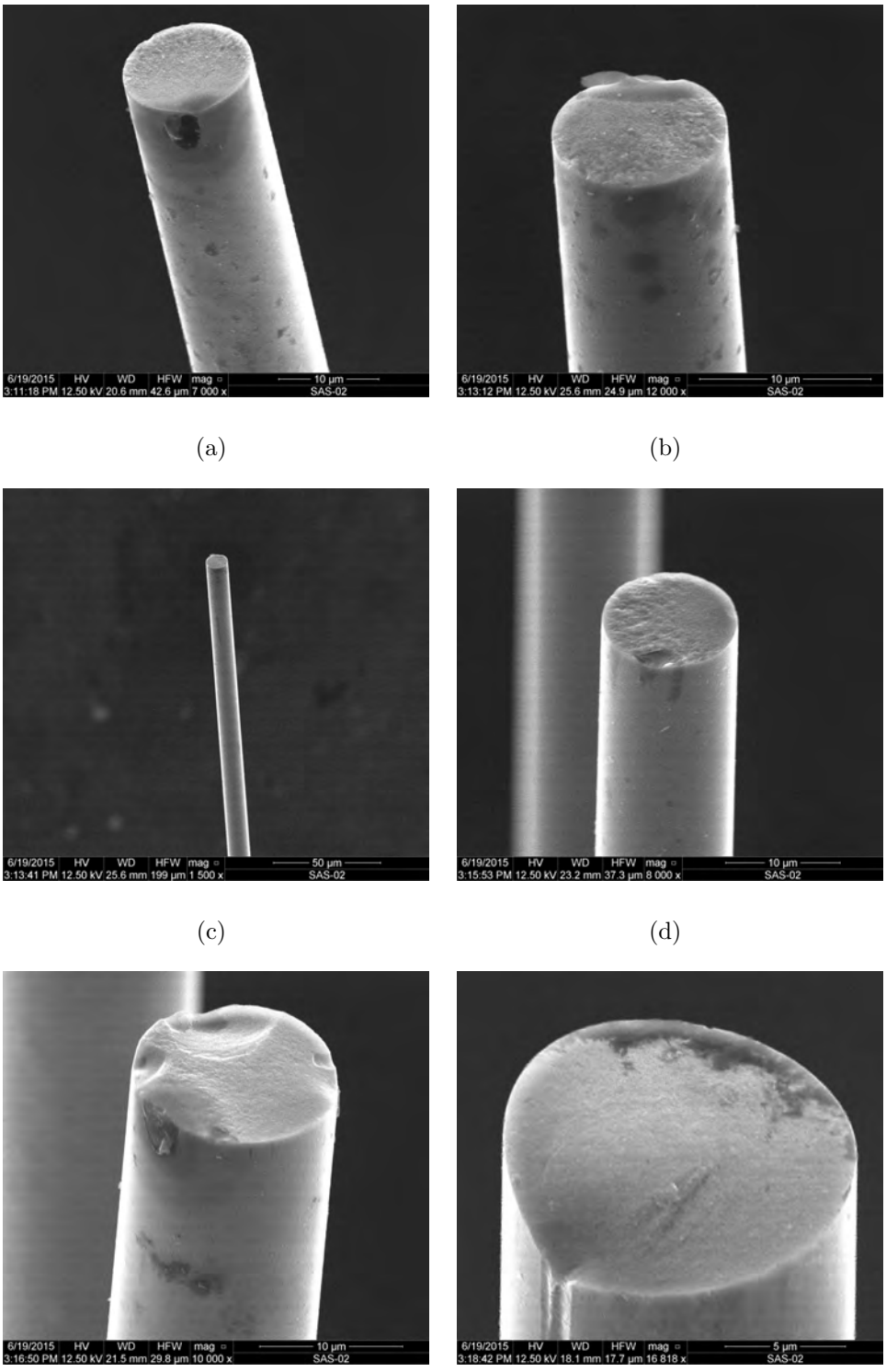
(a) (b)

Figure B.21. Hi-Nicalon^{TM} S fiber tow specimen A16, center section, (800°C, σ = 1023 MPa, t = 16.9 h)



(a) (b)

Figure B.22. Hi-Nicalon^{TM} S fiber tow specimen A16, fracture surfaces, (800°C, σ = 1023 MPa, t = 16.9 h)



(a) (b)

(c) (d)

(e) (f)

Figure B.23. Hi-Nicalon^{TM} S fiber tow specimen A16, fracture surfaces, (800°C, σ = 1023 MPa, t = 16.9 h)

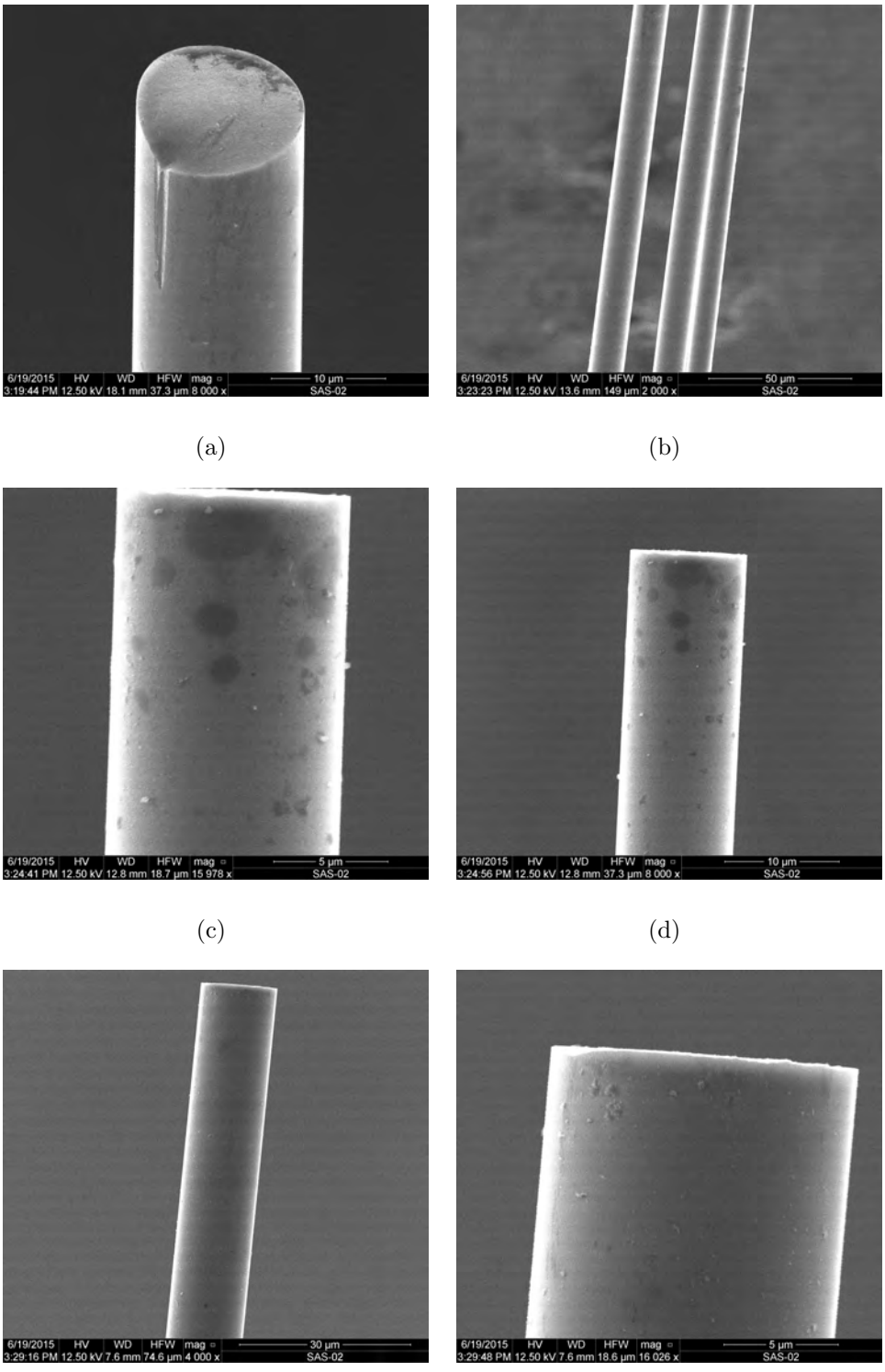


Figure B.24. Hi-Nicalon^{TM} S fiber tow specimen A16, fracture surfaces, (800°C, σ = 1023 MPa, t = 16.9 h)

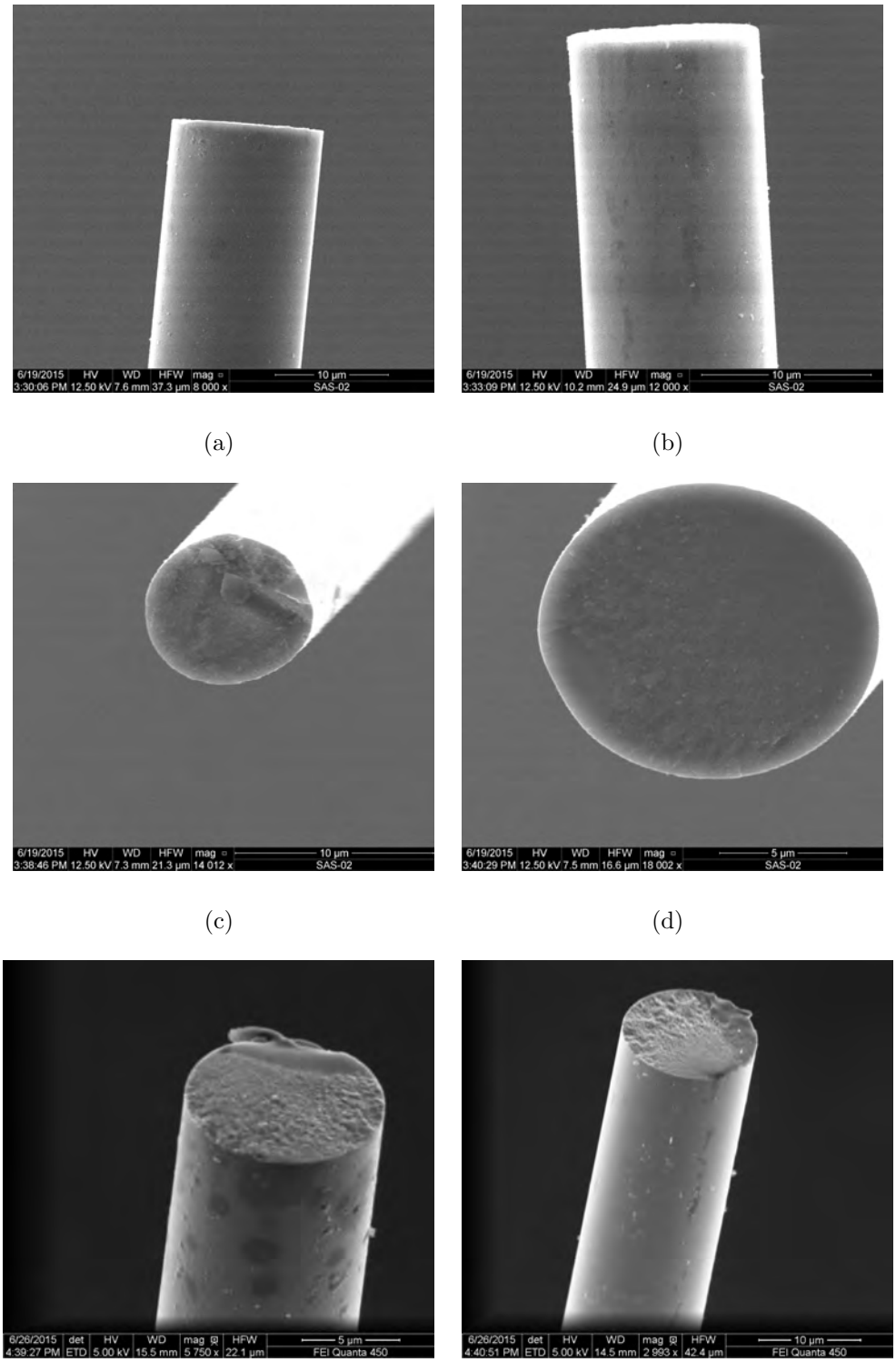
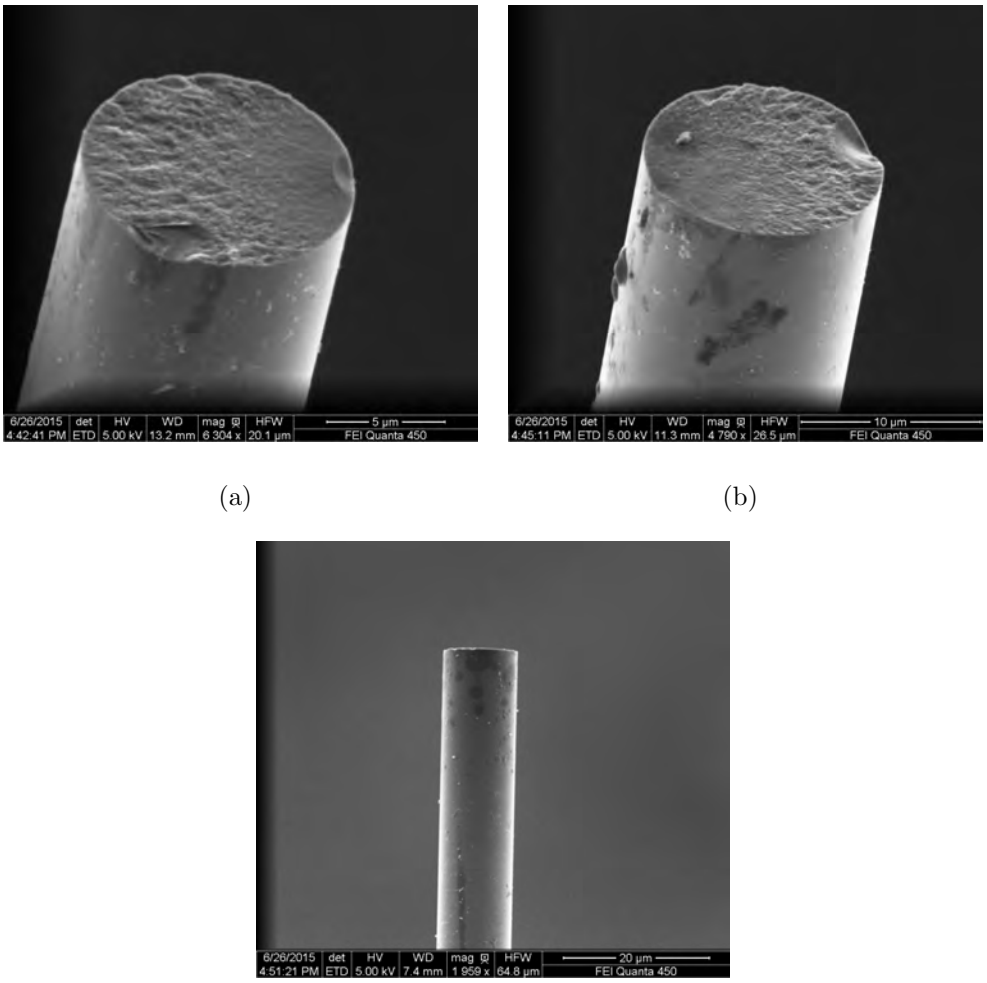


Figure B.25. Hi-Nicalon^{TM} S fiber tow specimen A16, fracture surfaces, (800°C, σ = 1023 MPa, t = 16.9 h)



(a) (b)

(c)

Figure B.26. Hi-Nicalon^{TM} S fiber tow specimen A16, fracture surfaces, (800°C, σ = 1023 MPa, t = 16.9 h)

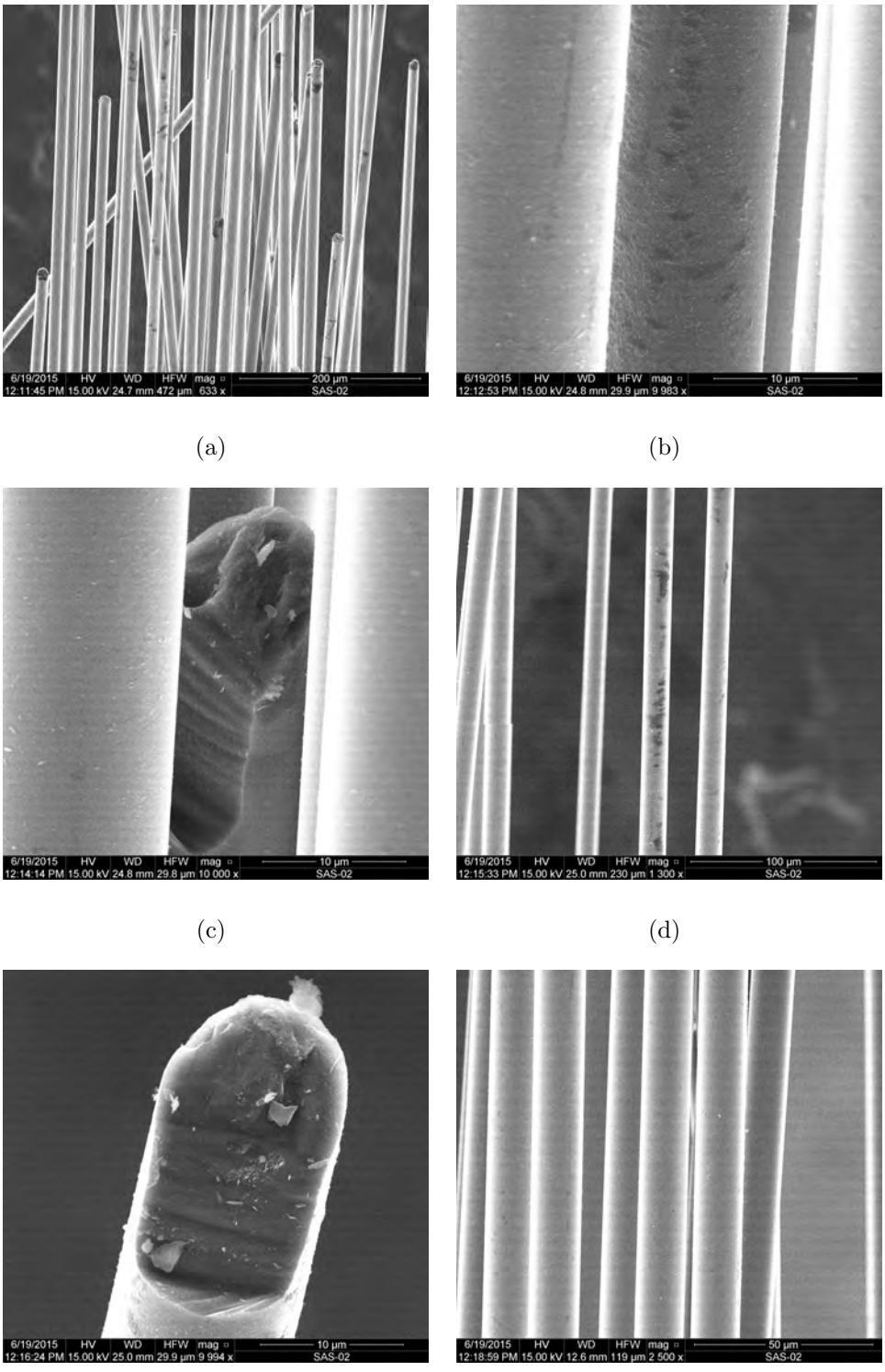


Figure B.27. Hi-Nicalon^{TM} S fiber tow specimen A17, center section, (800°C, σ = 980 MPa, t = 17.4 h)

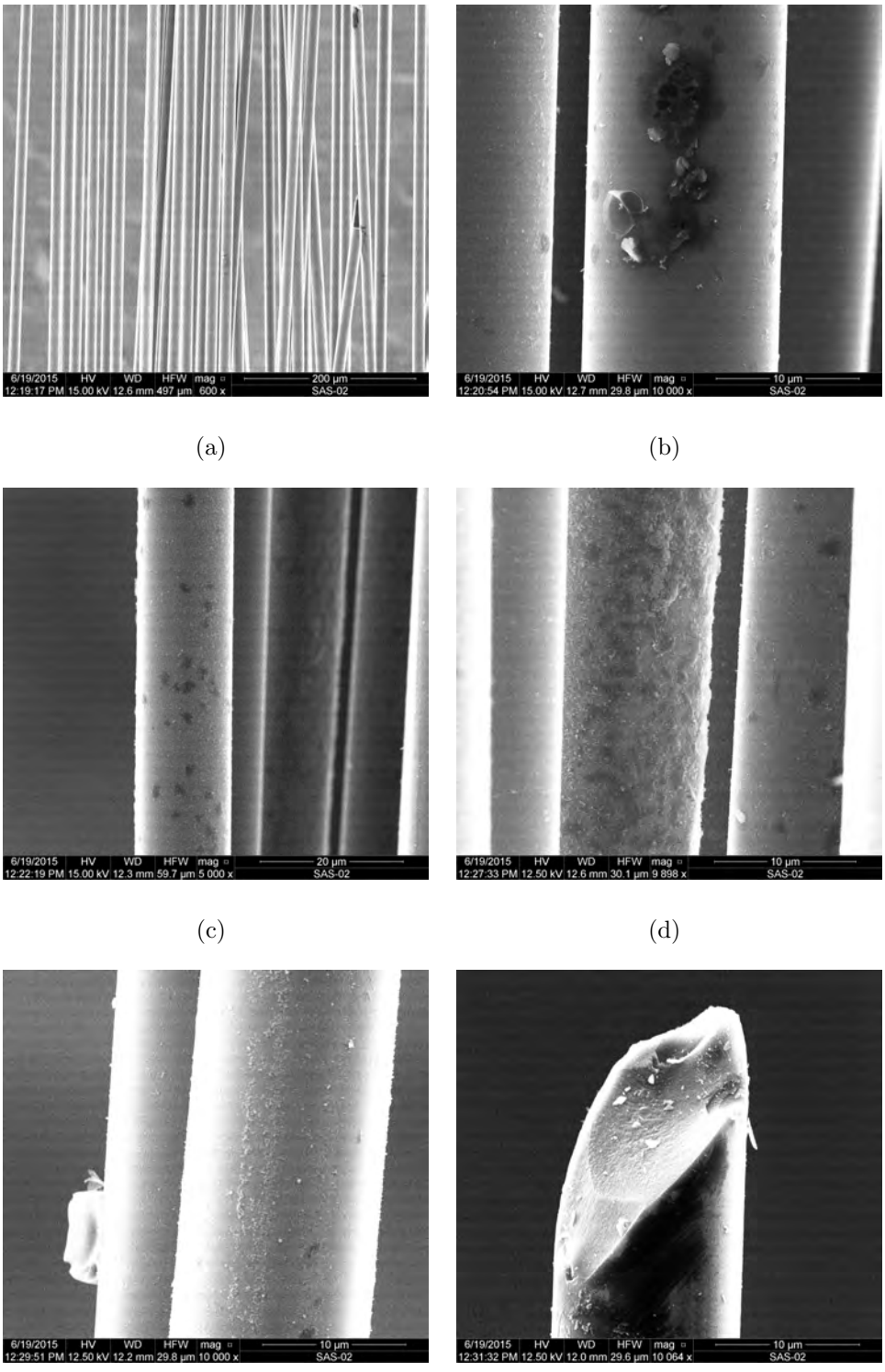
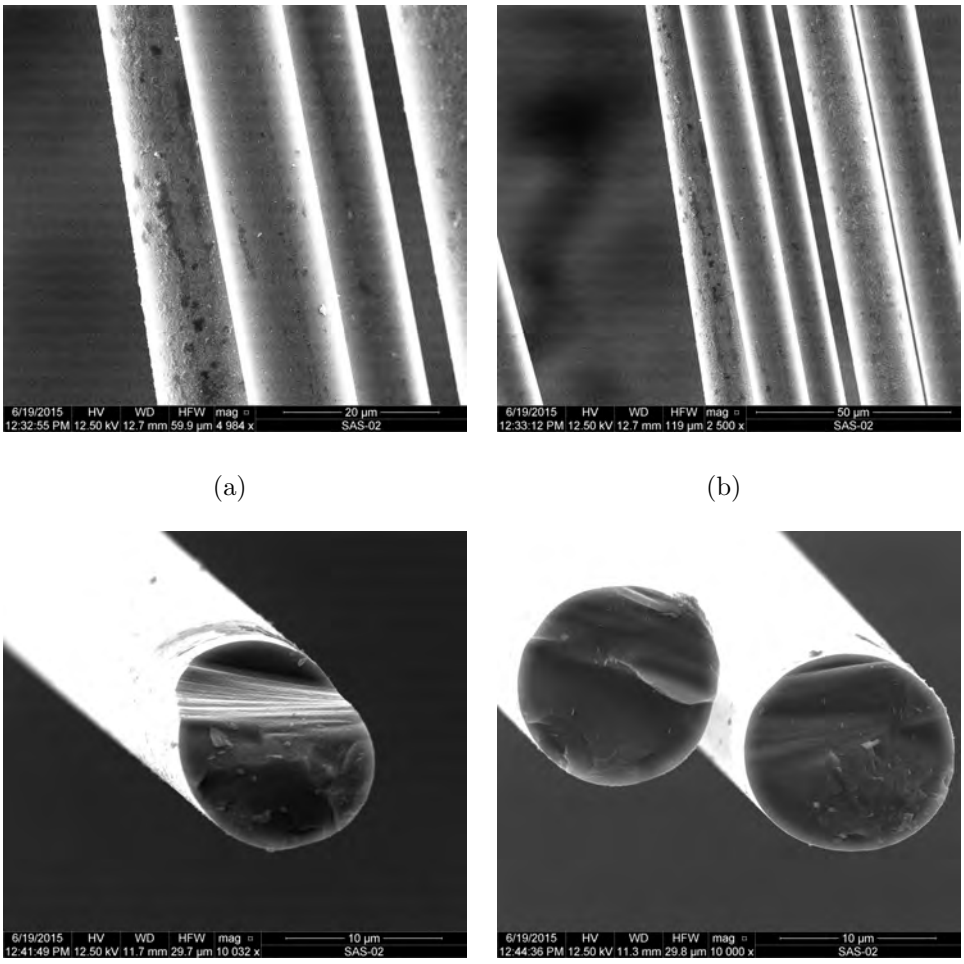


Figure B.28. Hi-Nicalon^{TM} S fiber tow specimen A17, center section, (800°C, σ = 980 MPa, t = 17.4 h)



(a) (b)

(c) (d)

Figure B.29. Hi-Nicalon^{TM} S fiber tow specimen A17, center section, (800°C, σ = 980 MPa, t = 17.4 h)

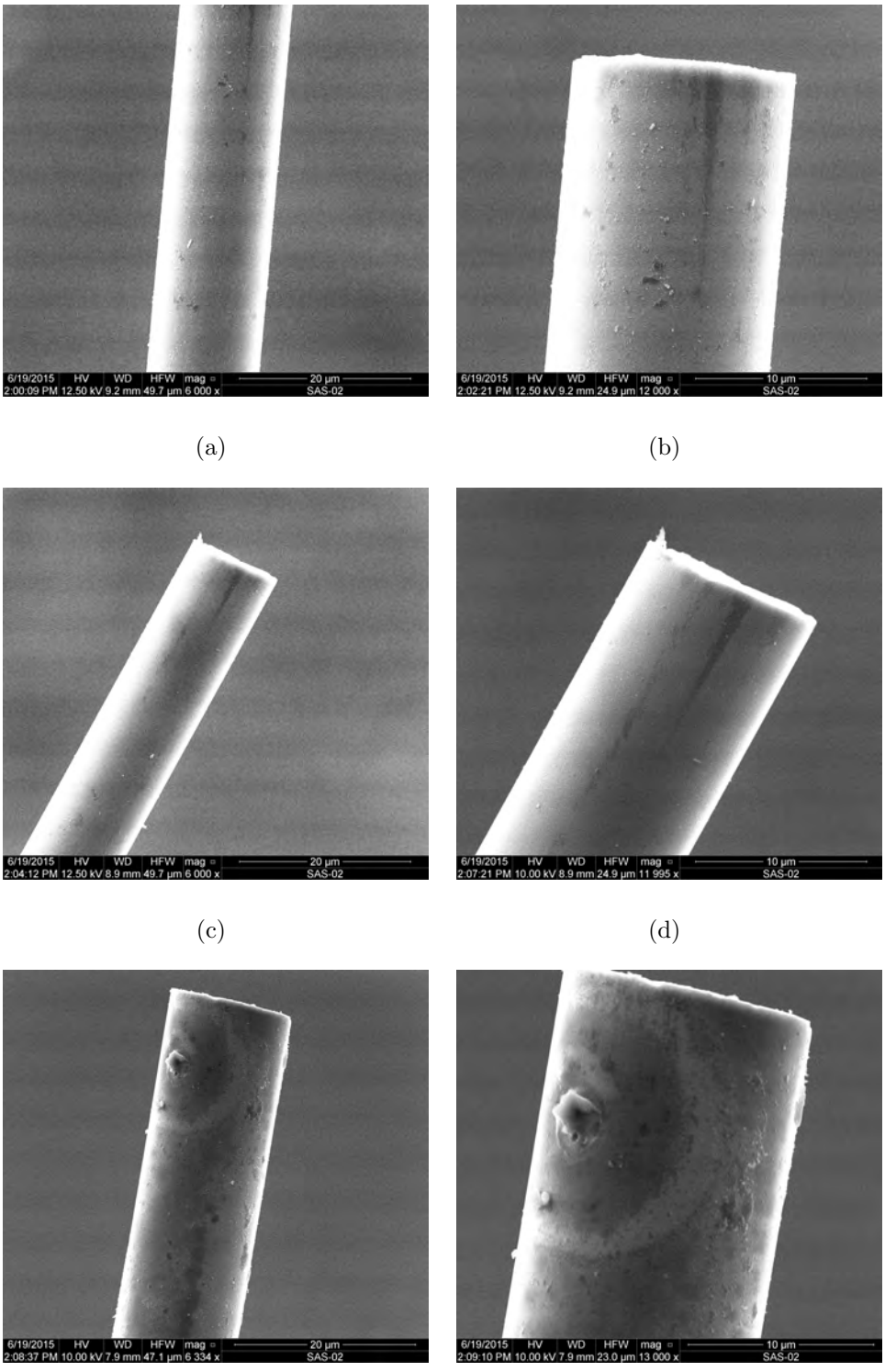


Figure B.30. Hi-Nicalon^{TM} S fiber tow specimen A17, fracture surfaces, (800°C, σ = 980 MPa, t = 17.4 h)

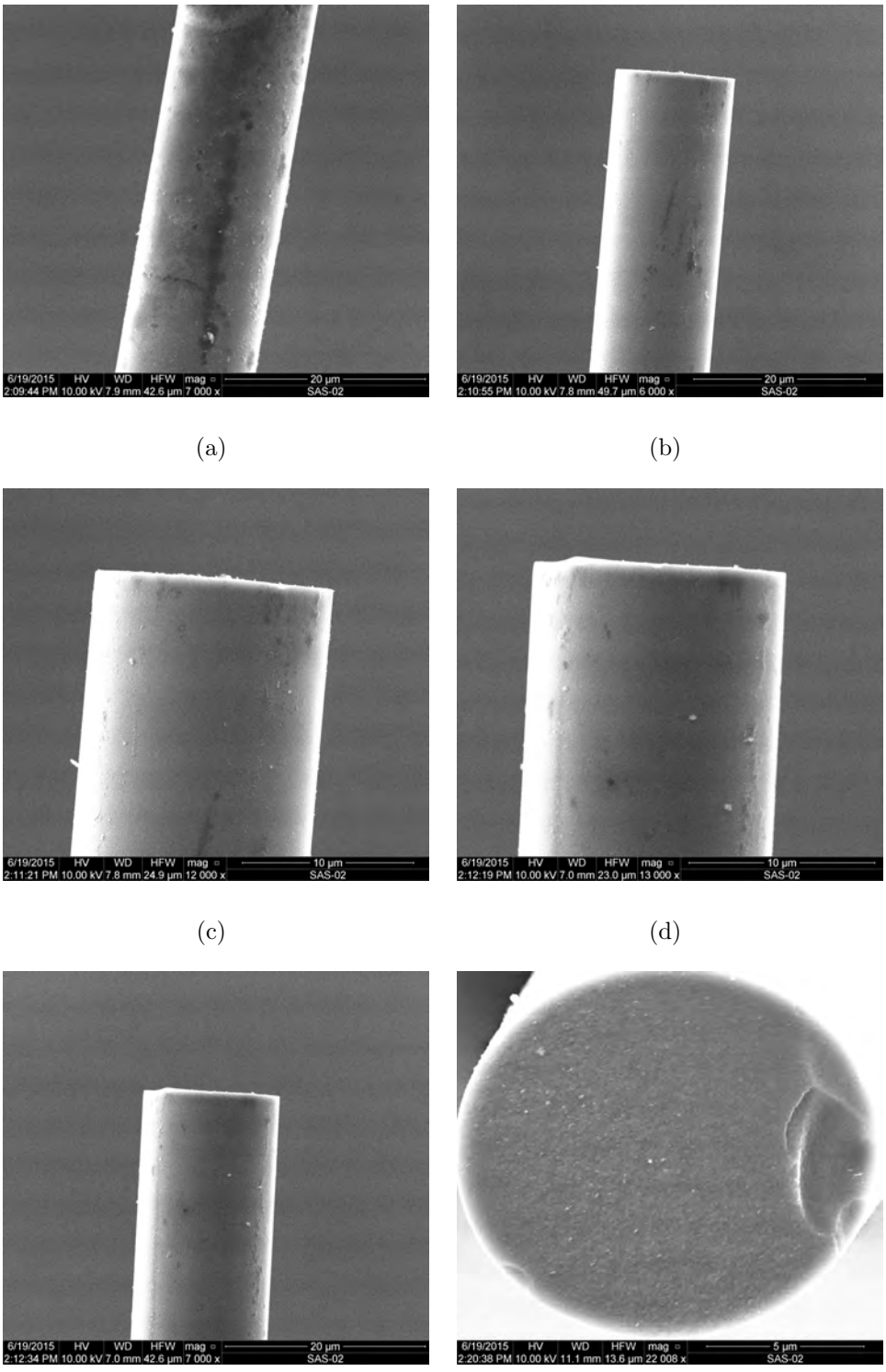


Figure B.31. Hi-Nicalon^{TM} S fiber tow specimen A17, fracture surfaces, (800°C, σ = 980 MPa, t = 17.4 h)

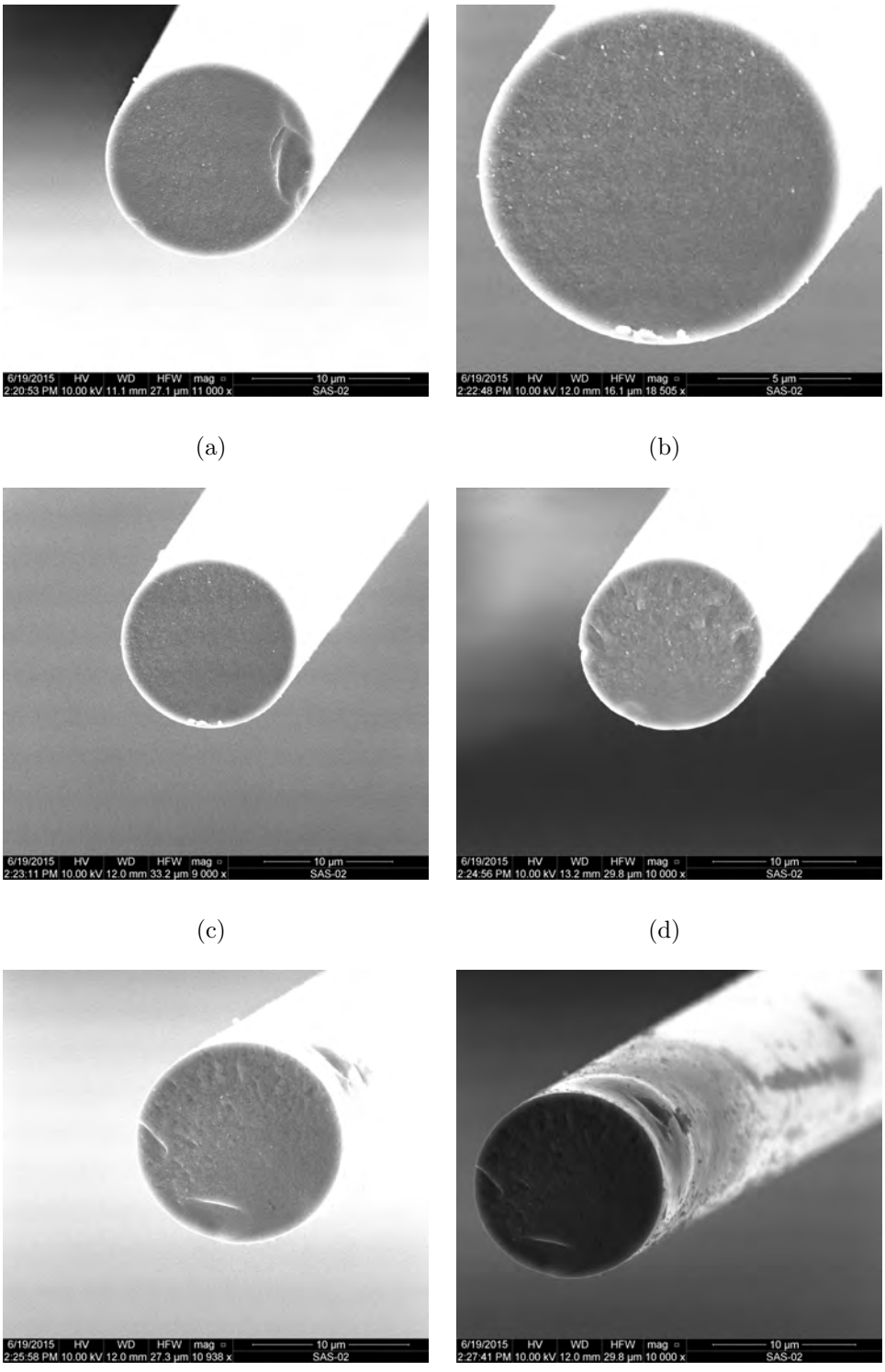


Figure B.32. Hi-Nicalon^{TM} S fiber tow specimen A17, fracture surfaces, (800°C, σ = 980 MPa, t = 17.4 h)

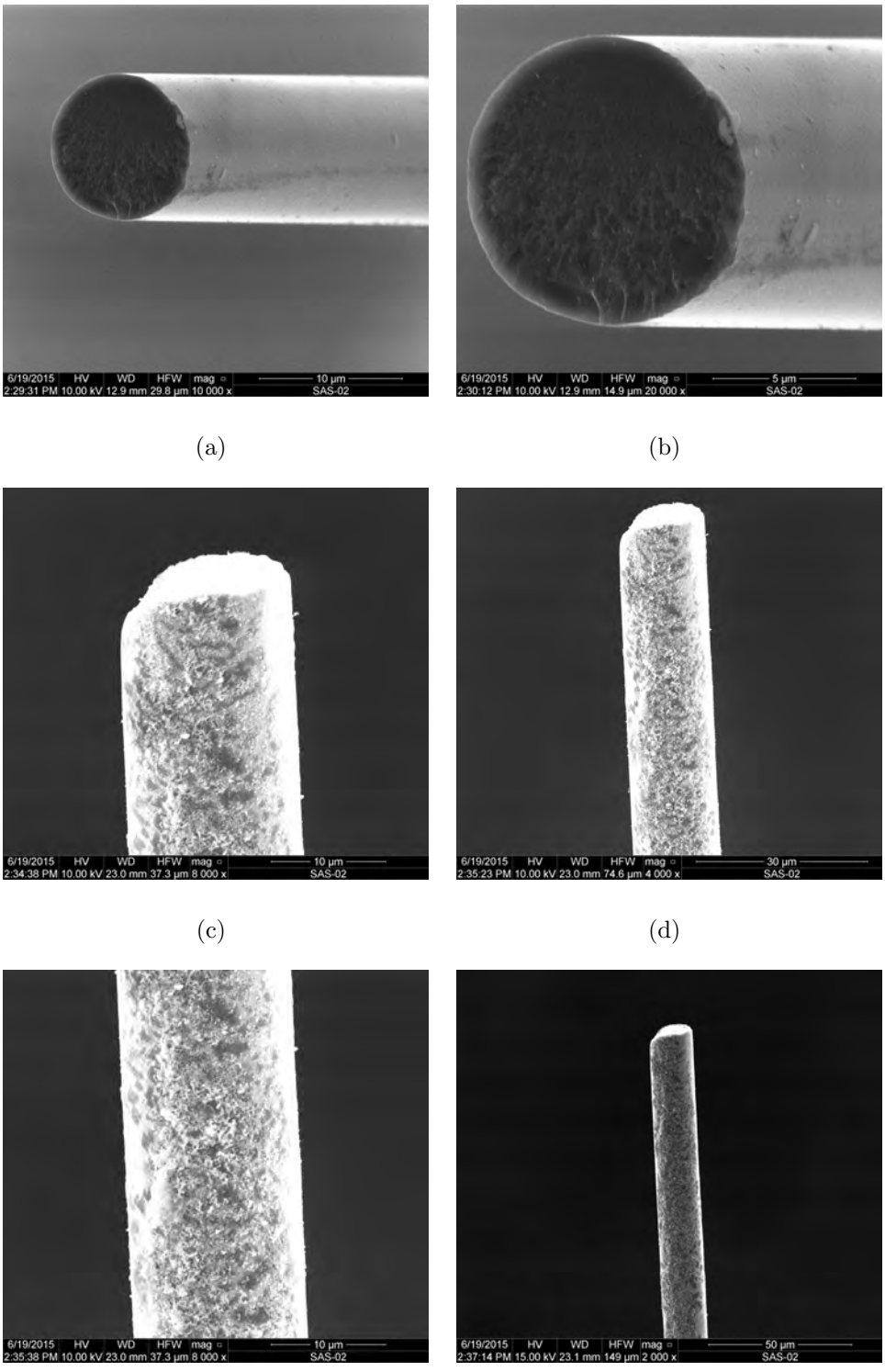


Figure B.33. Hi-Nicalon^{TM} S fiber tow specimen A17, fracture surfaces, (800°C, σ = 980 MPa, t = 17.4 h)

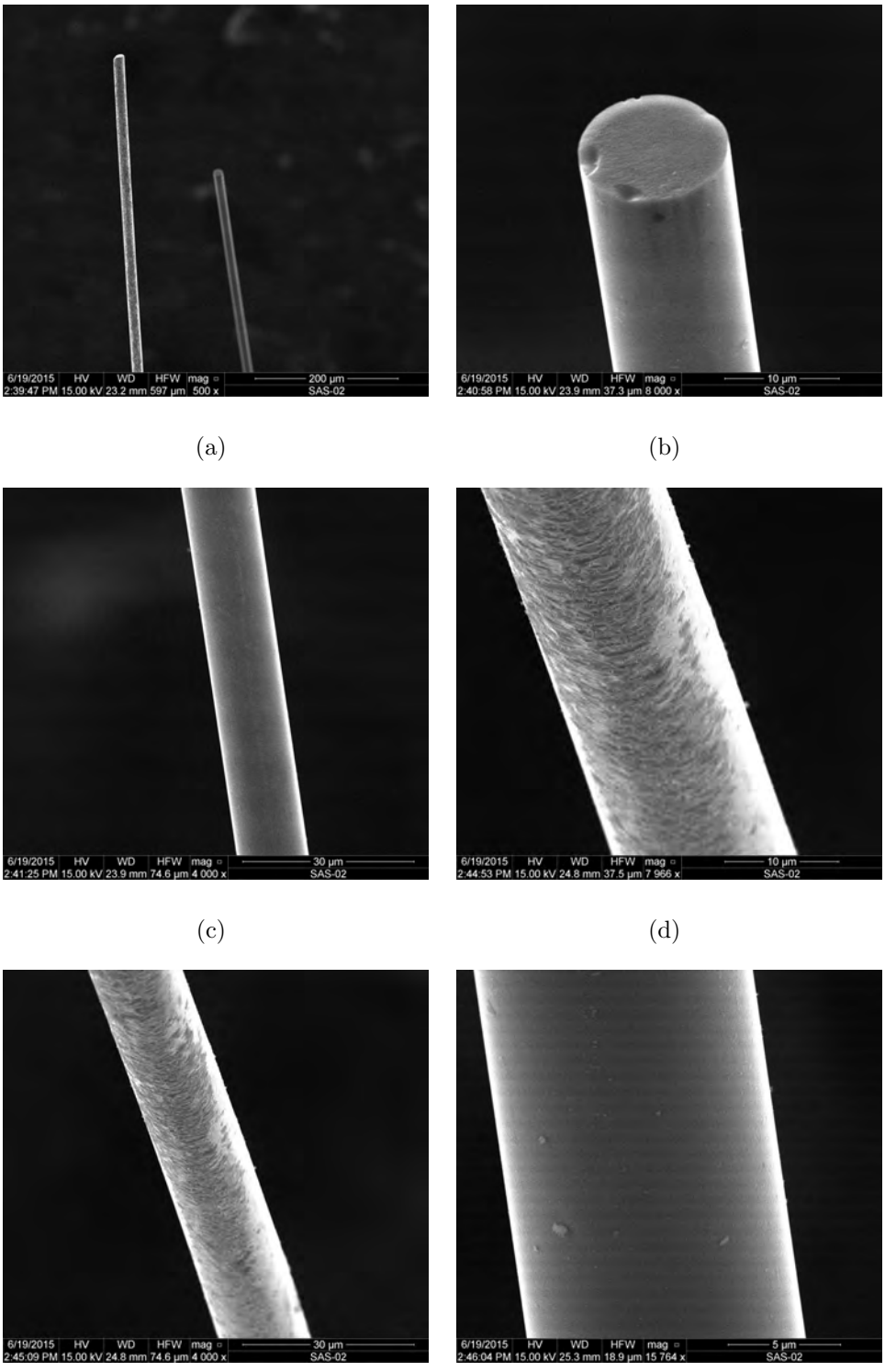
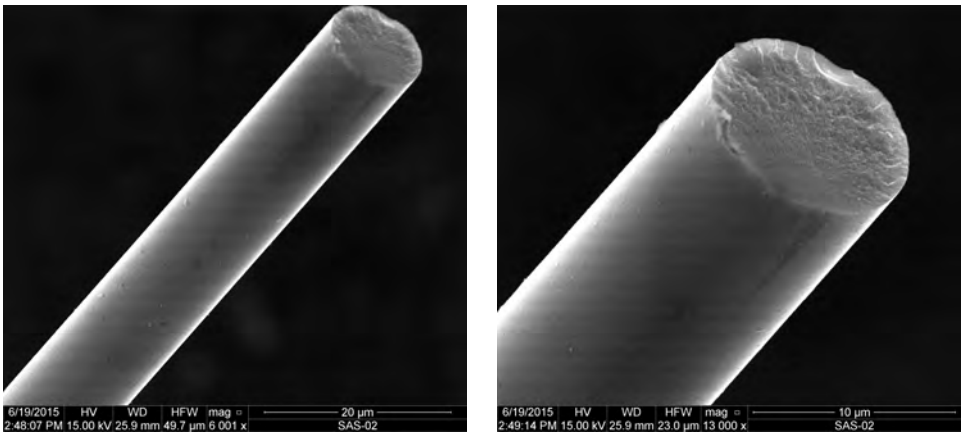
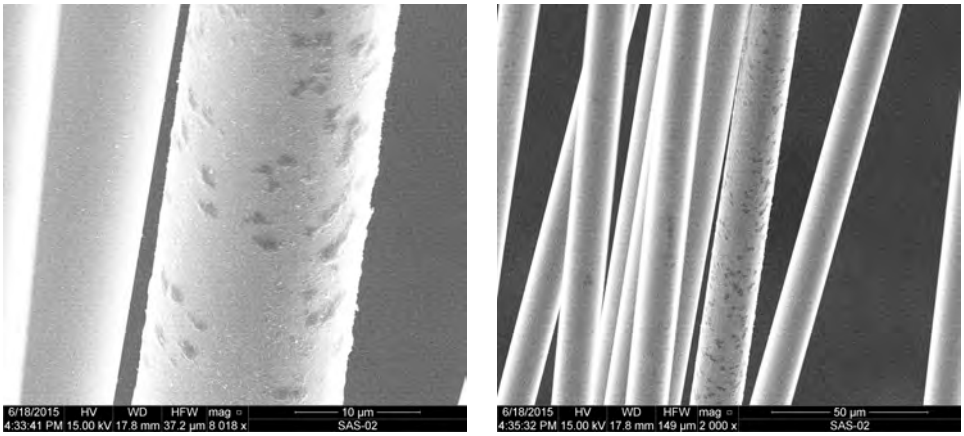


Figure B.34. Hi-Nicalon^{TM} S fiber tow specimen A17, fracture surfaces, (800°C, σ = 980 MPa, t = 17.4 h)



(a) (b)

Figure B.35. Hi-Nicalon^{TM} S fiber tow specimen A17, fracture surfaces, (800°C, σ = 980 MPa, t = 17.4 h)



(a) (b)

Figure B.36. Hi-Nicalon^{TM} S fiber tow specimen A21, center section, (800°C, σ = 960 MPa, t = 100 h)

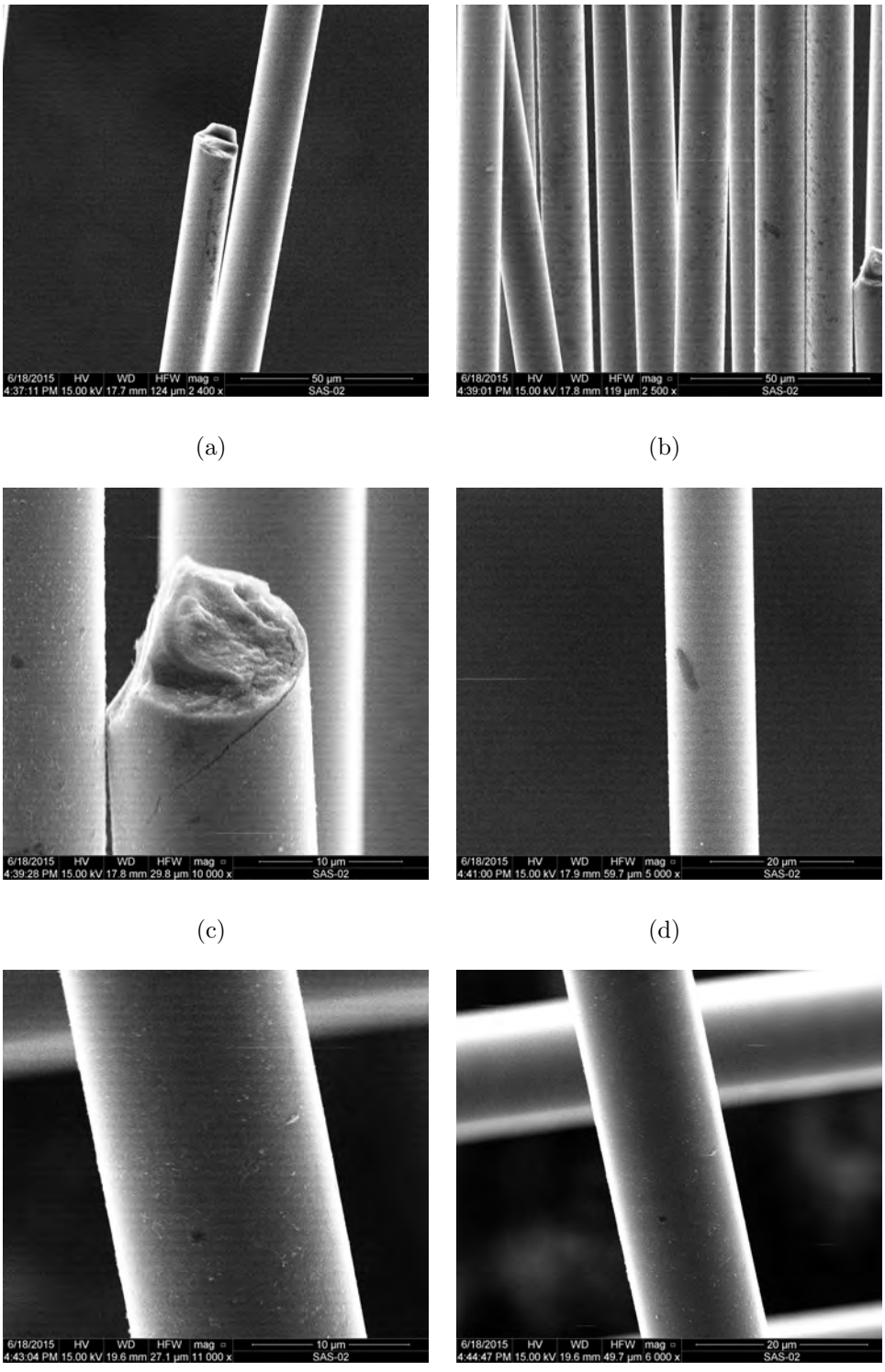


Figure B.37. Hi-Nicalon^{TM} S fiber tow specimen A21, center section, (800°C, σ = 960 MPa, t = 100 h)

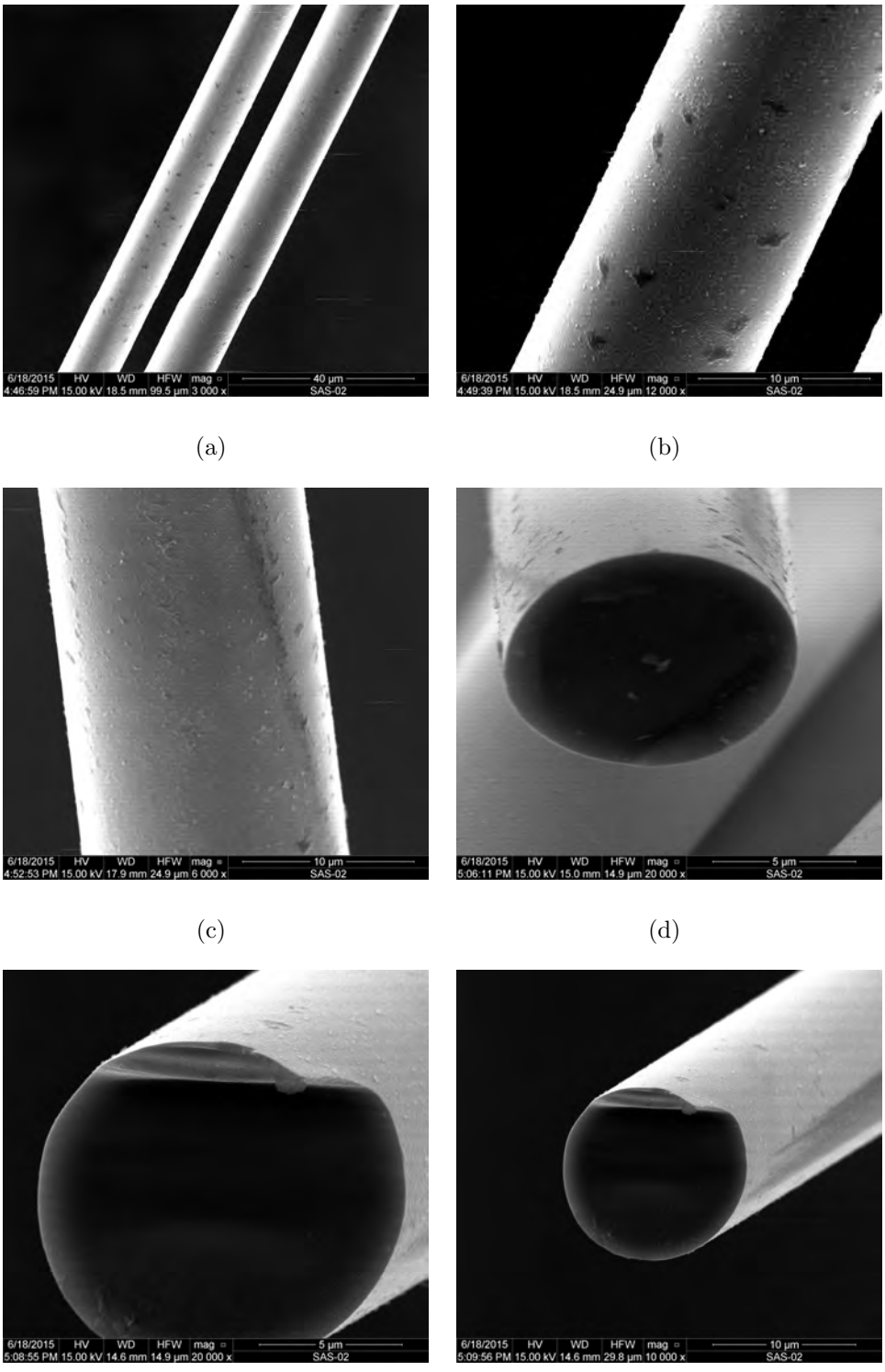
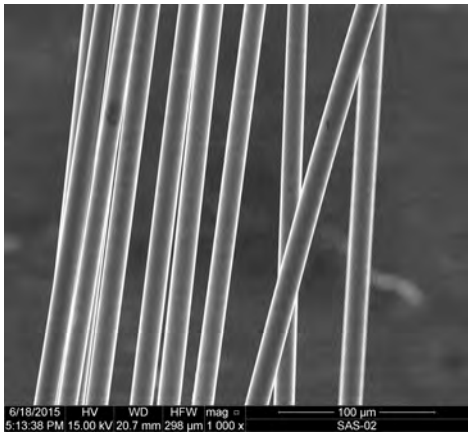


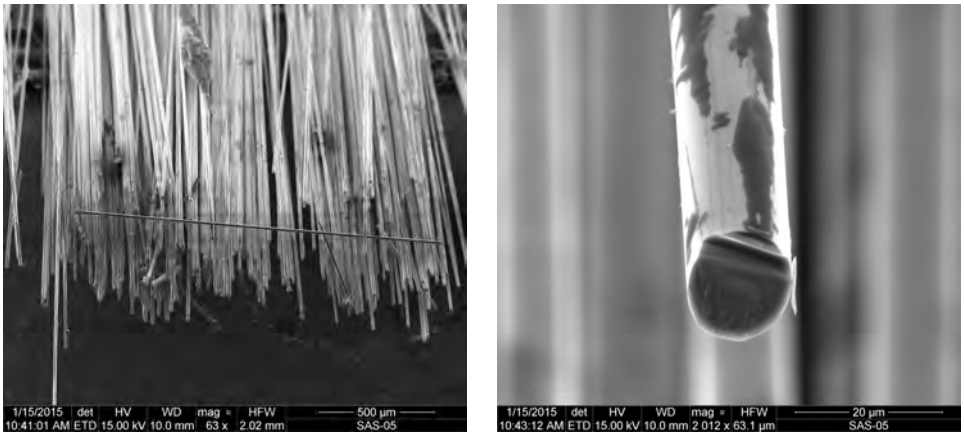
Figure B.38. Hi-Nicalon^{TM} S fiber tow specimen A21, center section, (800°C, σ = 960 MPa, t = 100 h)



(a)

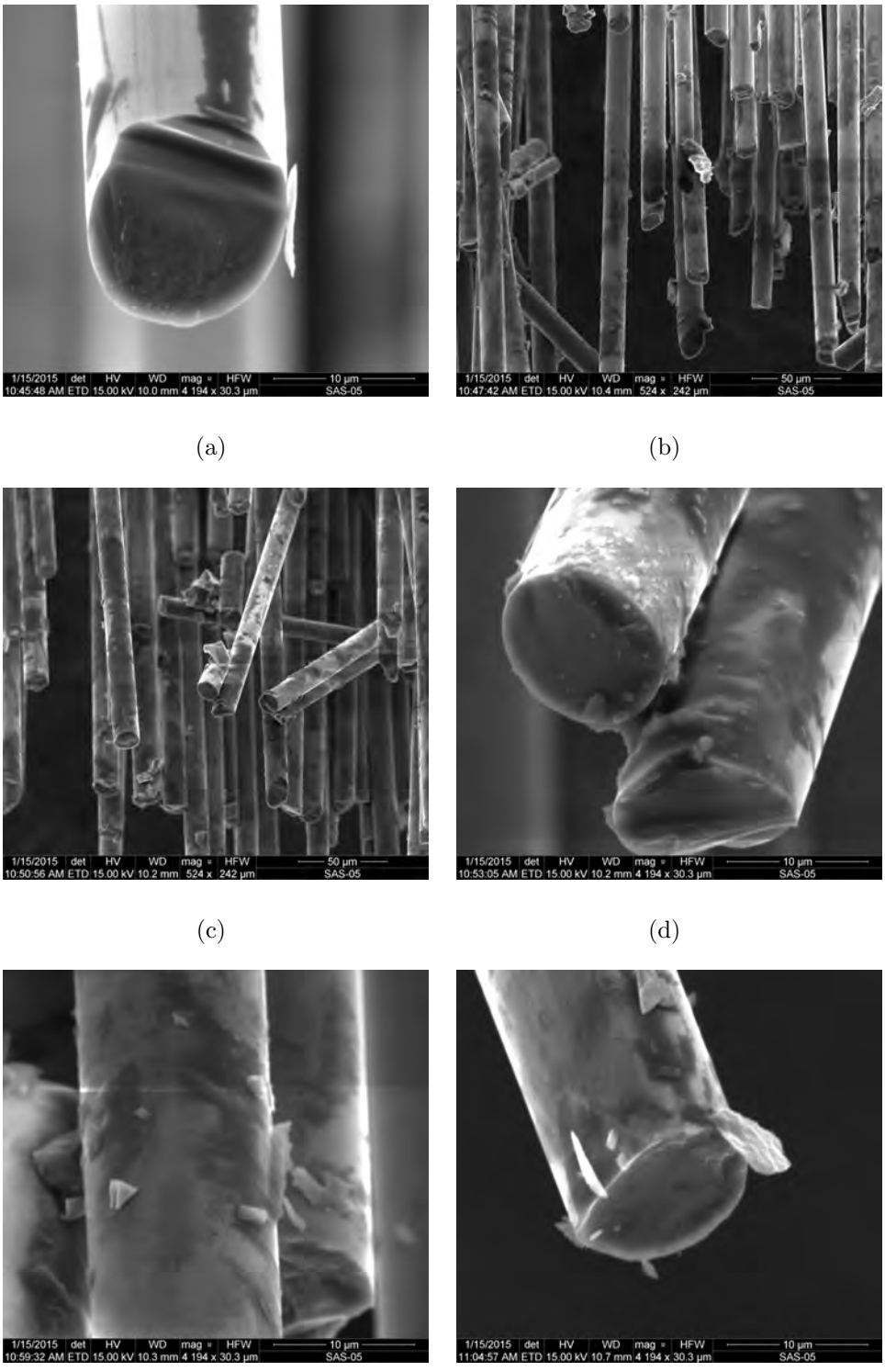
Figure B.39. Hi-Nicalon^{TM} S fiber tow specimen A21, center section, (800°C, σ = 960 MPa, t = 100 h)

B.2 Saturated Steam



(a) (b)

Figure B.40. Hi-Nicalon^{TM} S fiber tow specimen SS1, lower section, (800°C, σ = 2.96 MPa, t = 100 h)



(a) (b)

(c) (d)

(e) (f)

Figure B.41. Hi-Nicalon^{TM} S fiber tow specimen SS1, lower section, (800°C, σ = 2.96 MPa, t = 100 h)

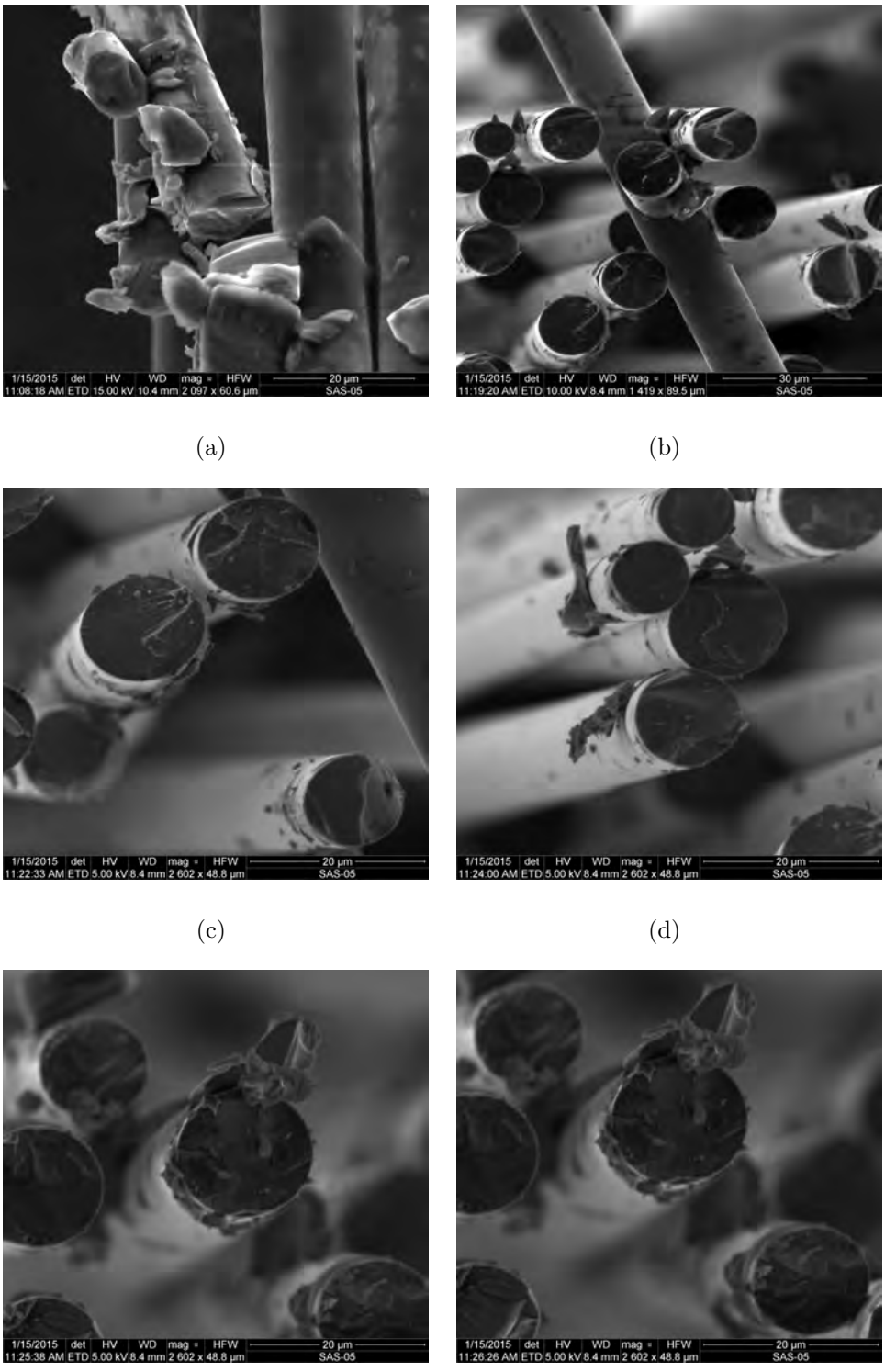


Figure B.42. Hi-Nicalon^{TM} S fiber tow specimen SS1, lower section, (800°C, σ = 2.96 MPa, t = 100 h)

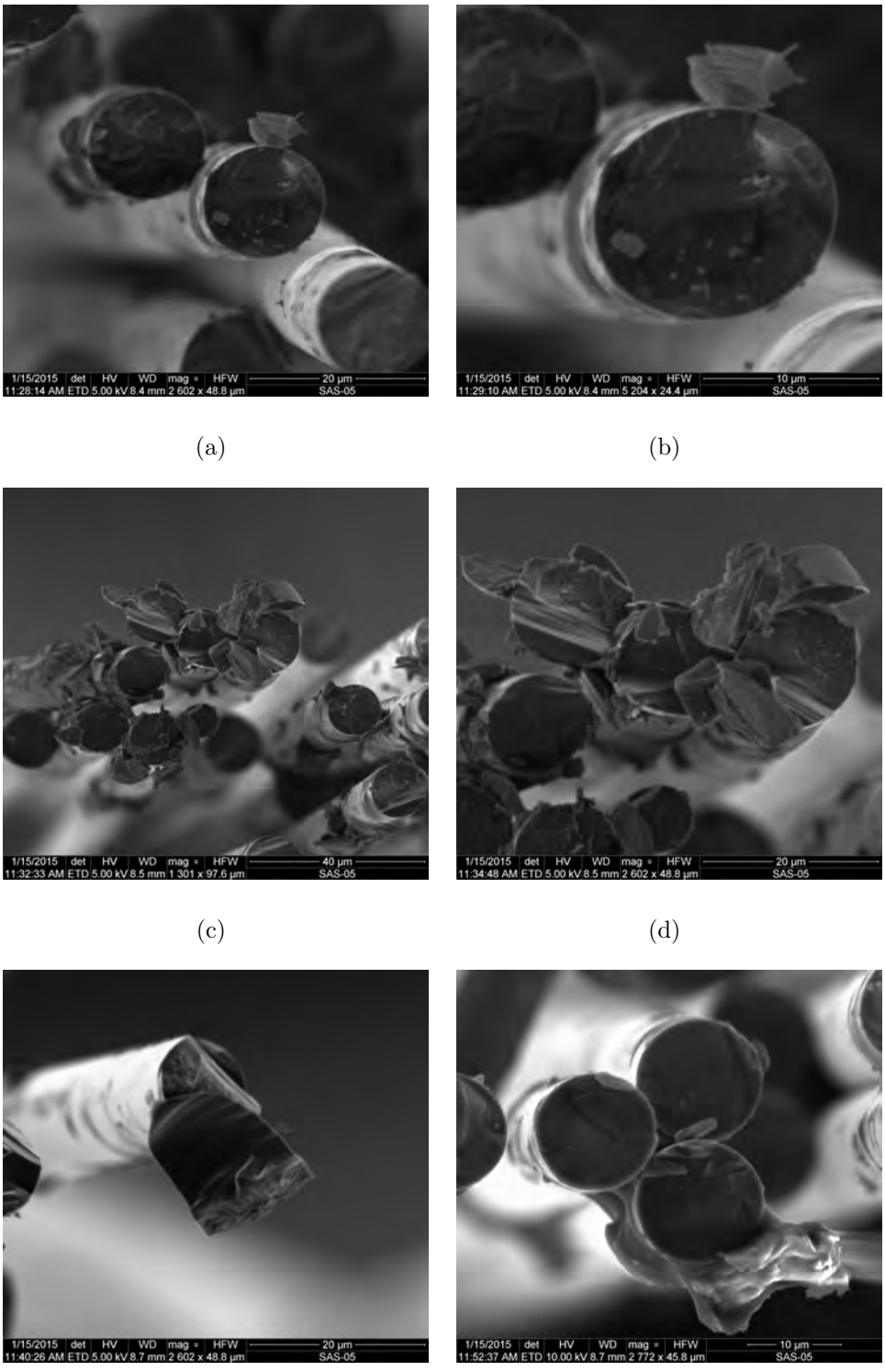
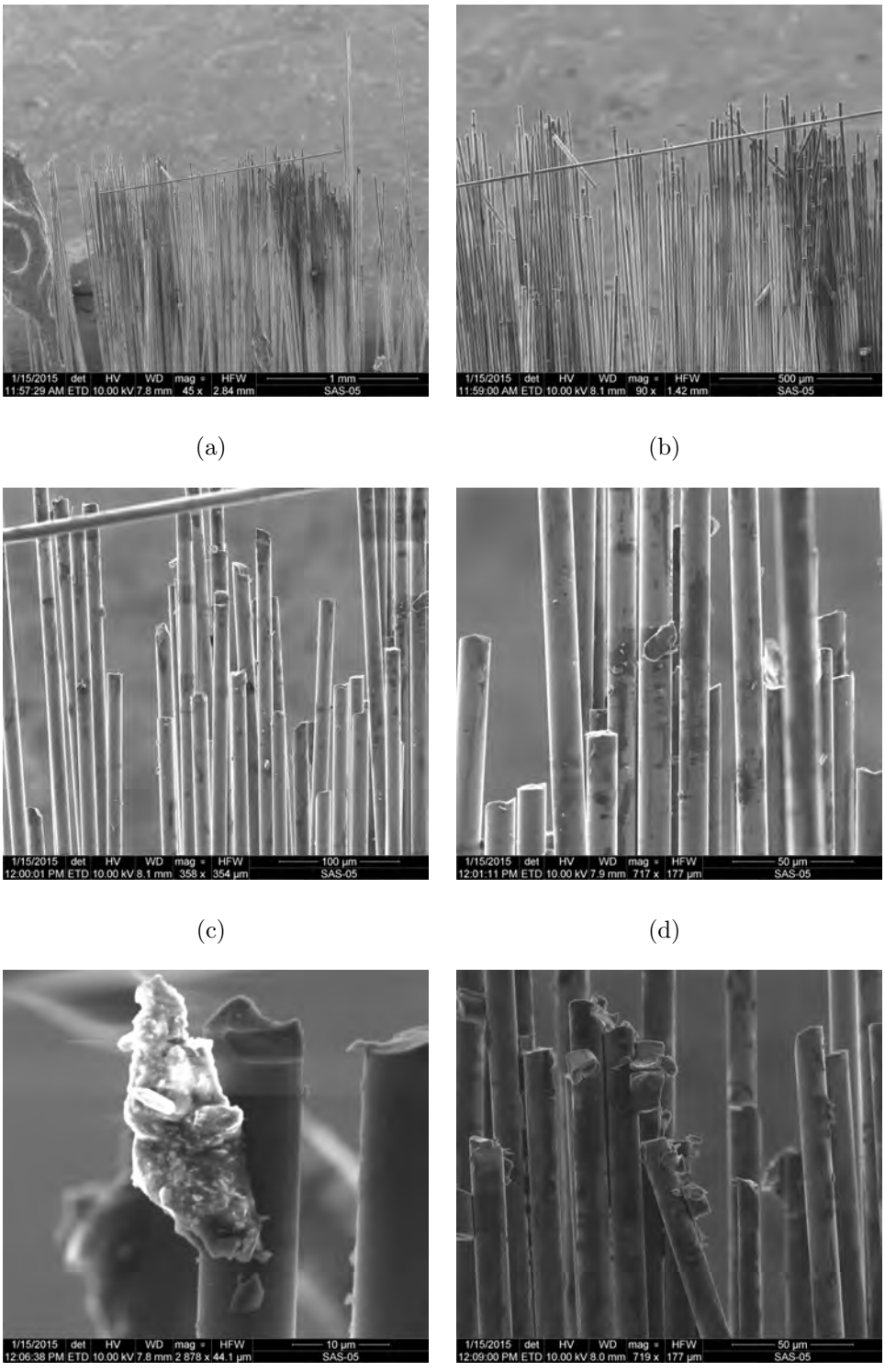


Figure B.43. Hi-Nicalon^{TM} S fiber tow specimen SS1, lower section, (800°C, σ = 2.96 MPa, t = 100 h)

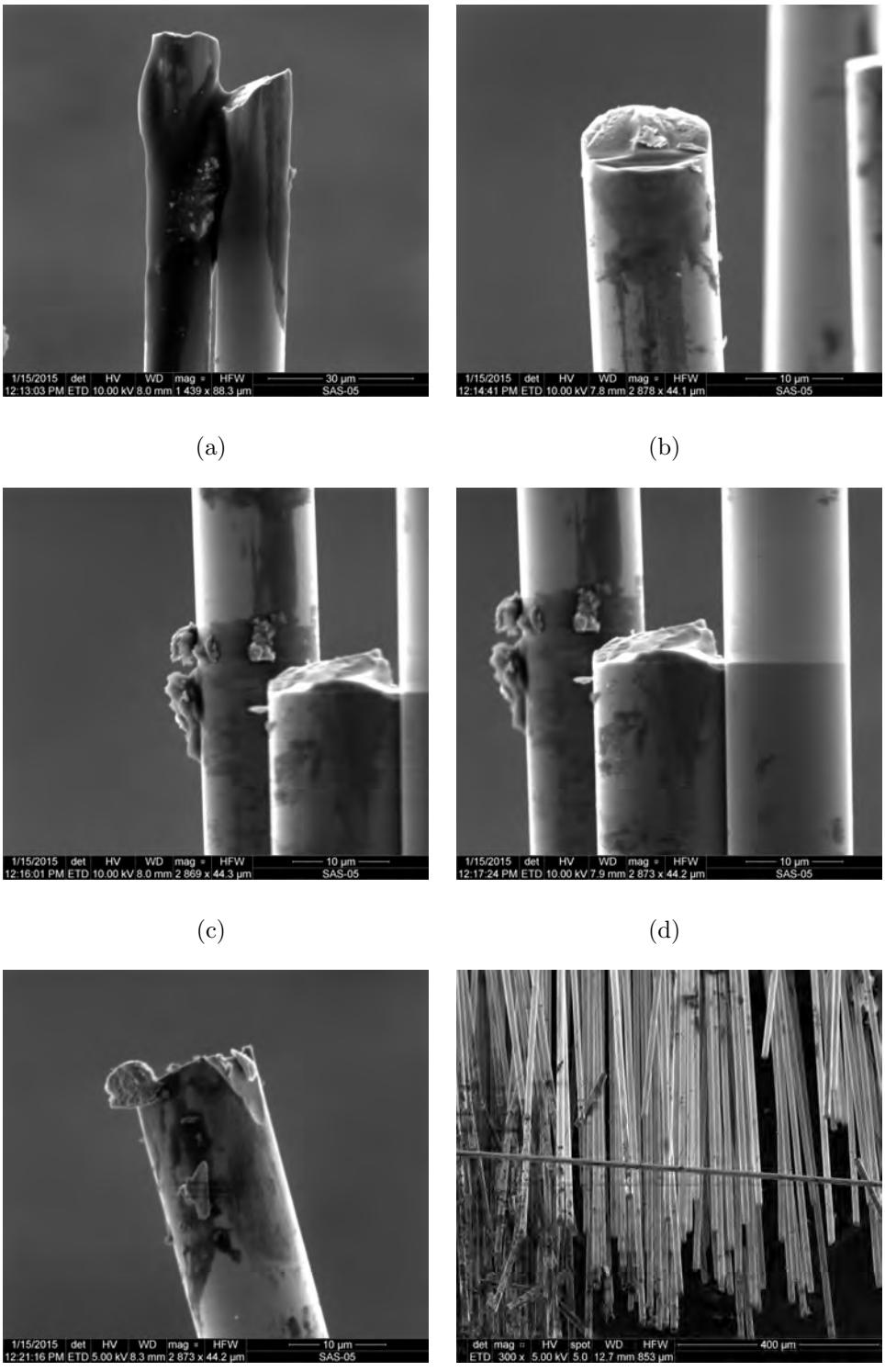


(a) (b)

(c) (d)

(e) (f)

Figure B.44. Hi-Nicalon^{TM} S fiber tow specimen SS1, lower section, (800°C, σ = 2.96 MPa, t = 100 h)

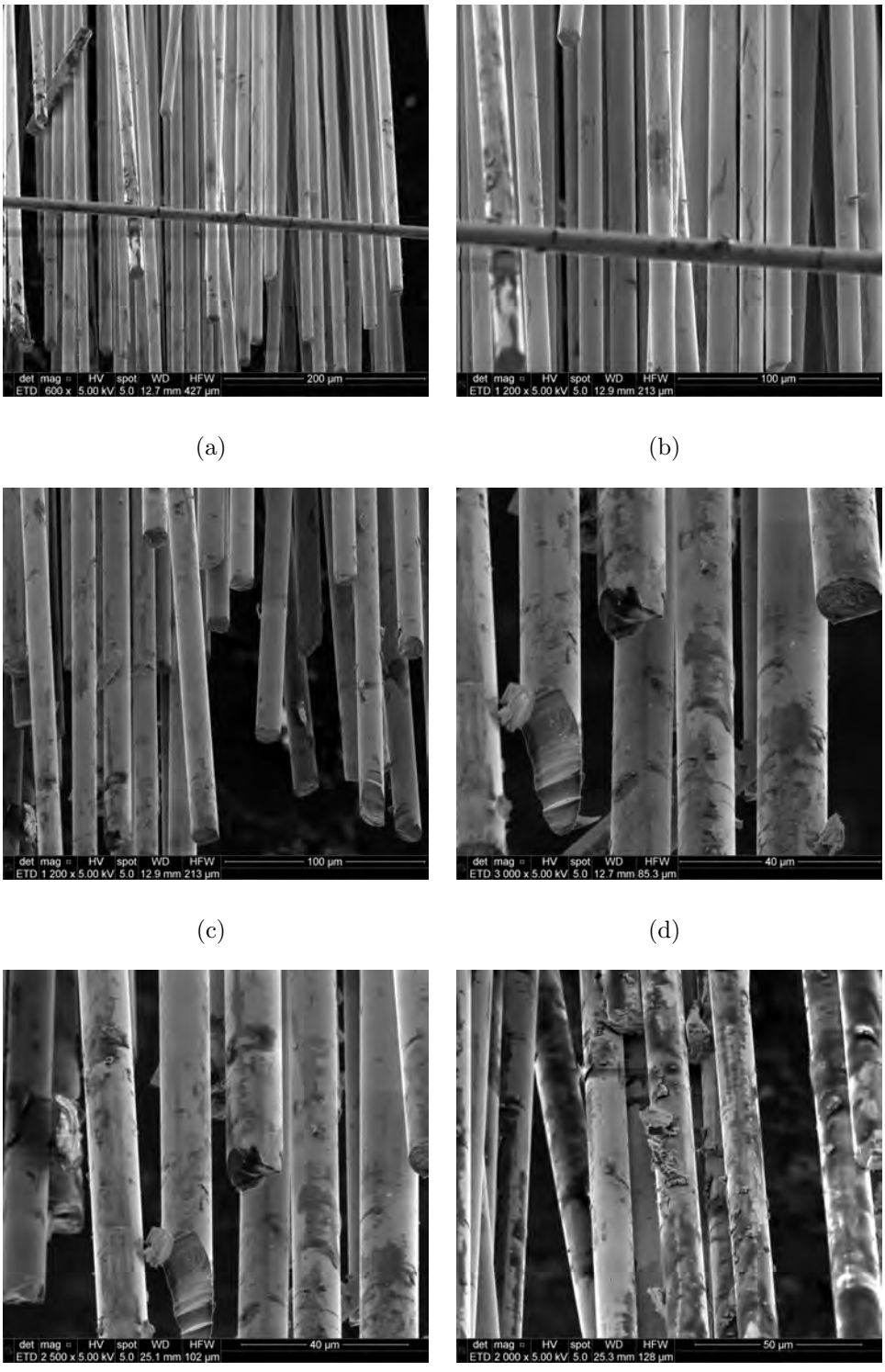


(a) (b)

(c) (d)

(e) (f)

Figure B.45. Hi-Nicalon^{TM} S fiber tow specimen SS1, lower section, (800°C, σ = 2.96 MPa, t = 100 h)



(a) (b)

(c) (d)

(e) (f)

Figure B.46. Hi-Nicalon^{TM} S fiber tow specimen SS1, lower section, (800°C, σ = 2.96 MPa, t = 100 h)

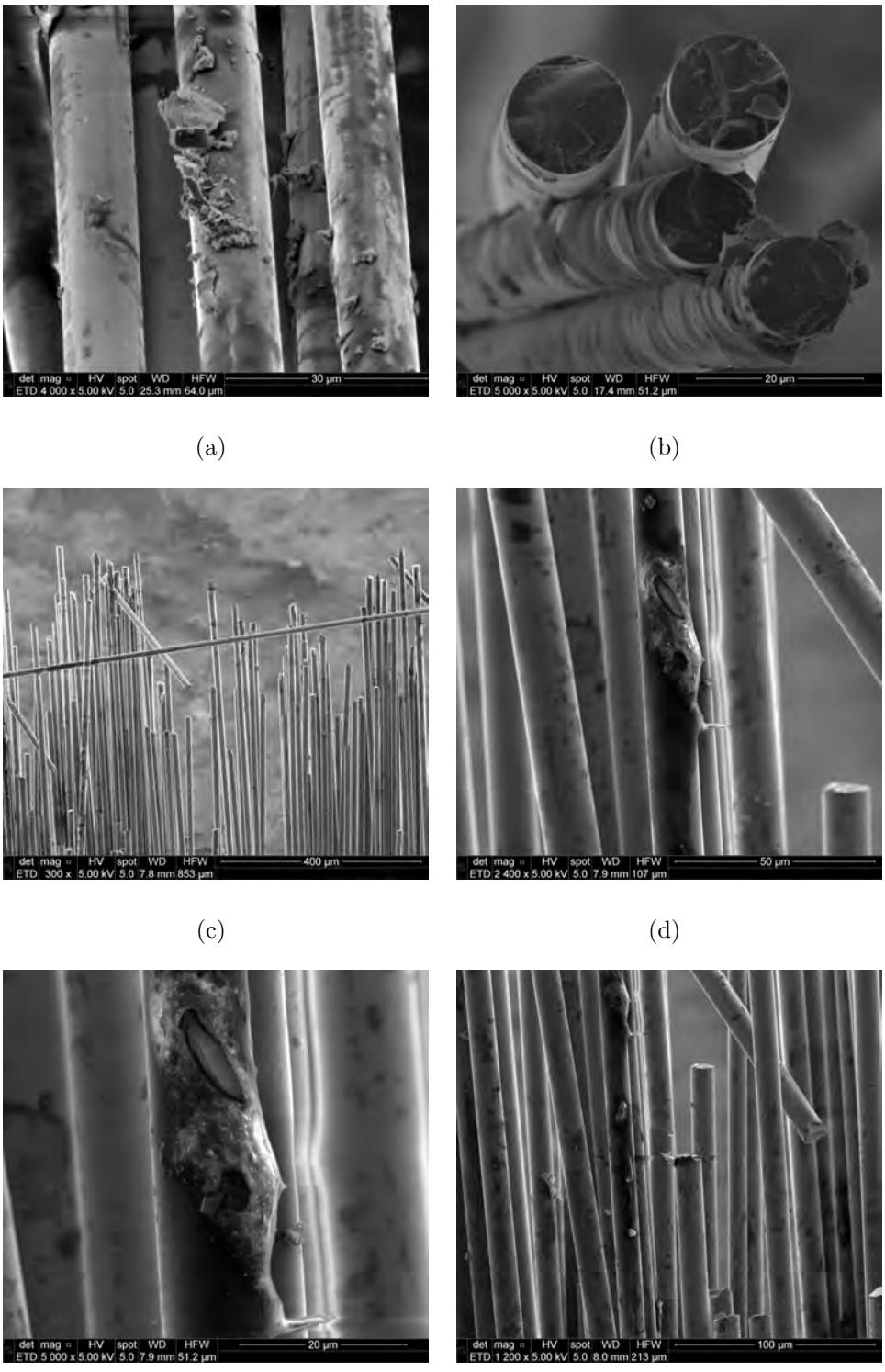
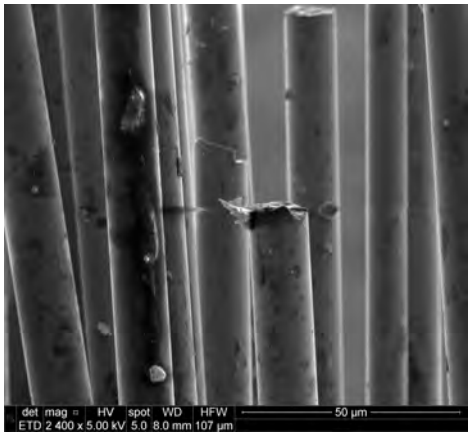
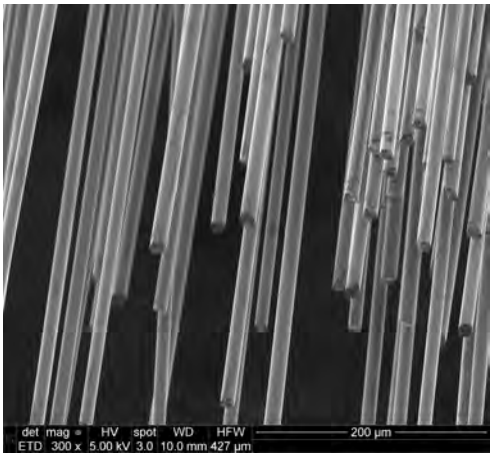


Figure B.47. Hi-Nicalon^{TM} S fiber tow specimen SS1, lower section, (800°C, σ = 2.96 MPa, t = 100 h)

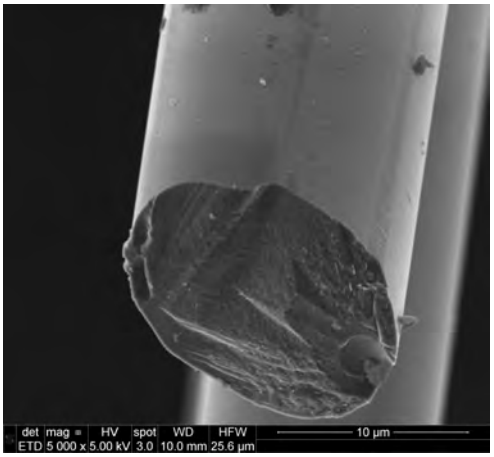


(a)

Figure B.48. Hi-Nicalon^{TM} S fiber tow specimen SS1, lower section, (800°C, σ = 2.96 MPa, t = 100 h)

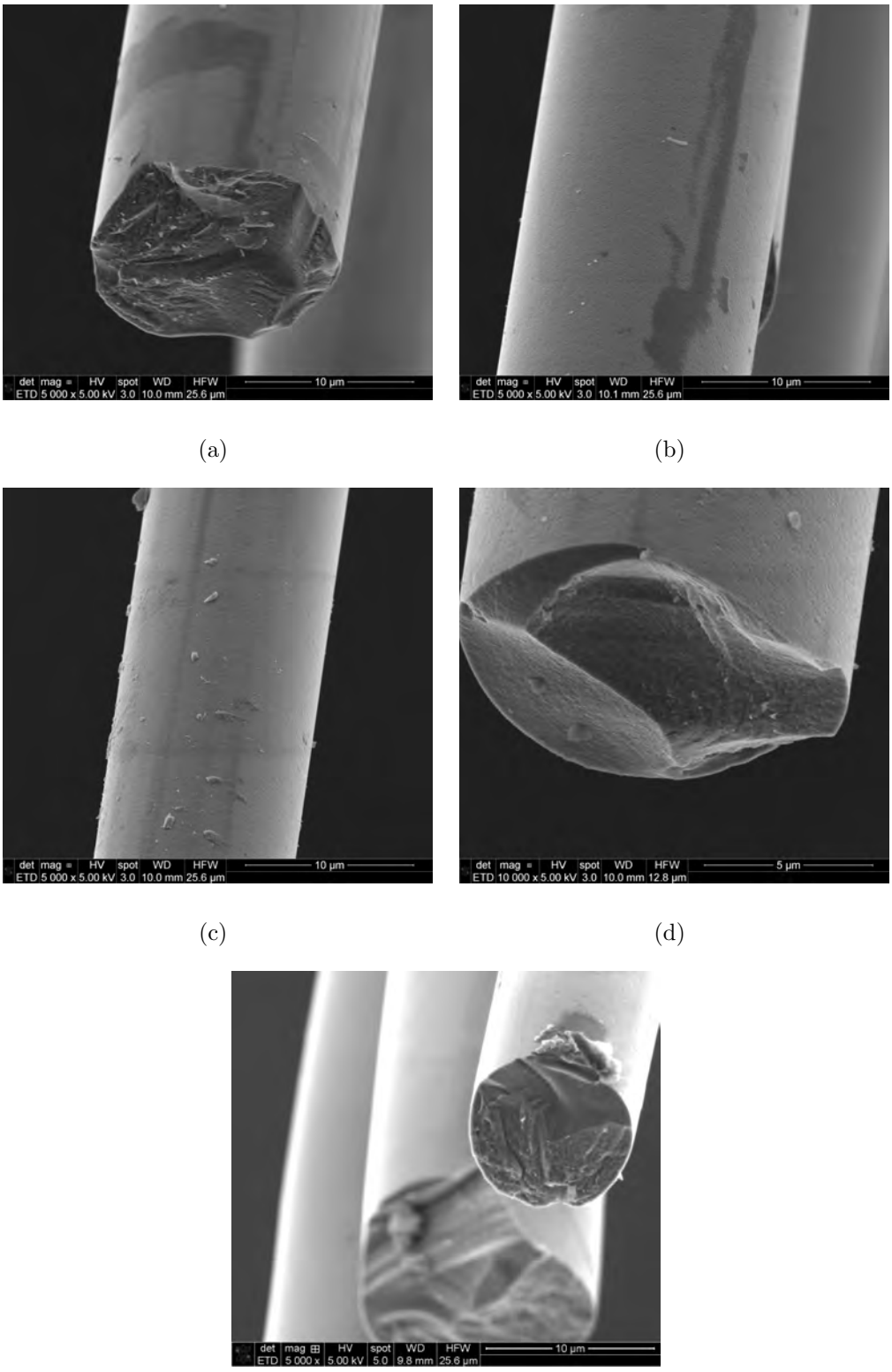


(a)



(b)

Figure B.49. Hi-Nicalon^{TM} S fiber tow specimen SS1, center section, (800°C, σ = 2.96 MPa, t = 100 h)

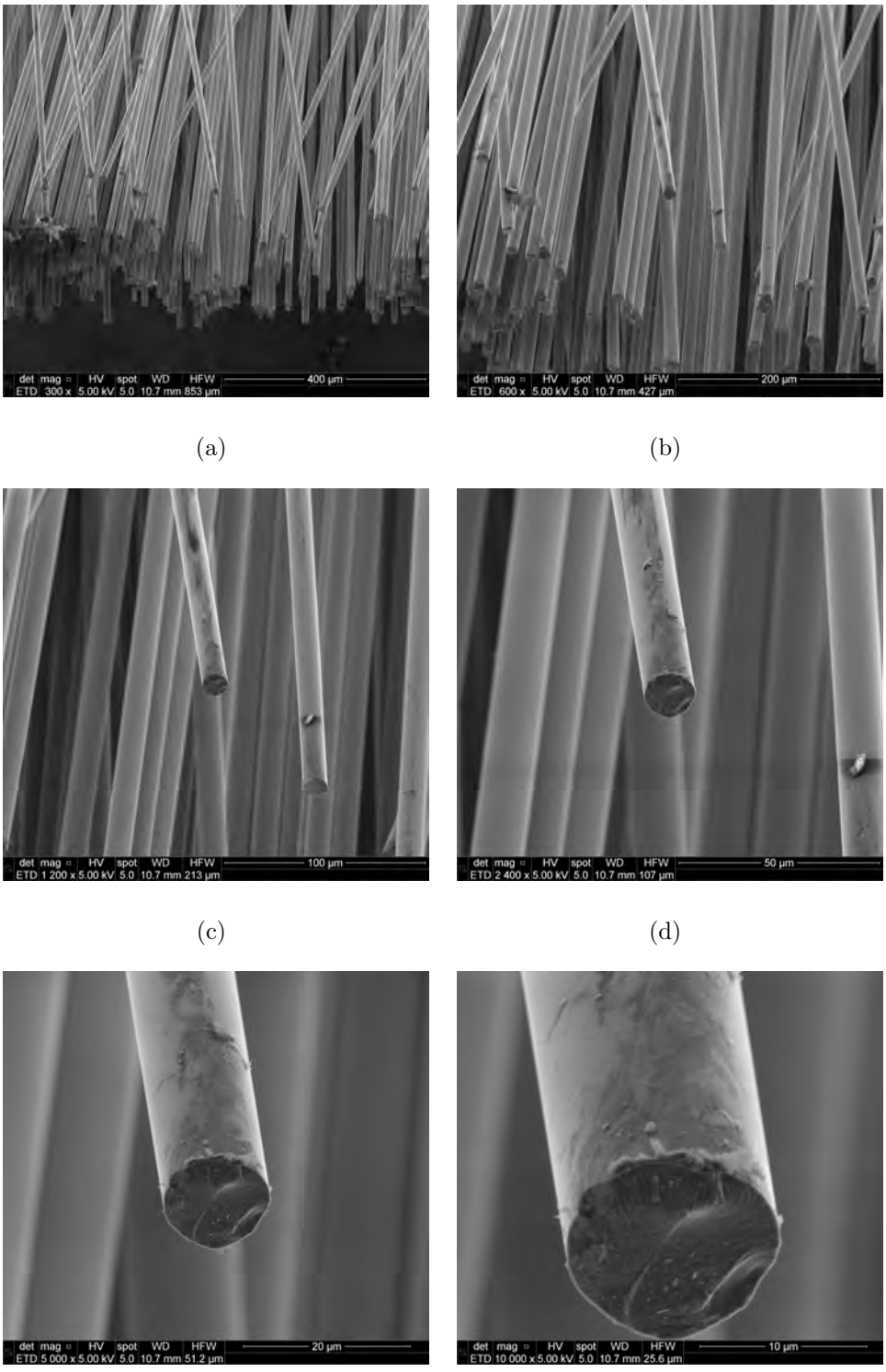


(a) (b)

(c) (d)

(e)

Figure B.50. Hi-Nicalon^{TM} S fiber tow specimen SS1, center section, (800°C, σ = 2.96 MPa, t = 100 h)

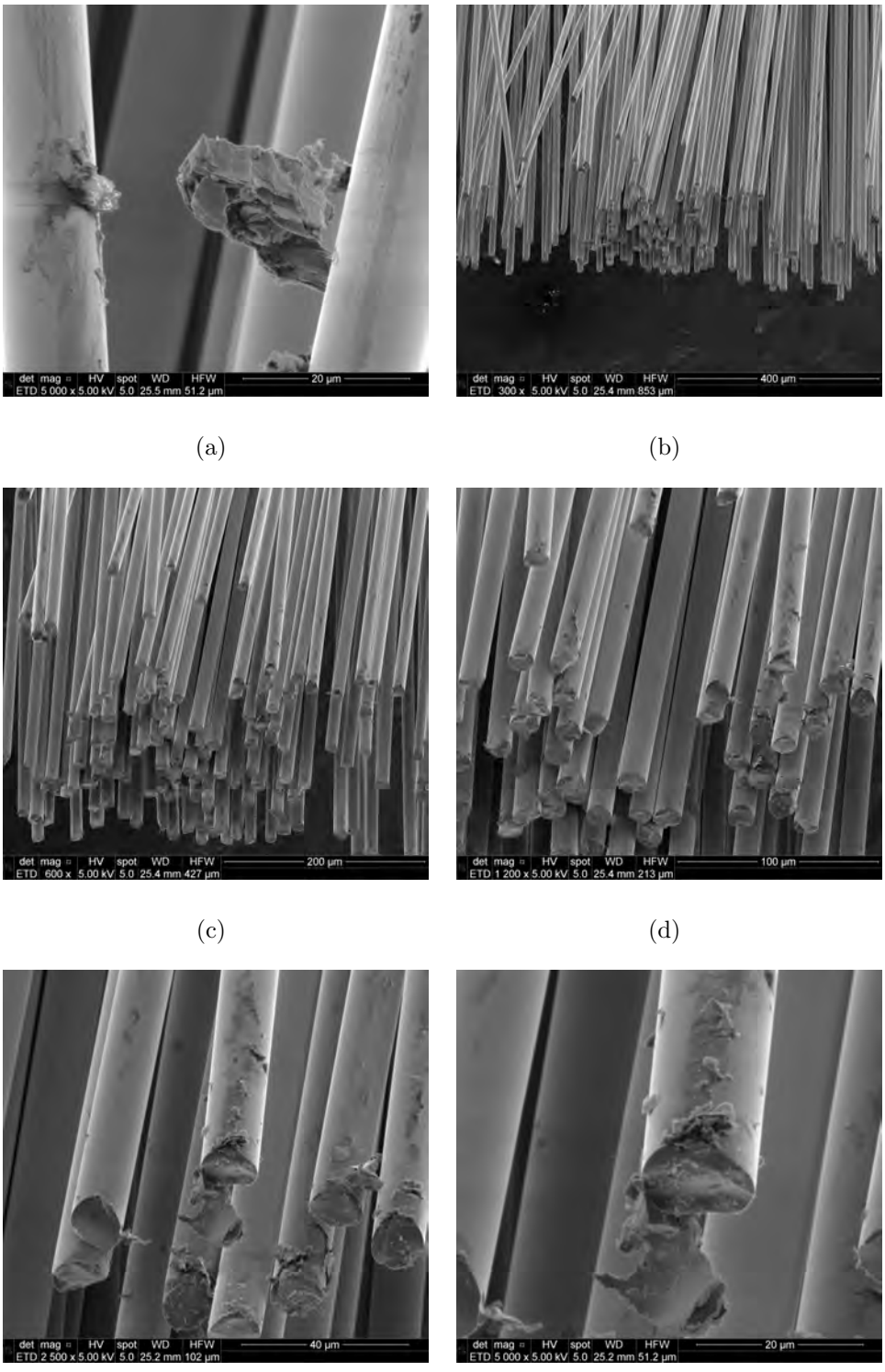


(a) (b)

(c) (d)

(e) (f)

Figure B.51. Hi-Nicalon^{TM} S fiber tow specimen SS1, upper section, (800°C, σ = 2.96 MPa, t = 100 h)



(a) (b)

(c) (d)

(e) (f)

Figure B.52. Hi-Nicalon^{TM} S fiber tow specimen SS1, upper section, (800°C, σ = 2.96 MPa, t = 100 h)

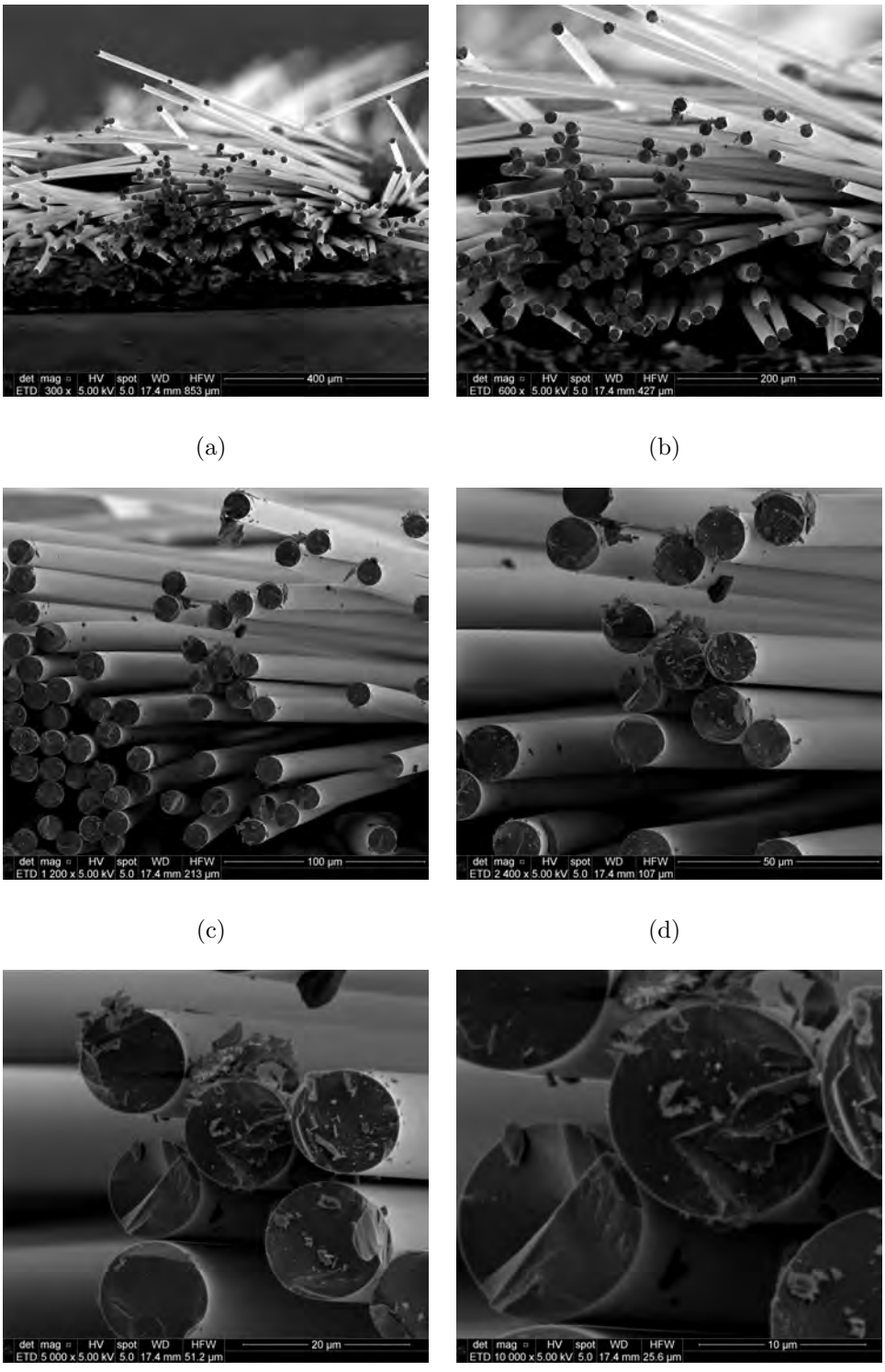
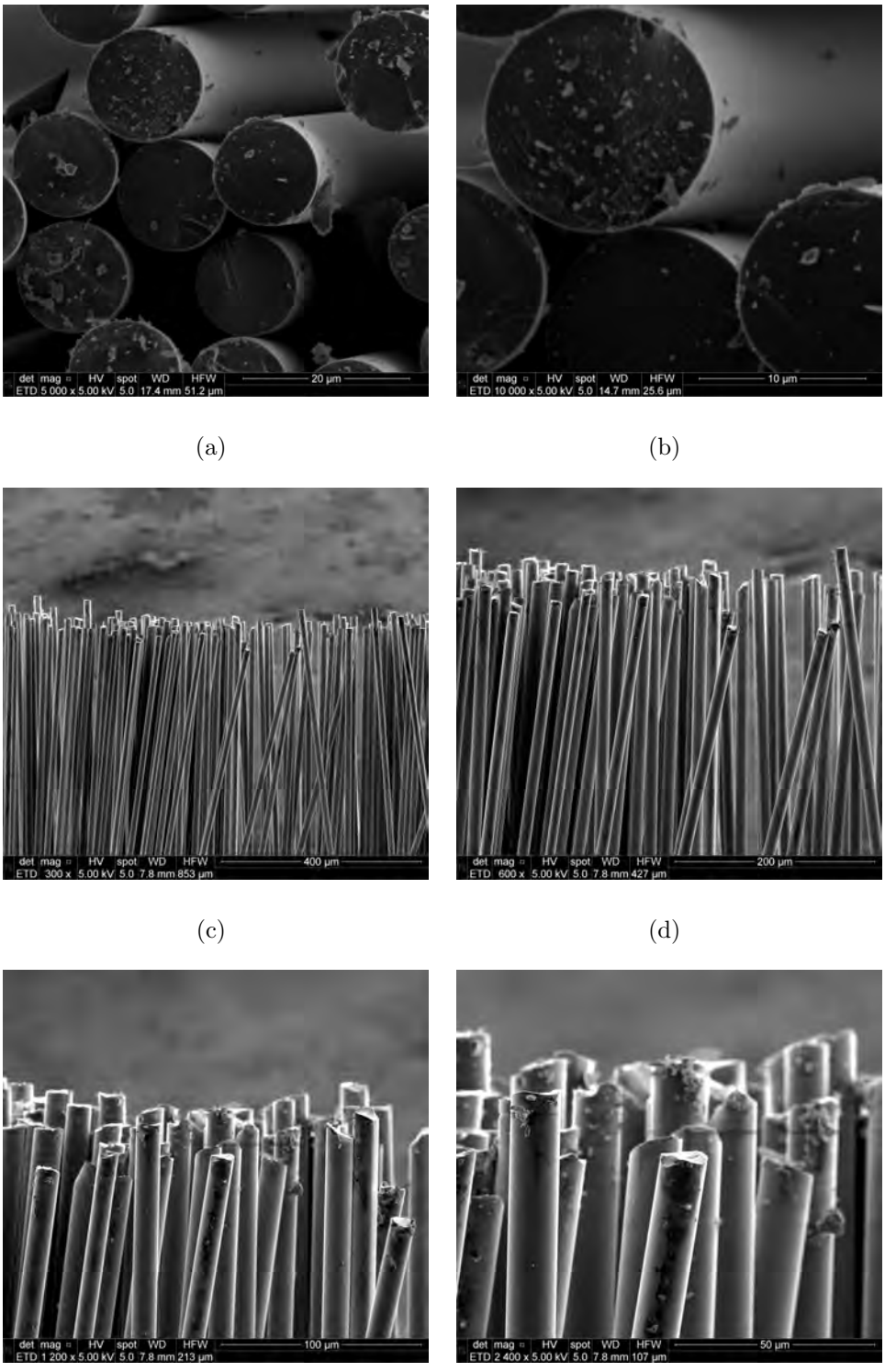


Figure B.53. Hi-Nicalon^{TM} S fiber tow specimen SS1, upper section, (800°C, σ = 2.96 MPa, t = 100 h)

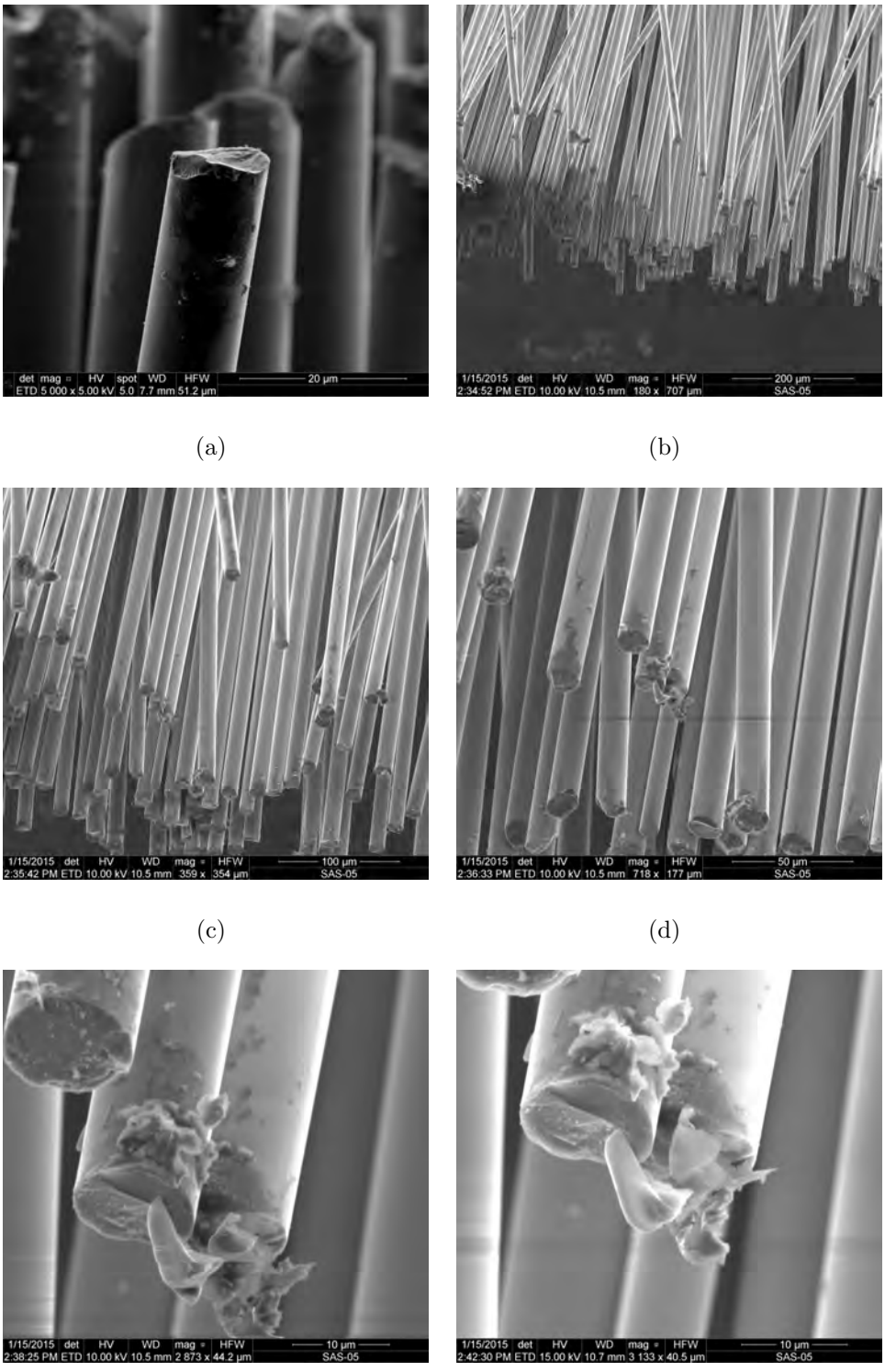


(a) (b)

(c) (d)

(e) (f)

Figure B.54. Hi-Nicalon^{TM} S fiber tow specimen SS1, upper section, (800°C, σ = 2.96 MPa, t = 100 h)

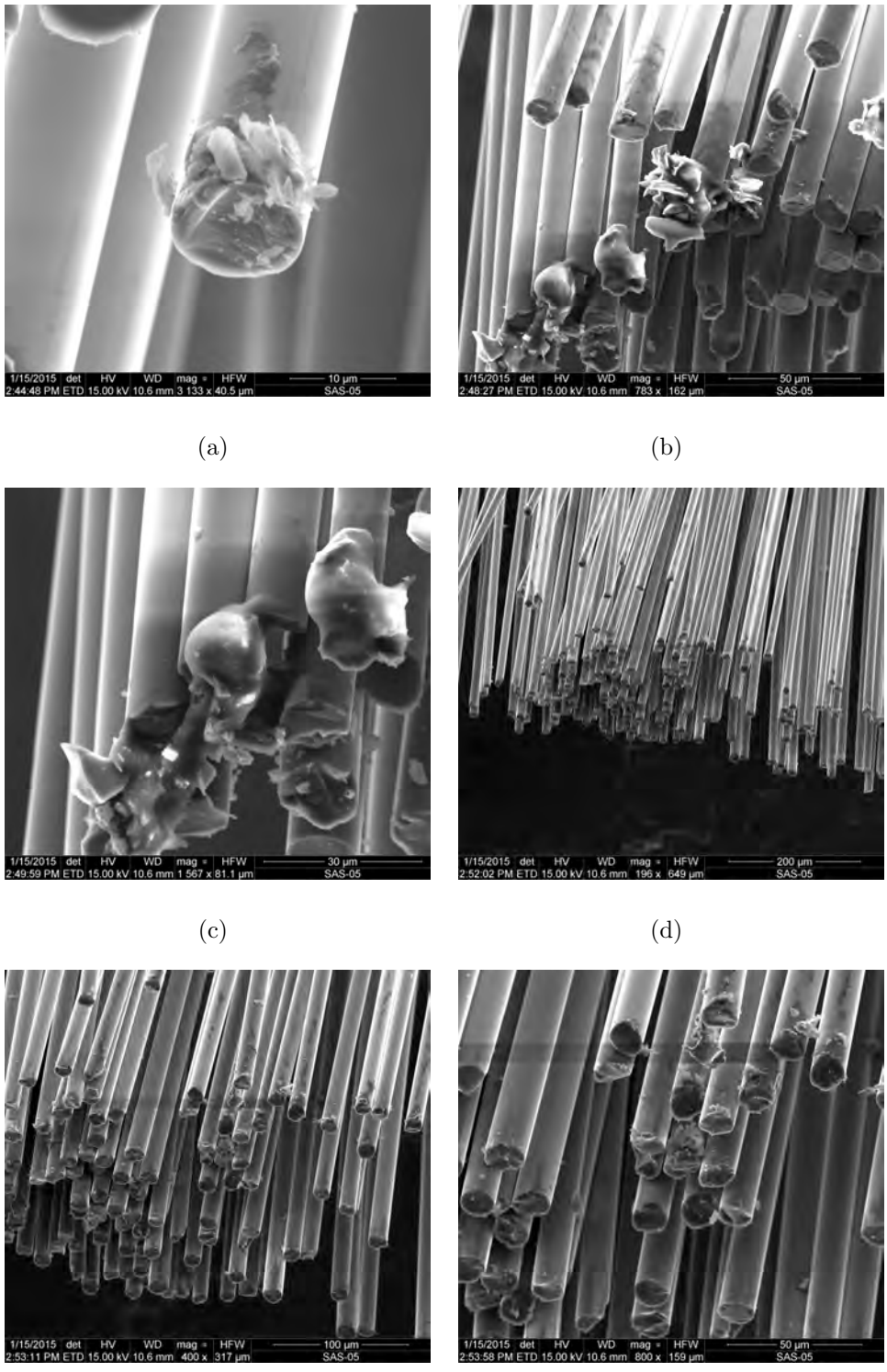


(a) (b)

(c) (d)

(e) (f)

Figure B.55. Hi-Nicalon^{TM} S fiber tow specimen SS1, upper section, (800°C, σ = 2.96 MPa, t = 100 h)

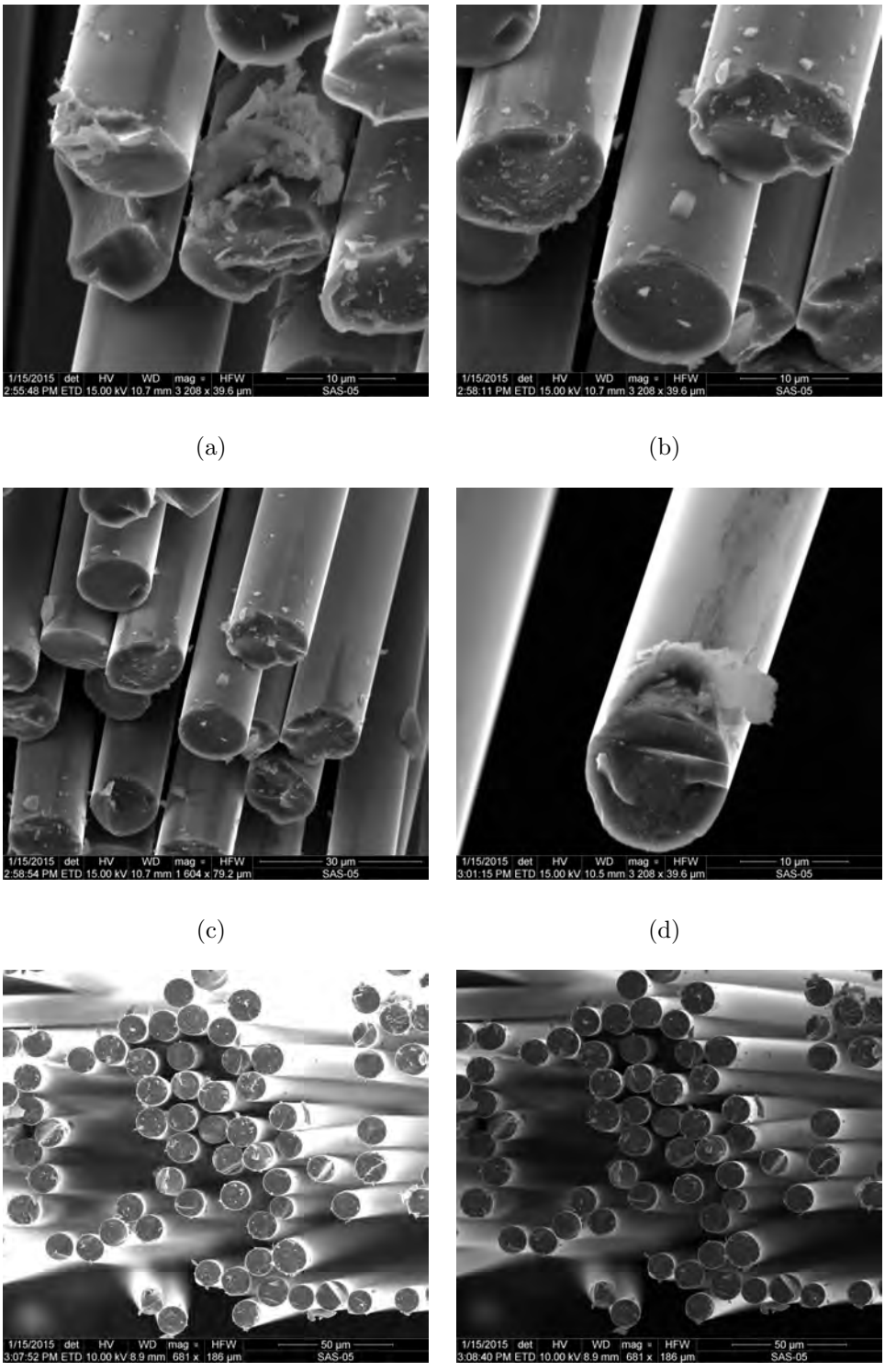


(a) (b)

(c) (d)

(e) (f)

Figure B.56. Hi-Nicalon^{TM} S fiber tow specimen SS1, upper section, (800°C, σ = 2.96 MPa, t = 100 h)

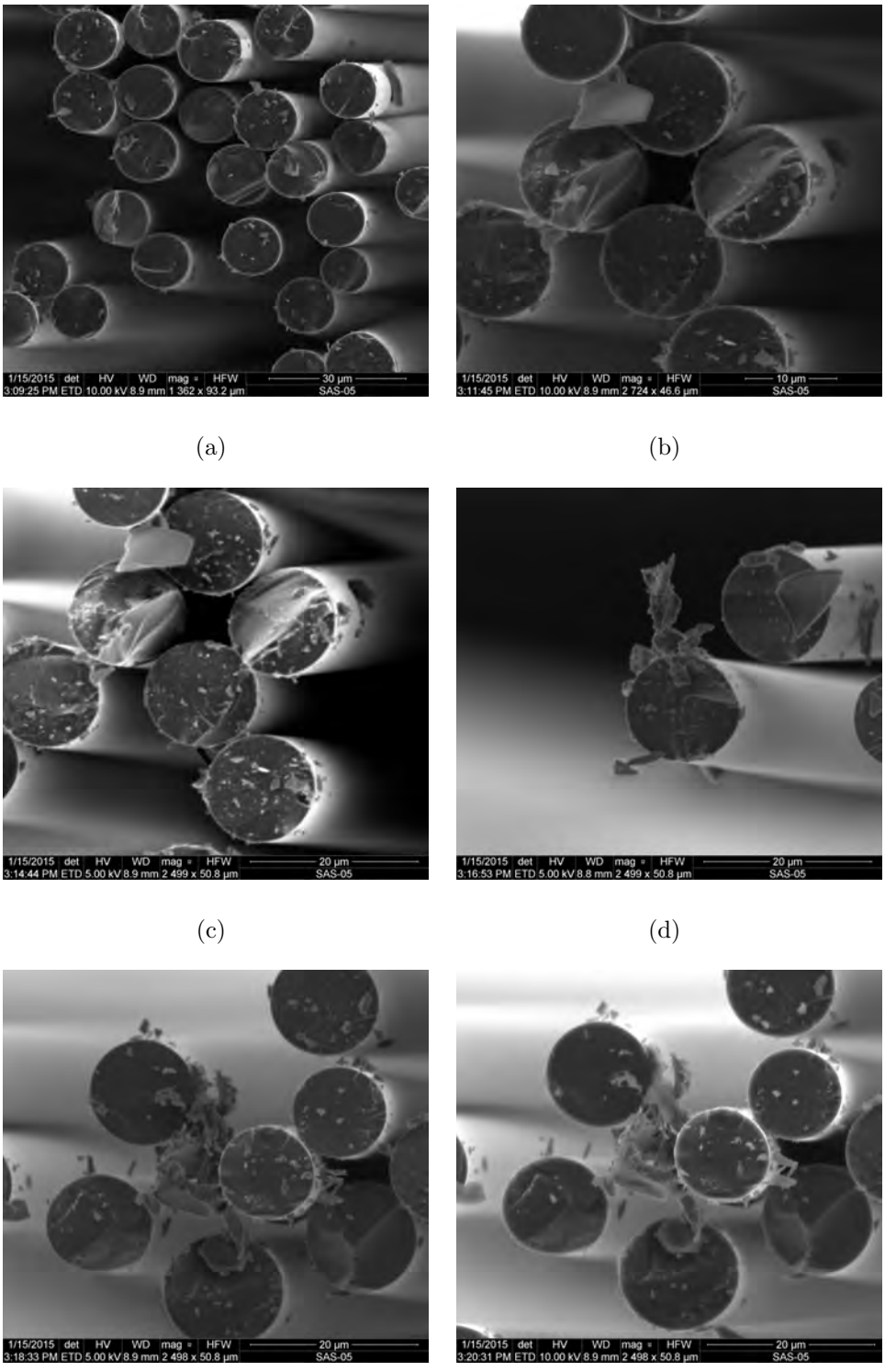


(a) (b)

(c) (d)

(e) (f)

Figure B.57. Hi-Nicalon^{TM} S fiber tow specimen SS1, upper section, (800°C, σ = 2.96 MPa, t = 100 h)



(a) (b)

(c) (d)

(e) (f)

Figure B.58. Hi-Nicalon^{TM} S fiber tow specimen SS1, upper section, (800°C, σ = 2.96 MPa, t = 100 h)

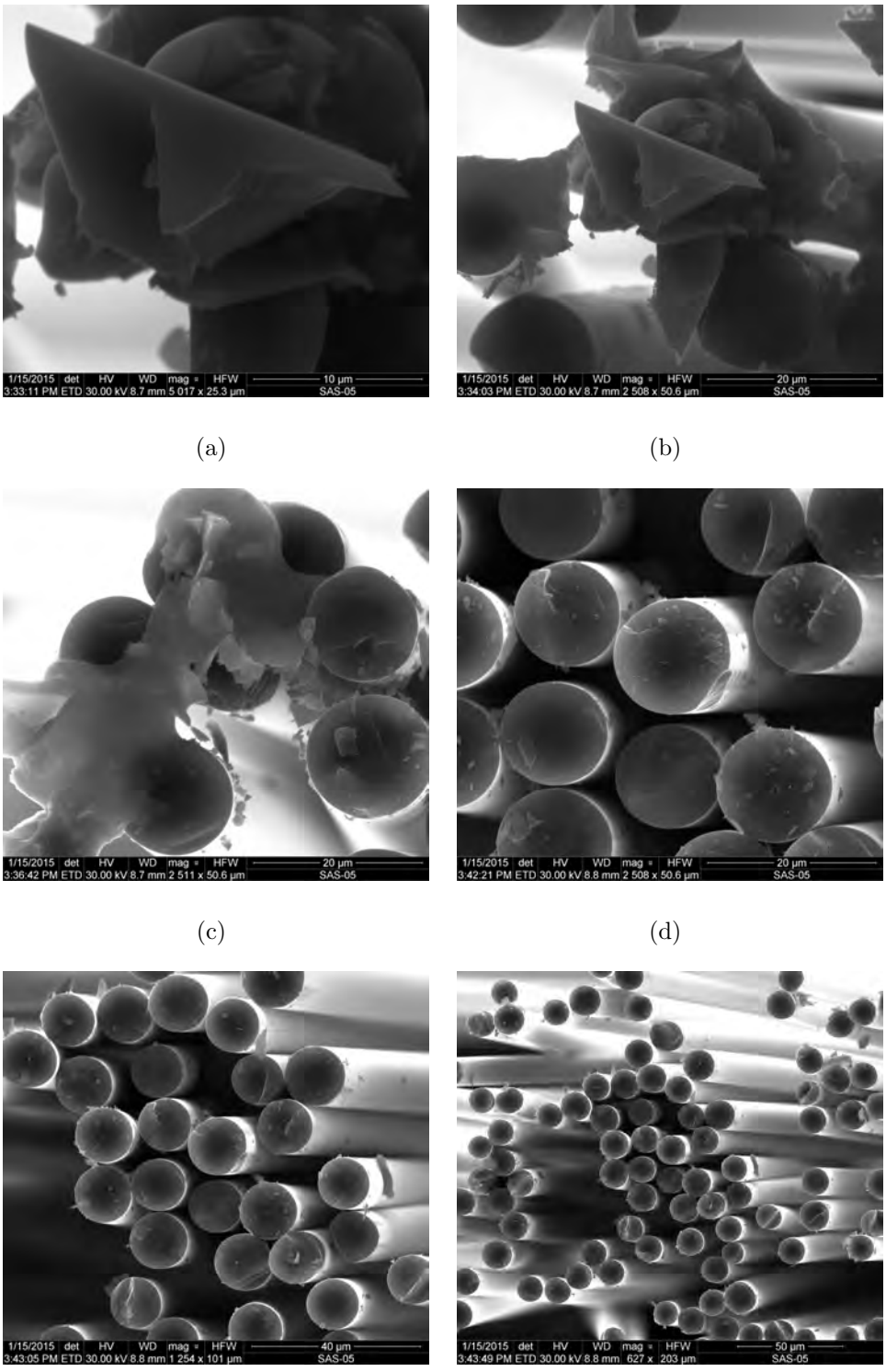


Figure B.59. Hi-Nicalon^{TM} S fiber tow specimen SS1, upper section, (800°C, σ = 2.96 MPa, t = 100 h)

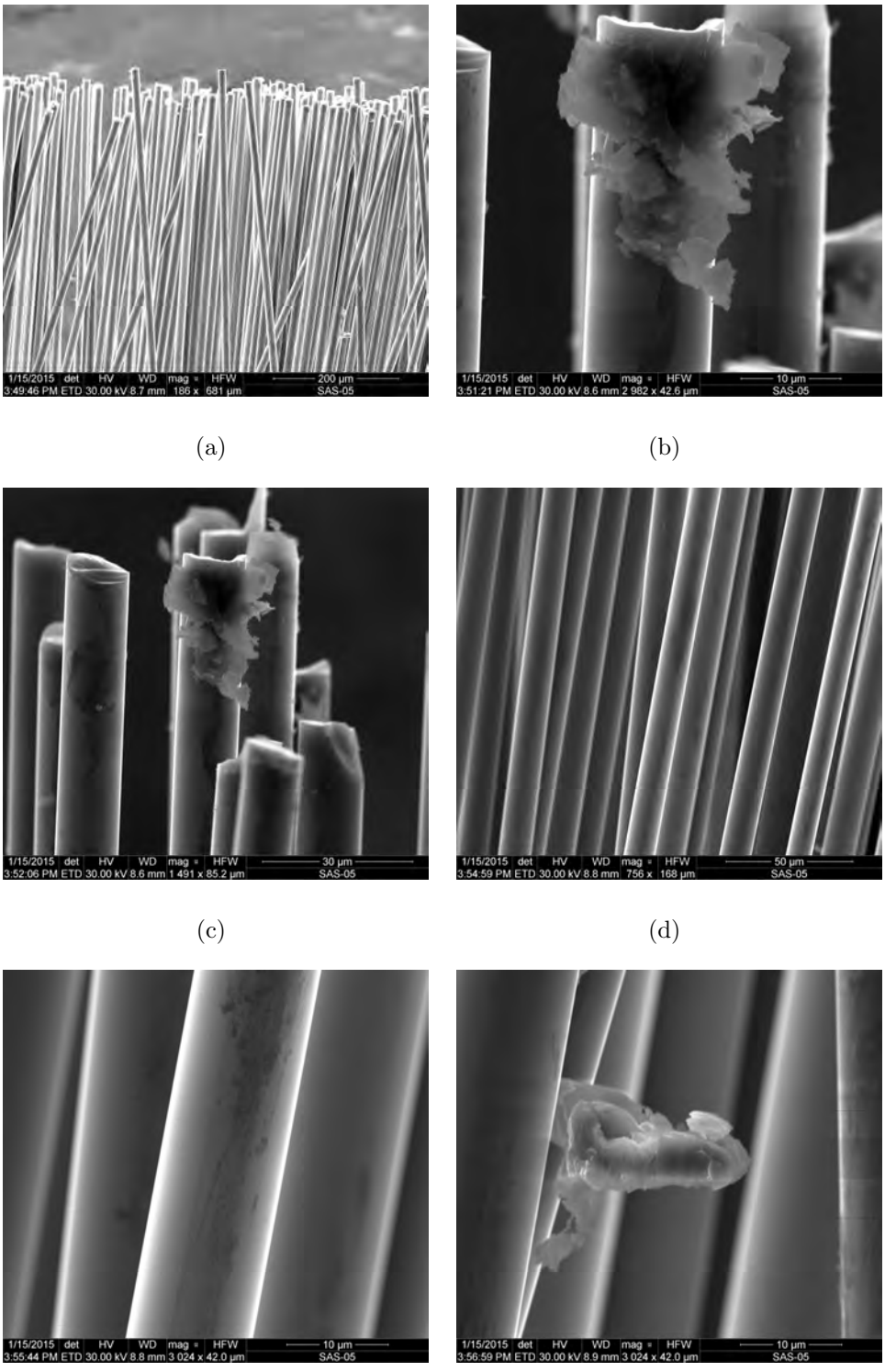
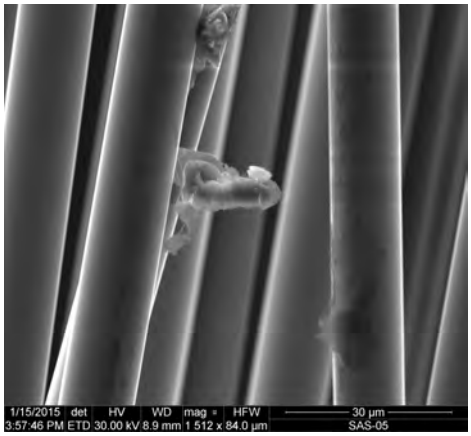
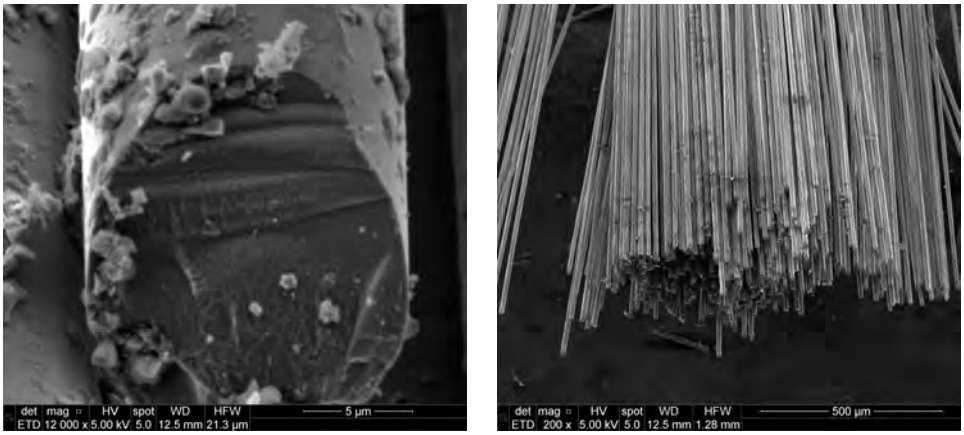


Figure B.60. Hi-Nicalon^{TM} S fiber tow specimen SS1, upper section, (800°C, σ = 2.96 MPa, t = 100 h)



(a)

Figure B.61. Hi-Nicalon^{TM} S fiber tow specimen SS1, upper section, (800°C, σ = 2.96 MPa, t = 100 h)



(a) (b)

Figure B.62. Hi-Nicalon^{TM} S fiber tow specimen SS2, lower section, (800°C, σ = 154 MPa, t = 100 h)

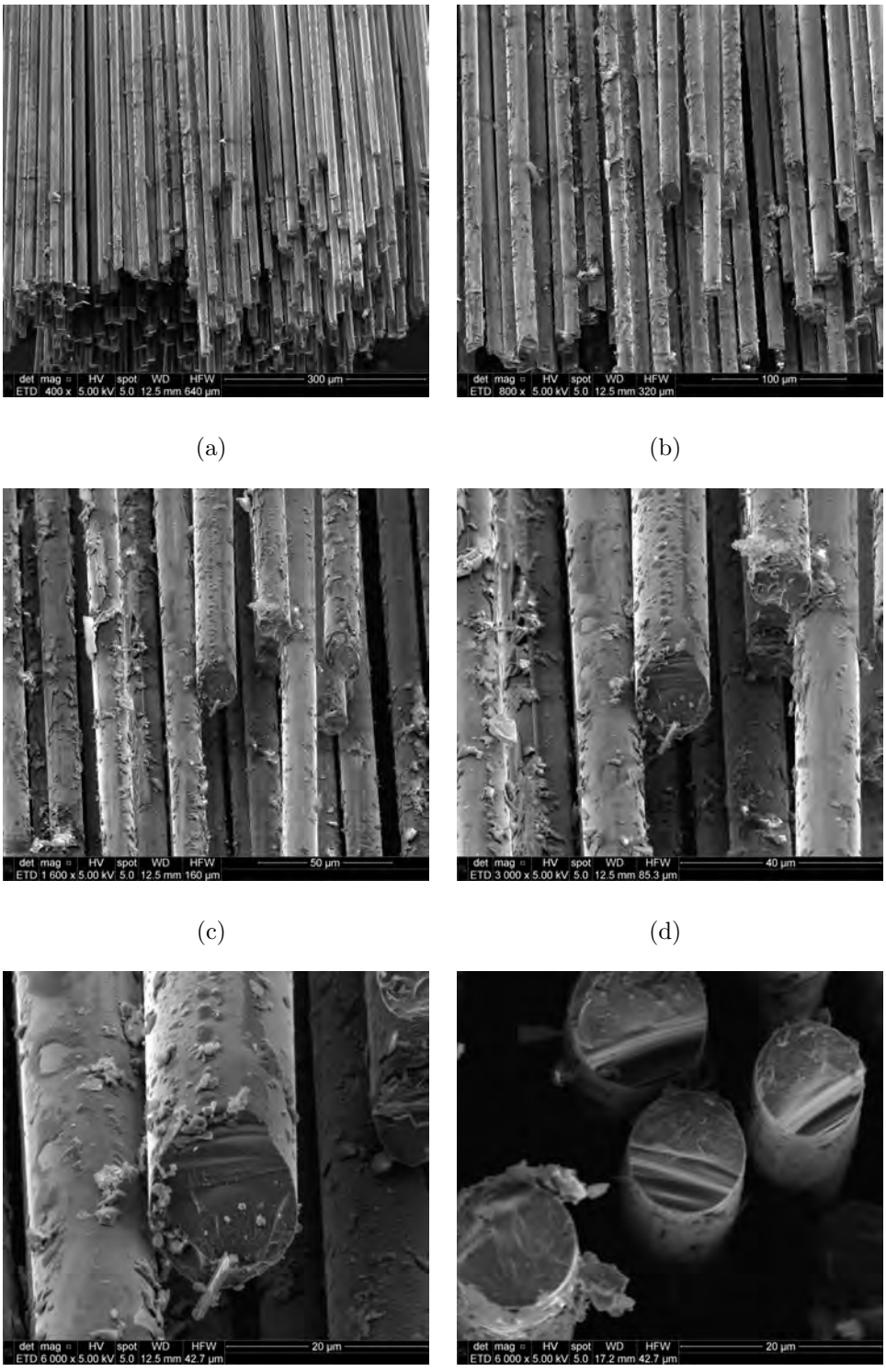
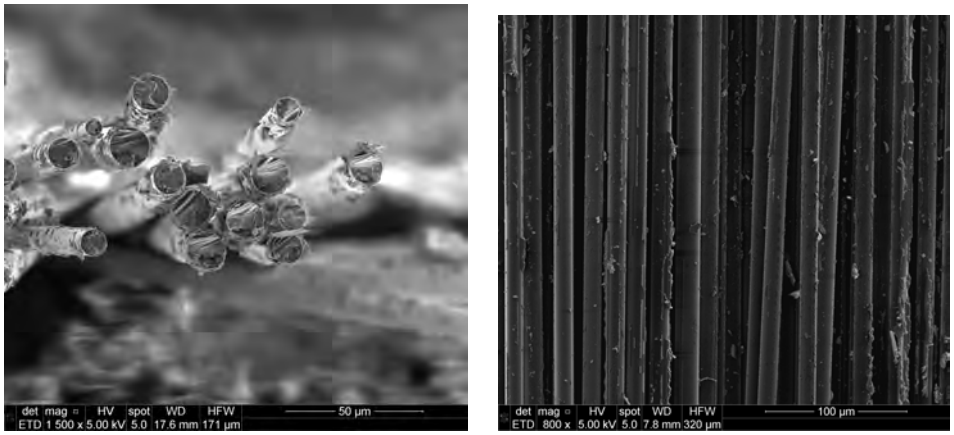
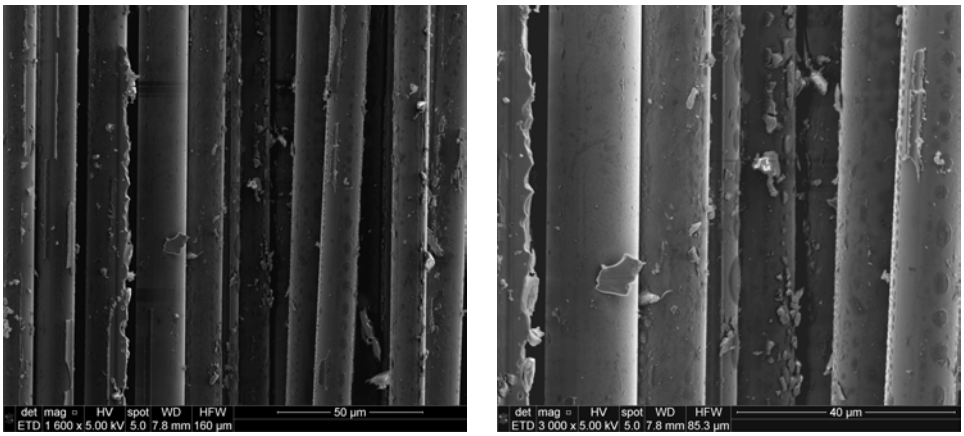


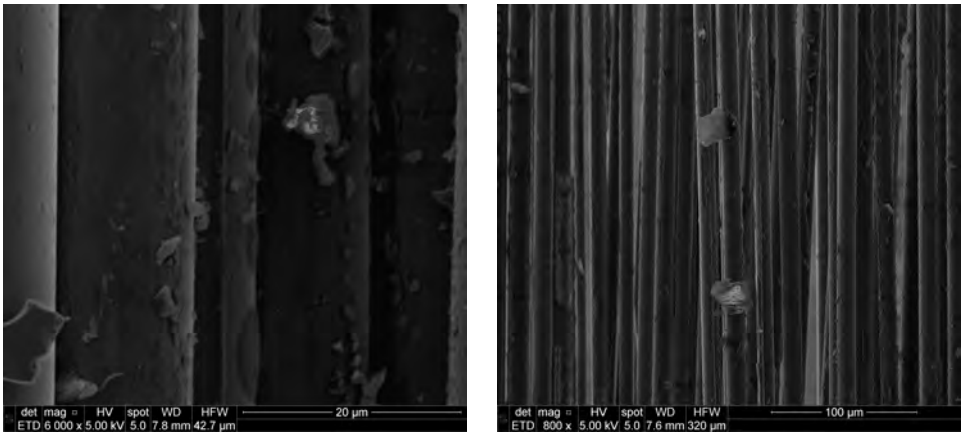
Figure B.63. Hi-Nicalon^{TM} S fiber tow specimen SS2, lower section, (800°C, σ = 154 MPa, t = 100 h)



(a) (b)

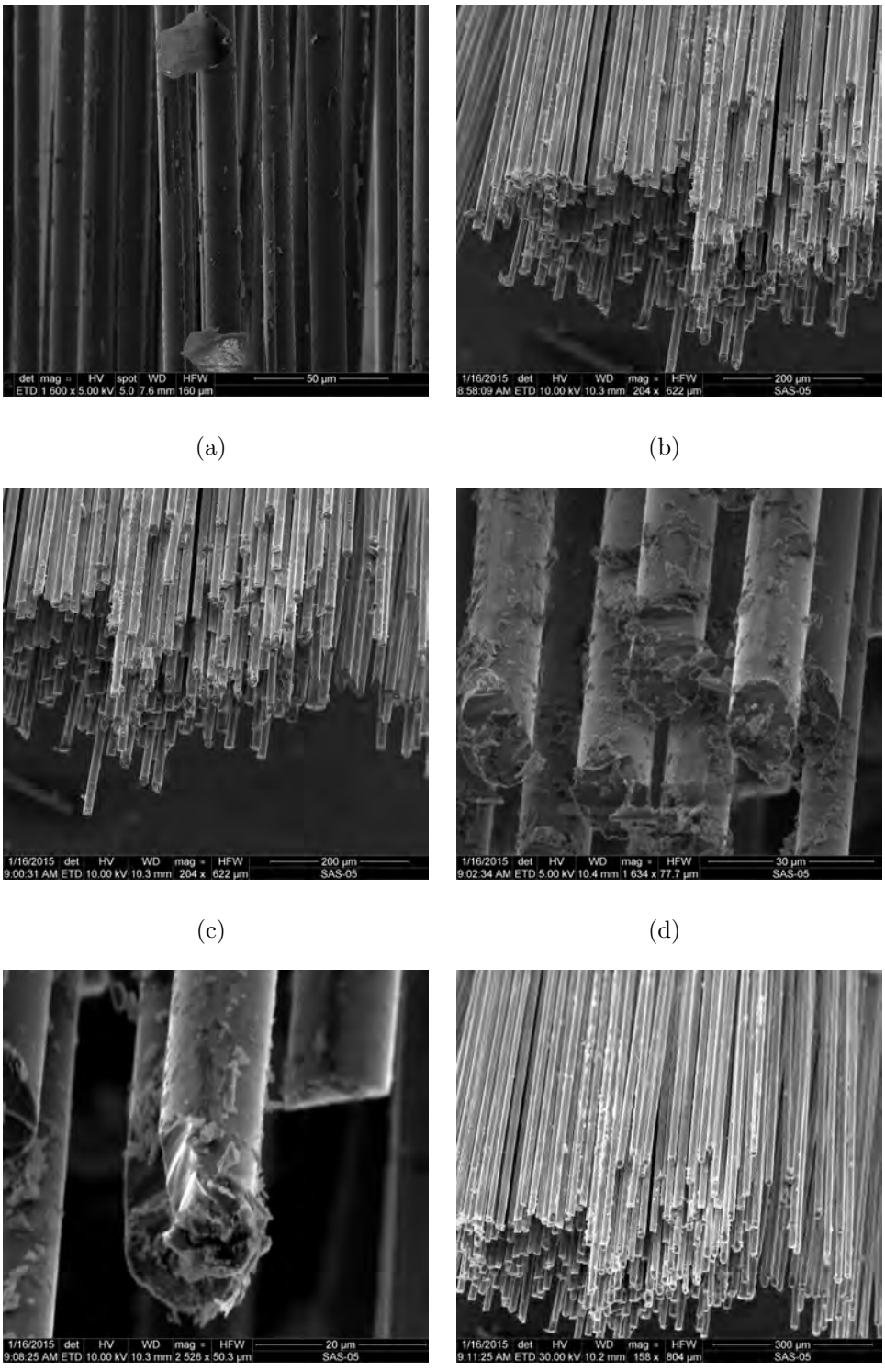


(c) (d)



(e) (f)

Figure B.64. Hi-Nicalon^{TM} S fiber tow specimen SS2, lower section, (800°C, σ = 154 MPa, t = 100 h)

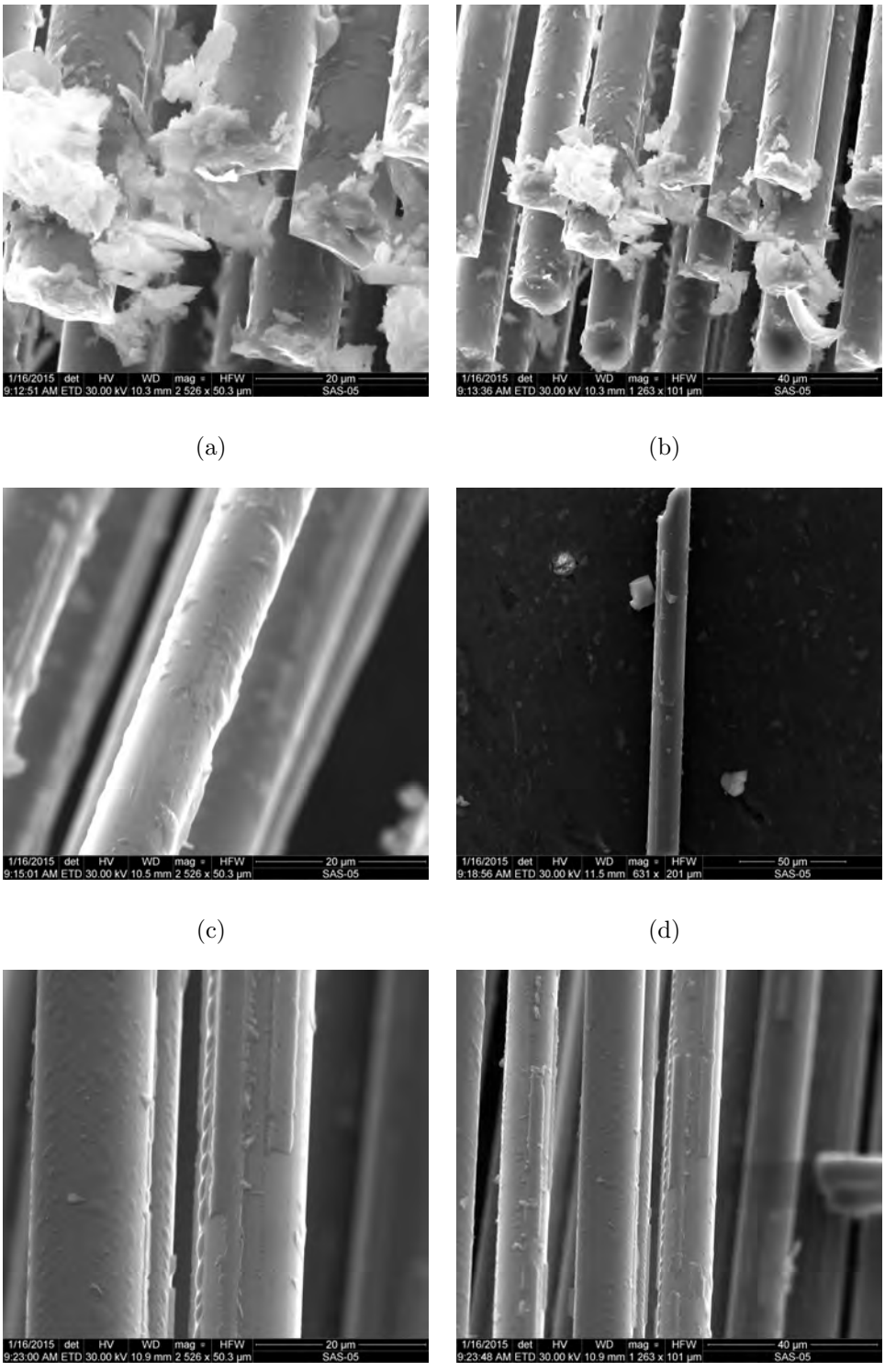


(a) (b)

(c) (d)

(e) (f)

Figure B.65. Hi-Nicalon^{TM} S fiber tow specimen SS2, lower section, (800°C, σ = 154 MPa, t = 100 h)

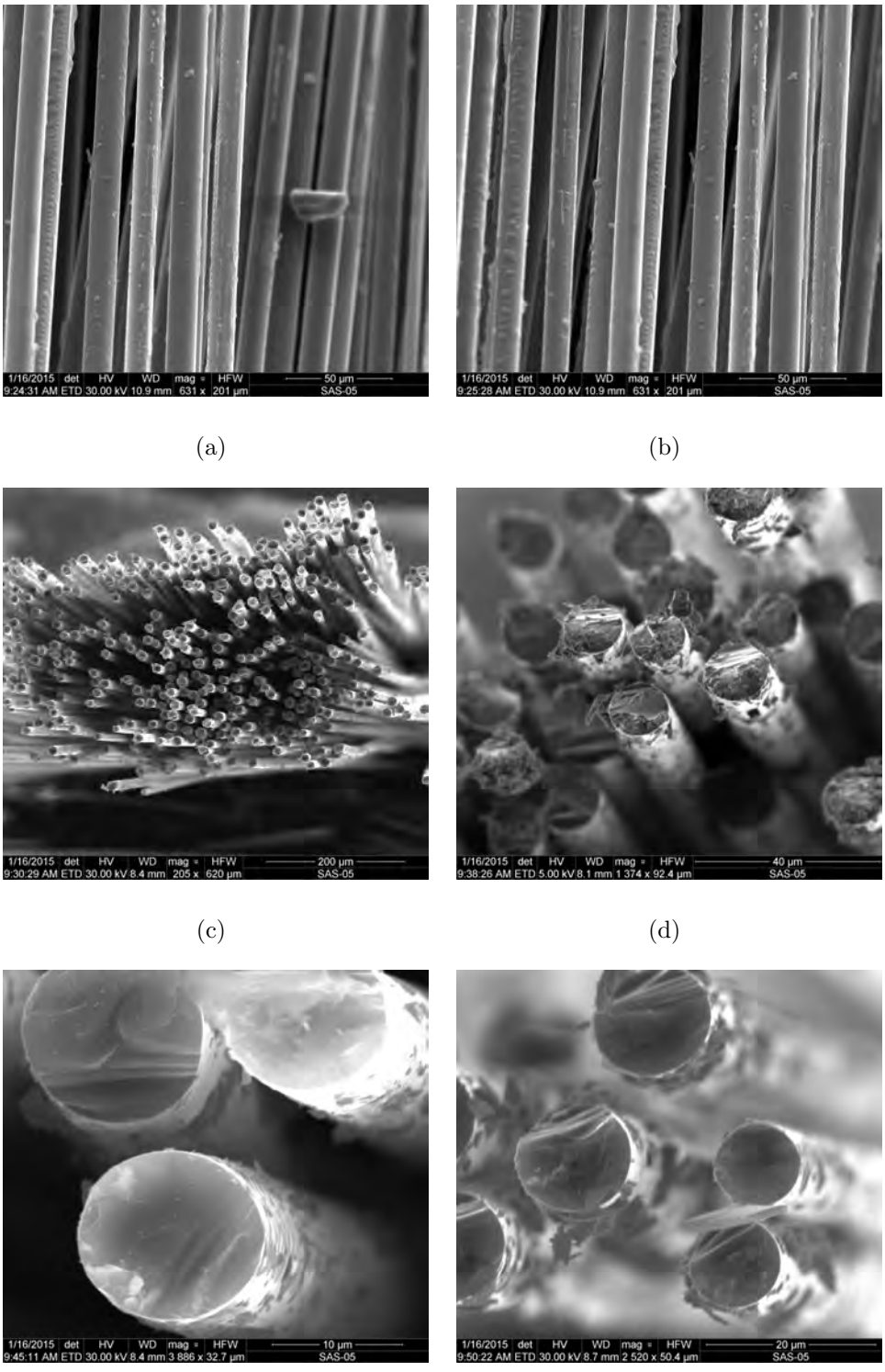


(a) (b)

(c) (d)

(e) (f)

Figure B.66. Hi-Nicalon^{TM} S fiber tow specimen SS2, lower section, (800°C, σ = 154 MPa, t = 100 h)



(a) (b)

(c) (d)

(e) (f)

Figure B.67. Hi-Nicalon^{TM} S fiber tow specimen SS2, lower section, (800°C, σ = 154 MPa, t = 100 h)

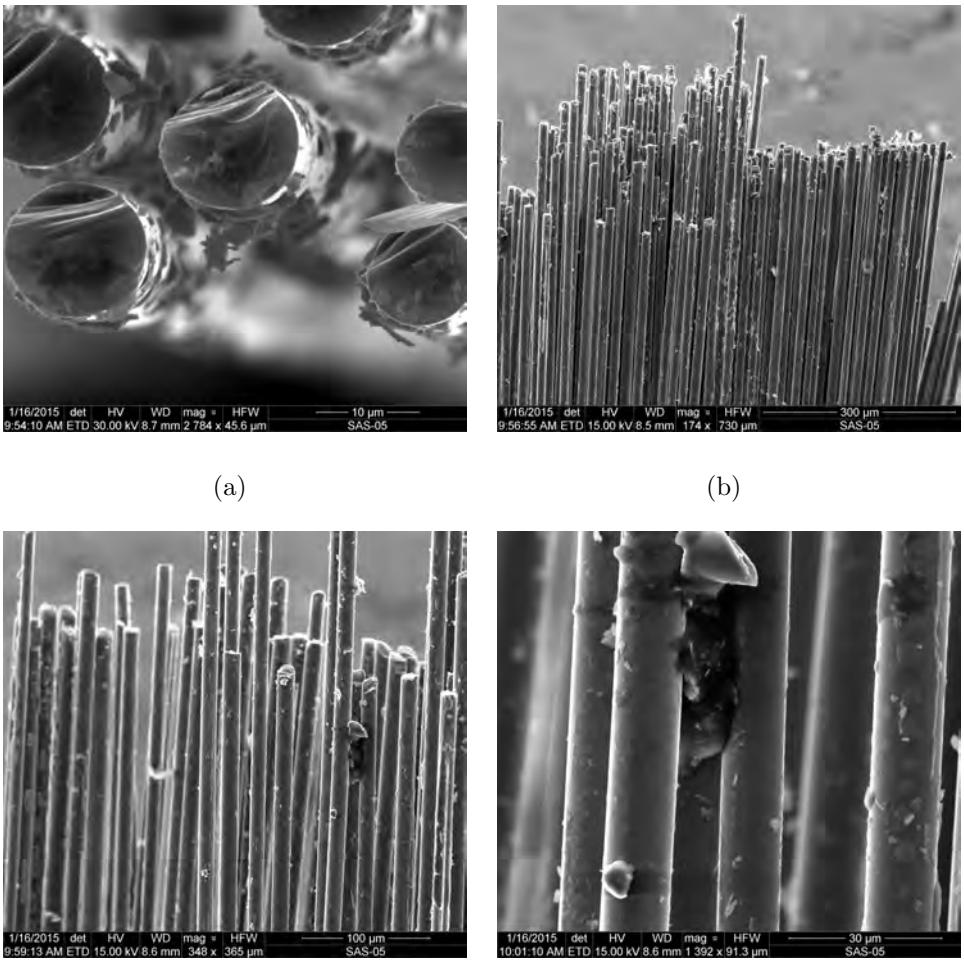
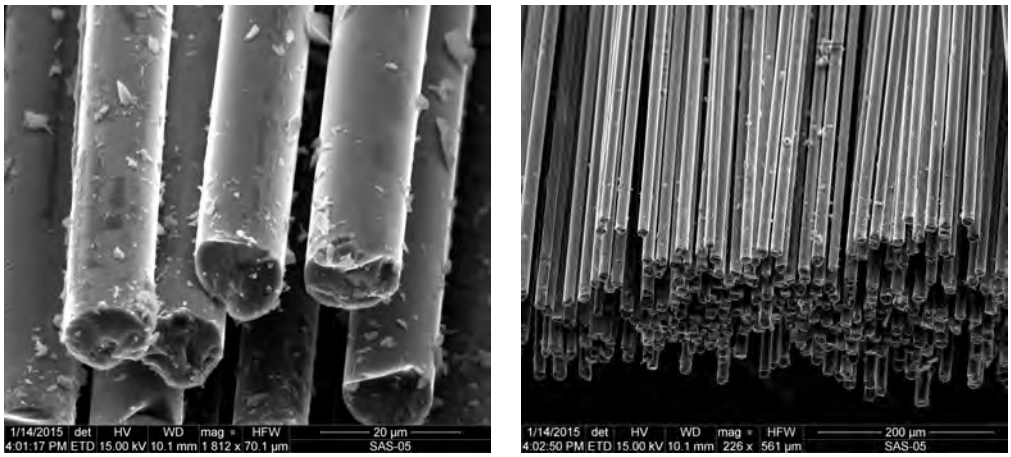
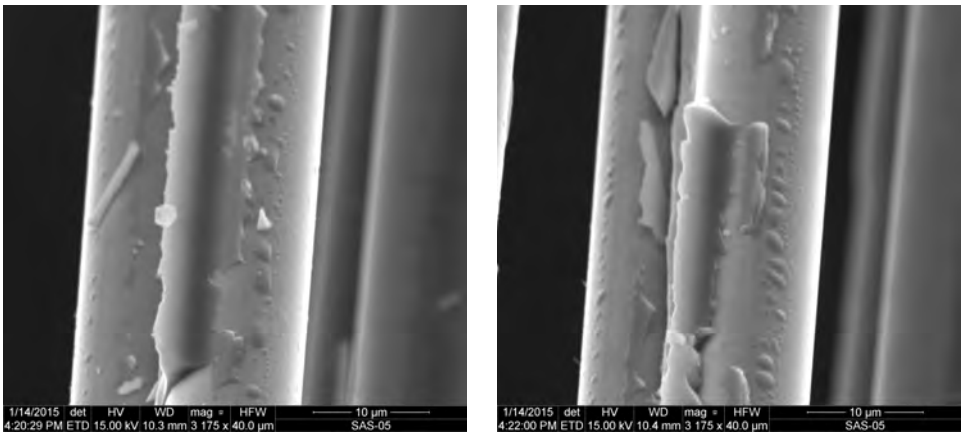


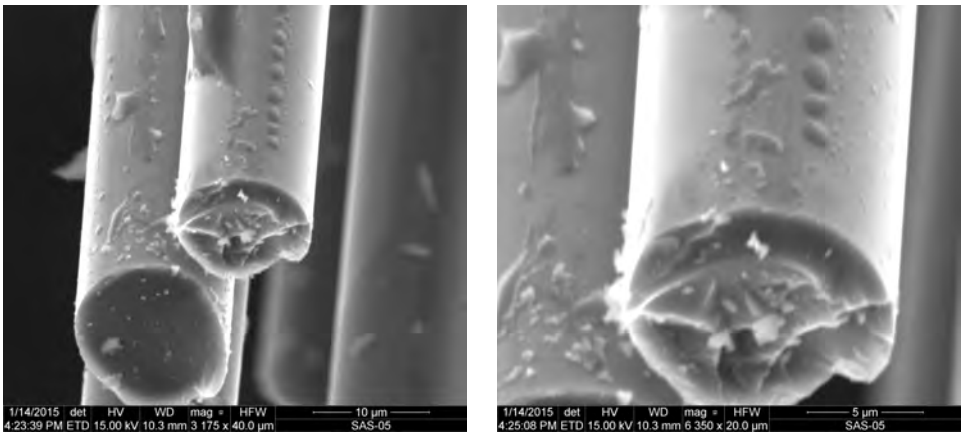
Figure B.68. Hi-Nicalon^{TM} S fiber tow specimen SS2, lower section, (800°C, σ = 154 MPa, t = 100 h)



(a) (b)



(c) (d)



(e) (f)

Figure B.69. Hi-Nicalon^{TM} S fiber tow specimen SS2, center section, (800°C, σ = 154 MPa, t = 100 h)

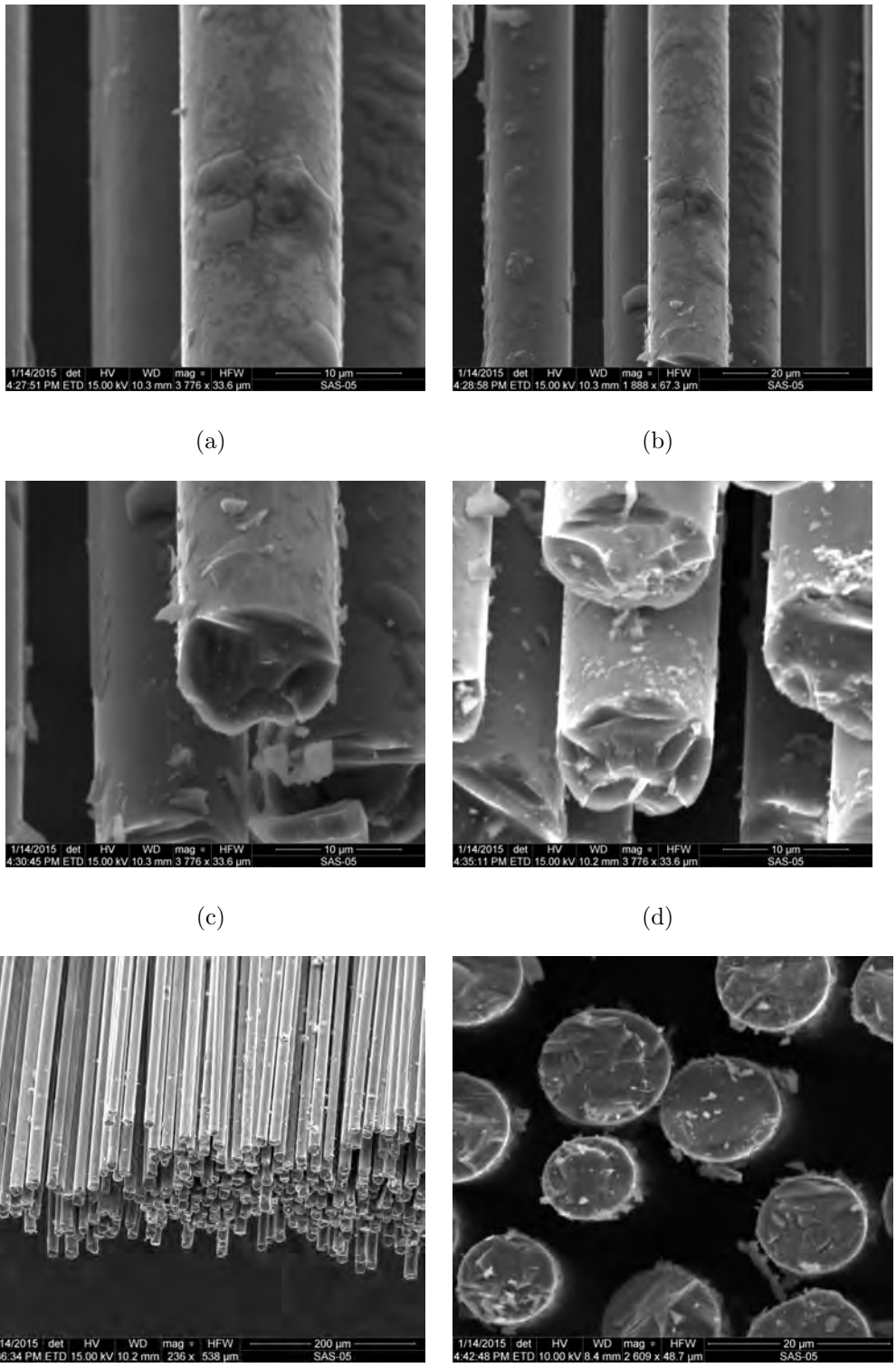
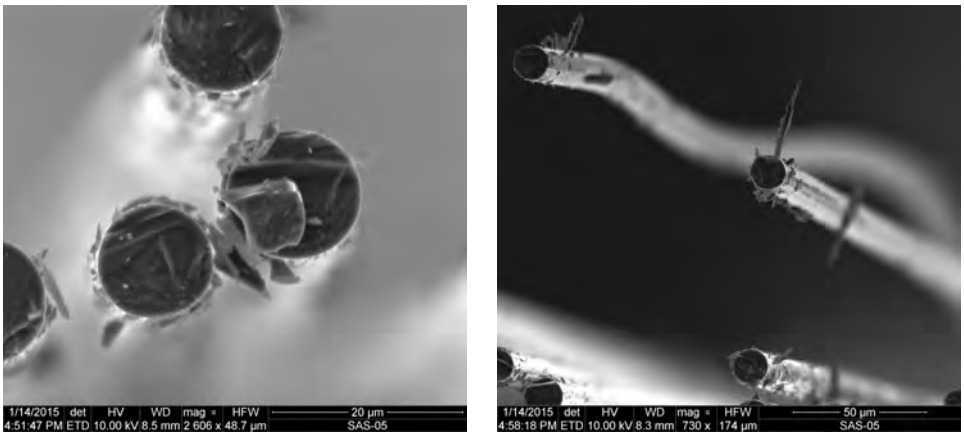
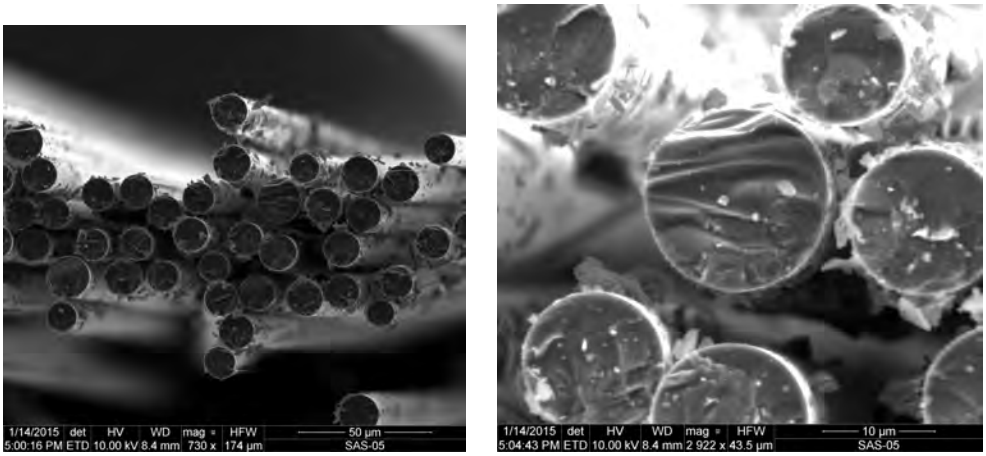


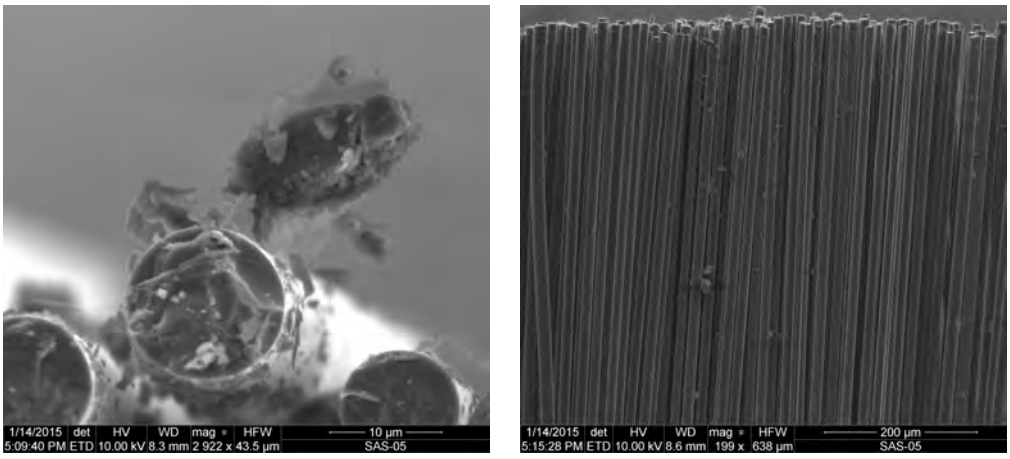
Figure B.70. Hi-Nicalon^{TM} S fiber tow specimen SS2, center section, (800°C, σ = 154 MPa, t = 100 h)



(a) (b)

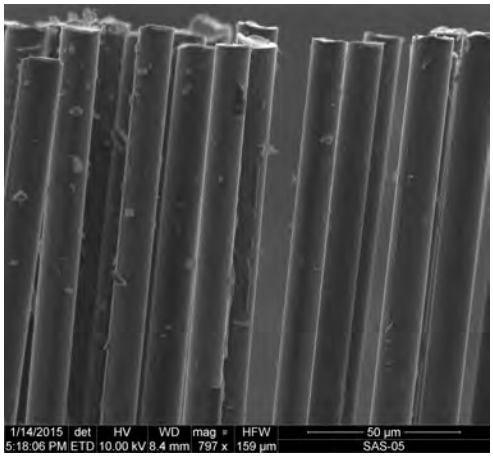


(c) (d)



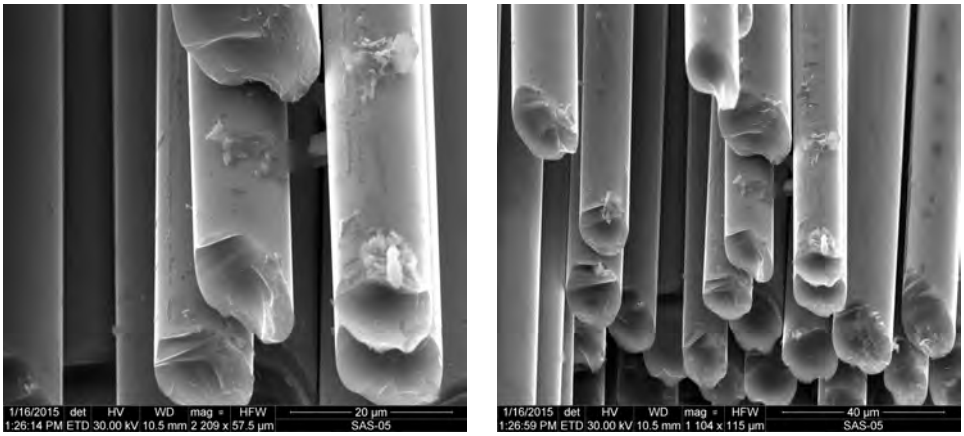
(e) (f)

Figure B.71. Hi-Nicalon^{TM} S fiber tow specimen SS2, center section, (800°C, σ = 154 MPa, t = 100 h)



(a)

Figure B.72. Hi-Nicalon^{TM} S fiber tow specimen SS2, center section, (800°C, σ = 154 MPa, t = 100 h)



(a) (b)

Figure B.73. Hi-Nicalon^{TM} S fiber tow specimen SS2, upper section, (800°C, σ = 154 MPa, t = 100 h)

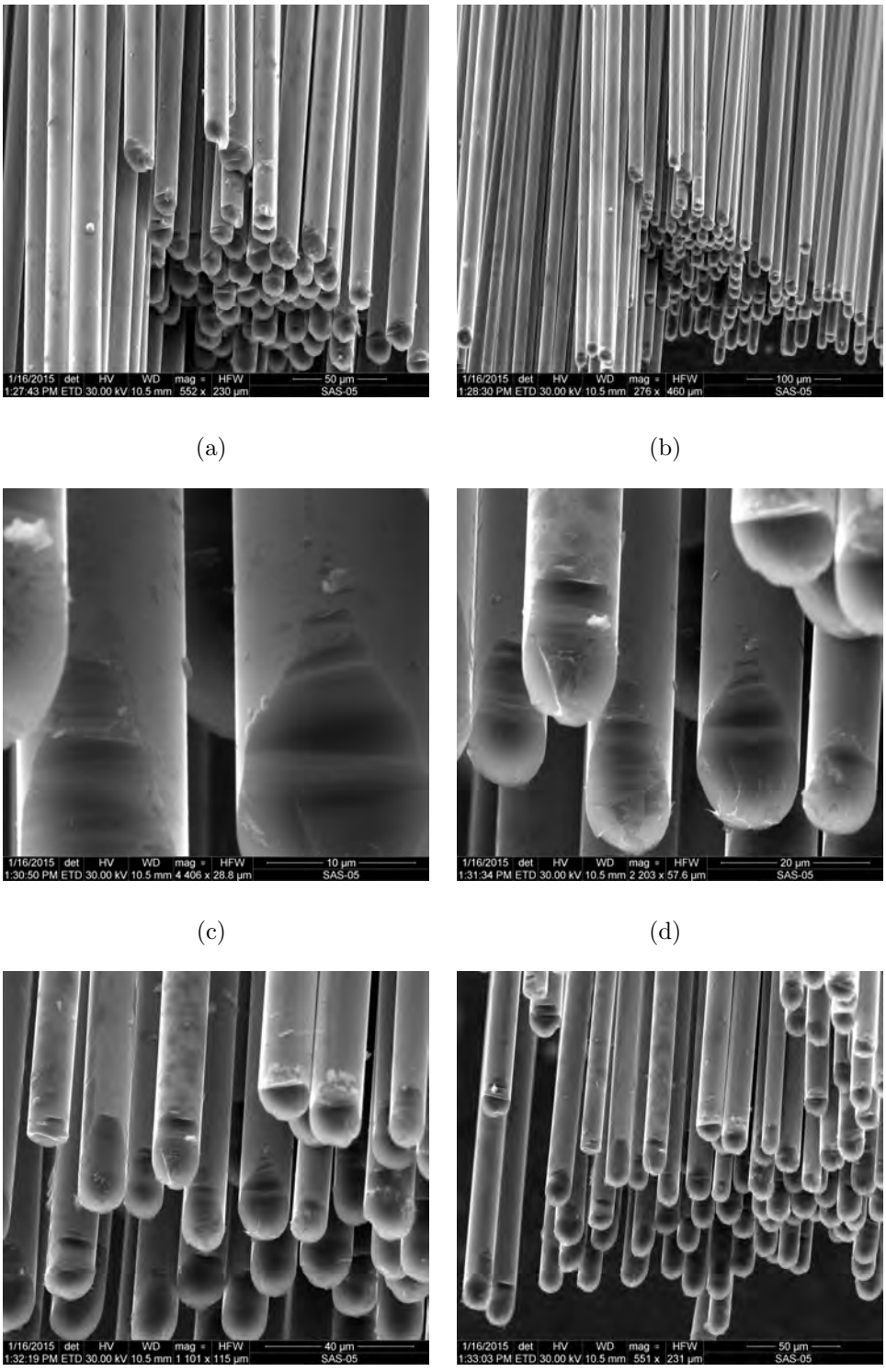
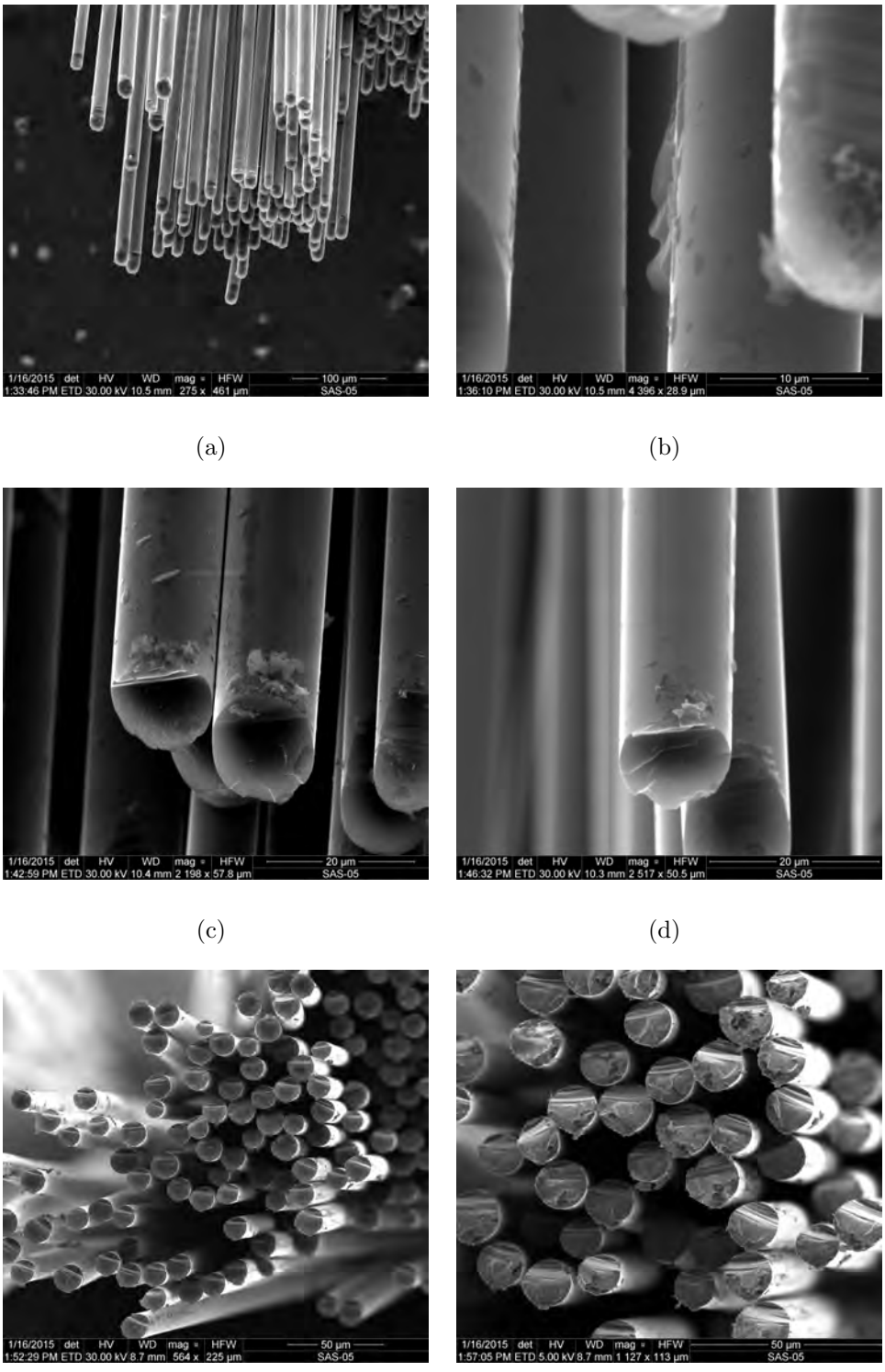


Figure B.74. Hi-Nicalon^{TM} S fiber tow specimen SS2, upper section, (800°C, σ = 154 MPa, t = 100 h)

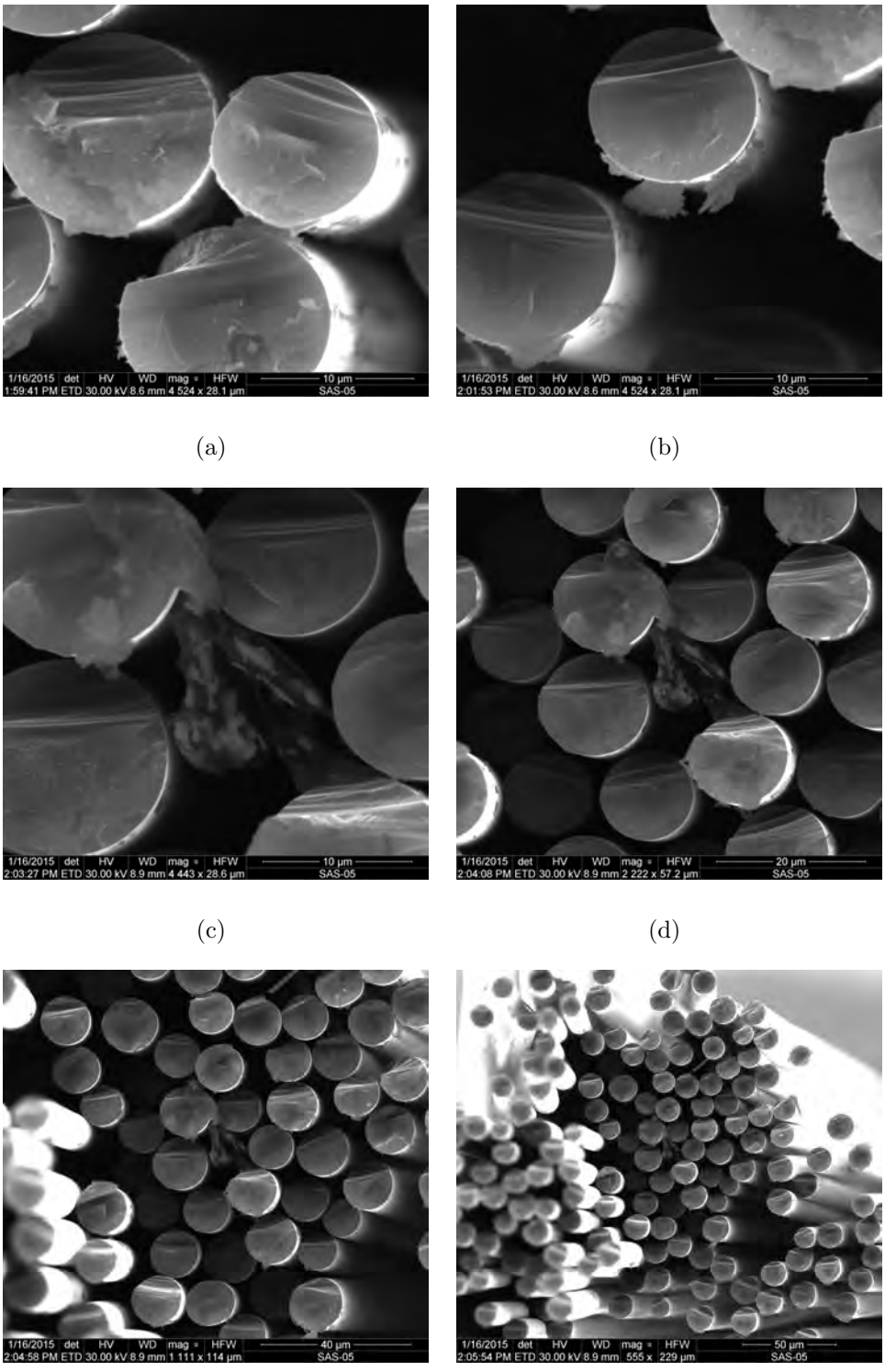


(a) (b)

(c) (d)

(e) (f)

Figure B.75. Hi-Nicalon^{TM} S fiber tow specimen SS2, upper section, (800°C, σ = 154 MPa, t = 100 h)

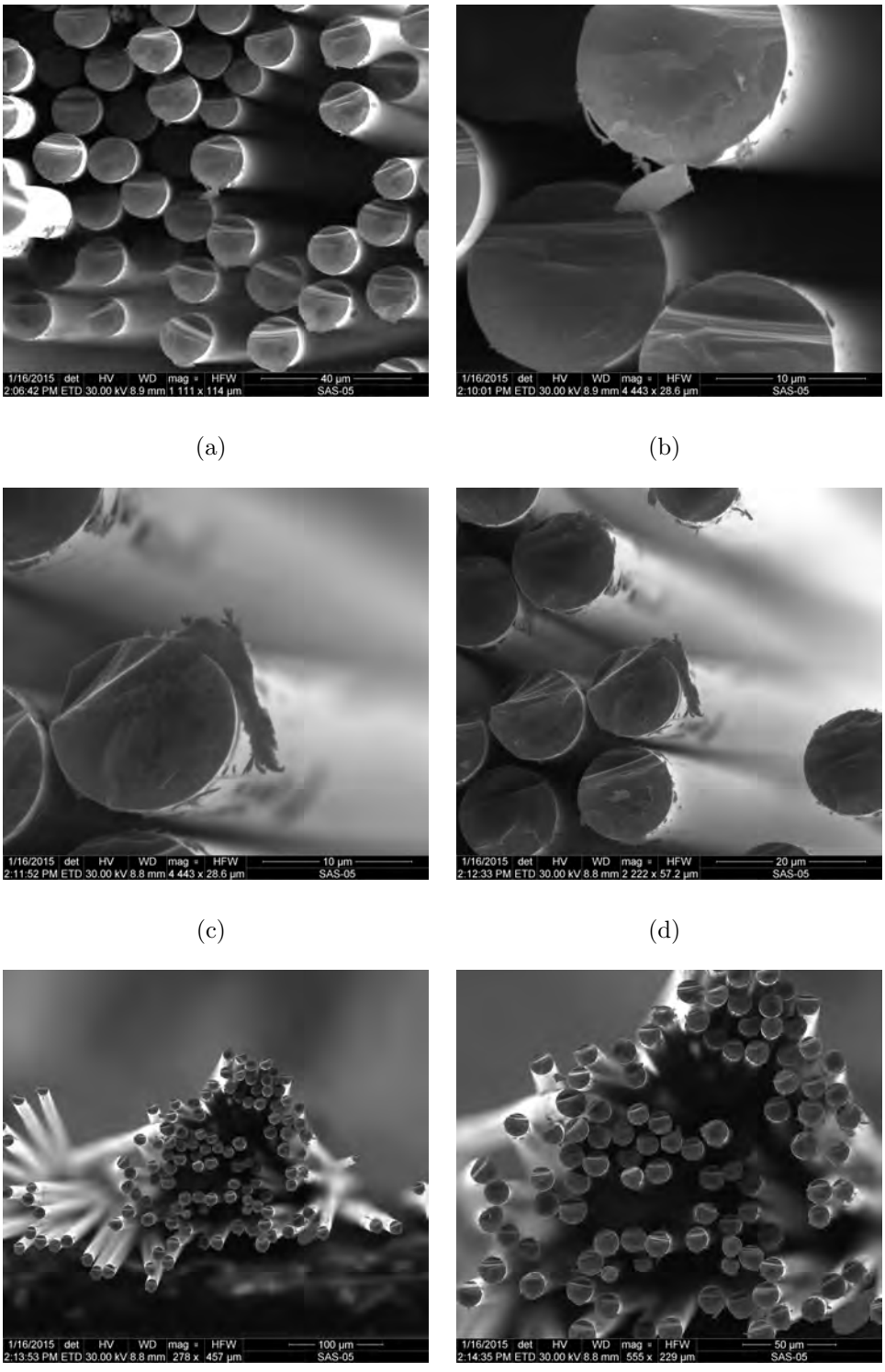


(a) (b)

(c) (d)

(e) (f)

Figure B.76. Hi-Nicalon^{TM} S fiber tow specimen SS2, upper section, (800°C, σ = 154 MPa, t = 100 h)



(a) (b)

(c) (d)

(e) (f)

Figure B.77. Hi-Nicalon^{TM} S fiber tow specimen SS2, upper section, (800°C, σ = 154 MPa, t = 100 h)

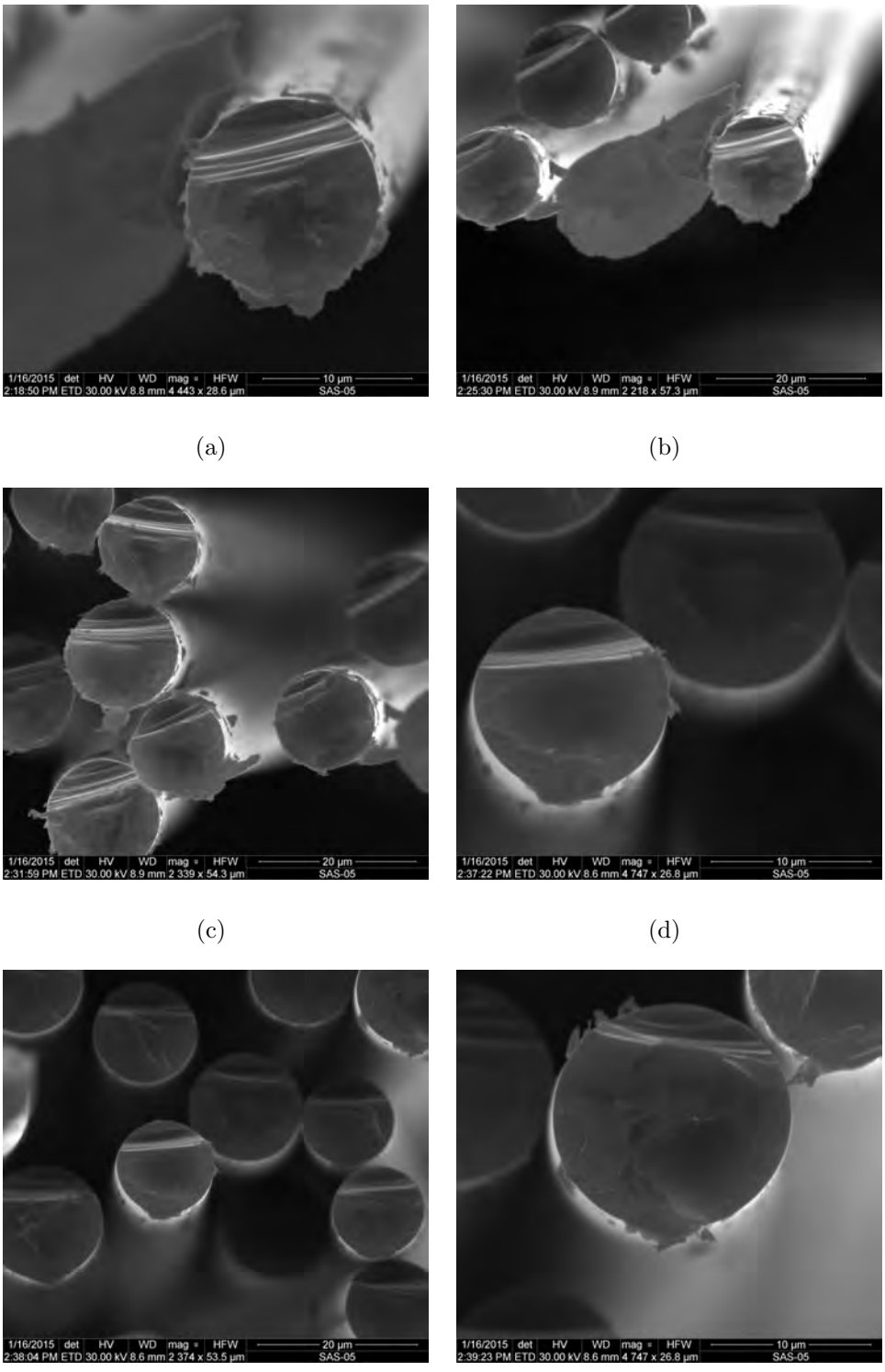


Figure B.78. Hi-Nicalon^{TM} S fiber tow specimen SS2, upper section, (800°C, σ = 154 MPa, t = 100 h)

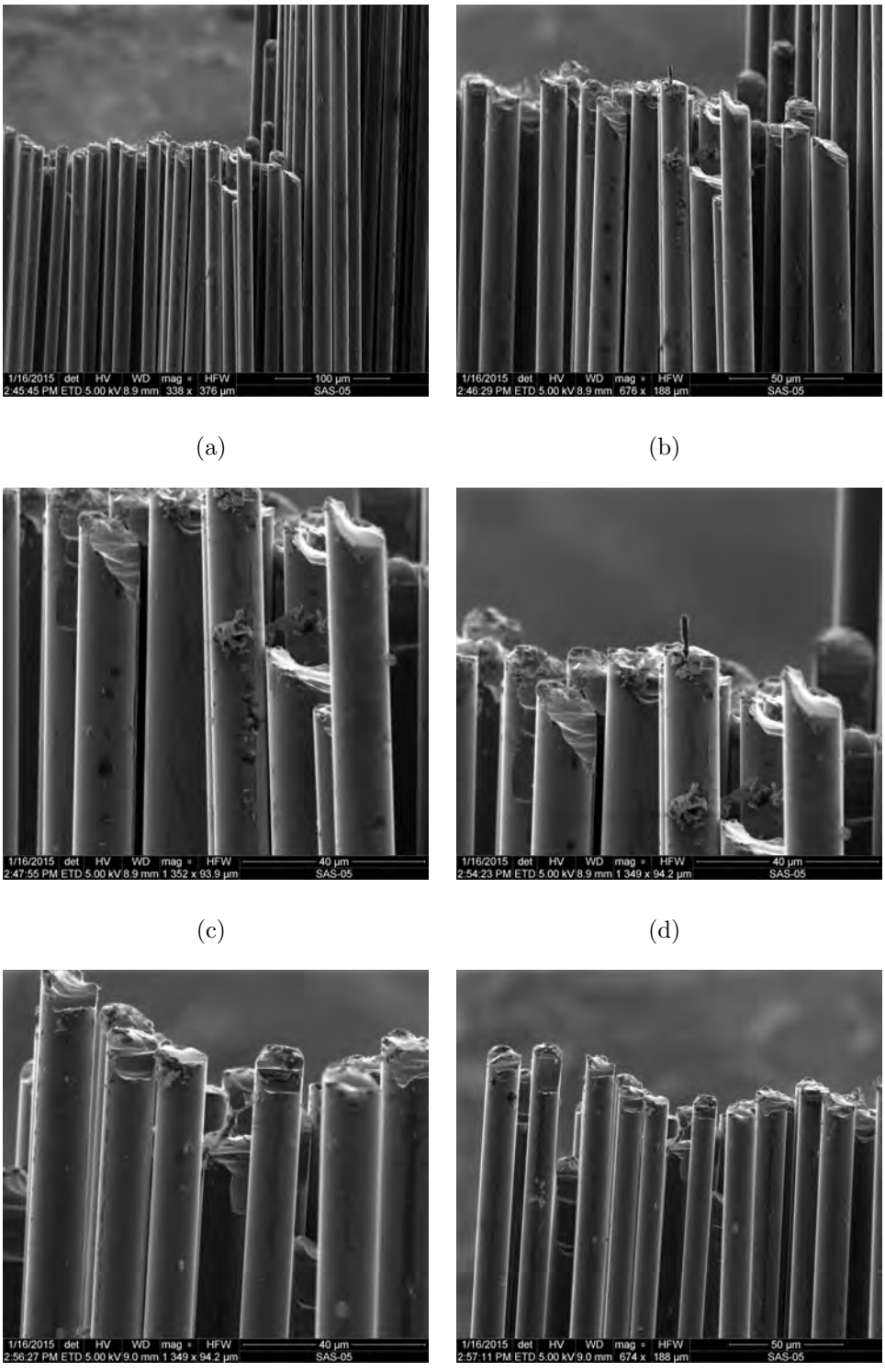
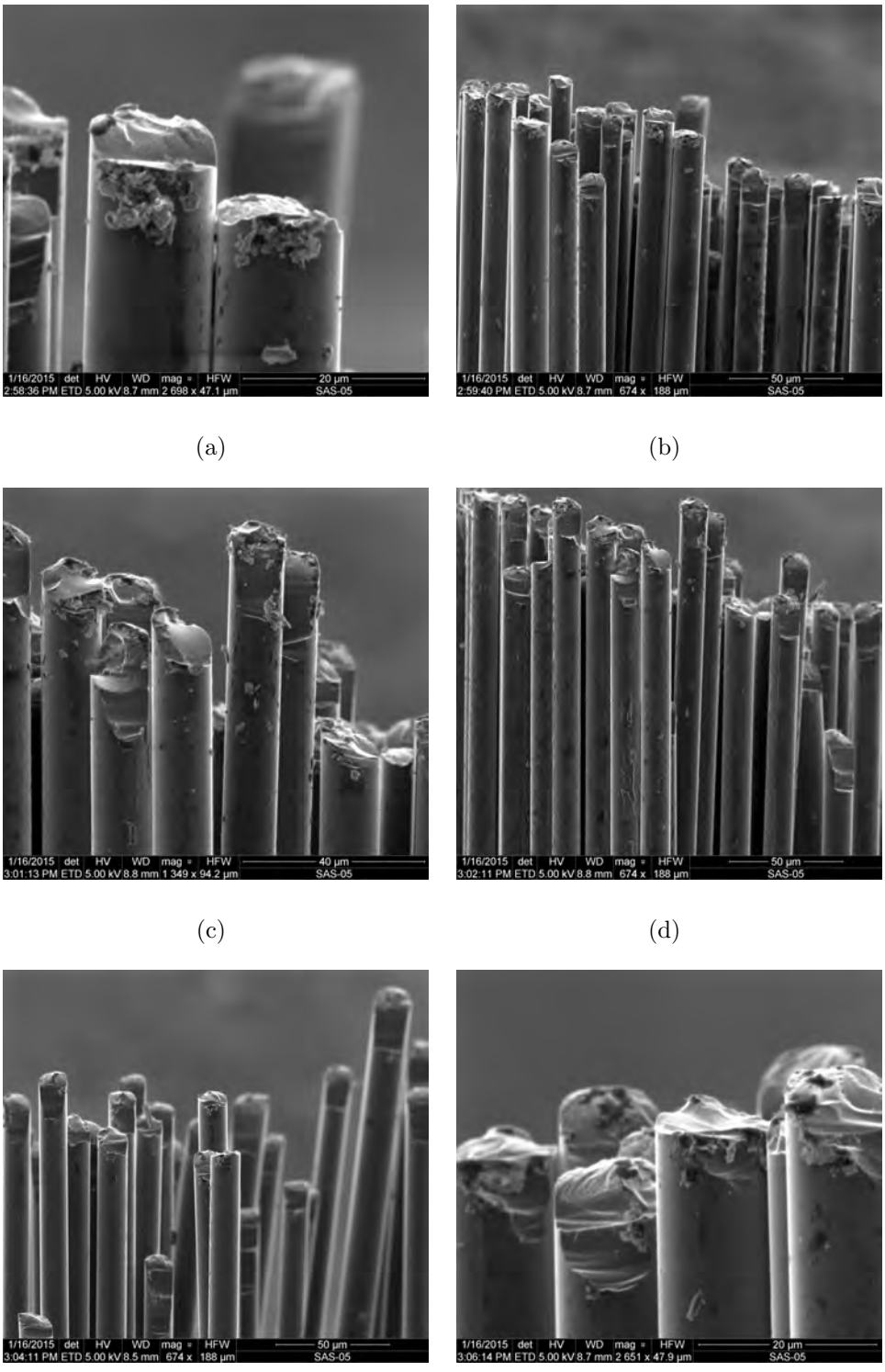


Figure B.79. Hi-Nicalon^{TM} S fiber tow specimen SS2, upper section, (800°C, σ = 154 MPa, t = 100 h)



(a) (b)

(c) (d)

(e) (f)

Figure B.80. Hi-Nicalon^{TM} S fiber tow specimen SS2, upper section, (800°C, σ = 154 MPa, t = 100 h)

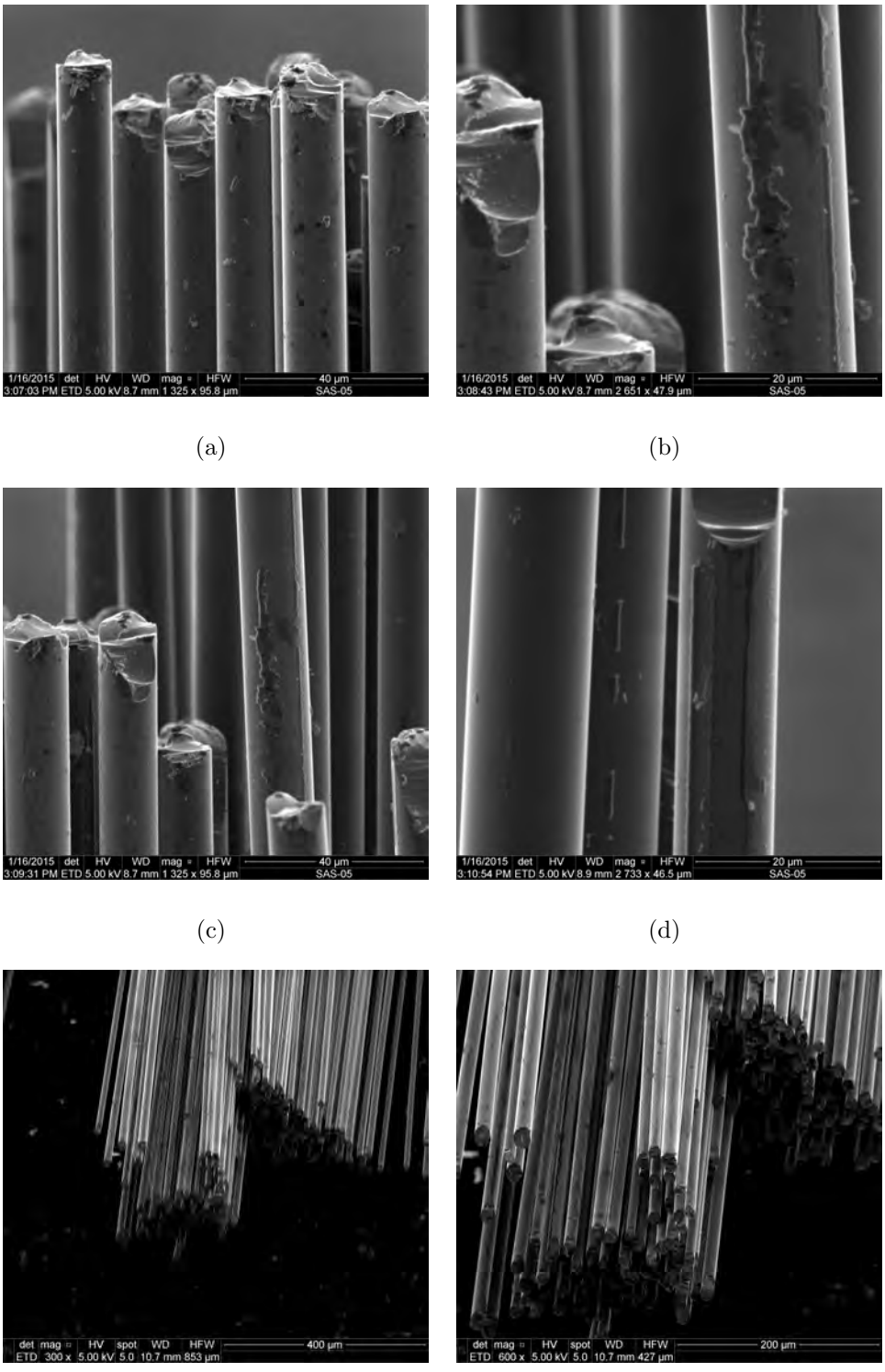
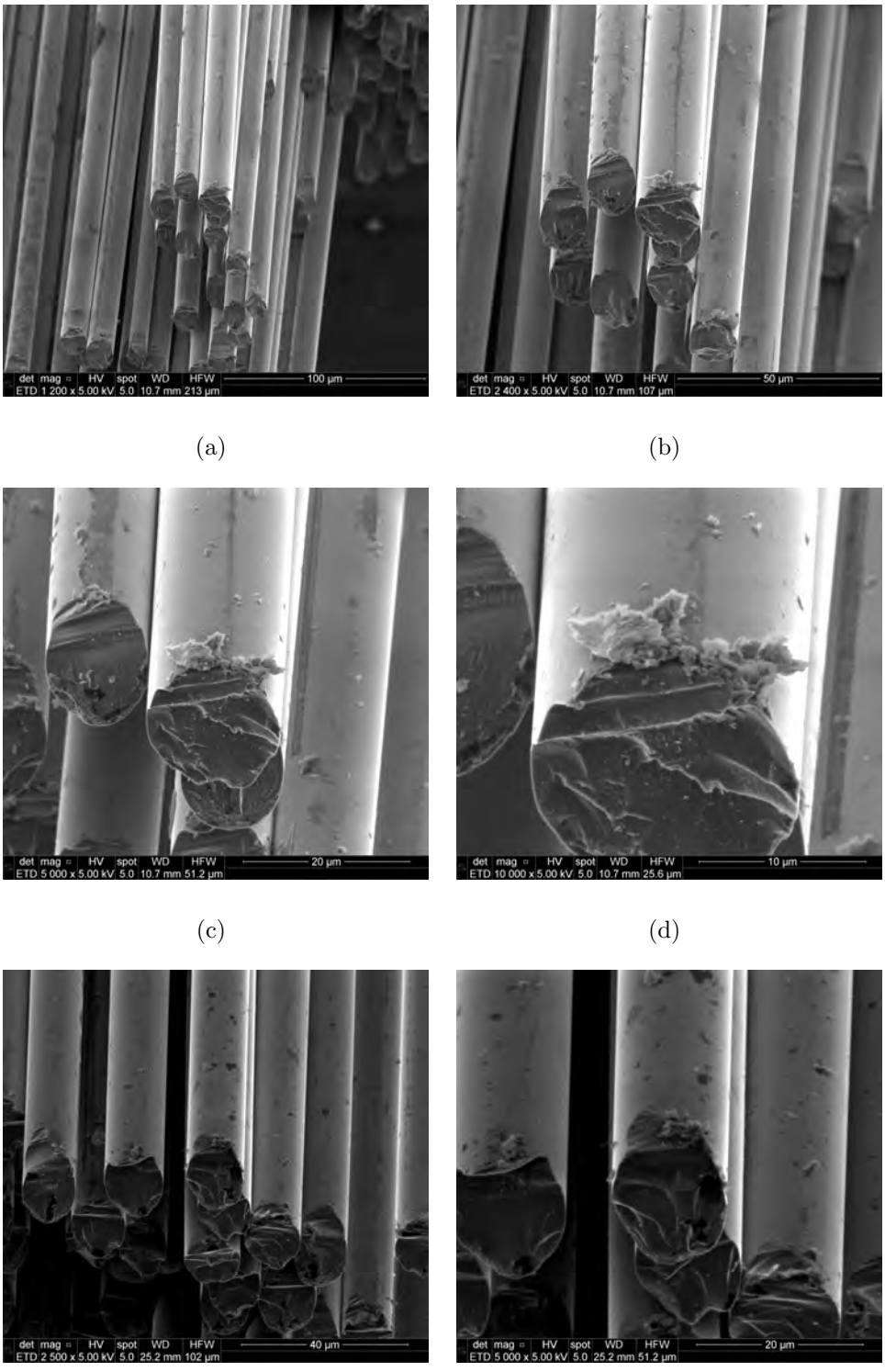


Figure B.81. Hi-Nicalon^{TM} S fiber tow specimen SS2, upper section, (800°C, σ = 154 MPa, t = 100 h)

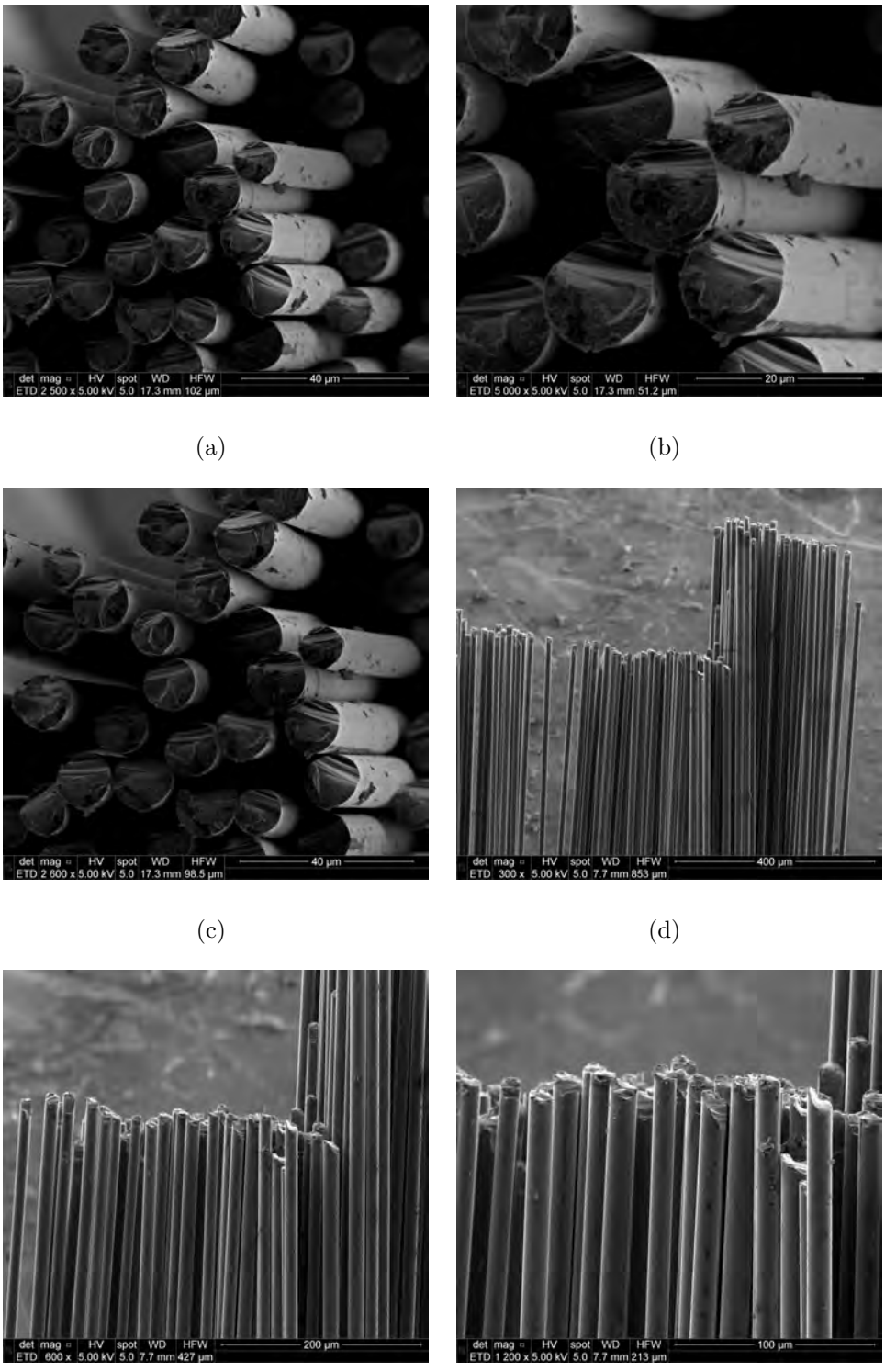


(a) (b)

(c) (d)

(e) (f)

Figure B.82. Hi-Nicalon^{TM} S fiber tow specimen SS2, upper section, (800°C, σ = 154 MPa, t = 100 h)

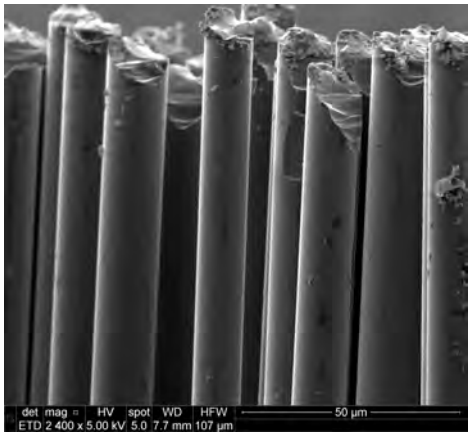


(a) (b)

(c) (d)

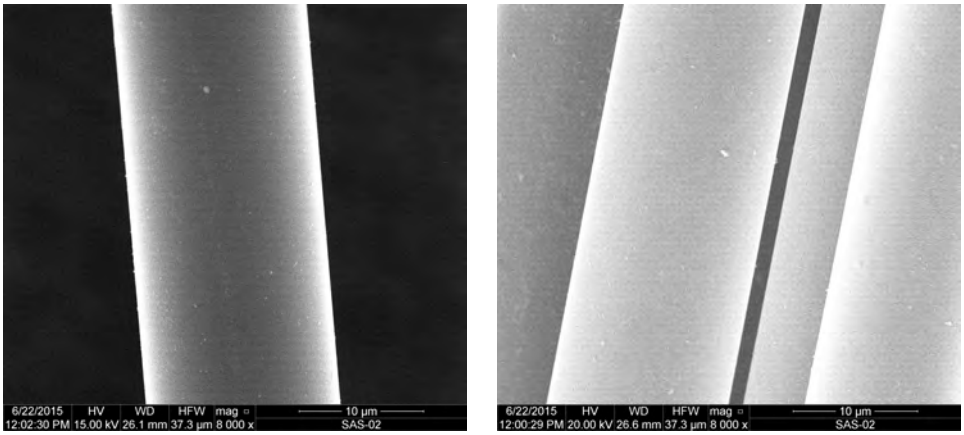
(e) (f)

Figure B.83. Hi-Nicalon^{TM} S fiber tow specimen SS2, upper section, (800°C, σ = 154 MPa, t = 100 h)



(a)

Figure B.84. Hi-Nicalon^{TM} S fiber tow specimen SS2, upper section, (800°C, σ = 154 MPa, t = 100 h)



(a) (b)

Figure B.85. Hi-Nicalon^{TM} S fiber tow specimen SS9, center section, (800°C, σ = 400 MPa, t = 100 h)

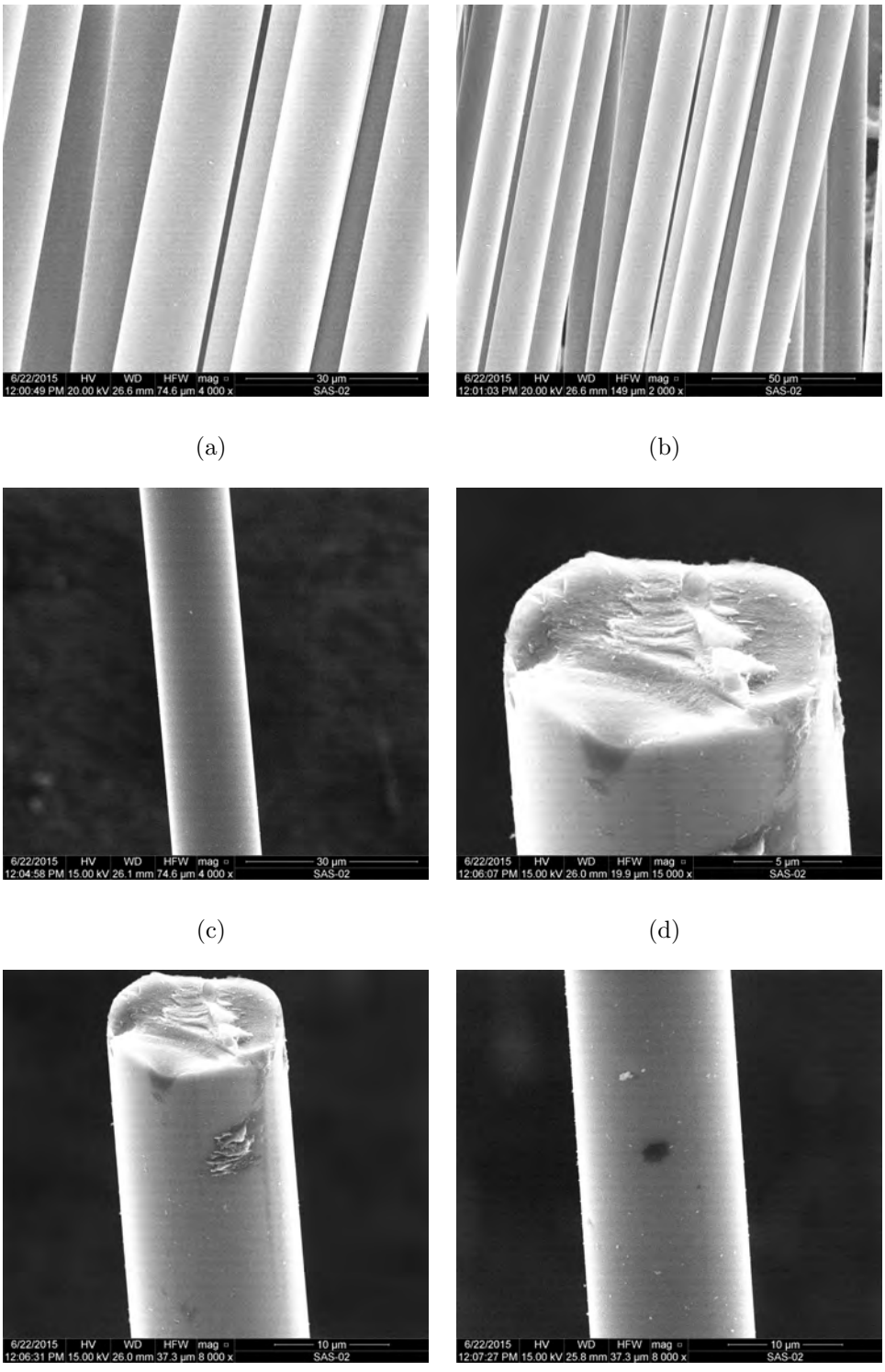


Figure B.86. Hi-Nicalon^{TM} S fiber tow specimen SS9, center section, (800°C, σ = 400 MPa, t = 100 h)

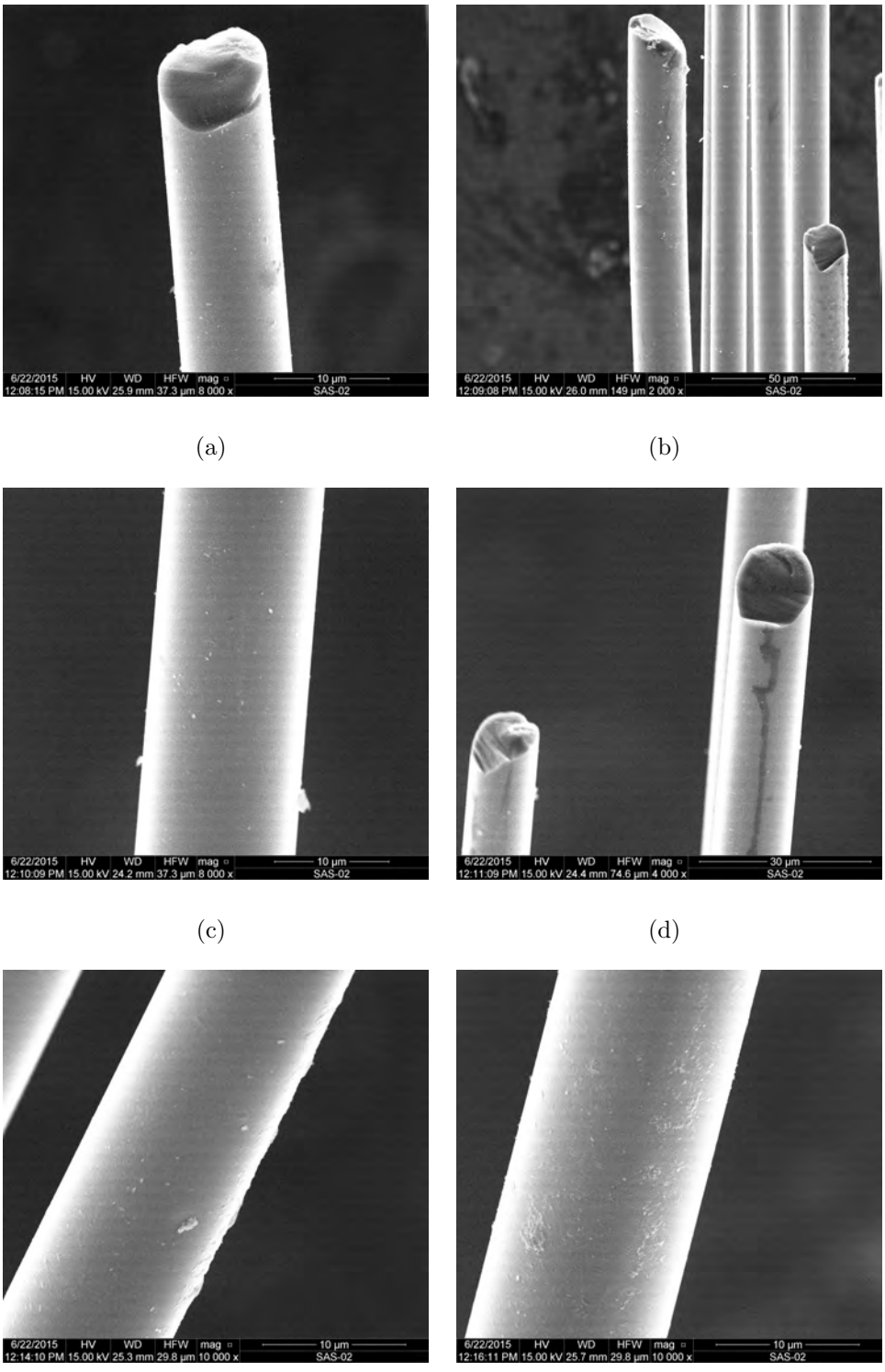


Figure B.87. Hi-Nicalon^{TM} S fiber tow specimen SS9, center section, (800°C, σ = 400 MPa, t = 100 h)

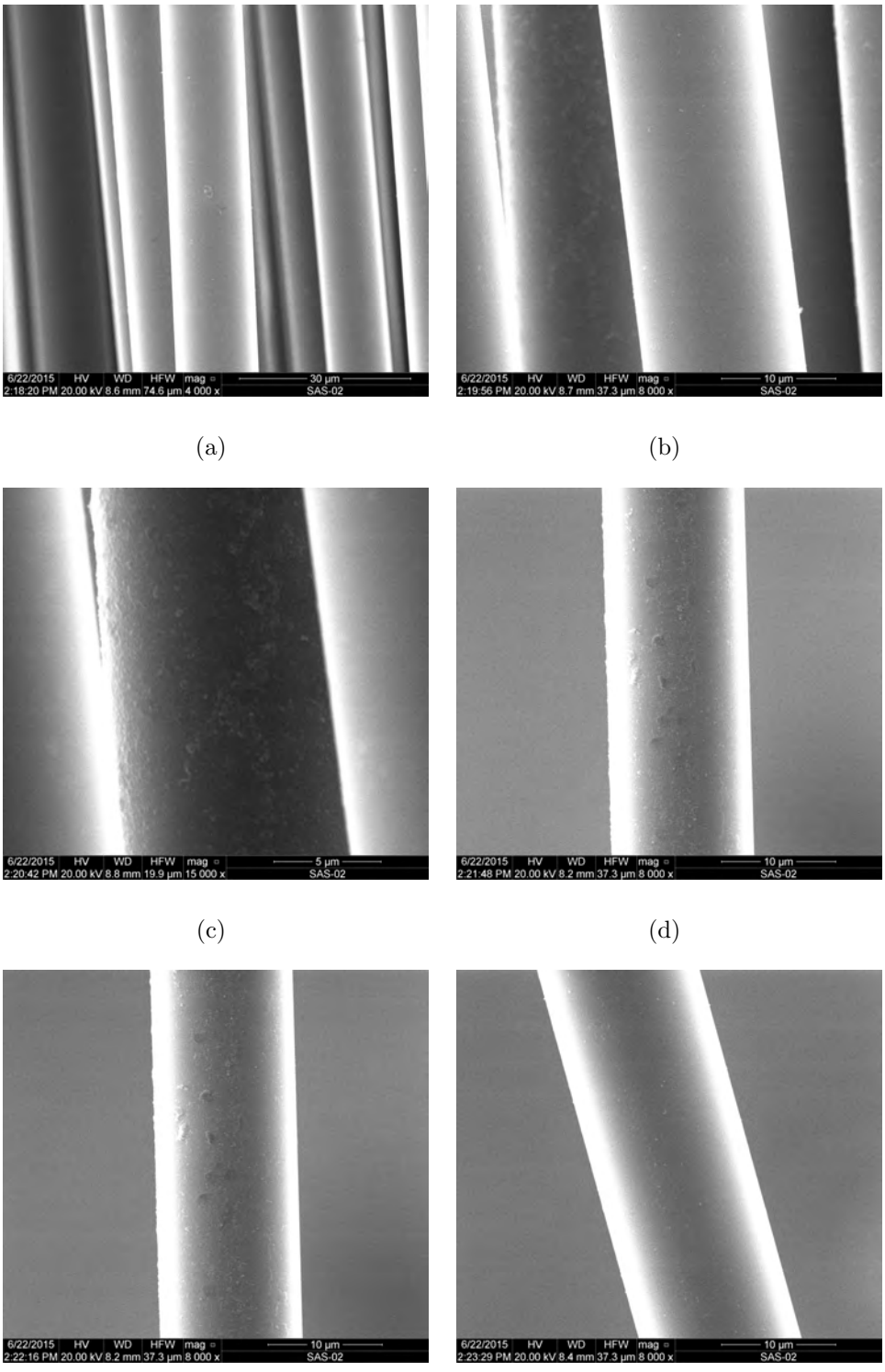
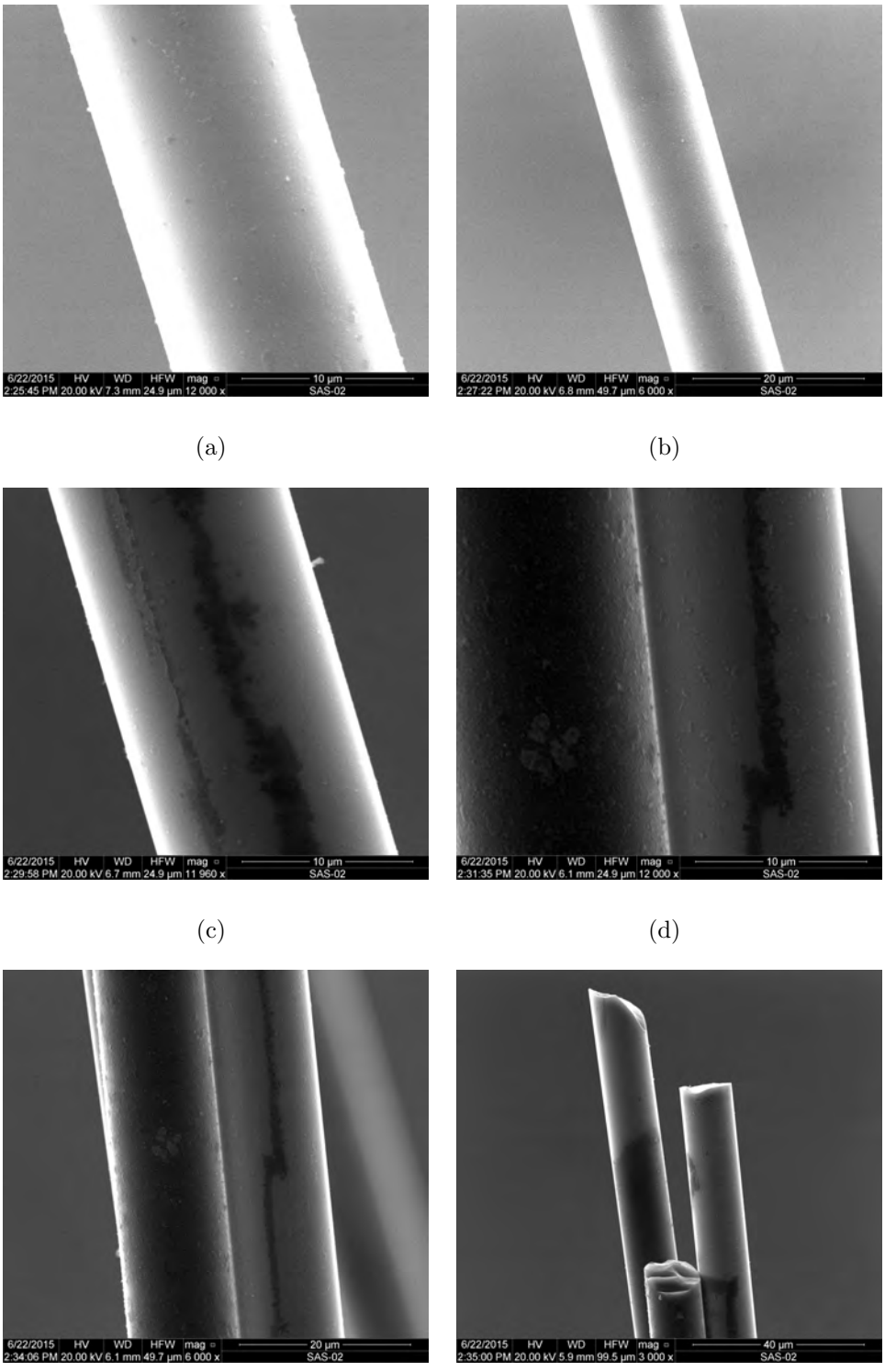


Figure B.88. Hi-Nicalon^{TM} S fiber tow specimen SS11, center section, (800°C, σ = 425 MPa, t = 100 h)



(a) (b)

(c) (d)

(e) (f)

Figure B.89. Hi-Nicalon^{TM} S fiber tow specimen SS11, center section, (800°C, σ = 425 MPa, t = 100 h)

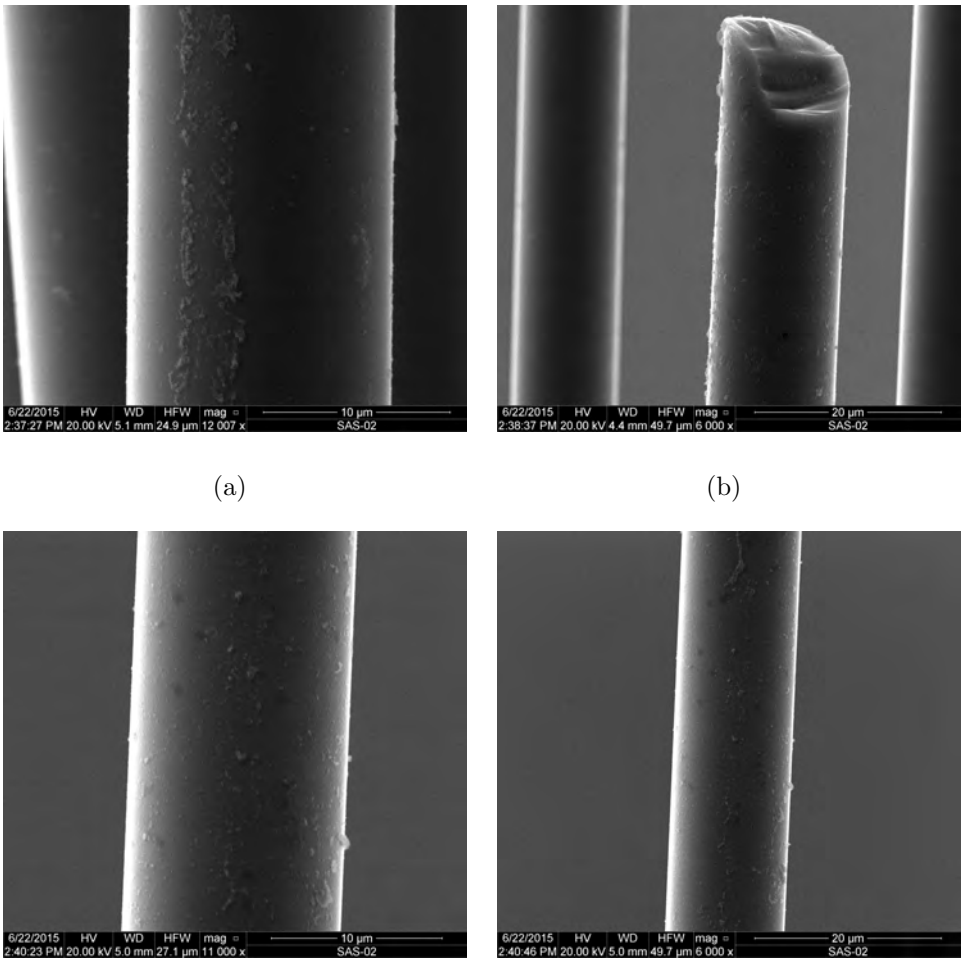


Figure B.90. Hi-Nicalon^{TM} S fiber tow specimen SS11, center section, (800°C, σ = 425 MPa, t = 100 h)

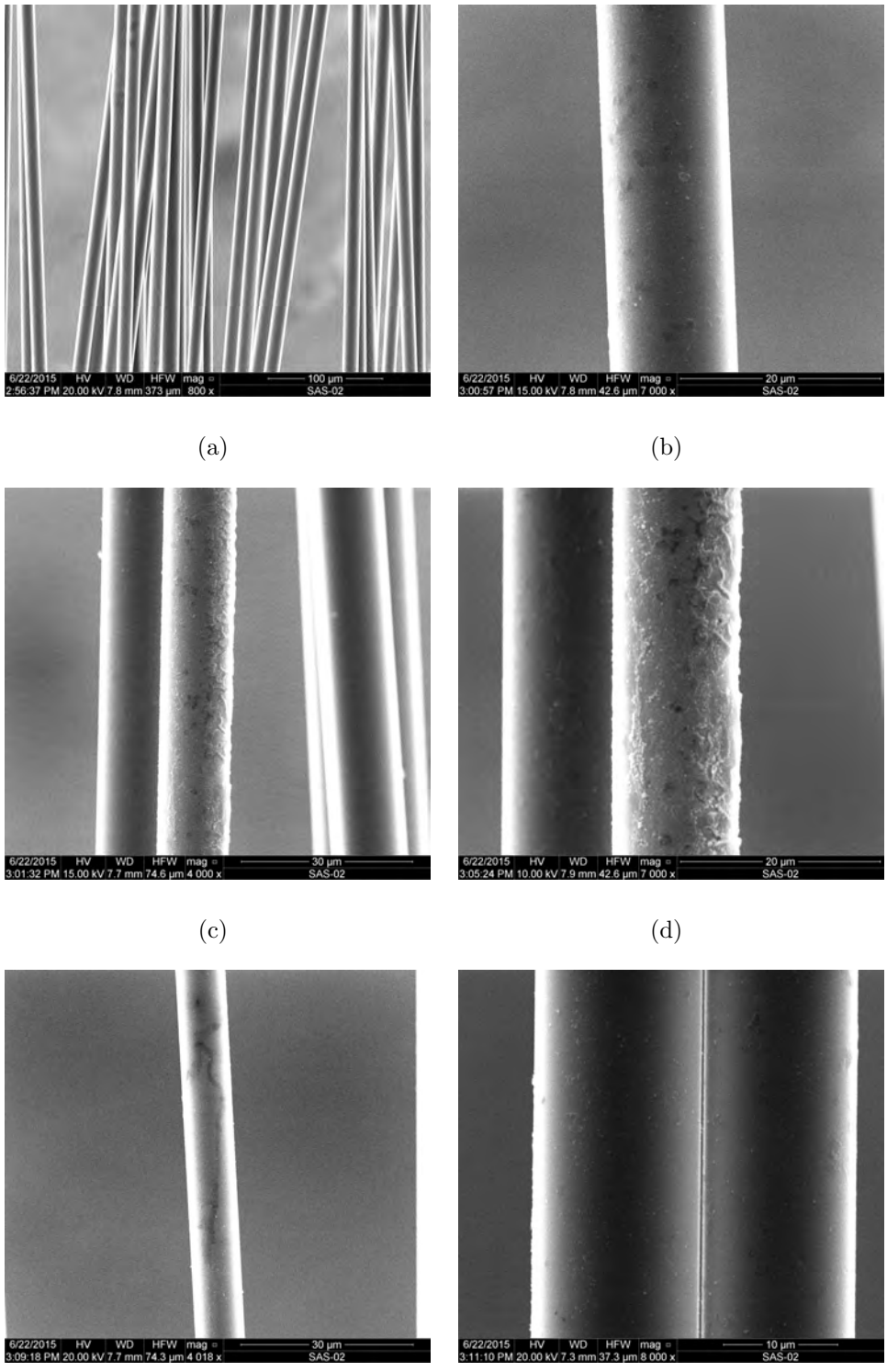
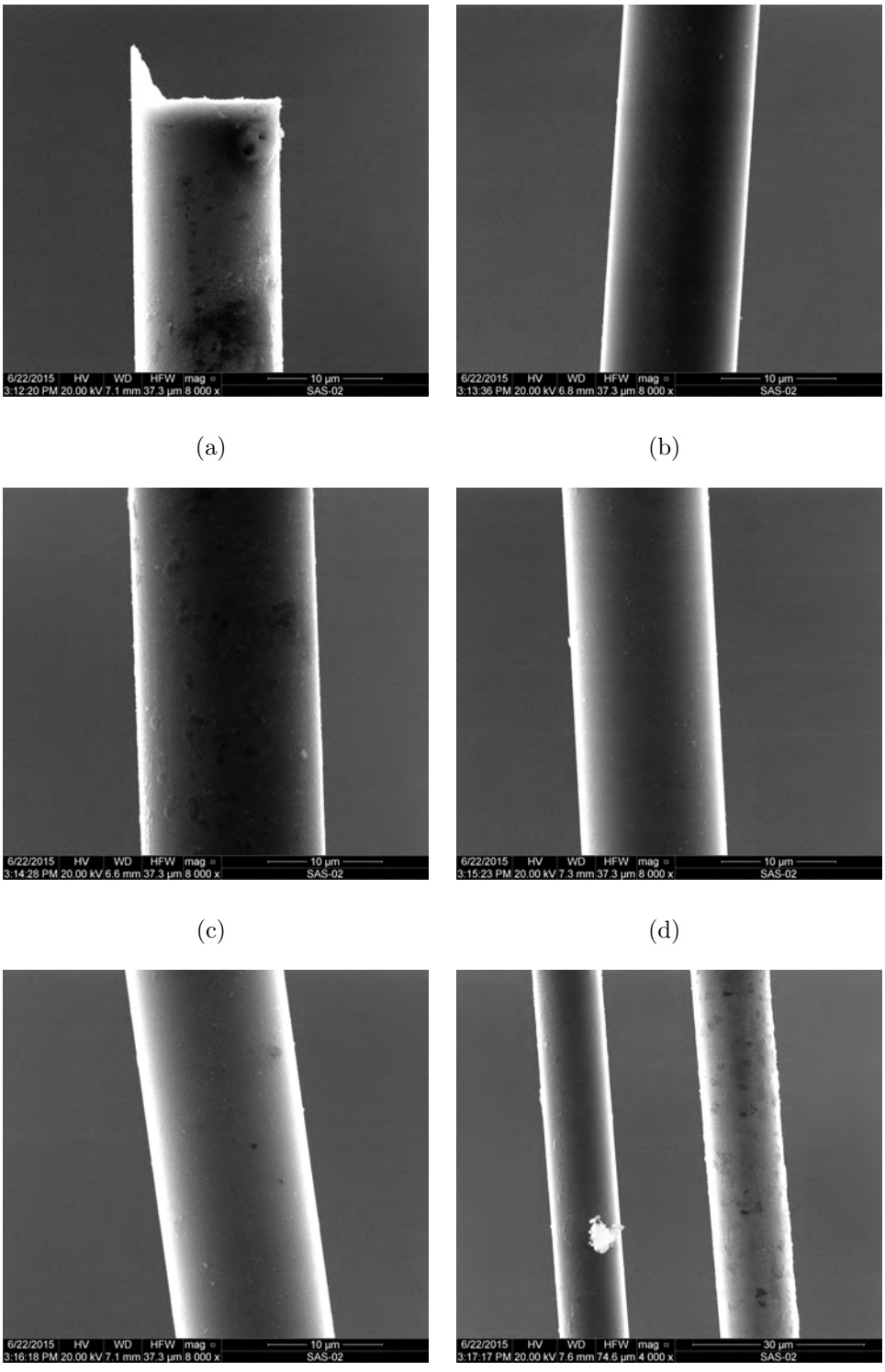


Figure B.91. Hi-Nicalon^{TM} S fiber tow specimen SS12, center section, (800°C, σ = 450 MPa, t = 100 h)

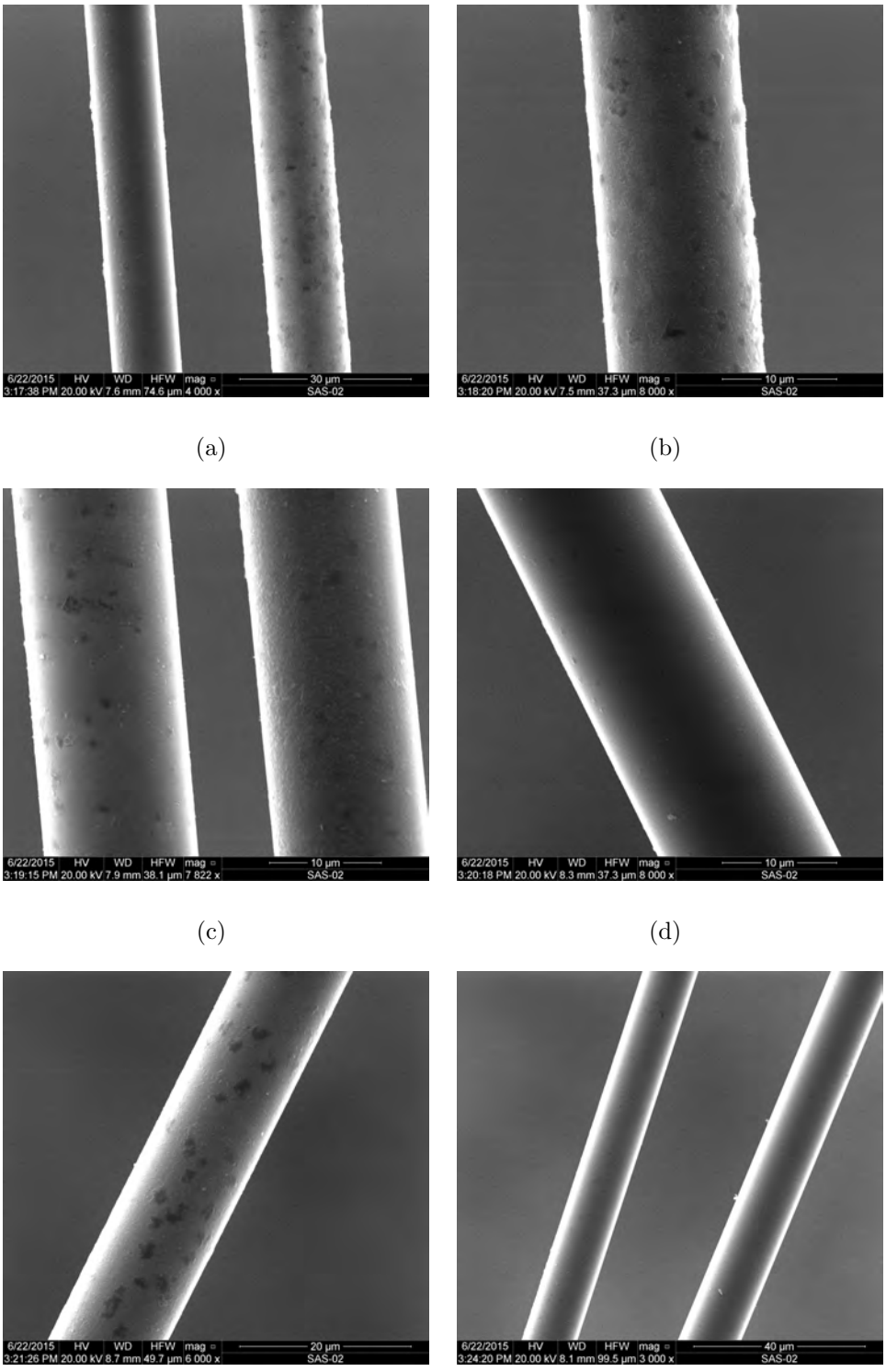


(a) (b)

(c) (d)

(e) (f)

Figure B.92. Hi-Nicalon^{TM} S fiber tow specimen SS12, center section, (800°C, σ = 450 MPa, t = 100 h)

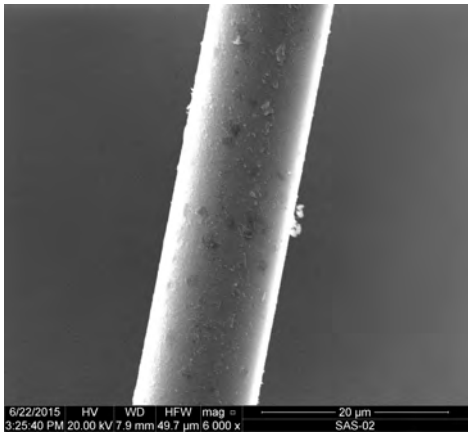


(a) (b)

(c) (d)

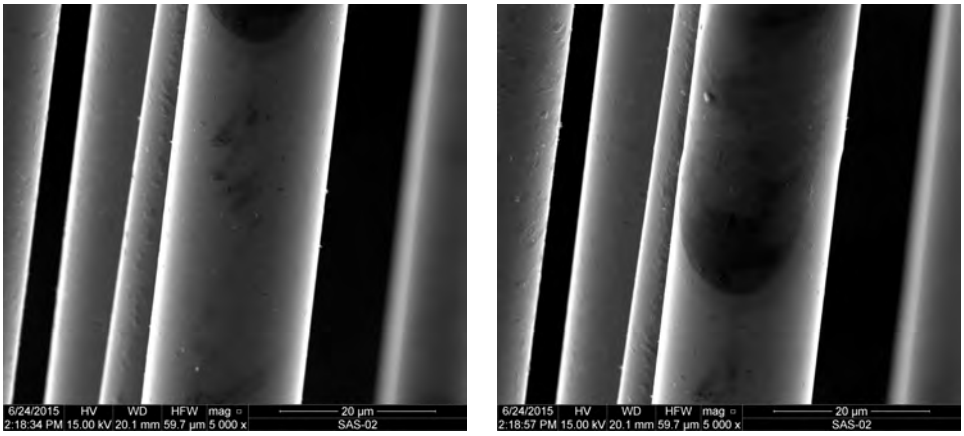
(e) (f)

Figure B.93. Hi-Nicalon^{TM} S fiber tow specimen SS12, center section, (800°C, σ = 450 MPa, t = 100 h)



(a)

Figure B.94. Hi-Nicalon^{TM} S fiber tow specimen SS12, center section, (800°C, σ = 450 MPa, t = 100 h)



(a) (b)

Figure B.95. Hi-Nicalon^{TM} S fiber tow specimen SS13, center section, (800°C, σ = 538 MPa, t = 76.8 h, prematurely terminated due to power outage)

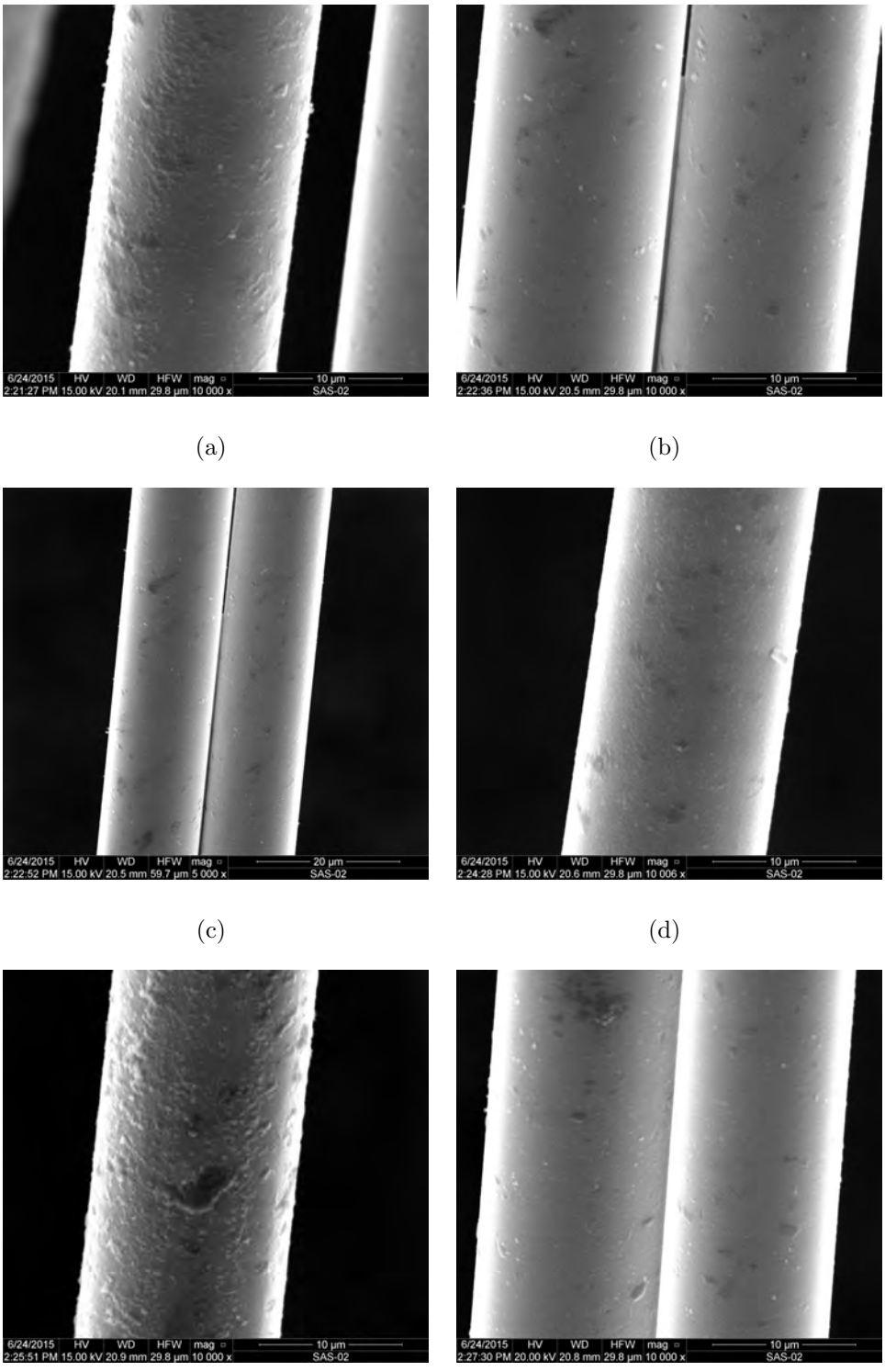


Figure B.96. Hi-Nicalon^{TM} S fiber tow specimen SS13, center section, (800°C, σ = 538 MPa, t = 76.8 h, prematurely terminated due to power outage)

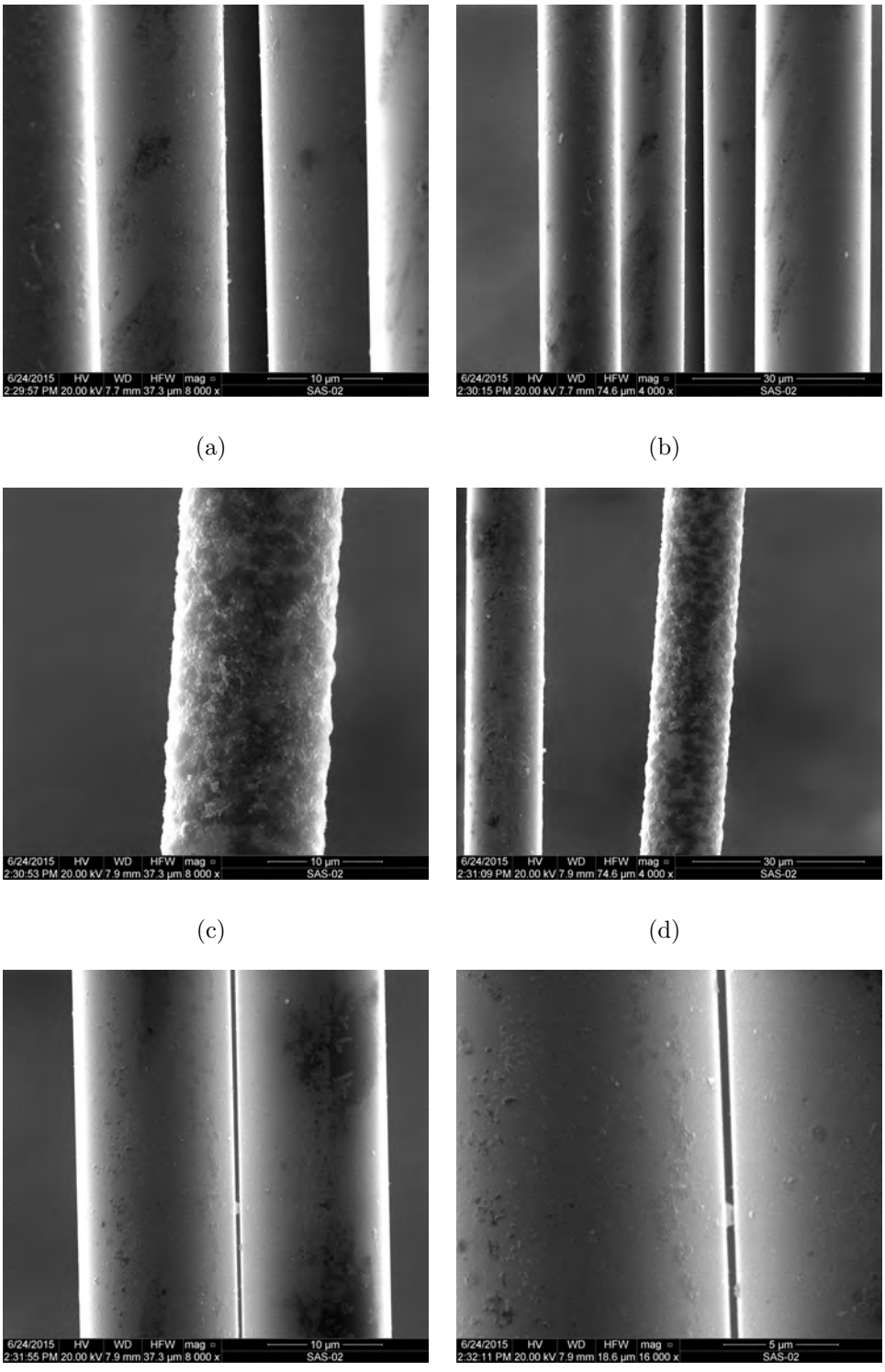


Figure B.97. Hi-Nicalon^{TM} S fiber tow specimen SS13, center section, (800°C, σ = 538 MPa, t = 76.8 h, prematurely terminated due to power outage)

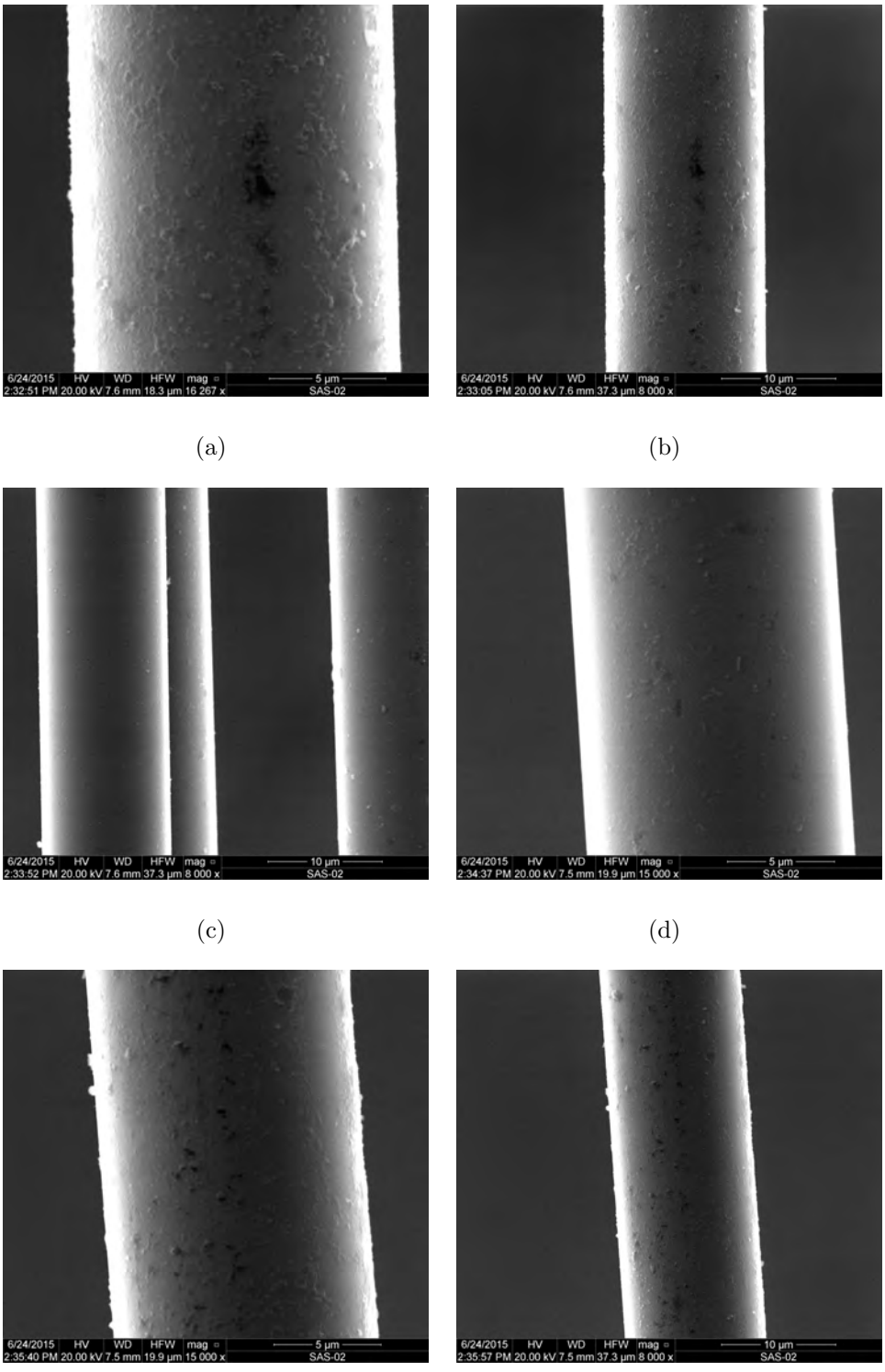


Figure B.98. Hi-Nicalon^{TM} S fiber tow specimen SS13, center section, (800°C, σ = 538 MPa, t = 76.8 h, prematurely terminated due to power outage)

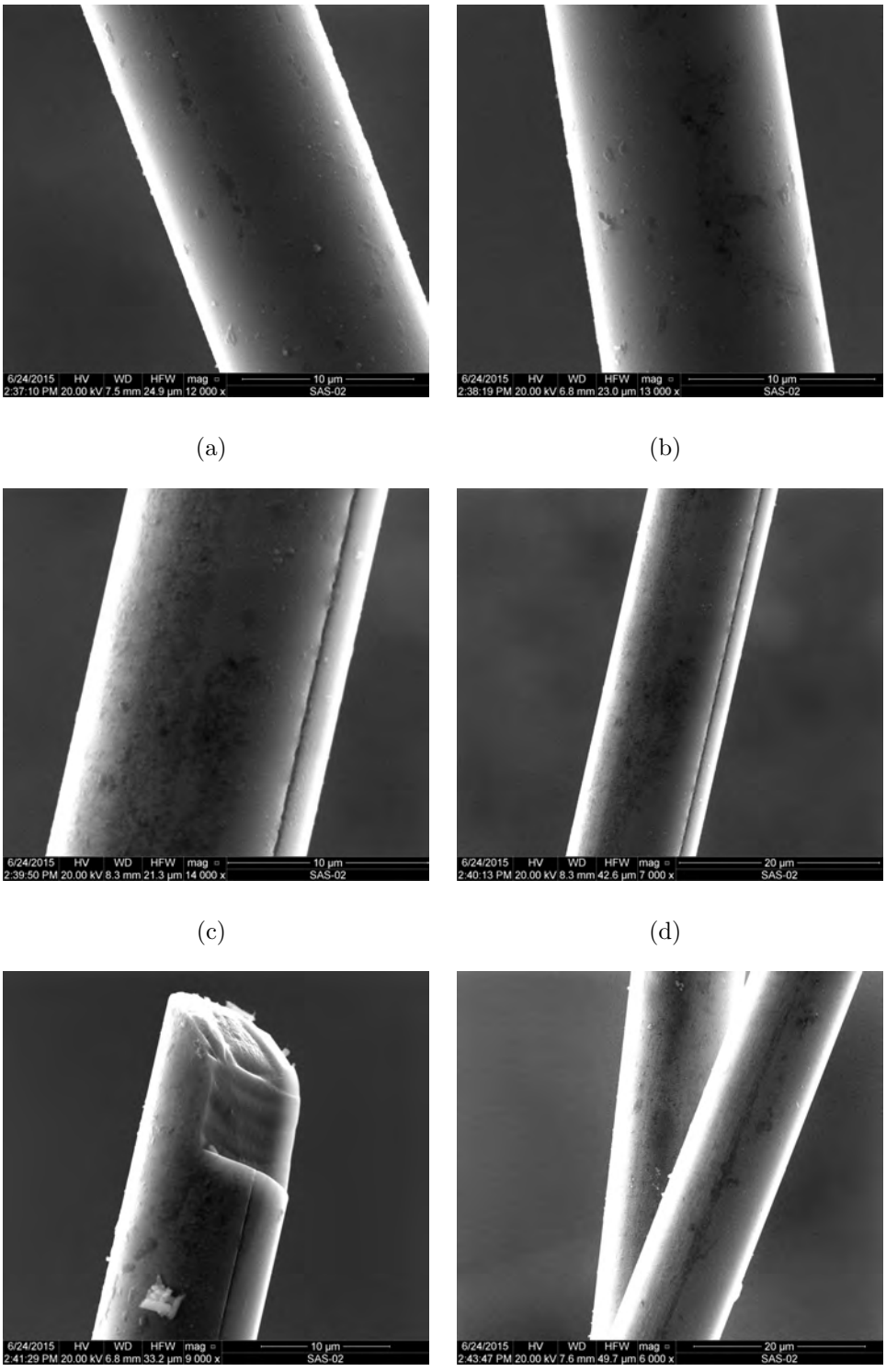
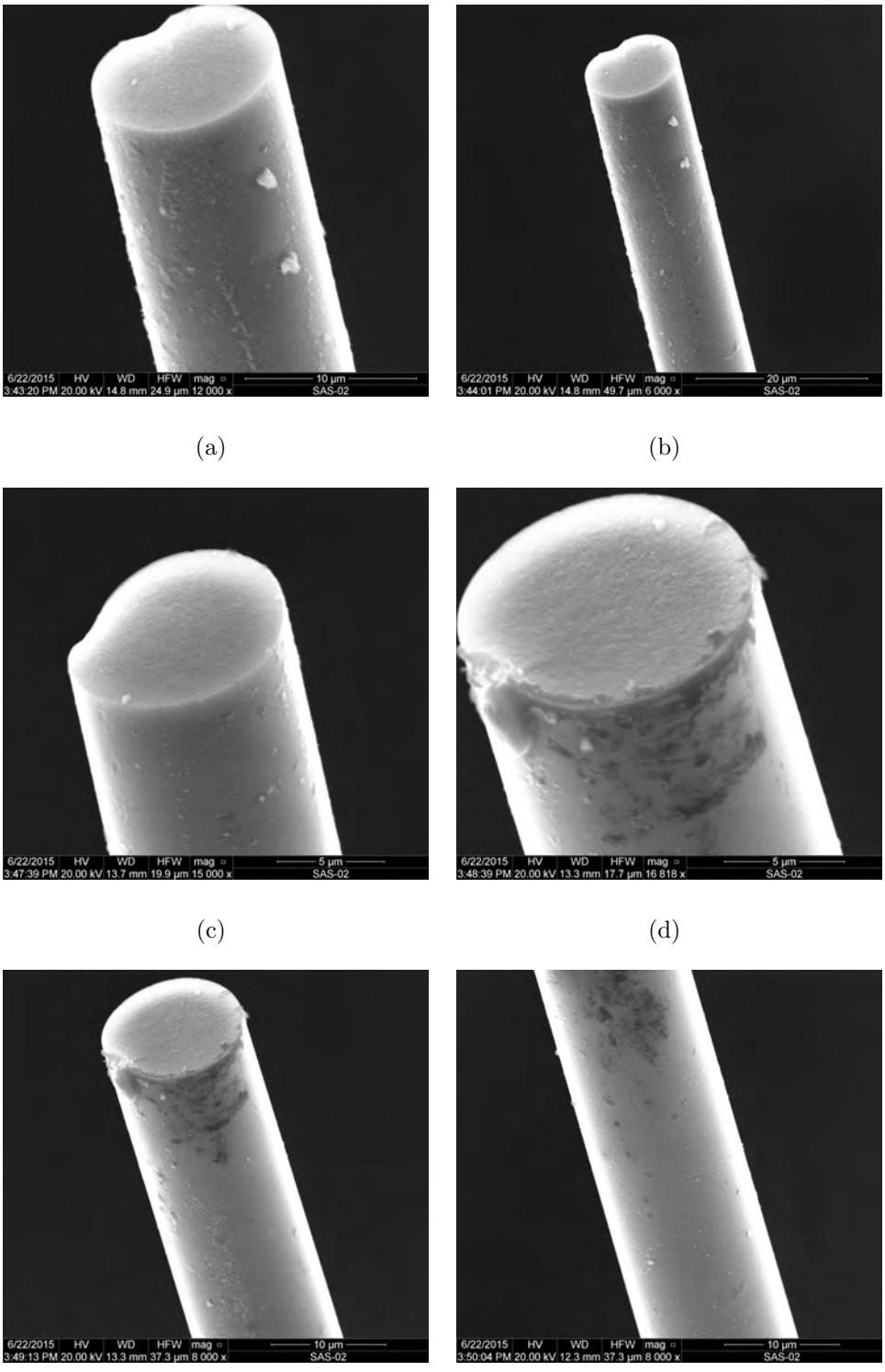


Figure B.99. Hi-Nicalon^{TM} S fiber tow specimen SS13, center section, (800°C, σ = 538 MPa, t = 76.8 h, prematurely terminated due to power outage)



(a) (b)

(c) (d)

(e) (f)

Figure B.100. Hi-Nicalon^{TM} S fiber tow specimen SS13, fracture surface, (800°C, σ = 538 MPa, t = 76.8 h, prematurely terminated due to power outage)

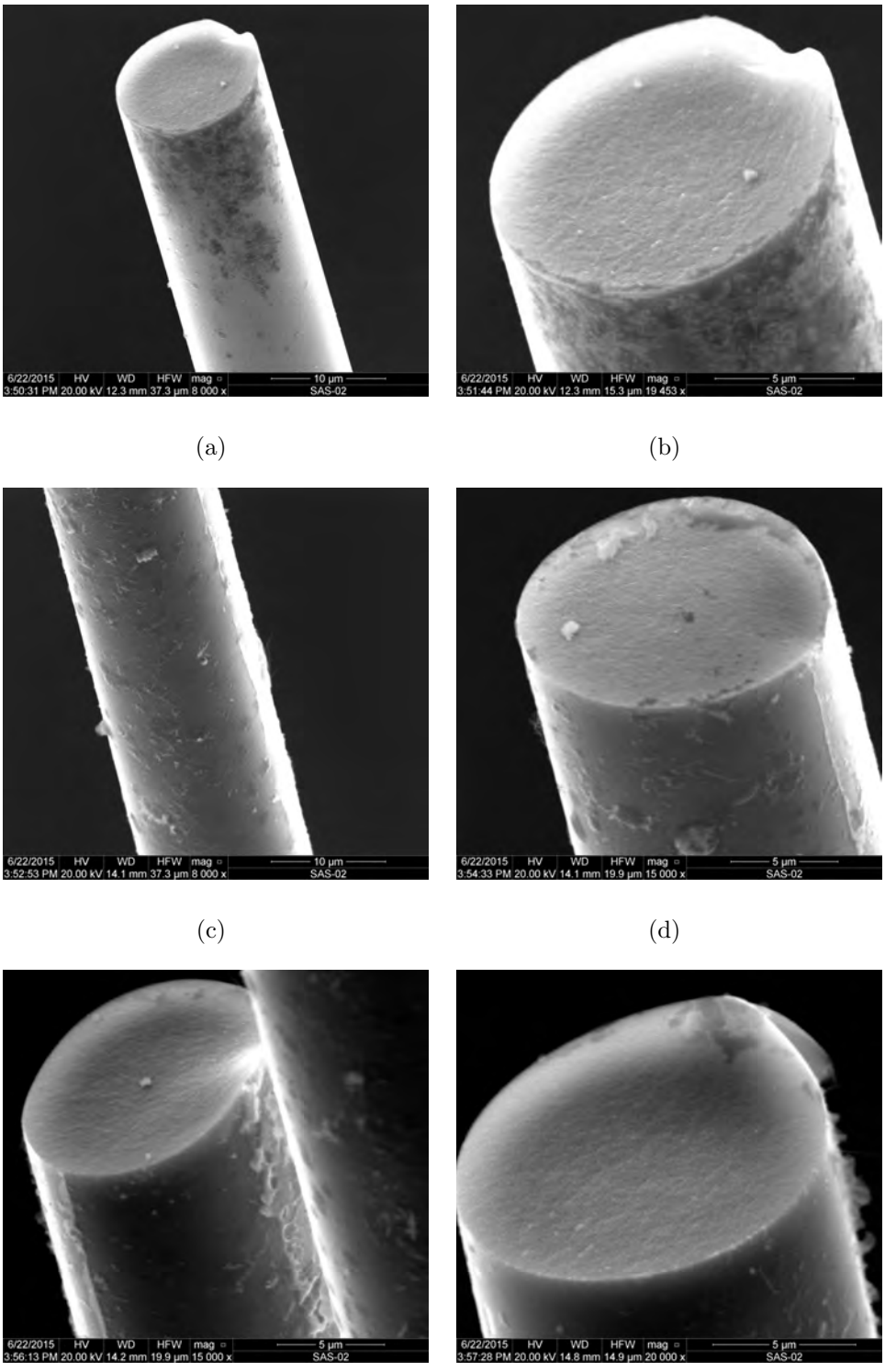


Figure B.101. Hi-Nicalon^{TM} S fiber tow specimen SS13, fracture surface, (800°C, σ = 538 MPa, t = 76.8 h, prematurely terminated due to power outage)

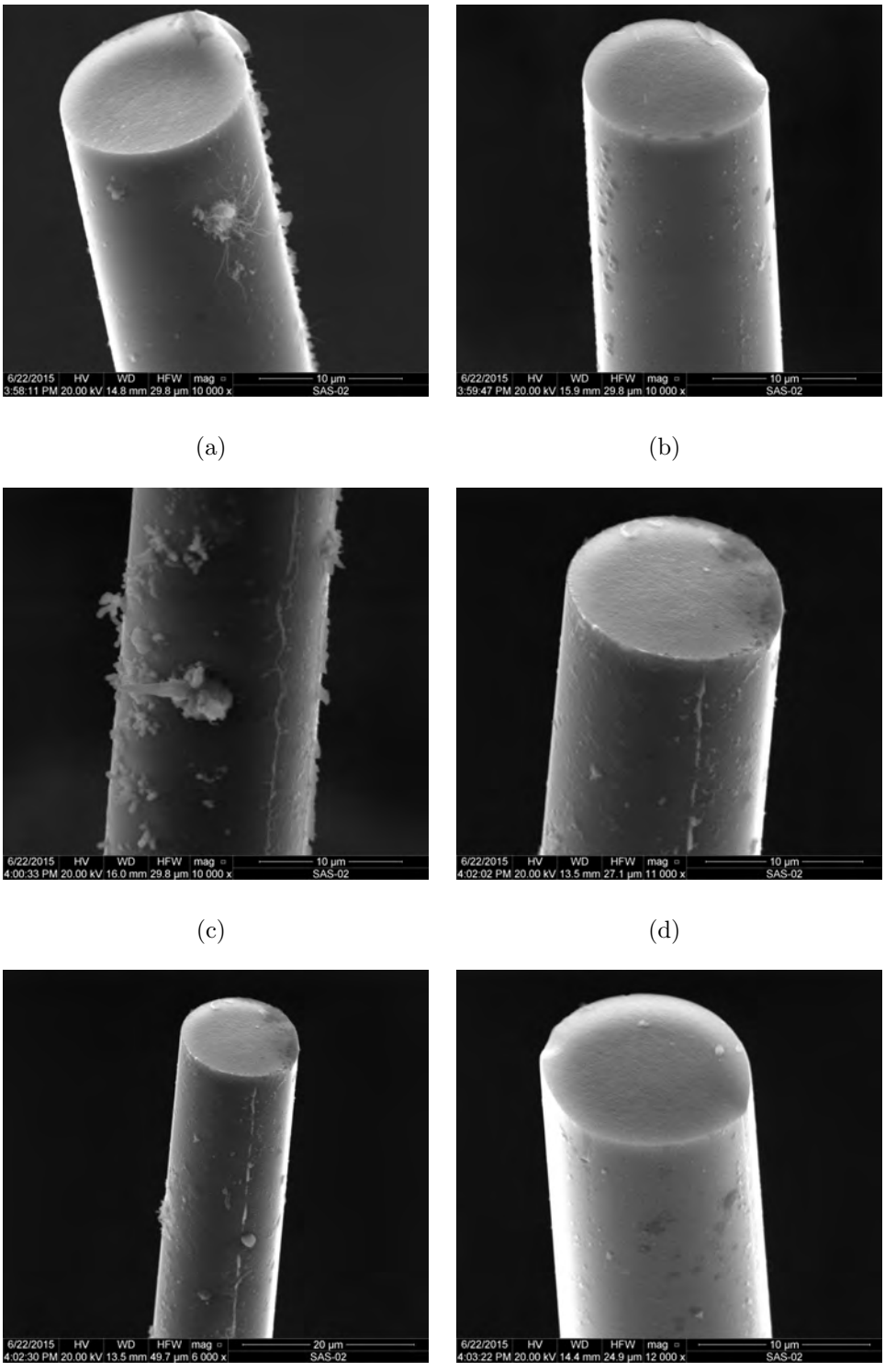
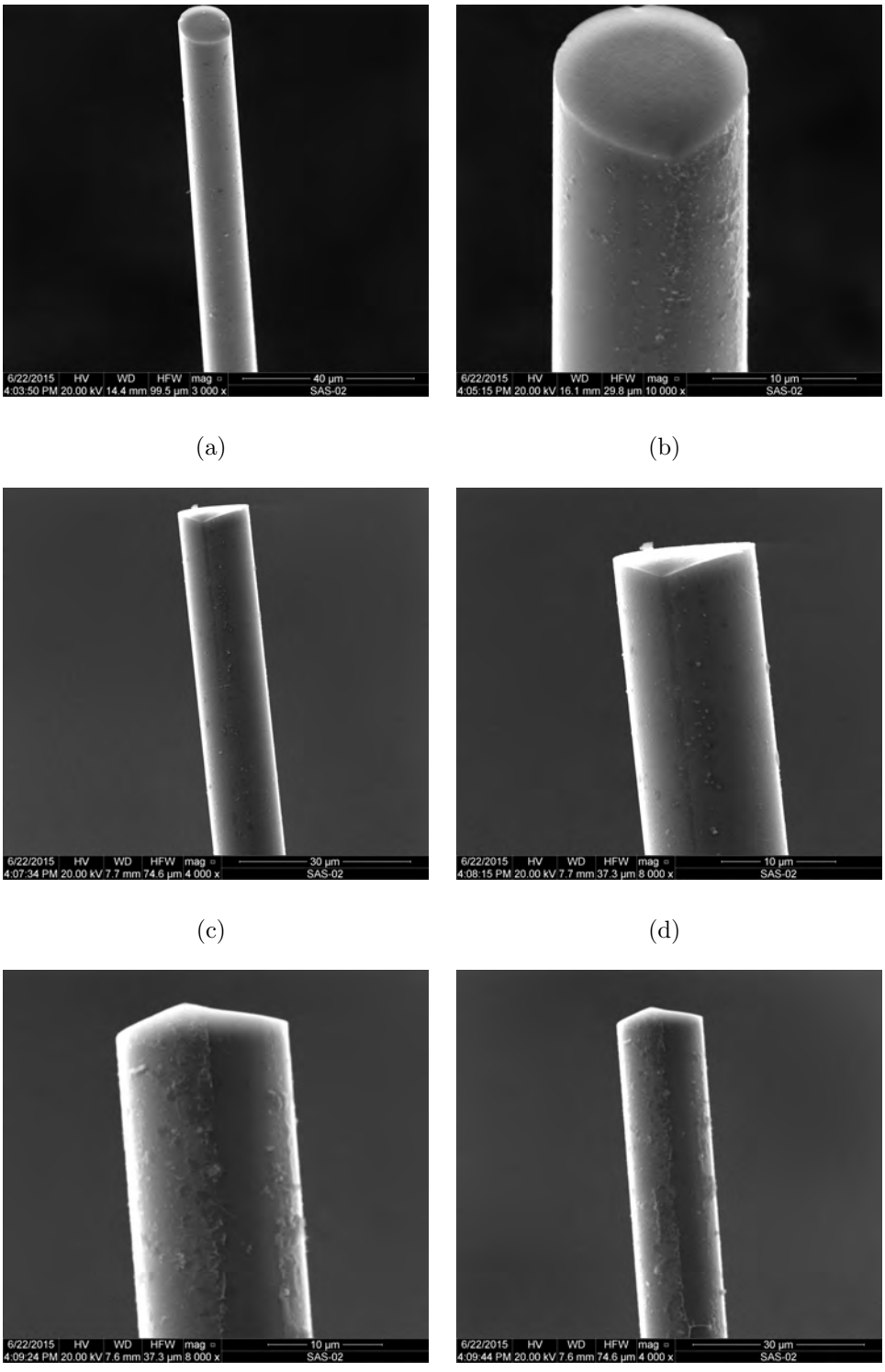


Figure B.102. Hi-Nicalon^{TM} S fiber tow specimen SS13, fracture surface, (800°C, σ = 538 MPa, t = 76.8 h, prematurely terminated due to power outage)



(a) (b)

(c) (d)

(e) (f)

Figure B.103. Hi-Nicalon^{TM} S fiber tow specimen SS13, fracture surface, (800°C, σ = 538 MPa, t = 76.8 h, prematurely terminated due to power outage)

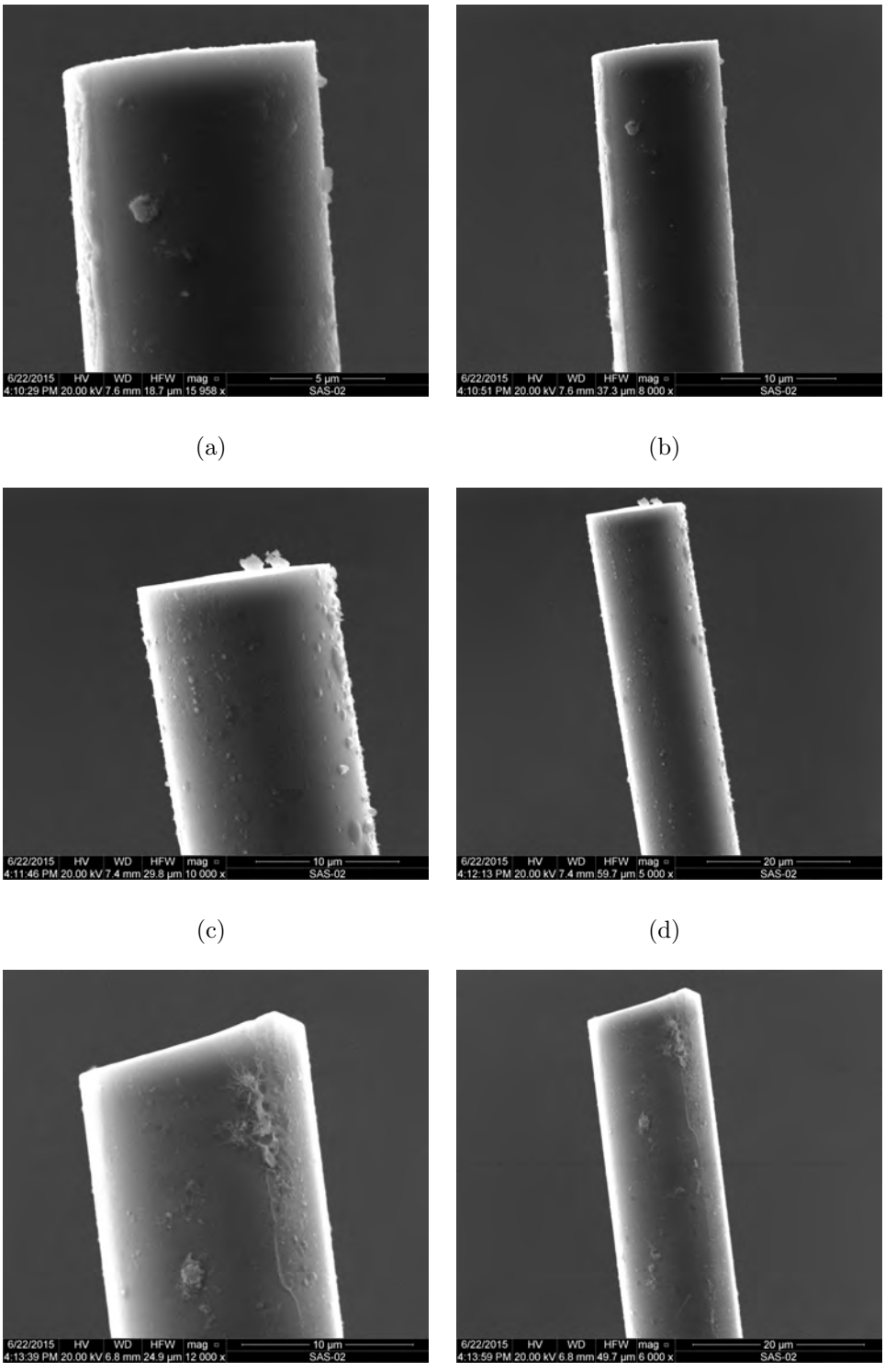
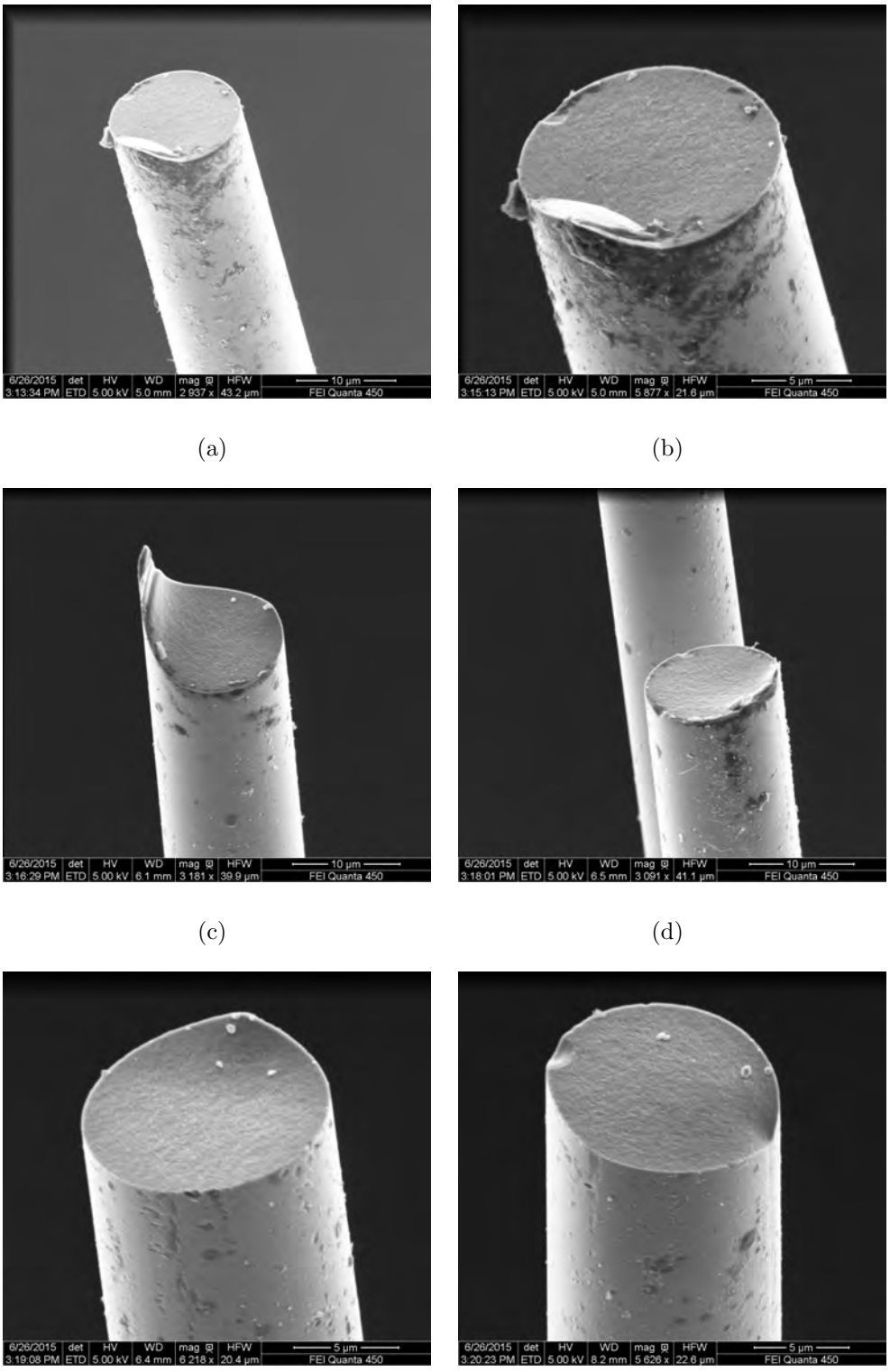


Figure B.104. Hi-Nicalon^{TM} S fiber tow specimen SS13, fracture surface, (800°C, σ = 538 MPa, t = 76.8 h, prematurely terminated due to power outage)



(a) (b)

(c) (d)

(e) (f)

Figure B.105. Hi-Nicalon^{TM} S fiber tow specimen SS13, fracture surface, (800°C, σ = 538 MPa, t = 76.8 h, prematurely terminated due to power outage)

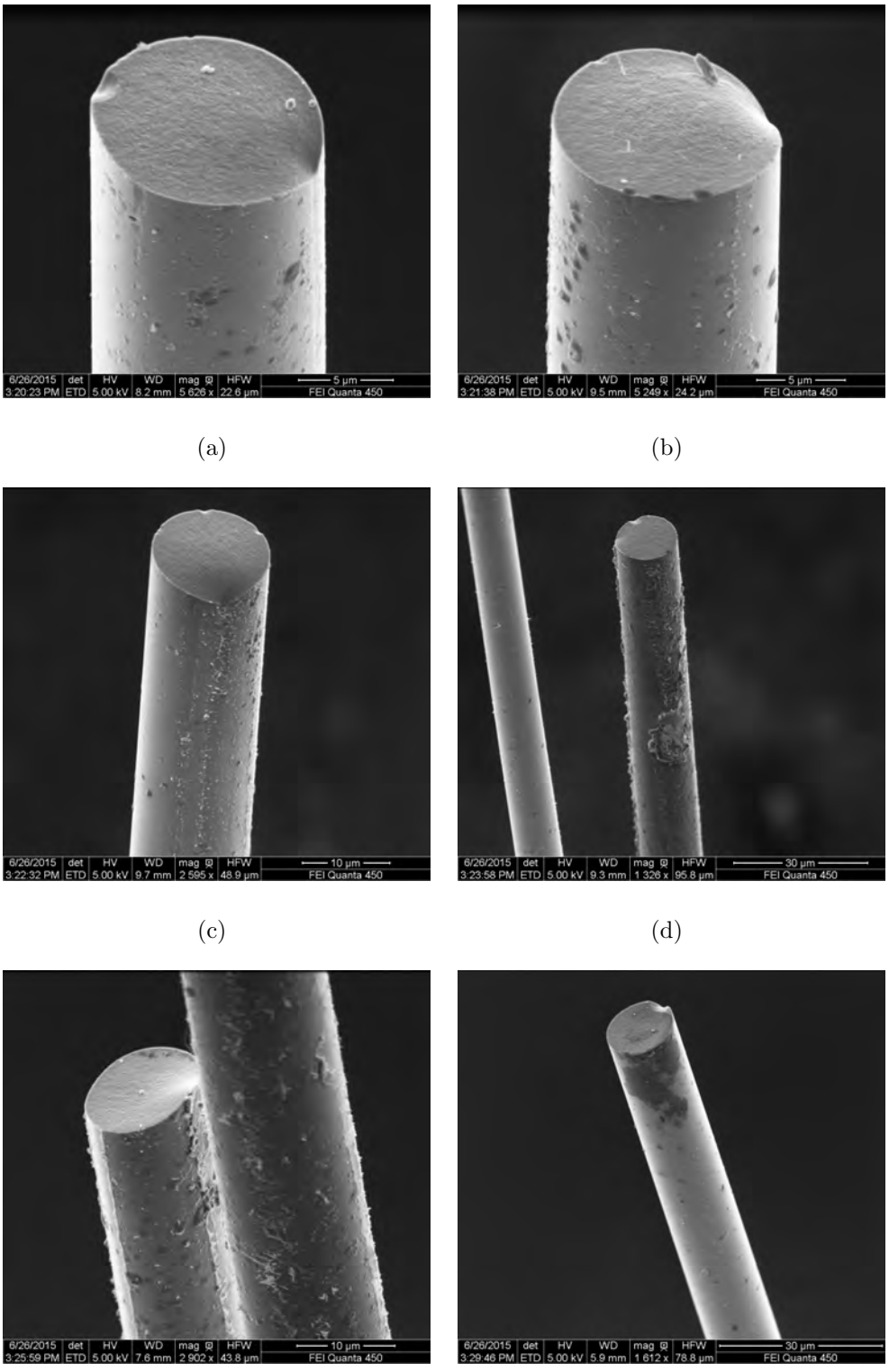
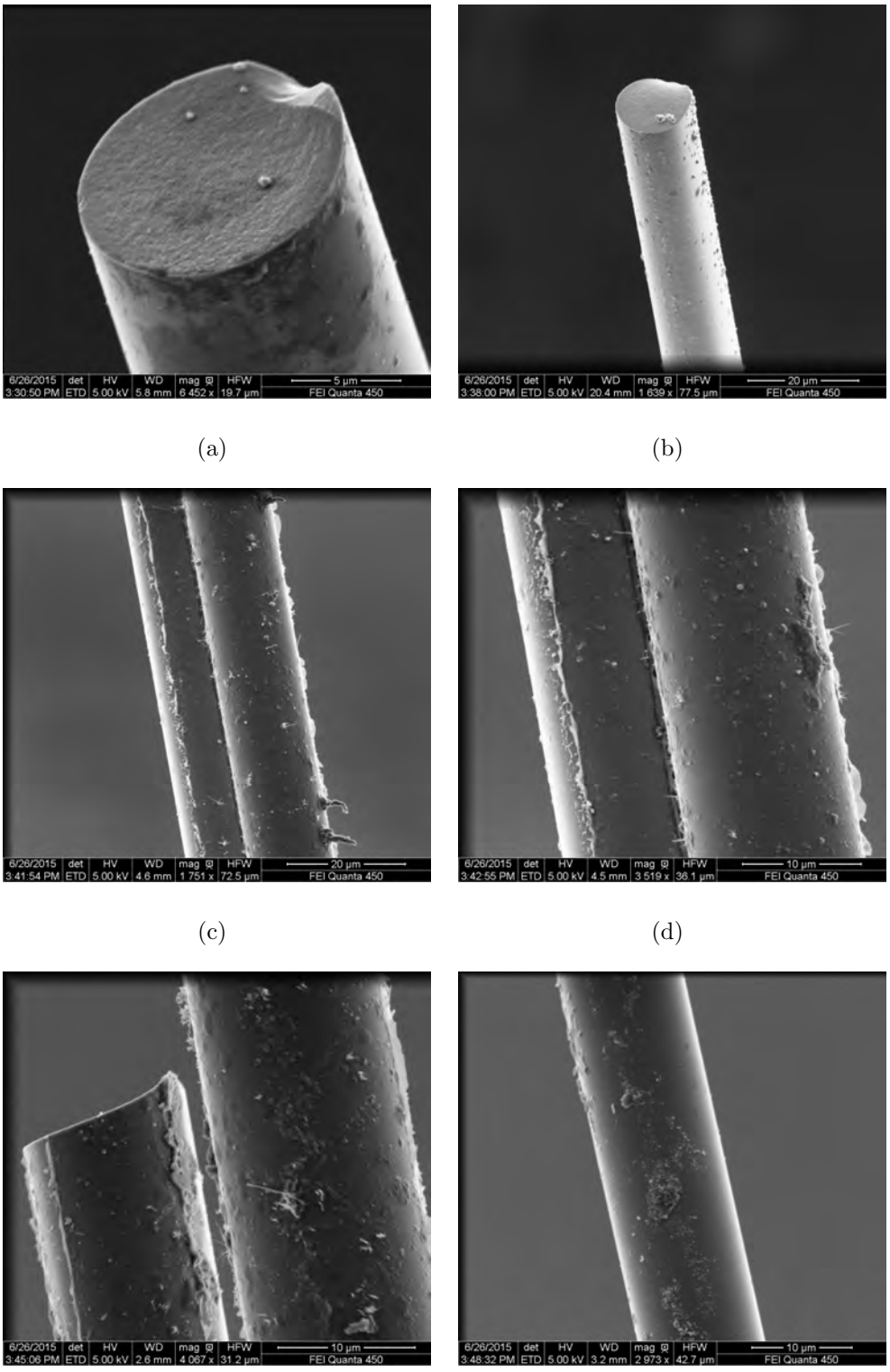


Figure B.106. Hi-Nicalon^{TM} S fiber tow specimen SS13, fracture surface, (800°C, σ = 538 MPa, t = 76.8 h, prematurely terminated due to power outage)



(a) (b)

(c) (d)

(e) (f)

Figure B.107. Hi-Nicalon^{TM} S fiber tow specimen SS13, fracture surface, (800°C, σ = 538 MPa, t = 76.8 h, prematurely terminated due to power outage)

Bibliography

1. B. R. Steffens. Creep of Hi-Nicalon S fiber tows at elevated temperature in air and in steam, 2012. MS Thesis, Air Force Institute of Technology (AU), March 2012.

2. H. R. Clauser. Advanced composite materials. *Scientific American*, 229(1):36–44, Jul 1973.

3. *Exodus*, chapter 5, pages 85–86. The Holy Bible: King James Version. The Church of Jesus Christ of Latter-Day Saints, Salt Lake City, UT, USA, 2013.

4. C. J. Armani. Creep performance of oxide ceramic fiber materials at elevated temperature in air and in steam, 2011. PhD Dissertation, Air Force Institute of Technology (AU), March 2011.

5. T. Johnson. History of composites, 2013.

6. American Composites Manufacturers Association. History of the composites industry, 2013.

7. C. E. Knox. *Fiberglass Reinforcement*, pages 136–159. Handbook of Composites. Van Nostrand Reinhold Company, New York, NY, USA, 1982.

8. A. B. Strong. History of composite materials – opportunities and necessities. *Composites Manufacturing*, 2002.

9. E. P. Scala. A brief history of composites in the u.s.–the dream and the success. *The Member Journal of the Minerals, Metals, & Materials Society*, 48(2):45–48, 1996.

10. C. T. Herakovich. *Mechanics of Fibrous Composites*. New York: John Wiley & Sons, Inc., 1998.

11. D. R. Tenney, J. G. Davis, R. B. Pipes, and N. Johnston. NASA composite materials development: Lessons learned and future challenges. In *NATO RTO AVT-164 Workshop on Support of Composite Systems; Bonn; 19-22 Oct. 2009; Germany*, volume LF99-9370, Oct 19, 2009.

12. K. K. Chawla. *Ceramic Matrix Composites*. Kluwer Academic, Boston, 2003.

13. S. Schmidt, S. Beyer, H. Knabe, H. Immich, R. Meistring, and A. Gessler. Advanced ceramic matrix composite materials for current and future propulsion technology applications. *Acta Astronautica*, 55(3-9):409–420, 2004.

14. J. Alting, F. Grauer, G. Hagemann, and J. Kretschmer. *Hot-firing of an advanced 40 kN thrust chamber*. American Institute of Aeronautics and Astronautics, July 8, 2001.

15. Department of Defense. *Ceramic Matrix Composites*, chapter 2, pages 43–46. Composite Materials Handbook, vol. 5. US Army Research Laboratory, 2002.

16. F. W. Zok and C. G. Levi. Mechanical properties of porous-matrix ceramic composites. *Advanced Engineering Materials*, 3(1-2):15–23, Jan 2001.

17. R. Naslain. *Ceramic Matrix Composite*, pages 213–216. EUROPEAN WHITE BOOK ON FUNDAMENTAL RESEARCH IN MATERIALS SCIENCE,. Max-Planck-Institut fur Metallforschung, Stuttgart, GE, 2001.

18. J. C. McNulty, M. Y. He, and F. W. Zok. Notch sensitivity of fatigue life in a Sylramic TM/SiC composite at elevated temperature. *Composites Science and Technology*, 61(9):1331–1338, Jul 2001.

19. A. R. Bunsell and A. Piant. A review of the development of three generations of small diameter silicon carbide fibres. *Journal of Materials Science*, 41(3):823–839, Feb 1, 2006.

20. T. Ishikawa. Advances in inorganic fibers. *Advances Polymer Science*, 178:109–144, 2005.

21. K. M. Prewo and J. J. Brennan. High-strength silicon carbide fibre-reinforced glass-matrix composites. *Journal of Materials Science*, 15(2):463–468, 1980.

22. J. J. Brennan and K. M. Prewo. Silicon carbide fibre reinforced glass-ceramic matrix composites exhibiting high strength and toughness. *Journal of Materials Science*, 17(8):2371–2383, 1982.

23. T. R. Shillig. Creep of Hi-Nicalon S fiber tows at elevated temperature in air and in steam, 2013. MS Thesis, Air Force Institute of Technology (AU), March 2013.

24. R. S. Hay, G. E. Fair, R. Bouffioux, E. Urban, J. Morrow, A. Hart, and M. Wilson. Hi-Nicalon-S SiC fiber oxidation and scale crystallization kinetics. *Journal of the American Ceramic Society*, 94(11):3983–3991, 2011.

25. N. F. Mott, S. Rigo, F. Rochet, and A. M. Stoneham. Oxidation of silicon. *Philosophical Magazine B (Physics of Condensed Matter, Electronic, Optical and Magnetic Properties)*, 60(2):189–212, Aug 1989.

26. D. H. Alsem, R. Timmerman, B. L. Boyce, E. A. Stach, J. Th M. De Hosson, and R. O. Ritchie. Very high-cycle fatigue failure in micron-scale polycrystalline silicon films: Effects of environment and surface oxide thickness. *Journal of Applied Physics*, 101(1):013515, Jan 1, 2007.

27. M. Navi and S. T. Dunham. A viscous compressible model for stress generation/relaxation in Sio2. *Journal of the Electrochemical Society*, 144(1):367–371, Jan 1997.

28. B. E. Deal and A. S. Grove. General relationship for the thermal oxidation of silicon. *Journal of Applied Physics*, 36(12):3770–3778, 1965.

29. F. W. Zok. Developments in oxide fiber composites. *Journal of the American Ceramic Society*, 89(11):3309–3324, 2006.

30. D. T. Christensen. Fatigue behavior of an advanced SiC/SiC composite at elevated temperature in air and in steam, 2009. MS Thesis, Air Force Institute of Technology (AU), Oct 2009.

31. A. G. Evans and F. W. Zok. The physics and mechanics of fiber-reinforced brittle-matrix composites. *Journal of Materials Science*, 29(15):3857–3896, Aug 1, 1994.

32. R. J. Kerans and T. A. Parthasarathy. Crack deflection in ceramic composites and fiber coating design criteria. *Composites Part A (Applied Science and Manufacturing)*, 30A(4):521–524, 1999.

33. R. J. Kerans, R. S. Hay, N. J. Pagano, and T. A. Parthasarathy. The role of the fiber-matrix interface in ceramic composites. *American Ceramic Society Bulletin*, 68(2):429–442, Feb 1989.

34. A.G. Hegedus. Ceramic bodies of controlled porosity and process for making same, May 1991. US Patent 5,017,522.

35. J. B. Davis, J. P. A. Lofvander, A. G. Evans, E. Bischoff, and M. L. Emiliani. Fiber coating concepts for brittle-matrix composites. *Journal of the American Ceramic Society*, 76(5):1249–1257, 1993.

36. F. F. Lange, W. C. Tu, and A. G. Evans. Processing of damage-tolerant, oxidation-resistant ceramic matrix composites by a precursor infiltration and pyrolysis method. *Materials Science and Engineering: A*, 195:145–150, Jun 1, 1995.

37. M. G. Harrison, M. L. Millard, and A. Szweda. Fiber reinforced ceramic matrix composite member and method for making, Feb 11, 1997. US Patent 5,601,674.

38. W. C. Tu, F. F. Lange, and A. G. Evans. Concept for a damage-tolerant ceramic composite with "strong" interfaces. *Journal of the American Ceramic Society*, 79(2):417–424, 1996.

39. K. A. Keller, T. Mah, T. A. Parthasarathy, and C. M. Cooke. Fugitive interfacial carbon coatings for oxide/oxide composites. *Journal of the American Ceramic Society*, 83(2):329–336, 2000.

40. L. P. Zawada and S. S. Lee. *Evaluation of Four CMCs for Aerospace Turbine Engine Divergent Flaps and Seals*, pages 337–339. Proceedings of the 19th Annual

Conference on Composites, Advanced Ceramics, Materials, and Structures A: Ceramic Engineering and Science Proceedings. John Wiley & Sons, Inc., 1995; 2008.

41. F. E. Heredia, J. C. Mcnulty, F. W. Zok, and A. G. Evans. Oxidation embrittlement probe for ceramic-matrix composites. *Journal of the American Ceramic Society*, 78(8):2097–2100, Aug 1995.

42. T. T. Kim, S. Mall, and L. P. Zawada. Fatigue behavior of Hi-Nicalon Type-S^{TM}/BN/SiC ceramic matrix composites in a combustion environment. *International Journal of Applied Ceramic Technology*, 8(2):261–272, Mar 2011.

43. T. Mah, N. L. Hecht, D. E. Mccullum, J. R. Hoenigman, H. M. Kim, A. P. Katz, and H. A. Lipsitt. Thermal-stability of SiC fibers (Nicalon). *Journal of Materials Science*, 19(4):1191–1201, 1984.

44. R.J. Kerans, R.S. Hay, and T.A. Parthasarathy. Structural ceramic composites. *Current Opinion in Solid State and Materials Science*, 4(5):445–451, Oct 1999.

45. R.E. Tressler. Recent developments in fibers and interphases for high temperature ceramic matrix composites. *Composites Part A: Applied Science and Manufacturing*, 30(4):429–437, Apr 1999.

46. J. A. DiCarlo, H. M. Yun, and J. B. Hurst. Fracture mechanisms for SiC fibers and SiC/SiC composites under stress-rupture conditions at high temperatures. *Applied Mathematics and Computation*, 152(2):473–481, May 5, 2004.

47. S. Bertrand, R. Pailler, and J. Lamon. SiC/SiC minicomposites with nanoscale multilayered fibre coatings. *Composites Science and Technology*, 61(3):363–367, Feb 2001.

48. S. Bertrand, R. Pailler, and J. Lamon. Influence of strong fiber/coating interfaces on the mechanical behavior and lifetime of Hi-Nicalon/(PyC/SiC)n/SiC minicomposites. *Journal of the American Ceramic Society*, 84(4):787, 2001.

49. M. C. Halbig, J. D. McGuffin-Cawley, A. J. Eckel, and D. N. Brewer. Oxidation kinetics and stress effects for the oxidation of continuous carbon fibers within a microcracked C/SiC ceramic matrix composite. *Journal of the American Ceramic Society*, 91(2):519, 2008.

50. K. L. Rugg, R. E. Tressler, C. E. Bakis, and J. Lamon. Creep of SiC-SiC microcomposites. *Journal of the European Ceramic Society*, 19(13-14):2285–2296, Oct 1999.

51. S. Bertrand, P. Forio, R. Pailler, and J. Lamon. Hi-Nicalon/SiC minicomposites with (pyrocarbon/SiC)(n) nanoscale multilayered interphases. *Journal of the American Ceramic Society*, 82(9):2465–2473, Sep 1999.

52. S. Bertrand, C. Droillard, R. Pailler, X. Bourrat, and R. Naslain. Tem structure of (PyC/SiC)(n) multilayered interphases in SiC/SiC composites. *Journal of the European Ceramic Society*, 20(1):1–13, Jan 2000.

53. S. Bertrand, F. Germain, R. Pailler, and J. Lamon. Thermomechanical behaviour of 2d-SiC/SiC composites with nanoscale-multilayered (PyC/SiC)(n) interphases. *Advanced Composites Letters*, 8(6):315–321, 1999.

54. S. Pasquier, J. Lamon, and R. Naslain. Tensile static fatigue of 2d SiC/SiC composites with multilayered (PyC-SiC)(n) interphases at high temperatures in oxidizing atmosphere. *Composites Part A-Applied Science and Manufacturing*, 29(9-10):1157–1164, 1998.

55. S. Bertrand, O. Boisron, R. Pailler, J. Lamon, and R. Naslain. (PyC/SiC)n and (BN/SiC)n nanoscale-multilayered interphases by pressure pulsed-CVI. *High Temperature Ceramic Matrix Composites III*, 164-1:357–360, 1999.

56. H. M. Yun, J. Z. Gyekenyesi, Y. L. Chen, D. R. Wheeler, and J. A. Dicarlo. *Tensile Behavior of SiC/SiC Composites Reinforced by Treated Sylramic SiC Fibers*, pages 521–531. 25th Annual Conference on Composites, Advanced Ceramics, Materials, and Structures: A: Ceramic Engineering and Science Proceedings. John Wiley & Sons, Inc., 2001.

57. J. A. DiCarlo, H. M. Yun, and J. J. Brennan. SiC/SiC composites with improved BN coating on fibers. NASA Tech Brief LEW 16864, NASA, 2000.

58. J. A. DiCarlo, H. M. Yun, G. N. Morscher, and R. T. Bhatt. SiC/SiC material development under the NASA UEET program. In *Proceedings of 25th Annual Conference on Ceramics, Metal, & Carbon Composites, Materials and Structures, Restricted Sessions, Paper F02*, 2001.

59. V. Calard and J. Lamon. A probabilistic-statistical approach to the ultimate failure of ceramic-matrix composites - part i: Experimental investigation of 2d woven SiC/SiC composites. *Composites Science and Technology*, 62(3):385–393, 2002.

60. S. Bertrand. Improvement of lifetime of SiC/SiC composites using multilayered interphases (PyC/SiC)n and (BN/SiC)n, 1998. PhD Dissertation.

61. L. Guillaumat and J. Lamon. Comportement mecanique et endommagement de composites 2d SiC/SiC. *Revue des Composites et des Materiaux Avances*, 9(2):183–203, 1999.

62. J. Martinez-Fernandez and G. N. Morscher. Room and elevated temperature tensile properties of single tow Hi-Nicalon, carbon interphase, CVI SiC matrix minicomposites. *Journal of the European Ceramic Society*, 20(14-15):2627–2636, Dec 2000.

63. P. Feissel. Suivi par emission acoustique de l'endommagement des composites a matrice ceramique (SiC/SiC). LCTS report, LCTS, 1999.

64. F. Lavaire. Investigation of the lifetime of SiC/SiC minicomposites at high temperatures. Report, LCTS, 1999.

65. P. Forio and J. Lamon. *Fatigue Behavior at High Temperatures in Air of a 2D SiC/Si-B-C Composite with a Self-Healing Multilayered Matrix*, pages 127–141. Advances in Ceramic Matrix Composites VII. The American Ceramic Society, 2006.

66. H. M. Yun, J. A. DiCarlo, R. T. Bhatt, and J. B. Hurst. Processing and structural advantages of the sylramic-iBN SiC fiber for SiC/SiC components. In *Ceramic Engineering and Science Proceedings*, pages 247–253, 2003.

67. A. Hasegawa, A. Kohyama, R. H. Jones, L. L. Snead, B. Riccardi, and P. Fenici. Critical issues and current status of SiC/SiC composites for fusion. *Journal of Nuclear Materials*, 283:128–137, Dec 2000.

68. J. L. Besson, B. Doucey, S. Lucas, D. Bahloul-Hourlier, and P. Goursat. SiCn nanocomposite: Creep behaviour. *Journal of the European Ceramic Society*, 21(7):959–968, Jul 2001.

69. F. Pailler. Predictions of lifetime at high temperatures in air for SiC/sibc composites, 2004. PhD Dissertation.

70. A. Laforet. Lifetime of SiC/SiC composites at high temperatures. LCTS Report RT06-0695, LCTS, 2006.

71. J. A. DiCarlo, HM Yun, GN Morscher, and R. T. Bhatt. *SiC Fiber-Reinforced SiC Matrix Composites for Thermostructural Applications to 1200° Cand Above*, pages 77–98. Handbook of Ceramic Composites. Kluwer Academic, New York, NY, USA, 2005.

72. G. N. Morscher, G. Ojard, R. Miller, Y. Gowayed, U. Santhosh, J. Ahmad, and R. John. Tensile creep and fatigue of sylramic-iBN melt-infiltrated SiC matrix composites: Retained properties, damage development, and failure mechanisms. *Composites Science and Technology*, 68(15-16):3305–3313, Dec 2008.

73. G. Ojard, A. Calomino, G. Morscher, Y. Gowayed, U. Santhosh, J. Ahmad, R. Miller, and R. John. Post creep/dwell fatigue testing of mi SiC/SiC composites. In *31st International Conference on Advanced Ceramics and Composites, January 21, 2007 - January 26*, volume 28, pages 135–143, Daytona Beach, FL, United states, 2008. Air Force Research Laboratory, AFRL/MLLMN, Wright-Patterson AFB, OH, American Ceramic Society.

74. V. V. Pujar and G. N. Morscher. Tensile creep behavior of melt-infiltrated SiC-SiC composites for gas turbine engine applications. In *2007 ASME Turbo Expo, May 14, 2007 - May 17*, volume 1, pages 261–266, Montreal, Que., Canada, 2007. Materials and Simulation Technical Center, Goodrich Corporation, Brecksville, OH, American Society of Mechanical Engineers.

75. S. Kalluri, D. N. Brewer, and A. M. Calomino. An assessment of variability in the average tensile properties of a melt-infiltrated SiC/SiC composite. *Ceramic Engineering and Science Proceedings*, 25(4):79–86, 2004.

76. G. N. Morscher. Stress-dependent matrix cracking in 2d woven SiC-fiber reinforced melt-infiltrated SiC matrix composites. *Composites Science and Technology*, 64(9):1311–1319, Jul 2004.

77. G. N. Morscher, H. M. Yun, and J. A. DiCarlo. Matrix cracking in 3d orthogonal melt-infiltrated SiC/SiC composites with various z-fiber types. *Journal of the American Ceramic Society*, 88(1):146–153, Jan 2005.

78. G. N. Morscher and J. D. Cawley. Intermediate temperature strength degradation in SiC/SiC composites. *Journal of the European Ceramic Society*, 22(14-15):2777–2787, 2002.

79. G. N. Morscher, H. M. Yun, and J. A. DiCarlo. In-plane cracking behavior and ultimate strength for 2d woven and braided melt-infiltrated SiC/SiC composites tensile loaded in off-axis fiber directions. *Journal of the American Ceramic Society*, 90(10):3185–3193, Oct 2007.

80. G. N. Morscher and V. V. Pujar. Creep and stress-strain behavior after creep for SiC fiber reinforced, melt-infiltrated SiC matrix composites. *Journal of the American Ceramic Society*, 89(5):1652–1658, Mar 2006.

81. G. N. Morscher. Matrix cracking in four different 2d SiC/SiC composite systems. In *35th International SAMPE Technical Conference Proceedings*, pages 1–14, Covina, 2003. Society for the Advancement of Material and Process Engineering (SAMPE).

82. G. N. Morscher. Modal acoustic emission of damage accumulation in a woven SiC/SiC composite. *Composites Science and Technology*, 59(5):687–697, 1999.

83. S. Le Gallet, F. Rebillat, A. Guette, X. Bourrat, and F. Doux. Influence of a multilayered matrix on the lifetime of SiC/BN/SiC minicomposites. *Journal of Materials Science*, 39(6):2089–2097, Mar 15, 2004.

84. A. Delcamp. Protection de fibres base SiC pour composites a matrice cerammique, 2008. PhD Dissertation.

85. M. Ruggles-Wrenn and M. T. Pope. Creep behavior in interlaminar shear of a SiC/SiC ceramic composite with a self-healing matrix. *Applied Composite Materials*, pages 1–13, 2013.

86. F. Nualas and F. Rebillat. A multi-scale approach of degradation mechanisms inside a SiC(f)/Si-B-C(m) based self-healing matrix composite in a dry oxidizing environment. *Oxidation of Metals*, 80(3):279–287, Oct 2013.

87. C. Zhang, S. Qiao, K. Yan, Y. Liu, Q. Wu, D. Han, and M. Li. Mechanical properties of a carbon fiber reinforced self-healing multilayered matrix composite at elevated temperatures. *Materials Science & Engineering: A (Structural Materials: Properties, Microstructure and Processing)*, 528(7-8):3073–3078, Mar 25, 2011.

88. S. W. Li, L. T. Zhang, Y. S. Liu, L. F. Cheng, Z. D. Feng, X. G. Luan, W. H. Zhang, and W. B. Yang. Self-healing behavior of 2D C/SiC modified by partial boron carbide matrix after annealing at low temperature in wet oxygen. *Journal of Inorganic Materials*, 25(11):1199–1203, Nov 2010.

89. M. B. Ruggles-Wrenn, J. Delapasse, A. L. Chamberlain, J. E. Lane, and T. S. Cook. Fatigue behavior of a Hi-Nicalon^{TM}/SiC-B4C composite at 1200°C in air and in steam. *Materials Science and Engineering: A*, 534(0):119–128, Feb 1, 2012.

90. M. B. Ruggles-Wrenn and G. Kurtz. Notch sensitivity of fatigue behavior of a Hi-Nicalon^{TM}/SiC-B4C composite at 1,200°C in air and in steam. *Applied Composite Materials*, 20(5):891–905, Oct 1, 2013.

91. M. B. Ruggles-Wrenn and T. P. Jones. Tension & compression fatigue of a SiC/SiC ceramic matrix composite at 1200°C in air and in steam. *International Journal of Fatigue*, 47(0):154–160, Feb 2013.

92. A. Delcamp, L. Maille, S. Saint Martin, R. Pailler, and A. Guette. Al-O-N and Al-O-B-N thin films applied on Si-O-C fibers. *Composites Science and Technology*, 70(4):622–626, Apr 2010.

93. H. M. Yun and J. A. DiCarlo. New high-performance SiC fiber developed for ceramic composites. NASA Tech Memo TM-2002-211333, NASA, 2001.

94. J. A. DiCarlo and H. M. Yun. *Non-oxide (Silicon Carbide) Fibers*, pages 33–52. Handbook of Ceramic Composites. Kluwer Academic, 2005.

95. S. M. Wiederhorn, B. J. Hockey, and J. D. French. Mechanisms of deformation of silicon nitride and silicon carbide at high temperatures. *Journal of the European Ceramic Society*, 19(13-14):2273–2284, Oct 1999.

96. S. Yajima, J. Hayashi, and M. Omori. Continuous silicon-carbide fiber of high-tensile strength. *Chemistry Letters*, (9):931–934, Jan 1975.

97. S. Yajima, J. Hayashi, M. Omori, and K. Okamura. Development of a silicon-carbide fiber with high-tensile strength. *Nature*, 261(5562):683–685, 1976.

98. S. Yajima, K. Okamura, J. Hayashi, and M. Omori. Synthesis of continuous SiC fibers with high-tensile strength. *Journal of the American Ceramic Society*, 59(7-8):324–327, 1976.

99. S. Yajima, Y. Hasegawa, J. Hayashi, and M. Iimura. Synthesis of continuous silicon-carbide fiber with high-tensile strength and high youngs modulus. 1. Synthesis of polycarbosilane as precursor. *Journal of Materials Science*, 13(12):2569–2576, 1978.

100. Y. Hasegawa, M. Iimura, and S. Yajima. Synthesis of continuous silicon-carbide fiber. 2. Conversion of polycarbosilane fiber into silicon-carbide fibers. *Journal of Materials Science*, 15(3):720–728, 1980.

101. G. Simon and A. R. Bunsell. Mechanical and structural characterization of the Nicalon silicon-carbide fiber. *Journal of Materials Science*, 19(11):3649–3657, 1984.

102. D. J. Pysher, N. Jia, R. J. Bodet, and R. E. Tressler. Creep behavior of ceramic fibers. In S. K. Das, C. P. Ballard, and F. Marikar, editors, *High performance composites for the 1990's Proc. of a TMS Northeast Regional Symposium sponsored by The Minerals, Metals & Materials Society-New Jersey Chapter held at Morristown, New Jersey, June 6-8, 1990*, pages 267–281, Warrendale, Pa., 1991. Minerals, Metals & Materials Society.

103. C. Laffon, A. M. Flank, P. Lagarde, M. Laridjani, R. Hagege, P. Olry, J. Cotteret, J. Dixmier, J. L. Miquel, H. Hommel, and A. P. Legrand. Study of Nicalon-based ceramic fibers and powders by exafs spectrometry, x-ray-diffractometry and some additional methods. *Journal of Materials Science*, 24(4):1503–1512, Apr 1989.

104. J. Lipowitz. Polymer-derived ceramic fibers. *American Ceramic Society Bulletin*, 70(12):1888–1894, Dec 1991.

105. M. H. Jaskowiak and J. A. Dicarlo. Pressure effects on the thermal-stability of silicon-carbide fibers. *Journal of the American Ceramic Society*, 72(2):192–197, Feb 1989.

106. L. Porte and A. Sartre. Evidence for a silicon oxycarbide phase in the Nicalon silicon-carbide fiber. *Journal of Materials Science*, 24(1):271–275, Jan 1989.

107. L. C. Sawyer, M. Jamieson, D. Brikowski, M. I. Haider, and R. T. Chen. Strength, structure, and fracture properties of ceramic fibers produced from polymeric precursors. 1. base-line studies. *Journal of the American Ceramic Society*, 70(11):798–810, Nov 1987.

108. G. Simon and A. R. Bunsell. Creep-behavior and structural characterization at high-temperatures of Nicalon SiC fibers. *Journal of Materials Science*, 19(11):3658–3670, 1984.

109. D. M. Mieskowski, T. E. Mitchell, and A. H. Heuer. Bubble formation in oxide scales on SiC. *Journal of the American Ceramic Society*, 67(1):C17–C18, 1984.

110. S. Yajima, K. Okamura, T. Matsuzawa, Y. Hasegawa, and T. Shishido. Anomalous characteristics of the microcrystalline state of SiC fibers. *Nature*, 279(5715):706–707, 1979.

111. T. J. Clark, R. M. Arons, J. B. Stamatoff, and J. Rabe. Thermal degradation of Nicalon SiC fibers. In *Ceramic Engineering and Science Proceedings*, volume 6, pages 576–588. American Ceramic Society, 1985.

112. T. J. Clark, E. R. Prack, M. Q. Haider, and L. C. Sawyer. Oxidation of SiC ceramic fiber. In *Ceramic Engineering and Science Proceedings*, volume 8, pages 717–731. American Ceramic Society, 1987.

113. R. Naslain. Design, preparation and properties of non-oxide CMCs for application in engines and nuclear reactors: An overview. *Composites Science and Technology*, 64(2):155–170, Feb 2004.

114. R. Bodet, X. Bourrat, J. Lamon, and R. Naslain. Tensile creep-behavior of a silicon carbide-based fiber with a low-oxygen content. *Journal of Materials Science*, 30(3):661–677, Feb 1, 1995.

115. H. M. Yun and J. A. DiCarlo. Thermomechanical behavior of advanced SiC fiber multifilament tows. NASA Tech Manual NASA TM-107366, Lewis Research Center, 1996.

116. H. M. Yun and J. A. DiCarlo. Thermomechanical characterization of SiC fiber tows and implications for CMC. NASA Tech Manual NASA / TM–1999-209283, Glenn Research Center, 1999.

117. V. H. Hammond and D. M. Elzey. Comparing the creep response of alumina tows and single filaments. *Scripta Materialia*, 46(4):287–291, Feb 28, 2002.

118. K. G. Dassios, M. Steen, and C. Filiou. Mechanical properties of alumina Nextel^{TM} 720 fibres at room and elevated temperatures: tensile bundle testing. *Materials Science and Engineering: A*, 349(1-2):63–72, May 25, 2003.

119. V. Calard and J. Lamon. Failure of fiber bundles. *Composites Science and Technology*, 64(5):701–710, Apr 2004.

120. P. Forio, F. Lavaire, and J. Lamon. Delayed failure at intermediate temperatures (600-700°C) in air in silicon carbide multifilament tows. *Journal of the American Ceramic Society*, 87(5):888, 2004.

121. W. Gauthier and J. Lamon. Delayed failure of Hi-Nicalon and Hi-Nicalon S multifilament tows and single filaments at intermediate temperatures (500-800°C). *Journal of the American Ceramic Society*, 92(3):702, 2009.

122. *Advanced Technical Ceramic-Ceramic Composites–Methods of Test for Reinforcements–Part 5: Determination of Distribution of Tensile Strength and Tensile Strain to Failure of Filaments within a Multifilament Tow at Ambient Temperature (ENV1007-5).* European Committee for Standardization, Brussels, 1997.

123. E. Lara-Curzio. Oxidation induced stress - rupture of fiber bundles. *Journal of Engineering Materials and Technology-Transactions of the ASME*, 120(2):105–109, Apr 1998.

124. W. Gauthier. Delayed failure at intermediate temperatures (800°C) of SiC-based tows and filaments, 2006. PhD Dissertation.

125. W. Gauthier, F. Pailler, J. Lamon, and R. Pailler. Oxidation of silicon carbide fibers during static fatigue in air at intermediate temperatures. *Journal of the American Ceramic Society*, 92(9):2067, 2009.

126. P. Ladeveze and M. Genet. A new approach to the subcritical cracking of ceramic fibers. *Composites Science and Technology*, 70(11):1575–1583, Oct 15, 2010.

127. M. R'Mili and J. Lamon. Investigation of subcritical crack growth using load relaxation tests on fiber bundles. *Acta Materialia*, 59(7):2850–2857, Apr 2011.

128. C. Sauder, A. Brusson, and J. Lamon. Influence of interface characteristics on the mechanical properties of Hi-Nicalon type-S or Tyranno-SA3 fiber-reinforced SiC/SiC minicomposites. *International Journal of Applied Ceramic Technology*, 7(3):291–303, 2010.

129. E. Buet, C. Sauder, S. Poissonnet, P. Brender, R. Gadiou, and C. Vix-Guterl. Influence of chemical and physical properties of the last generation of silicon carbide fibres on the mechanical behaviour of SiC/SiC composite. *Journal of the European Ceramic Society*, 32(3):547–557, Mar 2012.

130. E. Buet, C. Sauder, D. Sornin, S. Poissonnet, J.N. Rouzaud, and C. Vix-Guterl. Influence of surface fibre properties and textural organization of a pyrocarbon interphase on the interfacial shear stress of SiC/SiC minicomposites reinforced with Hi-Nicalon S and Tyranno SA3 fibres. *Journal of the European Ceramic Society*, 34(2):179–188, Feb 2014.

131. I. H. A. Shames and F. A. A. Cozzarelli. *Elastic and Inelastic Stress Analysis.* Taylor & Francis Group, Philadelpia, PA, 1997.

132. J. B. Wachtman, W. R. Cannon, and M. J. Matthewson. *Mechanical Properties of Ceramics.* John Wiley & Sons, 2nd edition, Apr 2009.

133. J. P. Poirier. *Creep of Crystals*. Cambridge University Press, New York, NY, 1985.

134. E. Arzt, M. F. Ashby, and R. A. Verrall. Interface controlled diffusional creep. *Acta Metallurgica*, 31(12):1977–1989, 1983.

135. R. M. Cannon, W. H. Rhodes, and A. H. Heuer. Plastic-deformation of fine-grained alumina (al2o3). 1. interface-controlled diffusional creep. *Journal of the American Ceramic Society*, 63(1-2):46–53, 1980.

136. J. J. Sha, J. S. Park, T. Hinoki, and A. Kohyama. Heat treatment effects on creep behavior of polycrystalline SiC fibers. *Materials Characterization*, 57(1):6–11, Jul 2006.

137. J. J. Sha, T. Nozawa, J. S. Park, Y. Katoh, and A. Kohyama. Effect of heat treatment on the tensile strength and creep resistance of advanced SiC fibers. *Journal of Nuclear Materials*, 329:592–596, Aug 1, 2004.

138. C. Sauder and J. Lamon. Tensile creep behavior of SiC-based fibers with a low oxygen content. *Journal of the American Ceramic Society*, 90(4):1146, 2007.

139. K. B. Sprinkle. Creep of sylramic-iBN fiber tows at elevated temperature in air and in silicic acid-saturated steam, 2015. MS Thesis, Air Force Institute of Technology (AU), June 2015.

140. H. M. Yun and J. A. DiCarlo. Comparison of the tensile, creep, and rupture strength properties of stoichiometric SiC fibers. NASA Tech Manual NASA / TM–1999-209284, Glenn Research Center, 1999.

141. W. Krenkel, editor. *Ceramic matrix composites: fiber reinforced ceramics and their applications*. Wiley-VCH, Weinheim, GE, Jun 23, 2008.

142. R. S. Hay. Growth stress in SiO2 during oxidation of SiC fibers. *Journal of Applied Physics*, 111(6):063527, Mar 15, 2012.

143. T. A. Parthasarathy, R. A. Rapp, M. Opeka, and M. K. Cinibulk. Modeling oxidation kinetics of SiC-containing refractory diborides. *Journal of the American Ceramic Society*, 95(1):338–349, 2012.

144. T. Shimoo, K. Okamura, and Y. Morisada. Active-to-passive oxidation transition for polycarbosilane-derived silicon carbide fibers heated in ar-o-2 gas mixtures. *Journal of Materials Science*, 37(9):1793–1800, May 1, 2002.

145. T. Shimoo, K. Okamura, and T. Morita. Thermal stability of low-oxygen silicon carbide fibers (Hi-Nicalon) in carbon monoxide. *Journal of Materials Science*, 38(14):3089–3096, Jul 15, 2003.

146. T. Shimoo, T. Morita, and K. Okamura. Oxidation behavior and thermal stability of Si-C-O fibers (Nicalon) in carbon dioxide. *Journal of Materials Science*, 37(15):3181–3188, Aug 1, 2002.

147. G. Chollon, R. Pailler, R. Naslain, F. Laanani, M. Monthioux, and P. Olry. Thermal stability of a pcs-derived SiC fibre with a low oxygen content (Hi-Nicalon). *Journal of Materials Science*, 32(2):327–347, Jan 15, 1997.

148. T. Shimoo, F. Toyoda, and K. Okamura. Thermal stability of low-oxygen silicon carbide fiber (Hi-Nicalon) subjected to selected oxidation treatment. *Journal - Amercian Ceramic Society*, 83:1450–1456, Jan 1, 2000.

149. T. Shimoo, H. Takeuchi, and K. Okamura. Thermal stability of polycarbosilane-derived silicon carbide fibers under reduced pressures. *Journal of the American Ceramic Society*, 84(3):566–570, Mar 2001.

150. T. Shimoo, F. Toyoda, and K. Okamura. Oxidation kinetics of low-oxygen silicon carbide fiber. *Journal of Materials Science*, 35(13):3301–3306, Jul 2000.

151. T. Shimoo, K. Okamura, and W. Mutoh. Oxidation behavior and mechanical properties of low-oxygen SiC fibers prepared by vacuum heat-treatment of electron-beam-cured poly(carbosilane) precursor. *Journal of Materials Science*, 38(8):1653–1660, Apr 15 2003.

152. E. J. Opila. Oxidation and volatilization of silica formers in water vapor. *Journal of the American Ceramic Society*, 86(8):1238–1248, Aug 2003.

153. R. S. Hay, G. E. Fair, R. Bouffioux, E. Urban, J. Morrow, A. Hart, and M. Wilson. *Relationships Between Fiber Strength, Passive Oxidation and Scale Crystallization Kinetics of Hi-Nicalon^{TM}-S SiC Fibers*, pages 37–51. Mechanical Properties and Performance of Engineering Ceramics and Composites VI. John Wiley & Sons, Inc., 2011.

154. N. S. Jacobson and D. L. Myers. Active oxidation of SiC. *Oxidation of Metals*, 75(1-2):1–25, Feb 1, 2011.

155. R. S. Hay, G. E. Fair, A. Hart, S. Potticary, and R. Bouffioux. *Kinetics of Passive Oxidation of Hi-Nicalon-S SiC Fibers in Wet Air: Relationships between SiO2 Scale Thickness, Crystallization, and Fiber Strength*, pages 253–260. Mechanical Properties and Performance of Engineering Ceramics and Composites VII. John Wiley & Sons, Inc., 2012.

156. T. A. Parthasarathy, R. S. Hay, and M. K. Cinibulk. Modeling environmental degradation of sic fibers and cmcs. In *Proceedings of the 38th Annual Conference on Composites, Materials, and Structures*, January 27-31, 2014.

157. E. J. Opila. Variation of the oxidation rate of silicon carbide with water-vapor pressure. *Journal of the American Ceramic Society*, 82(3):625–636, 1999.

158. M. Takeda, A. Urano, J. Sakamoto, and Y. Imai. Microstructure and oxidative degradation behavior of silicon carbide fiber Hi-Nicalon type S. *Journal of Nuclear Materials*, 258-263, Part 2(0):1594–1599, Oct 1998.

159. J. J. Sha, J. S. Park, T. Hinoki, and A. Kohyama. Tensile behavior and microstructural characterization of SiC fibers under loading. *Materials Science and Engineering: A*, 456(1-2):72–77, May 15, 2007.

160. J. J. Sha, J. S. Park, T. Hinoki, A. Kohyama, and J. Yu. Tensile properties and creep behavior of SiC-based fibers under various oxygen partial pressures. *Pricm 5: the Fifth Pacific Rim International Conference on Advanced Materials and Processing, Pts 1-5*, 475-479:1333–1336, 2005.

161. J. J. Sha, J. S. Park, T. Hinoki, and A. Kohyama. Tensile properties and microstructure characterization of Hi-Nicalon (TM) SiC fibers after loading at high temperature. *International Journal of Fracture*, 142(1-2):1–8, Nov 2006.

162. J. J. Sha, T. Hinoki, and A. Kohyama. Thermal and mechanical stabilities of Hi-Nicalon SiC fiber under annealing and creep in various oxygen partial pressures. *Corrosion Science*, 50(11):3132–3138, Nov 2008.

163. J. J. Sha, T. Hinoki, and A. Kohyama. Microstructure and mechanical properties of Hi-Nicalon^{TM} type S fibers annealed and crept in various oxygen partial pressures. *Materials Characterization*, 60(8):796–802, Aug 2009.

164. R. S. Hay, G. Fair, E. Urban, J. Morrow, J. Somerson, and M. Wilson. *Oxidation Kinetics and Strength Versus Scale Thickness for Hi-Nicalon^{TM}-S SiC Fiber*, pages 105–112. Design, Development, and Applications of Engineering Ceramics and Composites: A Collection of Papers Presented at the 8th Pacific Rim Conference on Ceramic and Glass Technology. John Wiley & Sons, Inc., Hoboken, NJ, USA, Sep 29, 2010.

165. Y. Song, S. Dhar, L. C. Feldman, G. Chung, and J. R. Williams. Modified deal grove model for the thermal oxidation of silicon carbide. *Journal of Applied Physics*, 95(9):4953–4957, 2004.

166. S. Wu, L. Cheng, and L. Zhang. Oxidation behavior of 3D Hi-Nicalon/SiC composite exposed in wet and simulated air environments. *Corrosion Science*, 66:111–117, Jan 2013.

167. M. B. Ruggles-Wrenn, D. T. Christensen, A. L. Chamberlain, J. E. Lane, and T. S. Cook. Effect of frequency and environment on fatigue behavior of a CVI SiC/SiC ceramic matrix composite at 1200°C. *Composites Science and Technology*, 71(2):190–196, Jan 17, 2011.

168. M. B. Ruggles-Wrenn and V. Sharma. Effects of steam environment on fatigue behavior of two SiC/[SiC+Si3N4] ceramic composites at 1300°C. *Applied Composite Materials*, 18(5):385–396, Oct 1, 2011.

169. R. J. Kerans, R. S. Hay, T. A. Parthasarathy, and M. K. Cinibulk. Interface design for oxidation-resistant ceramic composites. *Journal of the American Ceramic Society*, 85(11):2599–2632, Nov 2002.

170. J. F. Bell. *Mechanics of Solids, Vol. 1: The Experimental Foundation of Solid Mechanics*. Springer-Verlag, New York, NY, 1984.

171. R. M. Morrell. A tensile creep-testing apparatus for ceramic materials using simple knife-edge universal joints. *Journal of Physics E: Scientific Instruments*, 5(5):465–467, 1972.

172. F. A. Kandil and B. F. Dyson. Tensile creep of ceramics: the development of a testing facility. *International Journal of High Technology Ceramics*, 4(2-4):243–262, 1988.

173. J. A. DiCarlo. Property goals and test methods for high temperature ceramic fibre reinforcement. *Ceramics International*, 23(4):283–289, 1997.

174. H. M. Yun, J. A. DiCarlo, and J. C. Goldsby. Tensile creep and stress-rupture behavior of polymer derived SiC fibers. NASA Tech Manual NASA TM–106692, Lewis Research Center, 1994.

175. R. E. Tressler, K. L. Rugg, S. W. Martz, V. M. Sglavo, and S. A. Newcomb. Delayed failure of ceramic fibers at elevated temperatures. *High Temperature Ceramic Matrix Composites I (HT-CMC-2)*, 1:375–380, 1995.

176. S. R. Choi, N. P. Bansal, and M. J. Verrilli. Delayed failure of ceramic matrix composites in tension at elevated temperatures. *Journal of the European Ceramic Society*, 25(9):1629–1636, 6 2005.

177. S. R. Choi and J. P. Gyekenyesi. Load-rate dependency of ultimate tensile strength in ceramic matrix composites at elevated temperatures. *International Journal of Fatigue*, 27(5):503–510, 5 2005.

178. M. B. Ruggles-Wrenn and T. Kutsal. Effects of steam environment on creep behavior of Nextel^{TM}720/aluminamullite ceramic composite at elevated temperature. *Composites Part A: Applied Science and Manufacturing*, 41(12):1807–1816, 12 2010.

179. M. B. Ruggles-Wrenn and J. C. Braun. Effects of steam environment on creep behavior of Nextel^{TM}720/alumina ceramic composite at elevated temperature. *Materials Science and Engineering: A*, 497(12):101–110, 12/15 2008.

180. M. B. Ruggles-Wrenn and C. L. Genelin. Creep of Nextel^{TM}720/alumina-mullite ceramic composite at 1200°C in air, argon, and steam. *Composites Science and Technology*, 69(5):663–669, 4 2009.

181. A. G. Evans. Slow crack growth in brittle materials under dynamic loading conditions. *International Journal of Fracture*, 10(2):251–259, 1974.

182. G. K. Bansal and W. H. Duckworth. Effects of moisture-assisted slow crack growth on ceramic strength. *Journal of Materials Science*, 13(2):239–242, 1978.

183. S. R. Choi and J. P. Gyekenyesi. Fatigue strength as a function of preloading in dynamic fatigue testing of glass and ceramics. *Journal of Engineering for Gas Turbines and Power*, 119(3):493–499, July 1 1997.

184. S. M. Wiederhorn. *Subcritical Crack Growth in Ceramics*, pages 613–646. Springer US, Jan 1, 1974.

185. AH Rashed. Properties and characteristics of silicon carbide. *POCO Graphite Inc., Decatur*, 2002.

186. F. C. Monkman and N. J. Grant. An empirical relationship between rupture life and minimum creep rate in creep-rupture tests. In *proc. ASTM*, volume 56, pages 593–620, 1956.

187. J. A. DiCarlo and H. M. Yun. Factors controlling stress rupture of fiber-reinforced ceramic composites. 1999.

188. J. A. DiCarlo and H. M. Yun. Fiber test development for ceramic composite thermomechanical properties. *ASTM Special Technical Publication*, 1392:134–147, 2000.

189. M. N. Menon, H. T. Fang, D. C. Wu, M. G. Jenkins, and M. K. Ferber. Creep and stress rupture behavior of an advanced silicon nitride: Part iii, stress rupture and the monkmangrant relationship. *Journal of the American Ceramic Society*, 77(5):1235–1241, 1994.

190. M. K. Ferber and M. G. Jenkins. Evaluation of the strength and creepfatigue behavior of hot isostatically pressed silicon nitride. *Journal of the American Ceramic Society*, 75(9):2453–2462, 1992.

191. S. Zhu, M. Mizuno, Y. Nagano, Y. Kagawa, and H. Kaya. Tensile creep behavior of a SiC-fiber/SiC composite at elevated temperatures. *Composites Science and Technology*, 57(12):1629–1637, 1997.

192. S. J. Zhu, M. Mizuno, Y. Nagano, J. W. Cao, Y. Kagawa, and H. Kaya. Creep and fatigue behavior in an enhanced SiC/SiC composite at high temperature. *Journal of the American Ceramic Society*, 81(9):2269–2277, Sep 1998.

193. C. J. Armani, M. B. Ruggles-Wrenn, R. S. Hay, and G. E. Fair. Creep and microstructure of Nextel 720 fiber at elevated temperature in air and in steam. *Acta Materialia*, 61(16):6114–6124, Sep 2013.

194. Clinton J. Armani, Marina B. Ruggles-Wrenn, Geoff E. Fair, and Randall S. Hay. Creep of Nextel^{TM} 610 fiber at 1100°C in air and in steam. *International Journal of Applied Ceramic Technology*, 10(2):276–284, 2013.

195. J. A. DiCarlo and H. M. Yun. Factors controlling stress-rupture of fiber reinforced ceramic composites. *P ICCM 12 PAR FRANC*, 1999.

196. J. B. Hurst, A. Calomino, and G. Bakalini. In *Proceedings of the 25th Annual Conference on Composites, Materials and Structures*, 2001.

197. S. Zhu, M. Mizuno, Y. Kagawa, J. Cao, Y. Nagano, and H. Kaya. Creep and fatigue behavior in hi-nicalon-fiber-reinforced silicon carbide composites at high temperatures. *Journal of the American Ceramic Society*, 82(1):117–128, 1999.

198. R. S. Hay. Private communication, 2015.

199. J. Y. Yen and J. G. Hwu. Enhancement of silicon oxidation rate due to tensile mechanical stress. *Applied Physics Letters*, 76(14):1834–1835, Apr 3, 2000.

200. J. Y. Yen and J. G. Hwu. Stress effect on the kinetics of silicon thermal oxidation. *Journal of Applied Physics*, 89(5):3027–3032, Mar 1, 2001.

201. O. F. Tuttle and J. L. England. A preliminary report on the system SiO_2 - H_2O. *Bulletin, Geological Society of America*, 66:149–152, 1955.

202. N. S. Jacobson, E. J. Opila, D. L. Myers, and E. H. Copland. Thermodynamics of gas phase species in the SiOH system. *The Journal of Chemical Thermodynamics*, 37(10):1130–1137, 10 2005.

203. P. Mogilevsky. Private communication, 2015.

Vita

Scott J. Robertson is a Major in the United States Air Force and a PhD Candidate in Materials Engineering at the Air Force Institute of Technology, Wright-Patterson Air Force Base, Ohio. He began his professional career in 2002, graduating from Brigham Young University with a BS in Mechanical Engineering and earning a commission as a Second Lieutenant via the Reserve Officer Training Corps. While assigned to the Air Force Research Laboratory in Rome, New York, Scott applied his engineering degree in structural design and analysis in support of antenna testing on the F-15, F-22, F-35, and C-130 platforms. While in Rome, he earned his MS in Mechanical Engineering from National Technological University, which became the science and technology arm of Walden University, in 2005. From there, he was assigned to Warner Robins Air Logistics Center where he conducted flight tests of structural components, software, and hardware systems, on C-130, C-5, and HH-60 aircraft. Major Robertson then moved on to the Air Force Academy, where he taught courses in mechanics, structures, computer-aided design and engineering, served as an Academic Division Chief and attained the academic rank of Assistant Professor. Major Robertson began his PhD program at AFIT in the Fall of 2012.

REPORT DOCUMENTATION PAGE

Form Approved
OMB No. 0704–0188

The public reporting burden for this collection of information is estimated to average 1 hour per response, including the time for reviewing instructions, searching existing data sources, gathering and maintaining the data needed, and completing and reviewing the collection of information. Send comments regarding this burden estimate or any other aspect of this collection of information, including suggestions for reducing this burden to Department of Defense, Washington Headquarters Services, Directorate for Information Operations and Reports (0704–0188), 1215 Jefferson Davis Highway, Suite 1204, Arlington, VA 22202–4302. Respondents should be aware that notwithstanding any other provision of law, no person shall be subject to any penalty for failing to comply with a collection of information if it does not display a currently valid OMB control number. **PLEASE DO NOT RETURN YOUR FORM TO THE ABOVE ADDRESS.**

1. REPORT DATE *(DD–MM–YYYY)*	2. REPORT TYPE	3. DATES COVERED *(From — To)*
26–12–2015	DISSERTATION	August 2012 — December 2015

4. TITLE AND SUBTITLE

Creep of Hi-Nicalon^{TM} S Ceramic Fiber Tows at 800°C in Air and in Silicic Acid-Saturated Steam

5a. CONTRACT NUMBER

5b. GRANT NUMBER

5c. PROGRAM ELEMENT NUMBER

6. AUTHOR(S)

Robertson, Scott J., Major, USAF

5d. PROJECT NUMBER

5e. TASK NUMBER

5f. WORK UNIT NUMBER

7. PERFORMING ORGANIZATION NAME(S) AND ADDRESS(ES)

Air Force Institute of Technology
Graduate School of Engineering and Management (AFIT/EN)
2950 Hobson Way
WPAFB OH 45433-7765

8. PERFORMING ORGANIZATION REPORT NUMBER

AFIT-ENY-DS-15-S-067

9. SPONSORING / MONITORING AGENCY NAME(S) AND ADDRESS(ES)

AFRL/RXCC (Dr. Randall Hay)
2977 Hobson Way
Wright-Patterson AFB, OH 45433-7734
(937) 255-9825, Randall.Hay@us.af.mil

10. SPONSOR/MONITOR'S ACRONYM(S)

AFRL/RXCC

11. SPONSOR/MONITOR'S REPORT NUMBER(S)

12. DISTRIBUTION / AVAILABILITY STATEMENT

Distribution Statement A. Approved for Public Release;Distribution Unlimited.

13. SUPPLEMENTARY NOTES

This material is declared a work of the U.S. Government and is not subject to copyright protection in the United States.

14. ABSTRACT

The mechanical behavior of Hi-Nicalon^{TM} Type S fiber tows was investigated in air and in silicic acid-saturated steam environments at 800°C. A facility was demonstrated that successfully resolved problems highlighted by previous attempts to study SiC fibers in steam. Monotonic tension and creep tests were conducted to characterize the fibers. The tensile strength of the fibers showed little dependence on applied stress rate, indicating a resistance to environmentally assisted crack growth. Climb-controlled diffusion in air and grain boundary sliding in silicic acid-saturated steam were the dominant damage mechanisms. Silicic acid-saturated steam had a degrading effect on the mechanical performance of the fibers, but much less than unsaturated steam environments. The Monkman-Grant relationship was demonstrated for Hi-Nicalon^{TM} S fibers and may be used to predict creep lifetime of fibers, fiber tows, and CMCs. Microstructural analysis showed a dependence of oxide thickness on applied stress.

15. SUBJECT TERMS

SiC, fiber tow, ceramics, composites, steam, silicic acid, oxidation

16. SECURITY CLASSIFICATION OF:			17. LIMITATION OF ABSTRACT	18. NUMBER OF PAGES	19a. NAME OF RESPONSIBLE PERSON
a. REPORT	b. ABSTRACT	c. THIS PAGE			Dr. Marina B. Ruggles-Wrenn
U	U	U	UU	314	19b. TELEPHONE NUMBER *(include area code)* (937) 255-3636, x4641; mruggles@afit.edu